RUTHENIUM COMPLEXES AS MOLECULAR WATER OXIDATION CATALYSTS

Abolfazl Ghaderian

UNIVERSITAT ROVIRA i VIRGILI

Ruthenium complexes as molecular water oxidation catalysts

Abolfazl Ghaderian

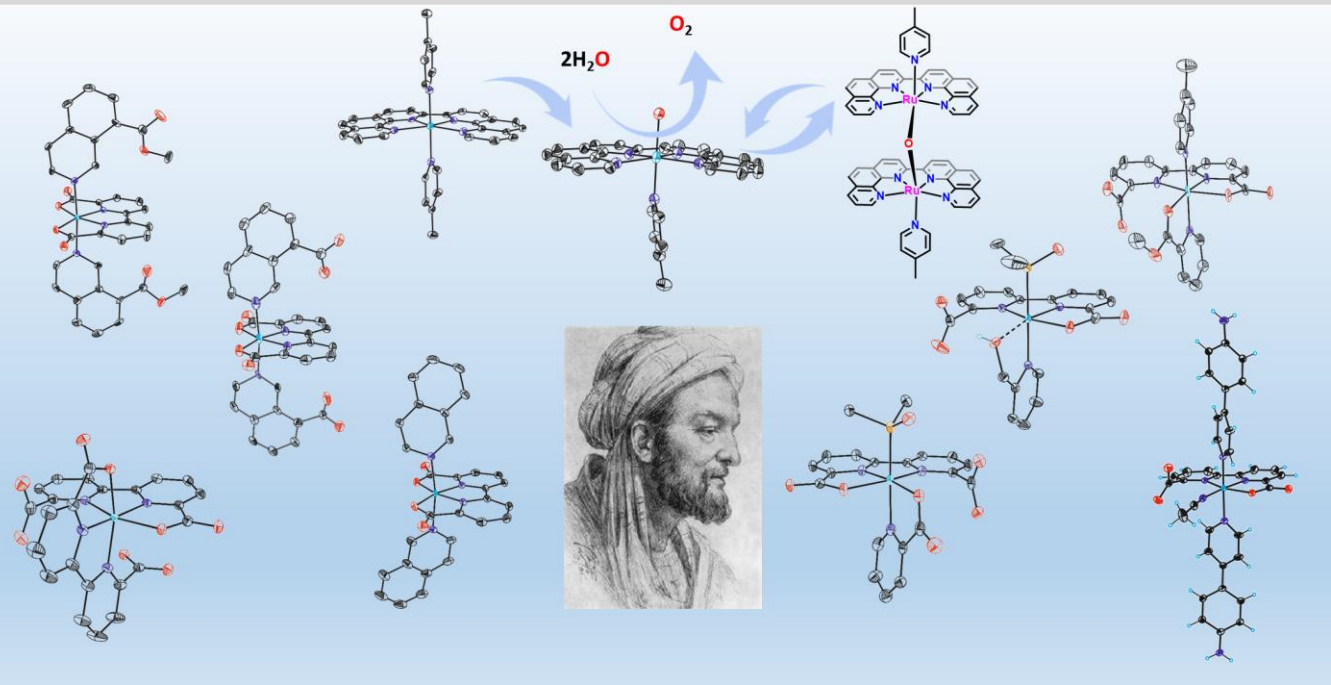

DOCTORAL THESIS
2020

UNIVERSITAT ROVIRA I VIRGILI
RUTHENIUM COMPLEXES AS MOLECULAR WATER OXIDATION CATALYSTS
Abolfazl Ghaderian

Abolfazl Ghaderian

Ruthenium complexes as molecular water oxidation catalysts

DOCTORAL THESIS

Supervised by

Prof. Antoni Llobet

&

Dr. Carolina Gimbert-Suriñach

Institute of Chemical Research of Catalonia

Tarragona

2020

UNIVERSITAT ROVIRA I VIRGILI
RUTHENIUM COMPLEXES AS MOLECULAR WATER OXIDATION CATALYSTS
Abolfazl Ghaderian

ICIQ - Institut Català d'Investigació Química

Avinguda Països Catalans 16,

43007 Tarragona (Spain)

As the supervisors of the Thesis, entitled "Ruthenium complexes as molecular water oxidation catalysts", presented by Abolfazl Ghaderian for the award of the degree of Doctor, we state that it has been carried out under our supervision at the Institute of Chemical Research of Catalonia (ICIQ).

Tarragona, November 26th, 2019

Doctoral Thesis Supervisors

Prof. Antoni Llobet

Dr. Carolina Gimbert-Suriñach

UNIVERSITAT ROVIRA I VIRGILI
RUTHENIUM COMPLEXES AS MOLECULAR WATER OXIDATION CATALYSTS
Abolfazl Ghaderian

Acknowledgements

The work performed in the present doctoral thesis has been possible thanks to the Institute of Chemical Research of Catalonia (ICIQ), Rovira i Virgili University (URV) and the funding of: MINECO for a FPI grant (BES-2015-073069) and Support from MINECO, FEDER and AGAUR are gratefully acknowledged through grants CTQ2016-80058-R, CTQ2015-73028-EXP, SEV 2013-0319, ENE2016-82025-REDT, CTQ2016-81923-REDC, and 2017-SGR-1631.

List of publications

Matheu, R.; **Abolfazl Ghaderian**; Francàs, L.; Chernev, P.; Ertem, M. Z.; Benet-Buchholz, J.; Batista, V. S.; Haumann, M.; Gimbert-Suriñach, C.; Sala, X.; Llobet, A., Behavior of Ru–bda Water-Oxidation Catalysts in Low Oxidation States. ***Chemistry – A European Journal***, 24 (**2018**) (49), 12838-12847.

Table of contents:

Graphical Abstracts

Chapter 1. General Introduction

This chapter presents the importance of renewable and clean energy in the context of the energy crisis and global warming. Natural photosynthesis is introduced and discussed briefly for its key role as a source of inspiration. Afterwards, the main factors for designing active and robust artificial catalysts for the water oxidation reaction are highlighted, followed by a detailed description of the mechanisms involved in artificial photosynthesis processes and in particular in the water oxidation to dioxygen reaction. Finally, a collection of the most relevant water oxidation catalysts is presented with main focus on the two families of complexes that have been developed in this PhD thesis.

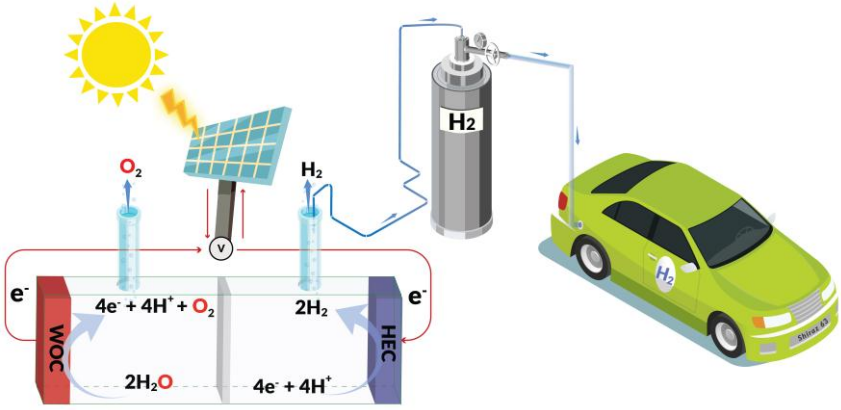

Chapter 2. Objectives

According to the challenges in the field of artificial photosynthesis and water oxidation catalysis addressed in Chapter 1, the objectives of the thesis are presented in the present chapter.

Chapter 3. Behavior of the Ru-bda water oxidation catalysts at low oxidation states

The multiple equilibria involved in complexes with the general formula [Ru(κ-N^2O^2-bda)$(L)_2$] (where bda = 2,2'-bipyridine-6,6'-dicarboxylate; L = monodentate axial ligand) in aqueous and organic solutions in low oxidation states are investigated. Moreover, the coordination modes of derivative complexes with general formula [Ru(κ-N^2O^1-bda)(X)$(L)_2$] (where X = NO^+, MeCN, or H_2O) are studied in the solid state through single-crystal x-ray diffraction, X-ray absorption spectroscopy, and in solution by variable-temperature NMR spectroscopy. DFT calculations are used to support the experimental findings.

Chapter 4. Water oxidation catalysis by Ru-bda complexes with isoquinoline axial ligands. Second coordination sphere effects

The goal of this chapter is the preparation of two ruthenium complexes of the Ru-bda family with isoquinoline axial ligands containing substituents in close proximity to the active catalytic center. A comprehensive structural and electrochemical characterization of the two compounds uncovers unexpected catalytic behaviour and give new clues on the factors that control the activity of these type of catalysts.

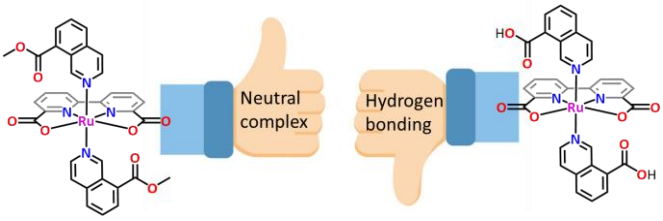

Chapter 5. A Ru-bda complex with a dangling carboxylate group: synthesis and electrochemical properties

The preparation of non-symmetric mononuclear ruthenium complexes of the Ru-bda family is described. Their structural and electrochemical characterization are presented and thoroughly discussed and compared with related Ru complexes. This work highlights the importance of geometry around the ruthenium metal center in complexes that are active for the water oxidation catalysis, as well as the ability of high valent Ru=O groups to intramolecularly oxidize neighboring aliphatic moieties.

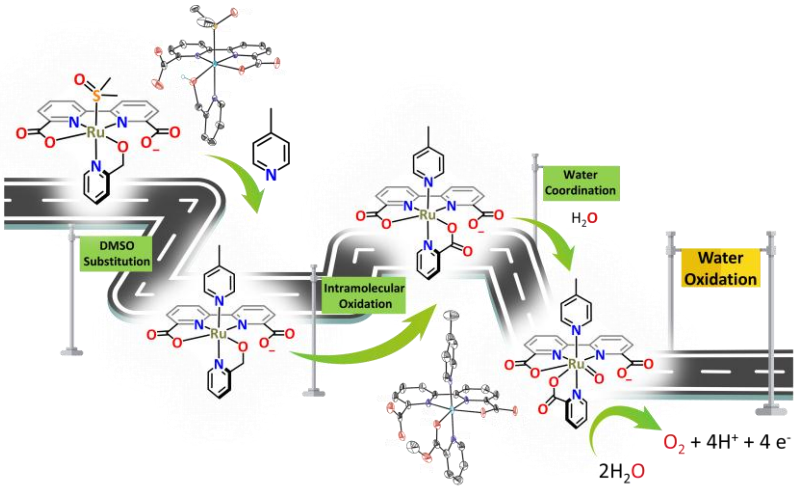

Chapter 6. A broad view at the complexity involved in water oxidation catalysis based on Ru-bpn complexes

A new Ru complex with general formula $[Ru(bpn)(pic)_2]Cl_2$ (where bpn is 2,2'-bi(1,10-phenanthroline) and pic stands for picoline) is prepared and fully characterized. Its transformation to a monomeric Ru-OH_2 complex active for the water oxidation reaction is studied in detail. We find that the latter evolves to a dimeric complex that is not active but that can serve as precursor of the monomeric active compound upon applying a reductive potential. A thorough spectroscopic and kinetic study allowed to have a full understanding of the whole process for the first time in this type of complexes.

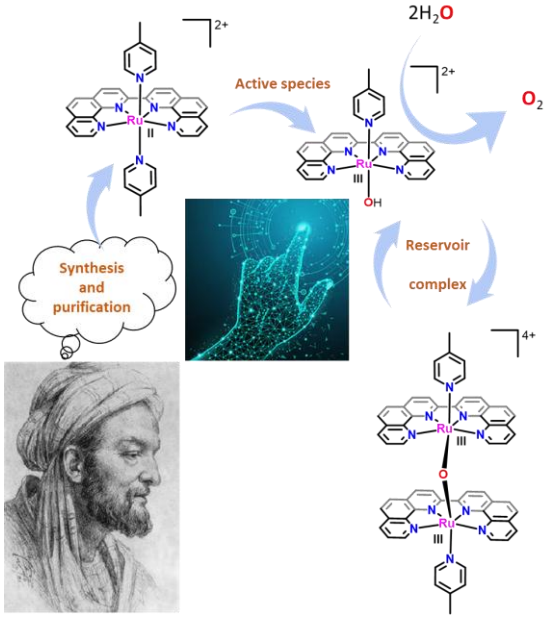

Chapter 7. Conclusions

An overview of the most important conclusions of the thesis is given in this chapter.

Chapter 1

Introduction

1·1-Natural photosynthesis as a source of inspiration

While the population increases, demand for a cheap source of energy such as fossil fuels soars and global warming increases, leading to devastating environmental impacts and health problems. Hence, finding a cheap and sustainable source of energy not only helps stopping the energy crisis, but also avoiding the undesired global warming phenomenon and its contamination consequences. One of the most abundant energy sources is sunlight which has been used in nature for the billions of years, by plants, algae and cyanobacteria through their photosynthetic systems. In the natural photosynthetic process, light is harvested and used to produce O_2 and carbohydrates, the latter being the main source of energy (fuel) of living organisms. The process takes place in chloroplasts, which have four main proteins called photosystem II (PSII), photosystem I (PSI), cytochrome b_6f complex (Cyt b_6f), and ATP Synthase (Figure 1).[1] The whole process will be discussed briefly for their relevance as inspiration to artificial photosynthetic systems.

Harvesting light in PSII results in charge separation generating an electron-hole pair in the picosecond timescale which contains the so called radical anion $Pheo^{\cdot-}$ (which is made by pheophytin) and radical cation $P680^{\cdot+}$.[2] The latter acts as oxidizing species with an oxidation potential of + 1.2 to + 1.3 V, the highest reported in biology, which triggers the demanding water oxidation to dioxygen reaction taking place in the oxygen evolving center (OEC).[3] Several electrons and protons produced in the water oxidation process are transferred by Cyt b_6f to PSI. Consequently, they are consumed for making bio-reducing agents such as adenosine triphosphate (ATP), by ATP Synthase, that creates the energy storage molecule ATP, and nicotinamide adenine dinucleotide phosphate hydrogen (NADPH) to be used in the Calvin cycle to reduce CO_2 to valuable carbohydrates (Figure 1).

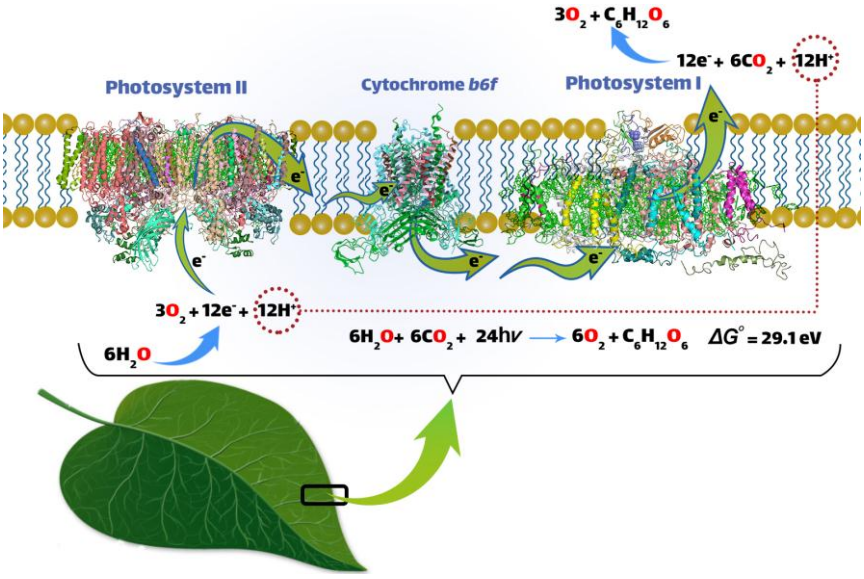

Figure 1. Schematic representation of the natural photosynthesis process.

1·2-The oxygen evolving center (OEC) and the Kok cycle

The high resolution structure of PSII was reported in 2011 at a resolution of 1.9 Å (Figure 2). The map of electron density showed that the reaction center called the oxygen evolving center (OEC) compromises 5 metals in a chair shape (four Manganese atoms, called Mn1, Mn2, Mn3, Mn4, and one Calcium atom) connected together through 5 oxygen atoms used as oxo-bridges which make the full Mn_4CaO_5 cluster. Two water molecules are coordinated to Ca and two of them coordinated to Mn4. It is proposed that these water molecules are involved in the water oxidation process (see Kok cycle below).[4] Ca has seven ligands in this structure, three μ_3-O, two bridging -COO^- and two H_2O molecules. The ligands around Mn4 are one μ_4-O, one μ_2-O, two bridging -COO^- and two water molecules (Figure 2).[4-5]

The OEC cluster is connected to the PSII protein by two hydrogen-bonded water networks which have a very important role in absorbing water as a substrate for water oxidation. The main hydrogen bonded water networks are mediated by D1-Tyr 161 (called YZ) that connects PSII reaction center and Mn_4CaO_5 cluster and the

second one are the two Cl^- binding sites that are at the entrance of the bulk solution of tubular organ towards the Mn_4CaO_5 cluster. Moreover, these two Cl^- anions also have a structural role to maintain the environment of the Mn_4CaO_5 cluster. Interestingly, replacing Cl^- by Br^- does not change the activity but it changed when it was replaced with I^- which inhibited water oxidation.[6]

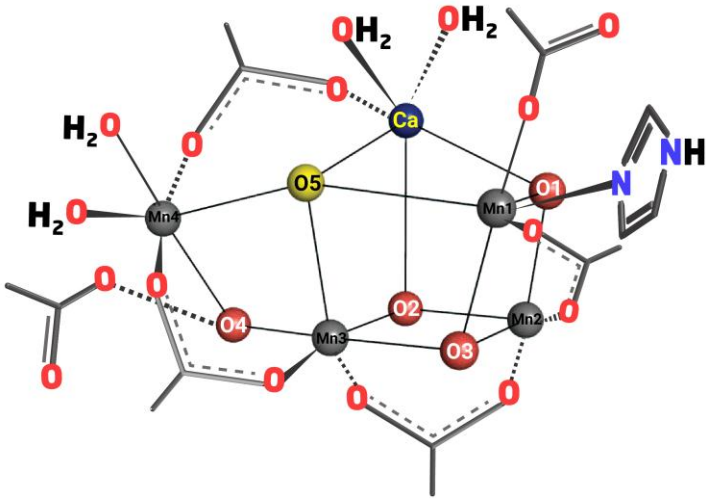

Figure 2. The structure of the $CaMn_4O_5(H_2O)_4$ cluster (OEC) that resembles a distorted chair, with an asymmetric cubane.

In 1969, Pierre Joliot discovered that PSII releases oxygen after four light flashes. This data showed that charge separation and storing oxidizing equivalents are necessary before one O_2 molecule releases. Moreover, this data is in line with water oxidation producing a single O_2 molecule by 4 e^- process.[7] In 1970, Kok *et al*. suggested a water oxidation cycle for O_2 evolving by four light absorption steps (Figure 3). It includes five states from S_0 to S_4, during which the manganese atoms of the OEC are oxidized by light and protons are released in a concerted manner, avoiding charge build up and facilitating the process. Finally, O_2 releases from the S_4 state closing the catalytic cycle.

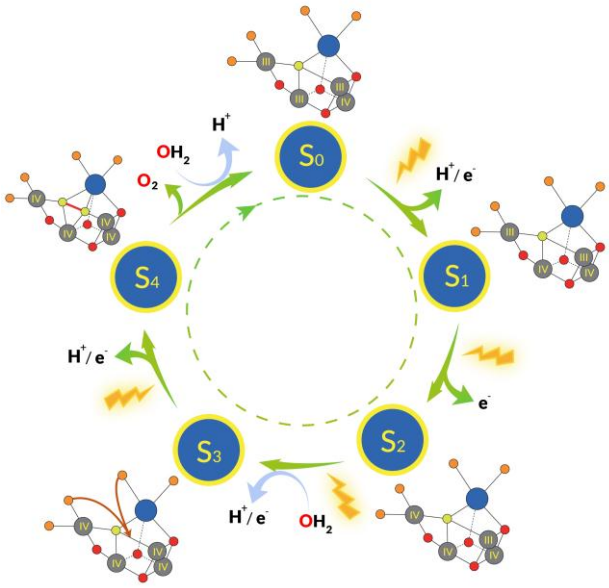

Figure 3. Kok cycle includes 5 basic states of the oxygen evolving center (S_0 to S_4) through which 2 water molecules are oxidized to give one oxygen molecule, 4 e^-, and 4 H^+, by the action of four light absorption steps. The oxidation state of each Mn atom within the cluster is indicated next to each state.

1·3-Artificial Photosynthesis

The natural photosynthesis process has been the source of inspiration of many researchers to develop clean and sustainable fuels that should replace fossil fuels thus contributing in solving the energy problem and avoiding global warming bad consequences. In a broad interpretation, these fuels could be derived from the reduction of abundant small molecules existing on the earth and atmosphere, such as N_2, CO_2, and H_2O (Figure 4 and Eq. 1-3).[8]

Ammonia production by the Haber-Bosch process, which uses N_2 gas, is a classic example to illustrate the potential of mimicking photosynthesis (Eq. 1). Ammonia is the main source for fertilizer production, used for cultivation. The percentage of N_2 in air is 78.09 %, which is an abundant source to be converted to ammonia.

However, the currently used industrial process uses high temperature and pressure conditions leading to an enormous energy consumption that is unfavorable for the increasing energy demand. Thus finding a process to undergo the reaction in Eq. 1 triggered by sunlight is of paramount importance.

On the other hand, carbon dioxide (CO_2) in the atmosphere can be a feedstock for production of liquid hydrocarbons, chemicals, polymers and so on in a parallel fashion to the natural process (Eq. 2 and Figure 1).

Finally, water, which covers 70.9 % of the earth, could potentially be used to generate hydrogen gas, which is a clean and fully renewable fuel.

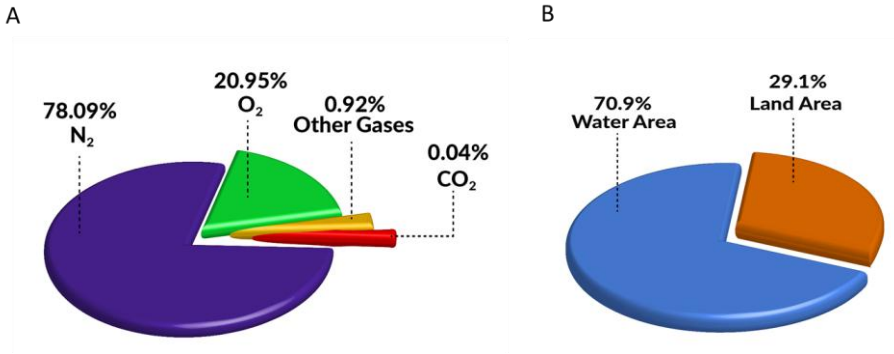

Figure 4. A) The percentages of N_2 (78.09 %), O_2 (20.95 %), and CO_2 (0.04 %) in the air, B) The percentage of water (70.9 %) and land area (29.1%) on the earth.

For the reduction of any of these molecules, reducing equivalents should ideally be provided by the oxidation of water to dioxygen, as it happens in the natural system (Eq. 4 and Figure 1). Therefore, the investigation of artificial catalysts for the water oxidation to dioxygen reaction inspired by the oxygen evolving center in nature is an active area of research and is the main topic of the present PhD thesis.

Reduction half-reactions

$N_2 + 6H^+ + 6e^- \longrightarrow 2\,NH_3$ Eq. 1

$CO_2 + 6H^+ + 6e^- \longrightarrow CH_3OH + H_2O$ Eq. 2

$2H^+ + 2e^- \longrightarrow H_2$ Eq. 3

Oxidation half-reaction

$2\,H_2O \longrightarrow O_2 + 4H^+ + 4e^-$ Eq. 4

Artificial photosynthesis devices and applications

In order to make a device for converting sunlight into energy, a suitable assembly of the light harvesting entity and the catalysts for the water oxidation (Eq. 4) and reduction reactions (Eq.1-3) is needed. The two half-reactions take place in two compartments, separated by an ion exchange membrane and connected with an external wire through the electrodes (Figure 5). The membrane allows the free movement of ions between the two compartments and avoids back reactions while the external wire completes the circuit for electron flow from the anodic side to the cathodic side. There are two ways to use catalysts in the anodic and cathodic compartments: (i) dissolve them in the solution (ii) or anchor them onto the electrode without changing the intrinsic catalytic properties of catalysts. From a practical point of view, the second is preferable because it is technologically more feasible to implement and scale-up. It also avoids diffusion of homogeneous catalyst to the second compartment through the membrane.

There are two main ways of introducing the light harvesting entity. The most straightforward one is to connect a photovoltaic (PV) device into an electrolyzer (Figure 5). The second one involves the use of one or two photoelectrode in a photoelectrochemical cell. A photoelectrode is made of a semiconductor with suitable band gap, or a semiconductor connected to a dye molecule to modulate the band gap. A suitable semiconductor or semiconductor/dye assembly must have: (i) large absorbance in the visible region; (ii) fast photo induced electron transfer

after excitation; and (iii) a proper oxidation/reduction potential to drive the desired reaction (Eq. 1-4).[9] Most of the time the semiconductor or semiconductor/dye assembly themselves are not able to perform the chemical reactions or if they do, it is too slow to be relevant and therefore a suitable catalyst is usually deposited on the surface of the photoelectrode.

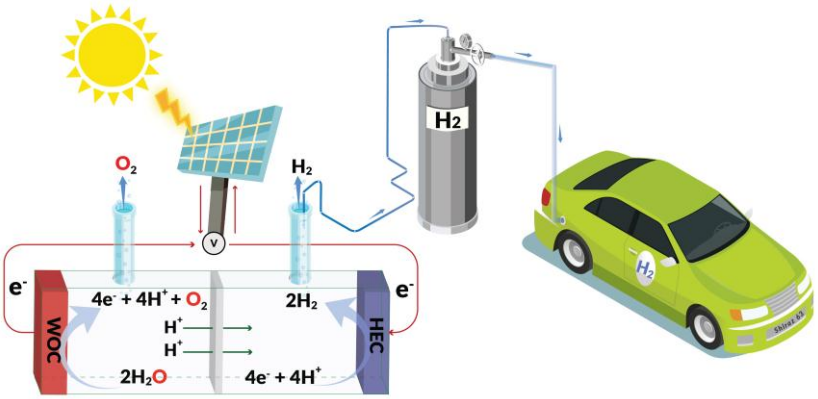

Figure 5. Representative example of an artificial photosynthesis device, in particular for water splitting, made of a photovoltaic cell connected to an electrolyzer (PV-EC). The electrolyzer contains an anode with the water oxidation catalyst, a cathode with the proton reduction catalyst and a membrane separating the two compartments cell.

1·4-Water oxidation with molecular catalysts

1·4·1-Challenge of the reaction and catalyst design

The water oxidation to dioxygen reaction (Eq. 4) is thermodynamically unfavorable ($\Delta G°$= 474.71 kJ mol^{-1}) and kinetically very complex as it involves the transfer of four electrons, four protons and the generation of an O-O bond.[10] As a consequence, the elucidation of water oxidation reaction mechanisms including determination of the rate limiting step, as well as producing catalysts with high durability and activity (rate) are the main goals of the research in this field.

Increasing the rate of a reaction can be achieved by either (i) increasing number of active centers, increasing loading of catalysts or designing polynuclear species[11] or

(ii) increasing the intrinsic activity of a specific catalyst. Taking into account the physical limitation of using multi centers catalysts, for example mass and charge transfer in electrochemical process[12] and low solubility in homogeneous catalysis,[12] the first approach based on increasing the number of reaction sites will be much limited than the second one, based on increasing the intrinsic activity. In addition, the experimental data in electrochemical measurement showed that the difference between a strong catalyst with high activity and a poor catalyst is 10 orders of magnitude;[13] however, the difference between low and high loading of a catalyst can change from one to three.[14] Atom economy is also very important in industrialization, and so, a single site catalyst that is faster will be preferentially selected before a less active mono- or multinuclear catalyst with lower performance.

In this context, there are several advantages in using mononuclear metal complexes: (i) design, synthesis and characterization of catalytic and intermediate species is much easier than in the case of a multinuclear complex, (ii) it is possible to change the mechanism, stability and efficiency (iii) kinetic studies with mononuclear complexes are simpler, (iv) from a commercializing point of view, combing several properties in one molecule is desirable.[15]

In order to design a water oxidation catalyst with high intrinsic activity several factors must be considered. Firstly, at least one H_2O must coordinate to the metal center. This will allow the complex to reach high oxidation states in a relatively narrow potential range by proton coupled electron transfer (PCET) processes that avoid building charge on the complex (see section 1·4·2 below). Secondly, water oxidation needs 1.23 V vs NHE (pH 0), as a consequence, the complex needs a ligand frame work with high stability in a wide range of pHs. Third, the metal center must have the ability to reach high oxidation states. Fourth, the presence of auxiliary ligand can have a strong effect on the mechanism of the reaction.

In order to comply with all the requirements described above, a careful design of the catalyst is needed. In this context, the versatility of molecular complexes provided by ligand framework and choice of the metallic center is key for successful development of more efficient catalysts. An illustrative example on how tuning the coordination sphere of a metal center can influence its reactivity is given in Scheme 1 for three mononuclear complexes. Despite, having the same metal center (ruthenium) and similar ligands based on pyridines, complexes **1**, **2** and **3** catalyze reactions as diverse as water oxidation,[16] hydrogen and oxygen evolvtion [17] or CO_2 reduction, respectively.[18] This is a consequence of the electronic and geometric structures of the ruthenium cores, which are precisely adjusted by the particular coordination environments created by the ligands. Thus, a molecular catalyst usually comprises a metal center as the active site and specific organic ligand(s) to produce the correct coordination environment for regulating the electronic structure of the active site.

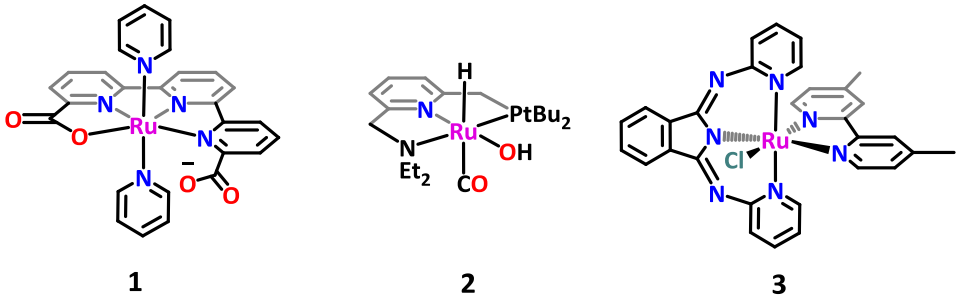

1 **2** **3**

Scheme 1. (Left) water oxidation catalyst, (middle) water splitting catalyst, (right) CO_2 reduction catalyst.

1·4·2-Mechanism of the water oxidation reaction

Proton-Coupled Electron Transfer Processes

Proton coupled electron transfer (PCET) was discovered as a result of the comproportionation reaction between $[Ru^{IV}=O]^{2+}$ and $[Ru^{II}\text{-}OH_2]^{2+}$ for production of $[Ru^{III}\text{-}OH]^{2+}$ in 1981.[19] PCET is a process that involves the transfer of protons and

electrons in a concerted manner. It allows to store multiple redox equivalents at a single site metal or cluster avoiding the building of charge at the metal center or cluster. An illustrative example of PCET is given by ruthenium-aquo complexes used in water oxidation catalysis (Ru-OH_2, Eq. 5 and 6). PCET gives access to reactive high oxidation states at relatively low potential and makes possible the catalysis of the demanding water oxidation reaction with the high thermodynamic potential of 1.23 V vs NHE.

Ru^{III}-OH + $1H^+$ + $1e^-$ → Ru^{II}-OH_2 Eq. 5 (PCET)

Ru^{IV}=O + $1H^+$ + $1e^-$ → Ru^{III}-OH Eq. 6 (PCET)

Ru^{IV}=O + $1e^-$ → $[Ru^{V}=O]^+$ Eq. 7 (Electron Transfer)

PCET are ubiquitous in biology, for instance in the oxidation of water to dioxygen by the OEC in PSII as described in detailed earlier (Kok cycle, section 1·2). Overall, natural photosynthesis involves the transfer of $24e^-$ and $24H^+$ as result of 48 photons consumption. In this reaction, water oxidation coupled with CO_2 reduction, stores 29.1 eV. This process stores 10^{11} tons of carbon which equals to 10^{18} kJ of energy.

A useful tool to identify and analyze PCET processes are Pourbaix diagrams, which provide precise information about the different redox potentials of a compound as a function of pH as well as the zone of predominance of the different species depending on their degree of protonation and oxidation states. From careful examination of these diagrams, it is possible to ascertain Nerstian behaviours, indicative of PCET.[20] For instance, a slope of -59 mV per pH unit, will indicate that a concerted loss of proton(s) and electron(s) (PCET) is taking place, while a slope of -29 mV per pH unit, will indicate that a single proton loss occurs per every two electron transfer process. Finally, a slope of -118 mV per pH unit, will indicate that per every two proton loss process, a single electron transfer occurs.

The O-O bond formation step

Once a high valent metal-oxo (M-O) species has been formed through PCET (Eq. 5-7), the oxygen-oxygen bond formation can take place in two different pathways (Figure 6): (i) water nucleophilic attack (WNA) from a solvent water molecule to the M-O, (ii) Interaction between two M-O entities, called I2M which can happen in an inter or intra-molecular fashion. In the former case, the driving force of the reaction is the energy difference between LUMO (*lowest unoccupied molecular orbital*) of the metal-oxo and HOMO (*highest occupied molecular orbital*) of H_2O, whilst the driving force for later is radical coupling between two entities. The final step of the catalytic process is the Metal-O cleavage liberating the oxygen molecule. Figure 6 shows the WNA, and I2M mechanism for Ru molecular complexes. [21]

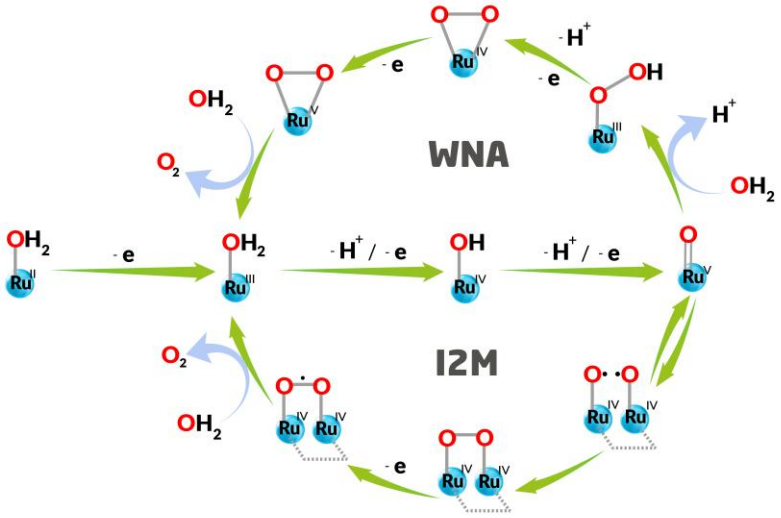

Figure 6. General mechanistic pathways for molecular water oxidation catalysis using ruthenium as metal center. Top, water nucleophilic attack (WNA). Bottom, interaction between two M–O entities in an inter or intra-molecular fashion (I2M).

Two examples of catalysts that follow the WNA and I2M mechanisms are $[Ru(tpy)(bpm)(OH_2)]^{2+}$ (complex **10** Scheme 2, where tpy is 2,2′:6′,2′′-terpyridine; bpm is 2,2′-bipyrimidine), and $[Ru(bda)(pic)_2]$ (complex **15** Scheme 3, where bda is

2,2´-bipyridine-6,6´-dicarboxylate, and pic stands for 4-methylpyridine), respectively, which will be briefly discussed in the following paragraphs.

In 2008, intensive mechanistic investigations were performed on $[Ru(tpy)(bpm)(OH_2)]^{2+}$ by Meyer *et al*. to disclose the mechanism of single site water oxidation catalysts. They used this catalyst because it showed slow water oxidation activity with Ce^{IV} as sacrificial agent in acidic pH, allowing to trap possible catalytic intermediates. The results showed that after one electron oxidation of $Ru^{IV}=O$ to give $Ru^{V}=O$ (or after adding 3 equivalents of Ce^{IV} to Ru^{II}-OH_2) (Eq. 8), one water molecule would attack the complex in its high oxidation state. By tentative interpretation of the UV-visible spectral changes (in particular at λ = 283 nm) it was suggested that the hydroperoxo complex $[Ru^{III}(tpy)(bpm)(OOH)]^{2+}$ (Ru^{III}-OOH) (Eq. 9) formed and after a new oxidation to $[Ru^{IV}(tpy)(bpm)(OO)]^{2+}$, O_2 released on a time scale of minutes to give $[Ru(tpy)(bpm)(OH_2)]^{2+}$ (Ru^{II}-OH_2) (Eq. 10 and 11).

$$Ru^{IV}=O + Ce^{IV} \longrightarrow Ru^{V}=O + Ce^{III} \quad \text{Eq. 8}$$

$$Ru^{V}=O + H_2O \longrightarrow Ru^{III}\text{-}OOH + H^{+} \quad \text{Eq. 9}$$

$$Ru^{III}\text{-}OOH + Ce^{IV} \longrightarrow Ru^{IV}\text{-}OO + H^{+} + Ce^{III} \quad \text{Eq. 10}$$

$$Ru^{IV}\text{-}OO + H_2O \longrightarrow Ru^{II}\text{-}OH_2 + O_2 \quad \text{Eq. 11}$$

Based on DFT (Density Functional Theory) calculations, the peroxo ligand coordinates to the metal center as a bidentate ligand and thus, the Ru center will be seven-coordinated. The crystal structure of seven-coordinated Ru has been reported before.[22] Moreover, DFT calculations supported that the reaction of $Ru^{V}=O$ with water is more favorable than the same reaction with $Ru^{IV}=O$ to release O_2, with $\Delta G°' = -0.90$ eV. In addition, DFT calculations illustrated that highly oxidized Ru=O species have ‘‘oxyl’’ character at the oxygen and thus has a more accessible LUMO

(lower energy), which make it a better acceptor facilitating O-O bond formation at the oxo.[23] The rate limiting step of the reaction (r.d.s) depends on the catalyst and reaction conditions usually can stand for the oxidation of Ru^{III}-OH to Ru^{IV}=O, O…O bond formation, and releasing O_2 from Ru^{IV}(OO). The whole water oxidation process is shown in Figure 7, together with side pathways that were also considered in the study of different Ru catalysts in different reaction conditions.

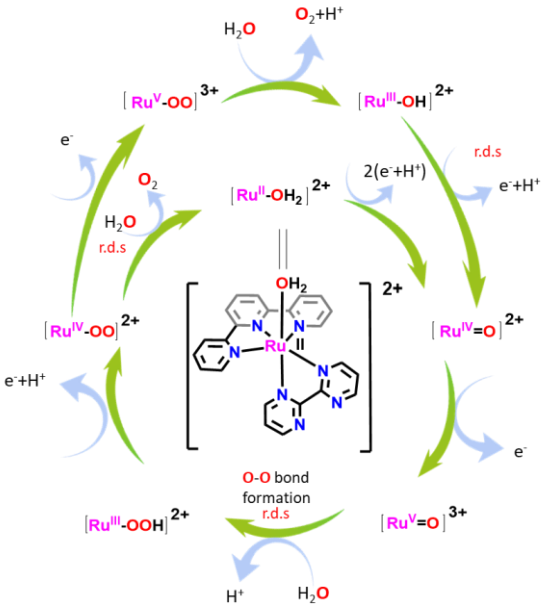

Figure 7. Proposed water oxidation mechanism by $[Ru(tpy)(bpm)(OH_2)]^{2+}$ (complex **10** scheme 2) based on a water nucleophilic attack (WNA) mechanism.[24]

One of the classic examples for the I2M mechanism is $[Ru(bda)(pic)_2]$ that was reported by L. Sun *et al.* in 2009.[25] A few years later, a mechanistic study under stoichiometric Ce^{IV} conditions at pH 1 disclosed the mechanism involved in the oxidation of water to O_2.[26] In this case, first Ru^{II}–OH_2 oxidizes to Ru^{III}–OH_2. Next, by two consecutive PCETs, Ru^{III}–OH_2 oxidizes to Ru^{IV}–OH, then Ru^{IV}–OH to Ru^{V}=O. The

latter species has radical character and is the active species which dimerizes to the Ru^{IV}–OO–Ru^{IV} peroxo compound which liberates molecular oxygen (Figure 8).

While the first and second steps were very fast, the oxidation of Ru^{IV}–OH to Ru^{V}=O was calculated with a rate constant k_{ET1} = 2.3 × 10^5 M^{-1} s^{-1} at 35°C. Moreover, the dimerization rate (radical coupling) between two Ru^{V}=O complexes was measured with a rate constant k_D = 1.1 × 10^5 M^{-1} s^{-1} at 35° C. The reaction is second order with regard to the catalyst and is independent of [Ce^{IV}] as the oxidant.[26]

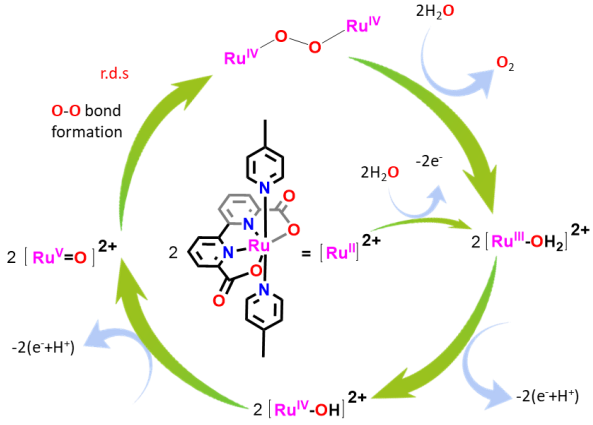

Figure 8. Proposed water oxidation mechanism by [Ru(bda)(pic)$_2$] (complex **15** Scheme 3), based on the interaction between two M–O entities (I2M). r.d.s = rate limiting step under stoichiometric Ce^{IV} conditions.

Avoiding high energy intermediates: second coordination effects and ATP

As described in detail in the previous section for catalysts [Ru(tpy)(bpm)(OH_2)]$^{2+}$ and [Ru(bda)(pic)$_2$], multiple intermediates are involved in the water oxidation catalytic pathway. In a general manner, this is illustrated in Figure 9. By rational design of the catalysts, we can avoid high-energy ('too active') and low-energy ('too stable') intermediates which have large energy barriers of activation.[27]

The energies of activation for each step will determine which is the r.d.s. By studying the mechanisms and ascertaining the r.d.s, it is possible to try to facilitate such step and increase the rate and overall performance of a specific catalyst. In water oxidation catalysis, the O-O bond formation (WNA or I2M) is usually the r.d.s, and researchers have found the key role of second coordination sphere effects in facilitating this step.

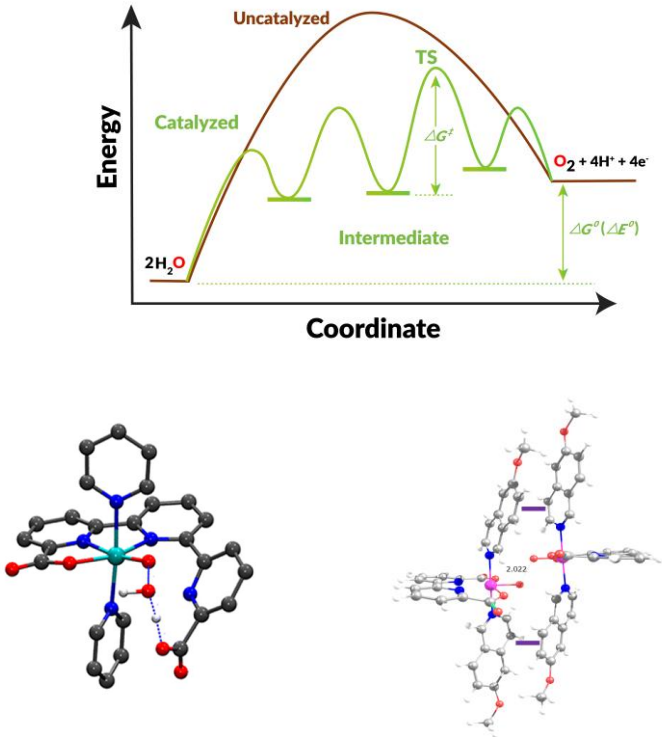

Figure 9. Top) The catalyzed and uncatalyzed energy profile for water oxidation reaction. TS = transition state.[27] Bottom left) TS for the O-O bond formation by WNA to a Ru^{V}=O assisted by a proximal carboxylate group, complex **12** in Scheme 2, section 1·4·4·1. Bottom right) TS for the O-O bond formation by I2M of two Ru^{V}=O groups assisted by π-π interactions of the axial ligands, complex **19** in Scheme 3, section 1·4·4·2.

For instance, in the case of WNA, the presence of a dangling carboxylate group in close proximity to the Ru=O center, has shown to have a beneficial effect on the rate of the catalysis by assisting the water nucleophilic attack and O-O bond

formation (Figure 9, bottom left).[16] On the other hand, in the case of I2M, placing π-conjugated systems in strategical positions of ligand backbones, favored π interactions between two Ru=O groups, increasing the catalysis (Figure 9, bottom right).[26, 28]

Another way to facilitate the O-O bond formation step is by atom proton transfer (APT), which occurs in a concerted manner with the O-O bond formation to avoid high energy species. An example is given in the Eq. 12, where water acts as a proton acceptor (pK_a (H_3O^+)= -1.7). Thus, it is possible to envision a significant rate enhancement by using bases as proton acceptors (B in Eq. 12) in the case of complexes having O-O bond formation as the rate limiting step.

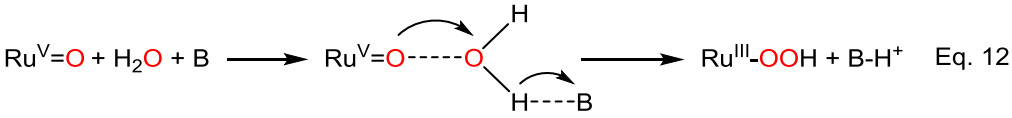

Eq. 12

In APT transfer, H^+ and e^- are transferred from the same orbital of one of the reactant; however, in PCET, e^- and H^+ donor and aceptor orbitals are from different molecules which intract electronically to provide coupled transfer. In both system there is a strong electronic intraction between reactants and the product; as a consequence, the difference between PCET and APT is very low.

1·4·3-Chemical, electrochemical and photo induced catalysis

The activation of water oxidation catalysts can be achieved in different ways as illustrated in Figure 10: A) using sacrificial chemical oxidants, B) electrochemically induced oxidation, C) photochemical induced oxidation using a photosensitizer (P) and a sacrificial electron acceptor and D) photelectrochemical oxidation.[9]

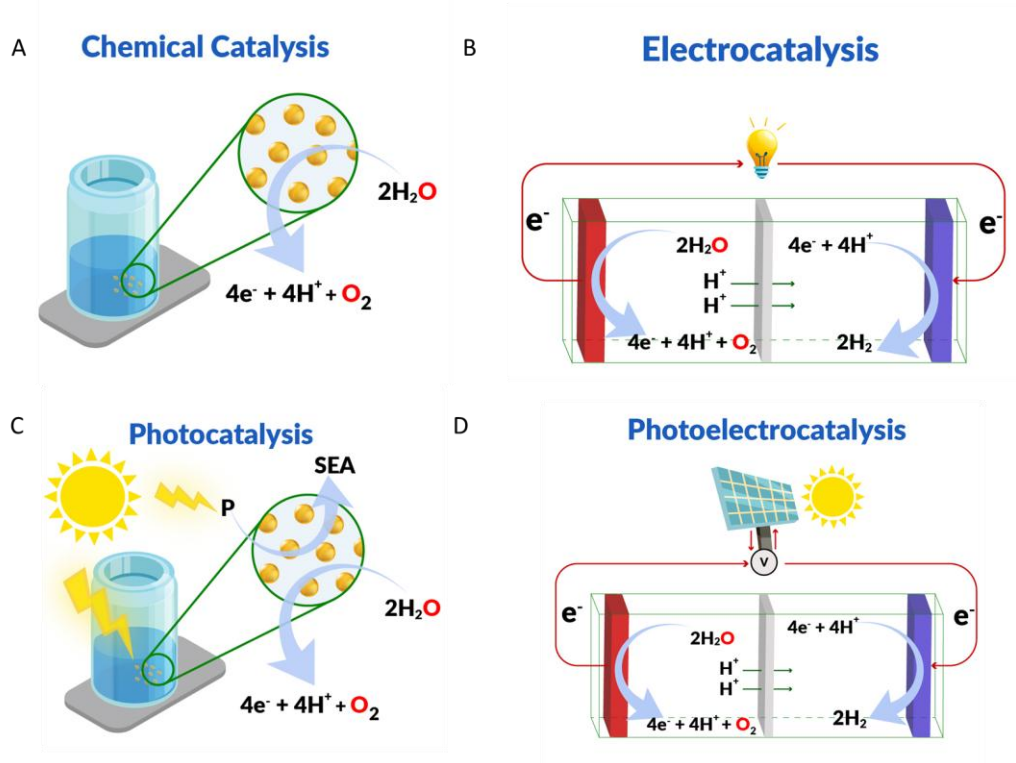

Figure 10. Four different ways to do water oxidation include chemical catalysis (A), electrocatalysis (B), photocatalysis (P= photosensitizer, SEA= sacrificial electron acceptor), and photoelectrocatalysis (D).

Chemically induced water oxidation catalysis

The primary investigation of catalysts toward water oxidation is generally performed by the use of a sacrificial chemical oxidant having a sufficient oxidation potential to oxidize the water oxidation catalyst in solution. By monitoring the oxygen gas evolved, it is possible to measure turnover frequencies (TOF) and turnover numbers (TON). One of the most wide-spread and reliable one electron oxidants at pH 1 is ceric ammonium nitrate (CAN). A number of properties make CAN attractive for use in water oxidation catalysis; (i) one-electron oxidation behavior, (ii) strong absorption band in the UV being useful for calculating the rate of water oxidation reactions, (iii) commercial access, (iv) stability over 4 hours under

dark and cold condition in solution. In addition, it has been reported that if a catalyst is active with CAN, it will be active electrochemically.[29] On the other hand, the main drawbacks are (i) stability range only at low pH (0.9-3) and (ii) an oxidation potential of 1.75 V at pH 0.9 giving an over potential of about 570 mV. The latter allows driving water oxidation with high activation barriers but at the same time may trigger the undesirable side reactions, for instance oxidation of ligand backbones, if they are not robust enough.

In order to do water oxidation at pH 7, using sodium periodate ($NaIO_4$) is a good choice. It has an oxidation potential of 1.6 V under standard condition giving an over-potential of approximately 390 mV for the oxidation of water.[29] The main advantage of $NaIO_4$ over CAN is its stability in a wide pH range (pH 2 to 7.5). It is worth to mention that the reduction of periodate to iodate needs one proton per electron which leads to the oxidation of water in constant pH, and as consequence in the same potential. Hence, using $NaIO_4$ provides mild conditions for catalyst with weak ligand framework.[30,31] It is also important to take into account that periodate is an oxo-transfer agent. Hence, the source of molecular oxygen produced by water oxidation must be characterized by isotopic labeling in order to make sure that it comes uniquely from water. Moreover, up to now, it is not clear if $NaIO_4$ is a two-electrons or a one-electron oxidant.[31] Three side reactions associated with the use of $NaIO_4$ as oxidant include direct water oxidation (Eq. 13), $NaIO_4$ dismutation (Eq. 14) and $NaIO_4$ equilibrium resulting in scrambling of ^{18}O labeling (Eq. 15).[32]

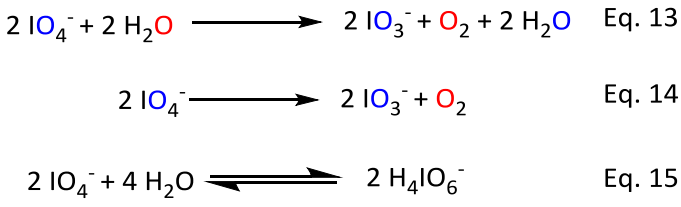

Electrochemical induced water oxidation catalysis

In electrochemical water oxidation a potentiostat is used to control the desired applied potential of the working electrode where the water oxidation reaction can happen in homogeneous or heterogeneous phase. An impressive example for homogeneous water oxidation is complex $[Ru(tda)(py)_2]$ where tda is [2,2′:6′,2″-terpyridine]-6,6″-dicarboxylate and py is pyridine (**12** in Scheme 2) which is by far the fastest ruthenium molecular catalyst reported to date with working voltage of 1.2 V. [33]

I

For practical applications the catalyst must be attached to a conducting surface while maintaining its activity.[34] In heterogeneous phase the catalyst can anchor on the surface of an electrode by (i) covalent bonding of the catalyst to the surface called chemisorption, (ii) Van der Waals forces called physisorption (iii) immobilizing the catalyst inside a matrix called encapsulation, and finally (iv) electrostatic interaction between the surface and the water oxidation catalyst which have different charges. One of the best examples in heterogeneous phase is again complex **12**, which was anchored on Multi-Walled Carbon Nanotubes (MWCNT) by π-π interactions. This molecular electroanode showed a million TONs at pH 7 with an E_{app}= 1.45 V.[35]

In the case of covalent bonding there are different types of linkage strategies for water oxidation on conducting oxides (an also to semiconducting oxides for photoelectrochemical catalysis, see below) such as carboxylic acid derivatives (-COOH), and phosphonic acid derivatives ($-PO_3H_2$). The former has been used for surface binding in non-aqueous solvent for dye sensitized solar cell application; however, it undergoes hydrolysis in water. The latter is more robust in acidic solution; albeit, by increasing the pH, the surface hydrolysis is also induced.[23]

In order to overcome the hydrolysis challenge of -COOH and $-PO_3H_2$ derivatives, polymer films have been used to stabilize surface bonding. Two examples of

polymers used as overlayer films are poly-(methylmethacrylate) known as PMMA and Poly[4,5-difluoro-2,2-bis(trifluoromethyl)-1,3-dioxole-co-tetrafluoroethylene] known as Dupont AF. The main drawback of PMMA is the easy oxidation of the -CH group at the high oxidation working potential.

Alternatively, atomic layer deposition (ALD) of robust metallic oxides such as titanium or aluminium oxides has also been used as an efficient method for the stabilization of molecular catalysts on the surface.[36,23]

Photo-induced water oxidation catalysis

The sun light energy is one of the cheap, clean, and abundant available sources. In order to perform photo-induced water oxidation catalysis, it is essential to use a light absorber responsible of harvesting light. In homogeneous photocatalysis, a soluble photosensitiser (P) absorbs light creating an excited state (P*) which can transfer an electron to a sacrificial electron acceptor (SEA) producing oxidative quenching (P^+) or accepting an electron from the catalyst generating reductive quenching (P^-). The former is more common, so the oxidized photosensitizer P^+ oxidizes the water oxidation catalyst (WOC), which in turn oxidizes water to dioxygen (Figure 11).[9] In order to have electron transfer between P^+ and catalyst, there should be a good match between oxidation potentials. In this method, it is important to keep in mind the degradation of commonly used photosensitizer (such as $[Ru(bpy)_3]^{2+}$) by singlet oxygen, which is produced within catalysis leading to deactivation of the photocatalytic system.[37]

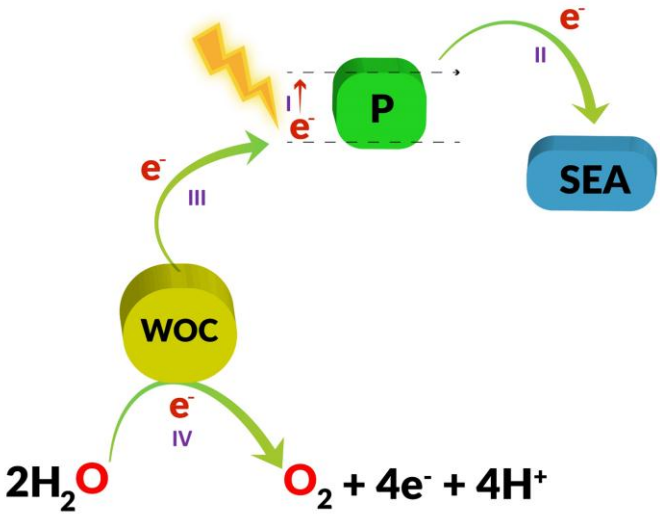

Figure 11. Photo-induced water oxidation catalysis by a three-component molecular system. The order of electron transfer is shown by I, II, III, IV. P: photosensitizer; SEA: sacrificial electron acceptor; WOC: water oxidation catalyst.

In the case of heterogeneous photo-induced water oxidation using visible light, the light harvesting unit is a narrow band gap n-type semiconductor or a dye sensitized wide band gap n-type semiconductor. In this case, the catalyst needs to be attached to the surface of the corresponding semiconductor following one of the strategies discussed above for electrochemically induced water oxidation.[23]

1·4·4-Relevant water oxidation catalysts (WOC) examples

1·4·4·1-Historical perspective of ruthenium WOC

As explained in detail in section 1·2, the Mn_4CaO_5 cluster in PSII is able to distribute the four oxidizing equivalents on five metal centers to stabilize catalytic intermediates. Therefore, it was long believed that for making molecular water oxidation catalysts, the presence of at least two metal centers was necessary to remove $4H^+$ and $4e^-$ from two water molecules and release O_2. Hence, it took many years to discover the first water oxidation catalyst in 1982, with the formula *cis,cis*-

$[(bpy)_2(OH_2)Ru^{III}\text{-}O\text{-}Ru^{III}(OH_2)(bpy)_2]^{4+}$ (where bpy is bipyridine) (**4** in Scheme 2), known as the blue dimer.

More than 20 years later, in 2004, the Ru-O-Ru bridge in blue dimer was replaced by the robust organic ligand derived from 2,2'-(1H-pyrazole-3,5-diyl)dipyridine (Hbpp). In the complex with the structure $[Ru_2^{II}(bpp)(tpy)_2(AcO)]^{2+}$ (where tpy is 2,2':6',2''-terpyridine and AcO is acetato), two Ru centers have been located near together thanks to the rigid backbone in which the equatorial ligand is bpp^- and acetato is a bridging ligand. Electrochemical and spectroscopic techniques confirmed that the acetato bridge is replaced by aqua ligand to make the real catalyst $[Ru_2^{II}(bpp)(tpy)_2(OH_2)_2]^{3+}$ (**5**, Scheme 2). The catalyst efficiency using CAN increased to 70% and TOF experienced a 3-fold enhancement as compared to the blue dimer under similar condition. Llobet *et al*. suggested that by the *in*,*in* configuration of the Ru-oxo groups, the intermolecular interaction of oxo-oxo is significant. As a consequence, intramolecular I2M pathway triggers O_2. This hypothesis was later confirmed with isotopic labeling analysis.[38]

The use of organic bridging ligands enabled synthetic chemists to rapidly develop new Ru WOCs. This synthetic strategy of avoiding O^{2-}-bridged species has since afforded a family of diruthenium complexes in which auxiliary ligands can control the mechanistic pathway through which O–O bond formation occurs. This finding is nicely illustrated in the case of $[(H_2O)Ru^{II}(tpm)(\mu\text{-}bpp)Ru^{II}(tpm)(OH_2)]^{3+}$ (**6** in Scheme 2, tpm = tris(2-pyridyl) methane), a derivative of **5** in which the meridional tpy ligand has been substituted with the facial tpm ligand. With this new structural arrangement, the two aquo groups that were facing one another in **5** are now situated *trans* to each other in **6**. As a result, the intramolecular I2M pathway is not accessible for **6** and O–O bond formation instead proceeds through an intermolecular I2M pathway.

Moving from the tetradentate ligand bpp^- to the hexadentate ligand bbp^- (where bbp^- is 3,5-bis(2,2'-bipyridin-6-yl)pyrazolate) affords yet another distinct motif. In $[(H_2O)Ru^{II}(py)_2(\mu\text{-}bbp)Ru^{II}(py)_2(OH_2)]^{3+}$ (**7** in Scheme 2, py = pyridine), for example, the equatorial bbp^- ligand constrains the bond angles at the Ru centers in the equatorial plane, thereby separating the two $Ru–OH_2$ moieties in **7** relative to those in **5**. Thus, **7** cannot participate in an I2M pathway but instead undergoes the O–O bond formation through a WNA path.

In order to confirm that for water oxidation, the presence of two close Ru centers are necessary, a mononuclear complex was prepared to mimic the half of dinuclear complex **8** which is active for water oxidation. Surprisingly, the mononuclear complex **9** in Scheme 2 showed water oxidation activity with TONs in the range of 20-260. This discovery was one of the most important breakthroughs in this field, because it helped the researchers to design catalyst structures in an easier way with atom economy.[39]

The activity of mononuclear complexes was puzzling because it was assumed that a dinuclear diaquo complex (or larger system) was needed to be able to remove $2H^+$ and $2e^-$ from each $Ru–OH_2$ group. This mystery was solved, a few years later when the mechanistic analysis of $[(tpy)(bpm)Ru^{II}(OH_2)]^{2+}$ (**10**, bpm = 2,2'-bipyrimidine) showed that one Ru site was enough to carry out H_2O oxidation catalysis, as explained in detail in section 1·4·2 above.

The discoveries of the mononuclear catalysts were real breakthroughs because of their ease of preparation and synthetic versatility. However, mononuclear $Ru–OH_2$ complexes have the propensity to form O_2^--bridged dinuclear and even polynuclear complexes through processes that may compete with H_2O oxidation catalysis.

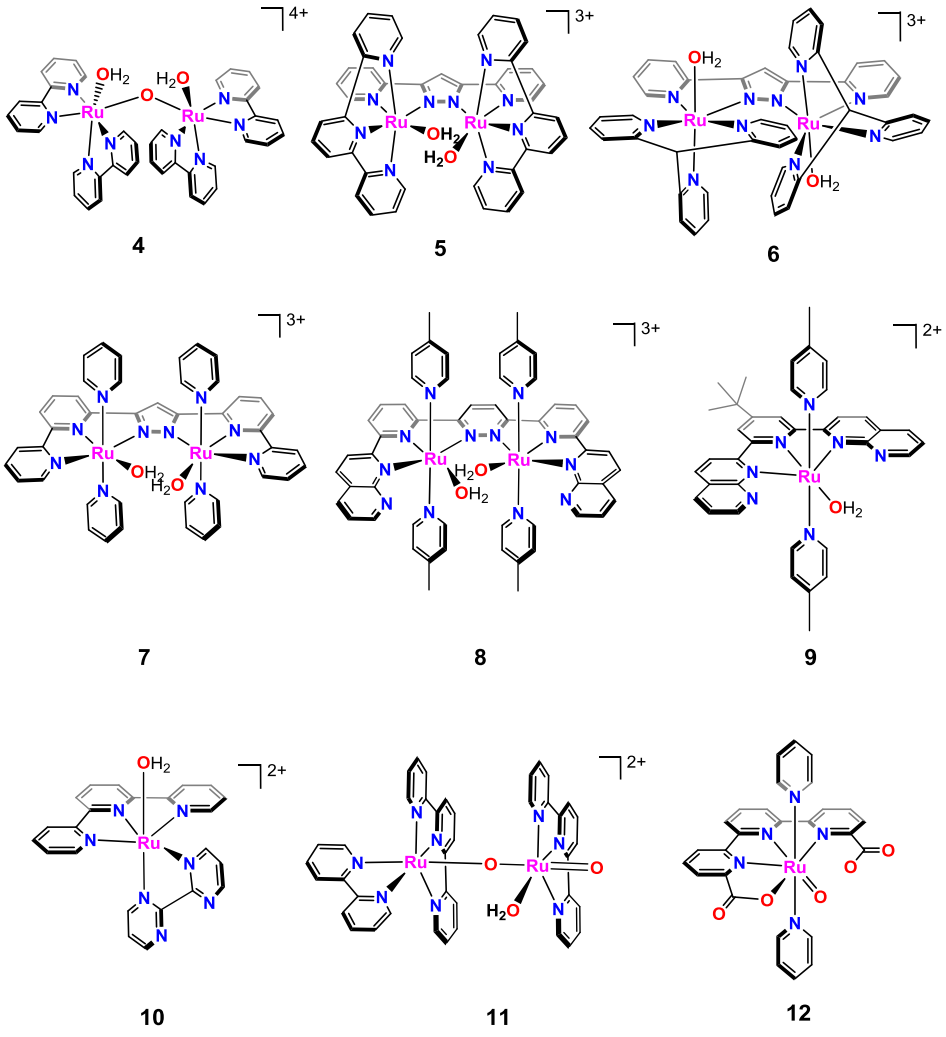

Scheme 2. Selected H_2O oxidation catalysts based on ruthenium.

Indeed, the terminal Ru=O/Ru–O$^{\cdot}$ can bridge to another Ru center instead of undergoing WNA or I2M. The formation of a bridged complex can spell deactivation of the catalyst but can also afford species that are active WOCs, as is the case for $[(tpy)(bpy)Ru^{II}(OH_2)]^{2+}$. In this case, the resulting O^{2-} bridged complex *trans*-$[(tpy)(bpy)Ru^{IV}(\mu\text{-}O)Ru^{IV}(tpy)(OH_2)(O)]^{4+}$ (**11** in Scheme 2) is actually a more active and robust catalyst than the parent complex.

Finally, in 2015, LIobet *et al*. reported catalyst **12** in Scheme 2, which is by far the best ruthenium molecular catalyst. This complex with the formula [Ru^{IV}(OH)(tda-κ-N^3O)$(py)_2$] showed an impressive turnover frequency record of 7700 s^{-1} at pH 7.0 and 50000 s^{-1} at pH 10.0 in homogenous solution after applying 1.2 V. As briefly discussed in section 1·4·3, this catalyst has also been used in heterogeneous phase producing the best electroanodes and photoanodes for the water oxidation catalysis available. Catalyst **12** together with the Ru-bda family of complexes, discussed in detail in the next section, are currently the fastest homogeneous water oxidation catalysts reported to date.

I

1·4·4·2-The [Ru(bda)$(L)_2$] family

In 2009, for the first time Sun *et al*. introduced carboxylato ligands for designing Ru-based complexes to decrease the overtpotential for the water oxidation reaction. They reported a *trans*-dimeric complex, which showed a TON of 4700 and a TOF of 0.28 s^{-1} (**13**, Scheme 3).[40] In 2010 the equatorial backbone of the catalyst was modified with phthalazine which gave this *cis*-dimeric complex **14** in Scheme 3. In this case the TON and TOF increased radically to 10400 and 1.2 s^{-1} respectively.[41] These two outstanding complexes showed that introducing carboxylate ligand to the backbone of the complex increases the stability and activity of the catalyst with low over-potential. In the next step, they decided to design a ligand with two carboxylic acid groups called bda, where bda is 2,2´-bipyridine-6,6´-dicarboxylate in the equatorial position, and two monodentate axial ligands (L) giving ruthenium complexes with the general formula [Ru(bda)$(L)_2$]. The first example with 4-picoline axial ligands showed an impressive TON and TOF of 2000 and 41 s^{-1} respectively and 0.18 V over potential for the water oxidation reaction (**15** in Scheme 3).

In 2013, the same group investigated the effect of electron withdrawing (EWG) and electron donating (EDG) groups on the axial ligands. The presence of EWG in the *Para* position of pyridine groups showed higher activity and stability. For instance,

introducing -CO_2Et increased TON and TOF to 4800 and 120 s^{-1} respectively (**16a** in Scheme 3). Interestingly, introducing halogen groups such as bromide, which is well known for electron donating by resonance, also showed high activity (TON= 4500 for **16b**).[42]

Investigation of the water oxidation mechanism followed by Ru-bda type of catalysts showed I2M mechanism,[26] being the dimerization of the two Ru^{V}=O groups the r.d.s (see Figure 8 and related text). In order to decrease the kinetic barrier of the dimerization process and induce better interaction between two centers they used pi-extended axial ligands such as isoquinoline (**17a**) and phthalazine (**17b**) as axial ligands. These two ligands improved the interaction between two catalysts boosting π-π stacking which decreased the energy barrier for the O-O bond formation via radical coupling.[26, 43] They reached impressive TONs of 1000000 and a TOF of 1000 s^{-1} for complexes **18b** and **18a** respectively by using halogen in the π–extended ligand.[44] In 2014, Llobet *et al*. introduced –OMe groups on the isoquinoline axial ligands and further confirmed that π-stacking interaction is the key factor that influence reactivity of Ru-bda oxidation catalysts (**19** in Scheme 3, see also Figure 9 bottom right). It is noteworthy to mention that the electron donating groups in the axial ligands just affect the Ru^{III}/Ru^{II} redox potential and there is no relation between first redox potential and catalytic activity. For example, the redox potential $Ru^{III/II}$ for complex **20** appeared at $E_{1/2}$= 0.78 V vs NHE, that showed 80 mV increases compare to complex **17a**. However, the two next oxidation potentials ($Ru^{IV/III}$ and $Ru^{V/IV}$) occur in lower potentials differences of only 20 and 10 mV respectively. Despite the similarities of the last $Ru^{V/IV}$ redox couple that generates the active species (only 10 mV difference), in the same conditions complex **17a** is much faster than complex **20** (TOFs are 127 s^{-1} and 1 s^{-1} for **17a** and **20** respectively).[28]

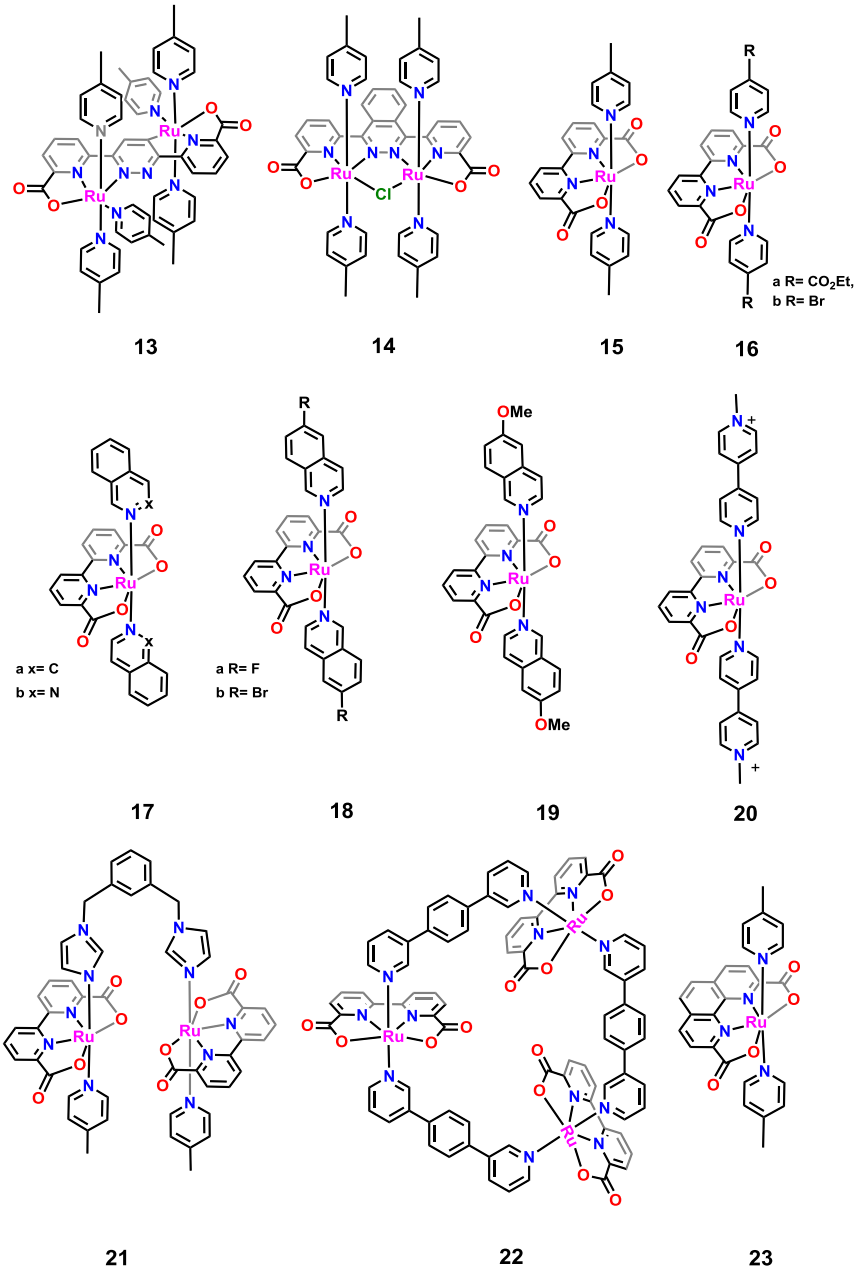

Scheme 3. Evolution of Ru-bda family of complexes.

The bimolecular mechanism of Ru-bda complexes limits the application of this family of complexes on the surface of electrodes, since the mobility is restricted after heterogenization. Consequently, in 2013, Sun *et al*. decided to design a dinuclear complex with a bridging ligand to overcome this limitation. Under optimum conditions they reached to an excellent TON of 42840 and an initial TOF of 40s^{-1} in homogeneous phase (**21** in Scheme 3).[45]

In 2016 Wurthner *et al*. synthesized a cyclic structure with three Ru-bda centers connected with the bridging 4,4'-bipyridine ligand (**22** in Scheme 3). The maycrocyclic structure of **22** triggered a change of mechanism and using this complex the reaction proceeded by WNA pathway and showed a TOF which exceed 100 s^{-1}. Moreover, the photo catalytic water oxidation showed a TON of 1255 and a TOF of 13.1 s^{-1} in nM concentration.[46]

In 2011, Sun *et al*. reported a Ru complex with pda (where pda is phenantroline dicarboxylate, **23** in Scheme 3) which has the similar enviroment with more rigidity and open site for heptacoordination. Surprisingly, this complex showed a TOF of 0.1 s^{-1}. Kinetic studies confirmed that this catalyst follows a WNA mechanism. DFT calculations suggested that the ridigidity of **23** is responsible for its lower performance.

The stability of complex **15** was investigated in acetonitrile at room temperature. After one day stirring, the color of solution changed from red to green. Electrospray Ionization Mass Spectrometry (ESI-MS) confirmed that there are three compound include oxidation of complex **15** and oxidation of $-CH_3$ group in py.[47]

After 10 years since the first report on the Ru-bda catalysts, several factors have been identified to lead to the impressive behavior of this family of complexes: (i) carboxylic groups stabilize high oxidation states; (ii) the bda ligand provides the open O-Ru-O angle of 124° for $[Ru(bda)(pic)_2]$ which is 34° larger than an octahedral structure and creates a highway for the coordination of water and allowing for

coordination seven (CN7); (iii) Flexibility of Ru(bda) core helps the complex to adjust its structure in transition states (iv) DFT calculations suggested that Ru-O$^{\cdot}$ has high oxyl radical character favouring I2M mechanism.

1·4·4·3-The $[Ru(N_4)(L)_2]^{2+}$ family

In 2008, after the introduction of mononuclear water oxidation catalysts, Thummel *et al.* prepared a series of neutral equatorial multidentate ligands derived from 1,10-phenantroline to follow two goals.[48] First, to inhibit conformational mobility occurring in previously reported complexes with general formula $[Ru(bpy)_2L_2]$.[49] Secondly, in order to act as an internal base for removing a proton from incoming water, when attacking the Ru=O center, in a similar manner to complex **12** in Figure 9 (bottom left). Interestingly, it was observed that instead of assisting H_2O attack, the peripheral sites of 1,10-phenantroline coordinated to the metal center (**25**, Scheme 4).

In a following step, the distal ligand on 1,10-phenantroline was changed from 6-membered pyridine rings to 5-membered imidazole rings in position 1,9 of the phenantroline to make this bond less favorable (**26**, Scheme 4). However, ^{1}H NMR and single crystal x-ray diffraction structure showed that there is also coordination between N-methyl Imidazole and the Ru center. Only when the rigid phenantroline group was replaced by 2,6 substituted pyridines, a tridentate fashion coordination was achieved, leaving two free pyridines (**24** in Scheme 4).

Comparing the TONs of complexes **25a, 25b** and **26** under chemically induced catalysis with CAN did not show much difference (TONs are 146, 213, and 281 for **25a, 25b** and **26** respectively during 48 hours).

By introducing EWG or EDG in position 1,9 of a tetradentate equatorial dpp-type ligand (where dpp is 2,9-di-(pyrid-20-yl)-1,10-phenanthroline), the rate of O_2 evolving was investigated and compared with complex **26** (complexes **27a-c** in

Scheme 4). Interestingly, just complex **26** showed high catalytic activity without induction time (Table 1). All complexes **27 a-c** and a related complex **28** showed induction times between 1 and 20 minutes. It is noteworthy to mention that the highest activity of complex **26** is due to the better electron donating abilities of the imidazole group compared to pyridine that helps the complex to reach high oxidation states easier. On the other hand, complex **26** has higher N-Ru-N angle that can facilitate entering a water molecule.

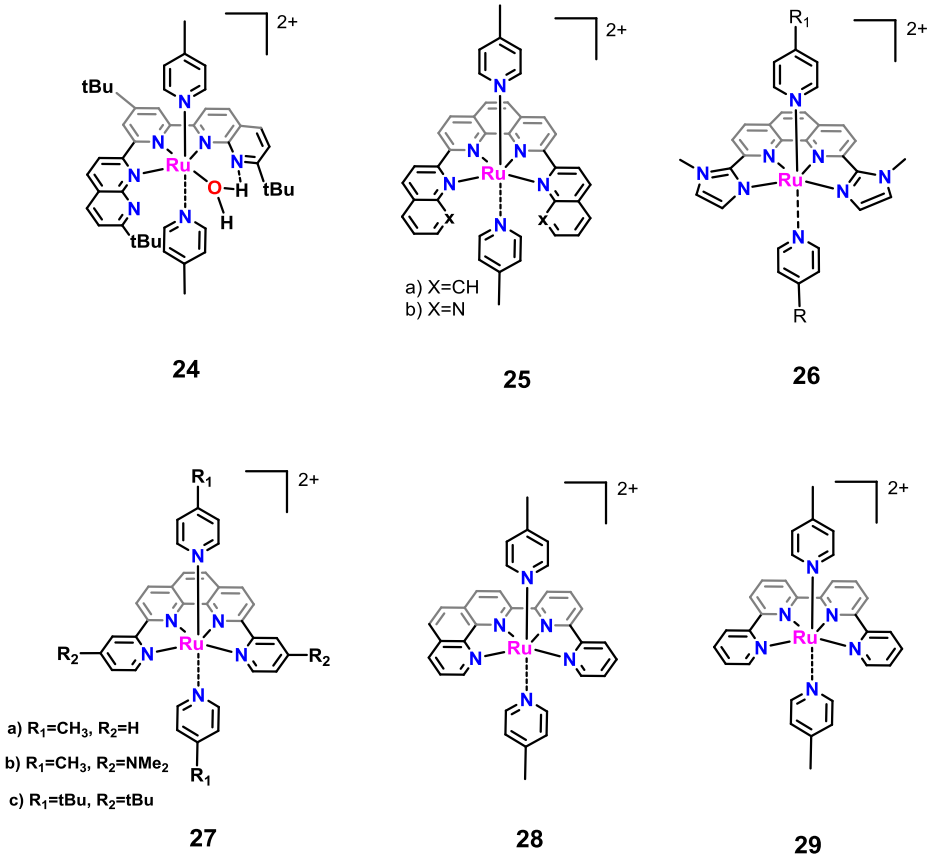

Scheme 4. Selected ruthenium water oxidation catalysts of the $[Ru(N_4)(L)_2]$ family.

So electronic and steric factors are proposed to be involved in water oxidation in complexes of the $[Ru(N_4)(L)_2]^{2+}$ family (where N_4 is a general term for a tetradentate neutral equatorial ligand and L is a monodentate neutral axial ligand, Figure 12).

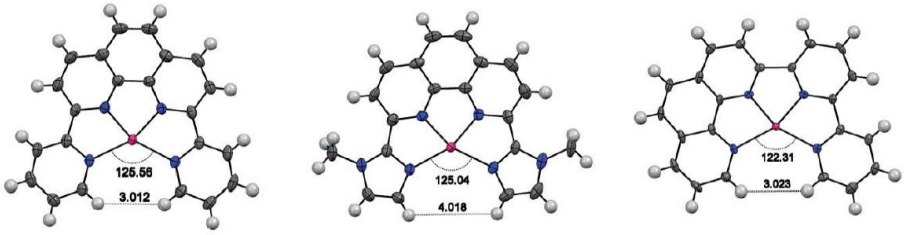

Figure 12. Thermal ellipsoid plot representation of the planer fragments of **27a** (left), **26** (middle), and **28** (right). Color code: Ruthenium (magenta), nitrogen (blue), carbon (dark gray) and hydrogen (light gray).

An interesting feature of Table 1 is the activity difference between complex **27a** and **27b**, which roots from the protonation of $–NMe_2$ in acidic solution that can change the ligand from electron donating to electron acceptor. This behavior is also observed when the $–NH_2$ group is located in the axial position.[39]

Table 1. Kinetic data for water oxidation catalyst **26**, **27b**, **27c**, **27d** and **28**

Complexes	**26**	**27a**	**27b**	**27c**	**28**
k_{obs}/initial TOF[a] (h^{-1})	69.2	43.2	18.5	16.5	57.3

a) the K_{obs}/initial TOFs were calculated from the slops of manometry measurements

In the next step, the role of axial ligands on the electronic properties of the complexes with the general formula $[Ru(N_4)(L)_2]^{2+}$ was investigated by Thummel *et al.* For this goal, they chose $-NMe_2$ and $-CH_3$ as electron donating groups and $-CF_3$ as electron withdrawing groups on the *para* position of axial ligands L of **27** in Scheme 4. The complex with $–CH_3$ groups showed the highest activity because of facilitating electron transfer during oxidation of Ru center. On the other hand, the low activity of the derivative with $-NMe_2$ groups is because of the protonation of the N in acidic

pH, as just mentioned above. On the other hand, these axial ligands have strong electronic effect on changing the metal to ligand charge transfer (MLCT) bands (Figure 13).[50]

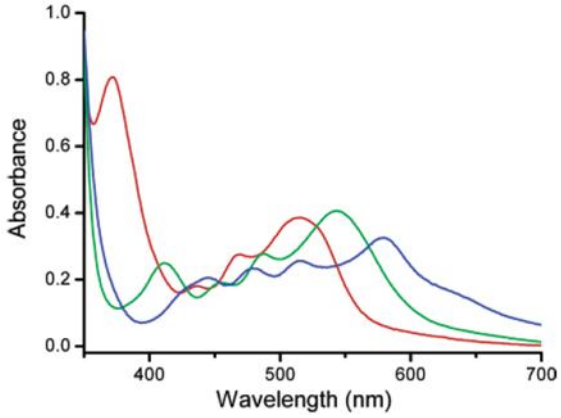

Figure 13. UV-vis spectra of $[Ru(dpp)(4\text{-}x\text{-}py)_2](PF_6)_2$, in CH_2Cl_2, where X= $-CF_3$ (red), Me (green), and $-NMe_2$ (blue).

Mechanistic studies using the related complex 9 in Scheme 2 (with tridentate equatorial ligand) showed a linear, which is the first breakthrough for introducing $[Ru(N_4)(L)_2]^{2+}$ family, showed a linear relationship between catalyst concentration and rate of water oxidation, rejecting any dimerization mechanism. In order to confirm these observations, in 2008, Thummel *et al*. designed a similar catalyst by putting t-butyl in 7'-positions of the 1,8-naphthyridine rings of the equatorial ligand to stop any interaction between two catalysts by strict hindrance (**24**). As expected, the new structure showed the same activity as complex **9** and it confirmed the reaction order in catalyst is one.

In 2014, comprehensive experiments were done on complex **28** to elucidate reaction mechanisms of $[Ru(N_4)(L)_2]^{2+}$ type of complexes. ^{1}HNMR and UV-vis experiments confirmed that there is no possibility of replacing of N(pyridyl) groups by water while ruthenium is in low oxidation states. Manometry experiment showed a linear dependence of the catalytic rate vs catalyst concentration,

suggesting an unimolecular mechanism. In the case of complex **28**, mass spectra showed that there is an extra O in the molecular structure after adding 4 equivalents of Ce^{IV}, that could be related to an oxo ligand coordinated to the Ru center. By combing experimental and computational results, Thummel *et al*. proposed that after oxidation of Ru^{II} to Ru^{III} one aqua ligand coordinates the Ru center and in the next step $2H^+/1e^-$ transfer takes place which creates the seven coordinated $[Ru^{IV}=O]^{2+}$ intermediate.[39] They suggested that $[Ru^{IV}=O]^{2+}$ has pentagonal bipyramidal geometry with C_2v symmetry and is the starting point in the catalytic cycle. However, no convincing experimental proof for the Ru=O group, nor the proposed mechanism were given.

I

As mentioned before, most of the catalysts of the $[Ru(N_4)(L)_2]^{2+}$ family show induction time before evolving oxygen. Muckerman *et al*. suggested that the formation of high oxidation state species derived from these type of complexes such as the $[Ru^{IV}(OOH)]^{3+}$ needs time. In 2014, Liu *et al*. reported that by adding Ce^{IV} to complex **29**, two outer nitrogen atoms of the tetradentate-pryidine ligand undergo oxidation, forming the corresponding N-oxide derivative. Hence, the aforementioned induction time could be related to the oxidation of outer nitrogen. However, the isolated oxidized complex also showed one minute induction time, leading to further confusion in the catalytic mechanism. Finally, in 2018, Pushkar *et al*. were able to characterized the 7 coordinated Ru complex $[Ru^{V}=O(pic)_2(dpp)]^{3+}$ derived from **26** by spectroscopic techniques, which undergoes two fast oxygen transfer to the equatorial ligand.[51]

Despite all the efforts in studying the mechanism of the $[Ru(N_4)(L)_2]^{2+}$ family, conclusive experimental evidence of the real catalytic species is still lacking and a better explanation of the induction time required to reach stable catalysis is needed.

References

1. Llobet, A., *Molecular Water Oxidation Catalysis: A Key Topic for New Sustainable Energy Conversion Schemes*. Wiley: **2014**.
2. Cardona, T.; Sedoud, A.; Cox, N.; Rutherford, A. W., Charge separation in photosystem II: a comparative and evolutionary overview. *Biochimica et Biophysica Acta (BBA)-Bioenergetics* **2012,** *1817* (1), 26-43.
3. Rappaport, F.; Guergova-Kuras, M.; Nixon, P. J.; Diner, B. A.; Lavergne, J., Kinetics and pathways of charge recombination in photosystem II. *Biochemistry* **2002,** *41* (26), 8518-8527.
4. Umena, Y.; Kawakami, K.; Shen, J.-R.; Kamiya, N., Crystal structure of oxygen-evolving photosystem II at a resolution of 1.9 Å. *Nature* **2011,** *473* (7345), 55.
5. Najafpour, M. M.; Moghaddam, A. N.; Allakhverdiev, S. I., Biological water oxidation: lessons from nature. *Biochimica et Biophysica Acta (BBA)-Bioenergetics* **2012,** *1817* (8), 1110-1121.
6. Kawakami, K.; Umena, Y.; Kamiya, N.; Shen, J.-R., Location of chloride and its possible functions in oxygen-evolving photosystem II revealed by X-ray crystallography. *Proceedings of the National Academy of Sciences* **2009,** *106* (21), 8567-8572.
7. Joliot, P.; Barbieri, G.; Chabaud, R., A new model of photochemical centers in system-II. *Photochemistry and Photobiology* **1969,** *10* (5), 309.
8. Seh, Z. W.; Kibsgaard, J.; Dickens, C. F.; Chorkendorff, I.; Nørskov, J. K.; Jaramillo, T. F., Combining theory and experiment in electrocatalysis: Insights into materials design. *Science* **2017,** *355* (6321), eaad4998.
9. Berardi, S.; Drouet, S.; Francas, L.; Gimbert-Suriñach, C.; Guttentag, M.; Richmond, C.; Stoll, T.; Llobet, A., Molecular artificial photosynthesis. *Chemical Society Reviews* **2014,** *43* (22), 7501-7519.
10. Murphy, A.; Barnes, P.; Randeniya, L.; Plumb, I.; Grey, I.; Horne, M.; Glasscock, J., Efficiency of solar water splitting using semiconductor electrodes. *International journal of hydrogen energy* **2006,** *31* (14), 1999-2017.
11. Murakami, M.; Hong, D.; Suenobu, T.; Yamaguchi, S.; Ogura, T.; Fukuzumi, S., Catalytic mechanism of water oxidation with single-site ruthenium–heteropolytungstate complexes. *Journal of the American Chemical Society* **2011,** *133* (30), 11605-11613.
12. Najafpour, M. M., Synthesis and Characterization of an Insoluble Ruthenium-Based Coordination Polymer Catalyst for Water Oxidation. *Molecular Crystals and Liquid Crystals* **2010,** *517* (1), 167-179.
13. Matheu, R.; Garrido-Barros, P.; Gil-Sepulcre, M.; Ertem, M. Z.; Sala, X.; Gimbert-Suriñach, C.; Llobet, A., The development of molecular water oxidation catalysts. *Nature Reviews Chemistry* **2019,** *3* (5), 331-341.
14. Benck, J. D.; Hellstern, T. R.; Kibsgaard, J.; Chakthranont, P.; Jaramillo, T. F., Catalyzing the hydrogen evolution reaction (HER) with molybdenum sulfide nanomaterials. *ACS Catalysis* **2014,** *4* (11), 3957-3971.
15. Cao, R.; Lai, W.; Du, P., Catalytic water oxidation at single metal sites. *Energy & Environmental Science* **2012,** *5* (8), 8134-8157.
16. Matheu, R.; Ertem, M. Z.; Benet-Buchholz, J.; Coronado, E.; Batista, V. S.; Sala, X.; Llobet, A., Intramolecular proton transfer boosts water oxidation catalyzed by a Ru complex. *J. Am. Chem. Soc.* **2015,** *137* (33), 10786-10795.
17. Eisenberg, R., Rethinking water splitting. *Science* **2009,** *324* (5923), 44-45.
18. (a) Ono, T.; Qu, S.; Gimbert-Suriñach, C.; Johnson, M. A.; Marell, D. J.; Benet-Buchholz, J.; Cramer, C. J.; Llobet, A., Hydrogenative Carbon Dioxide Reduction Catalyzed by Mononuclear Ruthenium Polypyridyl Complexes: Discerning between Electronic and Steric Effects. *ACS Catalysis* **2017,** *7* (9), 5932-5940; (b) Ono, T.; Planas, N.; Miró, P.; Ertem, M. Z.; Escudero-Adán, E. C.; Benet-Buchholz, J.; Gagliardi, L.; Cramer, C. J.; Llobet, A., Carbon dioxide reduction catalyzed by dinuclear ruthenium polypyridyl complexes. *ChemCatChem* **2013,** *5* (12), 3897-3903.

19. Weinberg, D. R.; Gagliardi, C. J.; Hull, J. F.; Murphy, C. F.; Kent, C. A.; Westlake, B. C.; Paul, A.; Ess, D. H.; McCafferty, D. G.; Meyer, T. J., Proton-Coupled Electron Transfer. *Chemical Reviews* **2012,** *112* (7), 4016-4093.
20. Elgrishi, N.; Rountree, K. J.; McCarthy, B. D.; Rountree, E. S.; Eisenhart, T. T.; Dempsey, J. L., A practical beginner's guide to cyclic voltammetry. *Journal of Chemical Education* **2017,** *95* (2), 197-206.
21. (a) Shaffer, D. W.; Xie, Y.; Szalda, D. J.; Concepcion, J. J., Manipulating the rate-limiting step in water oxidation catalysis by ruthenium bipyridine–dicarboxylate complexes. *Inorganic chemistry* **2016,** *55* (22), 12024-12035; (b) Song, N.; Concepcion, J. J.; Binstead, R. A.; Rudd, J. A.; Vannucci, A. K.; Dares, C. J.; Coggins, M. K.; Meyer, T. J., Base-enhanced catalytic water oxidation by a carboxylate–bipyridine Ru (II) complex. *Proceedings of the National Academy of Sciences* **2015,** *112* (16), 4935-4940.
22. (a) Shen, J.; Stevens, E. D.; Nolan, S. P., Synthesis and Reactivity of the Ruthenium(II) Dihydride Ru($Ph_2PNMeNMePPh_2$)$_2H_2$. *Organometallics* **1998,** *17* (18), 3875-3882; (b) Navarro Clemente, M. E.; Juárez Saavedra, P.; Cervantes Vásquez, M.; Paz-Sandoval, M. A.; Arif, A. M.; Ernst, R. D., Syntheses, Structures, and Reactivity Studies of Half-Open Ruthenocenes and Their Oxodienyl Analogues. *Organometallics* **2002,** *21* (4), 592-605.
23. Meyer, T. J.; Sheridan, M. V.; Sherman, B. D., Mechanisms of molecular water oxidation in solution and on oxide surfaces. *Chemical Society Reviews* **2017,** *46* (20), 6148-6169.
24. Concepcion, J. J.; Jurss, J. W.; Norris, M. R.; Chen, Z.; Templeton, J. L.; Meyer, T. J., Catalytic Water Oxidation by Single-Site Ruthenium Catalysts. *Inorganic chemistry* **2010,** *49* (4), 1277-1279.
25. Duan, L.; Fischer, A.; Xu, Y.; Sun, L., Isolated Seven-Coordinate Ru(IV) Dimer Complex with [HOHOH]–Bridging Ligand as an Intermediate for Catalytic Water Oxidation. *Journal of the American Chemical Society* **2009,** *131* (30), 10397-10399.
26. Duan, L.; Bozoglian, F.; Mandal, S.; Stewart, B.; Privalov, T.; Llobet, A.; Sun, L., A molecular ruthenium catalyst with water-oxidation activity comparable to that of photosystem II. *Nature chemistry* **2012,** *4* (5), 418-423.
27. Tong, L.; Thummel, R. P., Mononuclear ruthenium polypyridine complexes that catalyze water oxidation. *Chemical Science* **2016,** *7* (11), 6591-6603.
28. Richmond, C. J.; Matheu, R.; Poater, A.; Falivene, L.; Benet-Buchholz, J.; Sala, X.; Cavallo, L.; Llobet, A., Supramolecular Water Oxidation with Ru–bda-Based Catalysts. *Chemistry–A European Journal* **2014,** *20* (52), 17282-17286.
29. Parent, A. R.; Crabtree, R. H.; Brudvig, G. W., Comparison of primary oxidants for water-oxidation catalysis. *Chemical Society Reviews* **2013,** *42* (6), 2247-2252.
30. Parent, A. R.; Blakemore, J. D.; Brudvig, G. W.; Crabtree, R. H., Wilkinson's iridium acetate trimer as a water-oxidation catalyst. *Chemical Communications* **2011,** *47* (42), 11745-11747.
31. Parent, A. R.; Brewster, T. P.; De Wolf, W.; Crabtree, R. H.; Brudvig, G. W., Sodium periodate as a primary oxidant for water-oxidation catalysts. *Inorganic chemistry* **2012,** *51* (11), 6147-6152.
32. Graeupner, J.; Hintermair, U.; Huang, D. L.; Thomsen, J. M.; Takase, M.; Campos, J.; Hashmi, S. M.; Elimelech, M.; Brudvig, G. W.; Crabtree, R. H., Probing the viability of oxo-coupling pathways in iridium-catalyzed oxygen evolution. *Organometallics* **2013,** *32* (19), 5384-5390.
33. Matheu, R.; Ertem, M. Z.; Benet-Buchholz, J.; Coronado, E.; Batista, V. S.; Sala, X.; Llobet, A., Intramolecular proton transfer boosts water oxidation catalyzed by a Ru complex. *Journal of the American Chemical Society* **2015,** *137* (33), 10786-10795.
34. Garrido-Barros, P.; Matheu, R.; Gimbert-Suriñach, C.; Llobet, A., Electronic, mechanistic, and structural factors that influence the performance of molecular water oxidation catalysts anchored on electrode surfaces. *Current Opinion in Electrochemistry* **2019,** *15*, 140-147.
35. Creus, J.; Matheu, R.; Peñafiel, I.; Moonshiram, D.; Blondeau, P.; Benet-Buchholz, J.; García-Antón, J.; Sala, X.; Godard, C.; Llobet, A., A million turnover molecular anode for catalytic water oxidation. *Angewandte Chemie International Edition* **2016,** *55* (49), 15382-15386.
36. Wee, K.-R.; Brennaman, M. K.; Alibabaei, L.; Farnum, B. H.; Sherman, B.; Lapides, A. M.; Meyer, T. J., Stabilization of ruthenium (II) polypyridyl chromophores on nanoparticle metal-oxide

electrodes in water by hydrophobic PMMA overlayers. *Journal of the American Chemical Society* **2014,** *136* (39), 13514-13517.

37. Duan, L.; Xu, Y.; Gorlov, M.; Tong, L.; Andersson, S.; Sun, L., Chemical and Photochemical Water Oxidation Catalyzed by Mononuclear Ruthenium Complexes with a Negatively Charged Tridentate Ligand. *Chemistry – A European Journal* **2010,** *16* (15), 4659-4668.

38. Sens, C.; Romero, I.; Rodríguez, M.; Llobet, A.; Parella, T.; Benet-Buchholz, J., A new Ru complex capable of catalytically oxidizing water to molecular dioxygen. *Journal of the American Chemical Society* **2004,** *126* (25), 7798-7799.

39. Zong, R.; Thummel, R. P., A New Family of Ru Complexes for Water Oxidation. *Journal of the American Chemical Society* **2005,** *127* (37), 12802-12803.

40. Xu, Y.; Åkermark, T. r.; Gyollai, V.; Zou, D.; Eriksson, L.; Duan, L.; Zhang, R.; Åkermark, B. r.; Sun, L., A new dinuclear ruthenium complex as an efficient water oxidation catalyst. *Inorganic chemistry* **2009,** *48* (7), 2717-2719.

41. Xu, Y.; Fischer, A.; Duan, L.; Tong, L.; Gabrielsson, E.; Åkermark, B.; Sun, L., Chemical and light-driven oxidation of water catalyzed by an efficient dinuclear ruthenium complex. *Angewandte Chemie International Edition* **2010,** *49* (47), 8934-8937.

42. Duan, L.; Wang, L.; Inge, A. K.; Fischer, A.; Zou, X.; Sun, L., Insights into Ru-based molecular water oxidation catalysts: Electronic and noncovalent-interaction effects on their catalytic activities. *Inorganic chemistry* **2013,** *52* (14), 7844-7852.

43. Duan, L.; Araujo, C. M.; Ahlquist, M. S. G.; Sun, L., Highly efficient and robust molecular ruthenium catalysts for water oxidation. *Proceedings of the National Academy of Sciences* **2012,** *109* (39), 15584-15588.

44. Wang, L.; Duan, L.; Wang, Y.; Ahlquist, M. S. G.; Sun, L., Highly efficient and robust molecular water oxidation catalysts based on ruthenium complexes. *Chemical Communications* **2014,** *50* (85), 12947-12950.

45. Jiang, Y.; Li, F.; Zhang, B.; Li, X.; Wang, X.; Huang, F.; Sun, L., Promoting the Activity of Catalysts for the Oxidation of Water with Bridged Dinuclear Ruthenium Complexes. *Angewandte Chemie International Edition* **2013,** *52* (12), 3398-3401.

46. Schulze, M.; Kunz, V.; Frischmann, P. D.; Würthner, F., A supramolecular ruthenium macrocycle with high catalytic activity for water oxidation that mechanistically mimics photosystem II. *Nature chemistry* **2016,** *8*, 576.

47. Duan, L.; Xu, Y.; Zhang, P.; Wang, M.; Sun, L., Visible light-driven water oxidation by a molecular ruthenium catalyst in homogeneous system. *Inorganic chemistry* **2009,** *49* (1), 209-215.

48. Tseng, H.-W.; Zong, R.; Muckerman, J. T.; Thummel, R., Mononuclear ruthenium (II) complexes that catalyze water oxidation. *Inorganic chemistry* **2008,** *47* (24), 11763-11773.

49. Durham, B.; Wilson, S. R.; Hodgson, D. J.; Meyer, T. J., Cis-trans photoisomerization in $Ru(bpy)_2(OH_2)_2^{2+}$. Crystal structure of trans-$[Ru(bpy)_2(OH_2)(OH)](ClO_4)_2$. *Journal of the American Chemical Society* **1980,** *102* (2), 600-607.

50. Zong, R.; Thummel, R. P., 2,9-Di-(2'-pyridyl)-1,10-phenanthroline: A Tetradentate Ligand for Ru(II). *Journal of the American Chemical Society* **2004,** *126* (35), 10800-10801.

51. Pineda-Galvan, Y.; Ravari, A. K.; Shmakov, S.; Lifshits, L.; Kaveevivitchai, N.; Thummel, R.; Pushkar, Y., Detection of the site protected 7-coordinate Ru^{V}= O species and its chemical reactivity to enable catalytic water oxidation. *Journal of Catalysis* **2019,** *375*, 1-7.

I

Chapter 2

Objectives

II

The most relevant progress in the field of molecular water oxidation has been summarized in the previous chapter. There are still a few challenges ahead in order to see molecular catalysts in working artificial photosynthetic devices. Among them, it is still necessary to reach optimum catalytic rate on (photo)electrode surfaces and this is directly related to the mechanistic pathways followed by a specific catalyst. To reach this goal, the different steps and multiple intermediates involved in the whole catalytic process must be investigated.

This thesis will focus on different aspects related to the mechanism of water oxidation catalysis by studying two families of ruthenium complexes with the tetradentate equatorial ligands in Figure 1. Thus, the first objective of this thesis is to prepare a series of complexes with the general formulas $[Ru(bda)(L)_2]$ (Ru-bda family, Chapters 3, 4 and 5) and $[Ru(bpn)(L)_2]^{2+}$ (Ru-bpn family, Chapter 6), where L is a monodentate axial ligand.

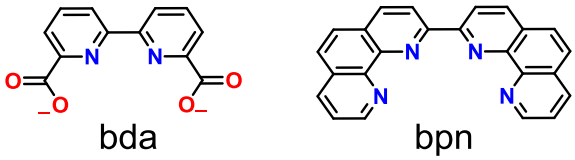

Figure 1. Equatorial ligands used to stabilize ruthenium complexes for the water oxidation catalysis studied in this thesis. Left) dianionic 2,2'-bipyridine-6,6'-dicarboxylato (bda). Right) neutral 2,2'-bi(1,10-phenanthroline) (bpn).

One of the important aspects of a water oxidation catalyst is that it must be flexible enough to rearrange itself in different oxidation states (*e.g.* Ru^{II} to Ru^{V}) and coordination numbers (*e.g.* six or seven for Ru). Particularly important is their capacity to accept water in its coordination sphere. The second objective of this thesis is to study the nature, dynamic behavior and coordination modes of the equatorial ligand bda in ruthenium water oxidation catalysts with the formula $[Ru(bda)(N\text{-}NH_2)_2]$ (where $N\text{-}NH_2$ is 4-(pyridin-4-yl)aniline) in water and organic solvent (Figure 2).

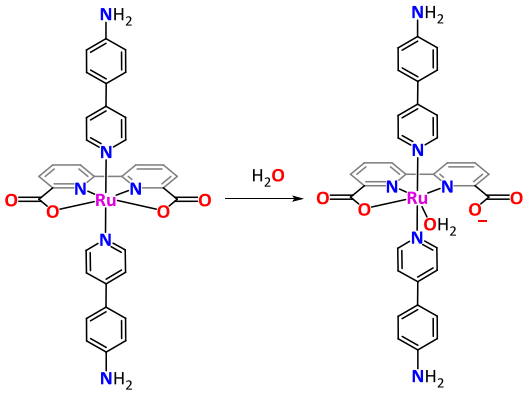

Figure 2. [Ru(bda)(N-NH_2)$_2$] in presence of H_2O, discussed in Chapter 3.

Molecular water oxidation catalysis provides an excellent platform to change mechanistic pathways by modification of the ligands, allowing for the manipulation of electronic and steric properties as well as second coordination sphere effects. The third objective of this thesis is focused on introducing carboxylic acid groups in close proximity of the metallic center of complexes of the Ru-bda family. This objective will be addressed in two different chapters.

In chapter 4, Ru-bda complexes with isoquinoline axial ligands will be prepared and the second coordination sphere influence of having acid or ester groups in strategically chosen position will be thoroughly investigated (Figure 3, left).

In Chapter 5, the carboxylic acid will be placed in the ortho position of a non-symmetric Ru-bda complex (Figure 3, right). In this case, geometric effects derived from the bidentate coordination fashion of the axial ligand will also be considered.

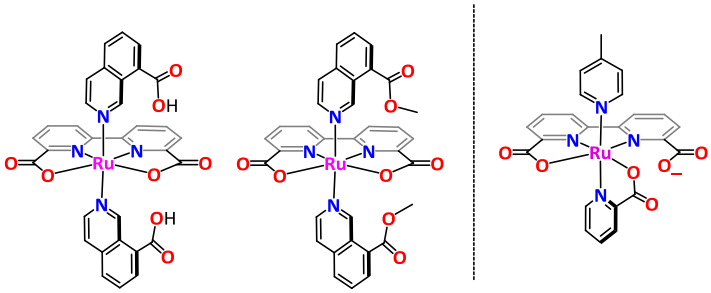

Figure 3. Left) [Ru(bda)(R-8-isoquinoline)$_2$], where R-8-isoquinoline is 8-isoquinolinecarboxilic acid and methyl isoquinoline-8-carboxylate discussed in Chapter 4. Right) [Ru(bda)(pic)(pyC)] where pic is 4-picoline and pyC is 2-pyridinecarboxylato discussed in Chapter 5.

II

Finally, the fourth and last objective of this thesis is to explore the real active species involved in the water oxidation mechanism by ruthenium complexes containing the bpn ligand in the equatorial position (Figure 4). This objective will be fully addressed in Chapter 6.

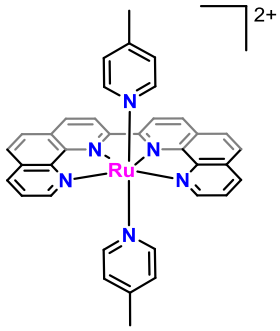

Figure 4. [Ru(bpn)(pic)$_2$] discussed in Chapter 6.

Chapter 3

Behavior of the Ru-bda water oxidation catalysts at low oxidation states

This chapter has been developed together with a former PhD student and in collaboration with other research groups. Abolfazl Ghaderian synthesized and characterized all the new compounds and performed the electrochemical, structural and spectroscopic analysis. The full content of this chapter is published according to the following reference.

Matheu, R.; **Abolfazl Ghaderian**; Francàs, L.; Chernev, P.; Ertem, M. Z.; Benet-Buchholz, J.; Batista, V. S.; Haumann, M.; Gimbert-Suriñach, C.; Sala, X.; Llobet, A., Behavior of Ru–bda Water-Oxidation Catalysts in Low Oxidation States. ***Chemistry – A European Journal***, 24 (**2018**) (49), 12838-12847

III

Abstract

The Ru complex $[Ru^{II}(bda\text{-}\kappa\text{-}N^2O^2)(N\text{-}NH_2)_2]$, **1**, ($bda^{2-}$ = 2,2'-bipyridine-6,6'-dicarboxylate; N-NH_2 = 4-(pyridin-4-yl)aniline) is used as a synthetic intermediate to prepare new Ru-bda complexes that contain the NO^+, acetonitrile (MeCN) or H_2O ligands at oxidation states II and III. Complex **1** in acidic solutions reacts with excess NO^+ (generated *in situ* from sodium nitrite) to form a new Ru complex where the aryl amines ligand N-NH_2 in **1** are transformed into diazonium salts (N-N_2^+ = 4-(pyridin-4-yl)benzenediazonium)) together with the formation of a new Ru-NO group at the equatorial zone, to generate $[Ru^{II}(bda\text{-}\kappa\text{-}N^2O)(NO)(N\text{-}N_2)_2]^{3+}$, $\mathbf{2}^{3+}$. Here the bda ligand only acts in a tridentate manner as $\kappa\text{-}N^2O$ with a dangling carboxylato group. Similarly complex **1** can also react with a coordinating solvent, such as MeCN, at room temperature leading to complex $[Ru^{II}(bda\text{-}\kappa\text{-}N^2O)(MeCN)(N\text{-}NH_2)_2]$, **3**. Finally in acidic aqueous solutions a related reaction occurs where solvent water coordinates the Ru center forming $\{[Ru^{II}(bda\text{-}\kappa\text{-}(NO)^3)(H_2O)(N\text{-}NH_3)_2](H_2O)_n\}^{2+}$, $\mathbf{4}^{2+}$, that is strongly hydrogen bonded with additional water molecules at the second coordination sphere. Furthermore, under acidic conditions the aniline ligands are also protonated forming the corresponding anilinium cationic ligands N-NH_3^+. We have additionally characterized the one electron oxidized complex $\{[Ru^{III}(bda\text{-}\kappa\text{-}(NO)^{3.5})(H_2O)(N\text{-}NH_3)_2](H_2O)_n\}^{3+}$, $\mathbf{5}^{3+}$. The fractional value of κ notation, indicates the presence of an additional contact to the pseudo-octahedral geometry of the Ru metal center. The coordination mode (or modes) of the complexes has (have) been studied both in the solid state and in solution through single-crystal X-ray diffraction, X-ray absorption spectroscopy, variable-temperature NMR and density functional theory calculations. While the $\kappa\text{-}N^2O$ is the main coordination mode for $\mathbf{2}^{3+}$ and **3**, an equilibrium that involves isomers with $\kappa\text{-}N^2O$ and $\kappa\text{-}NO^2$ coordination modes and neighboring hydrogen bonded water molecules is observed for $\mathbf{4}^{2+}$ and $\mathbf{5}^{3+}$.

1-Introduction

The field of water oxidation catalysis (WOC) by molecular transition metal complexes has evolved enormously since the early work of Meyer and co-workers on the blue dimer[1] back in the early eighties up to now.[2] Extremely rugged molecular WOCs based on Ru complexes with turnover numbers (TON) in some cases over a million have been recently reported with confirmed molecular structure maintained over the entire catalytic performance.[3-5] A prominent family of these catalysts are Ru complexes based on the tetradentate ligand 2,2'-bipyridine-6,6'-dicarboxylato (bda^{2-}; see Chart 1 for a drawing of all the ligands described in this work), named Ru-bda type of complexes that have been recently reported.[6-10] In some cases these complexes have catalytic activity that is comparable to that of the natural oxygen evolving complex of photosystem II (OEC-PSII) in green plants and algae.[11-12] Further, even faster catalysts have been reported recently containing a related pentadentate ligand, such as 2,2':6',2"-terpyridine-6,6"-dicarboxylate (tda^{2-}, see Chart 1).[13-14]

The Ru-bda complexes of general formula $[Ru(bda)(N\text{-}Ax)_2]$ (N-Ax is a neutral monodentate pyridyl type of ligand in axial position) constitute a family of complexes that are easy to prepare and whose properties can be nicely tuned through the axial ligand. Indeed, the different nature of the axial ligand can exert steric, electronic or supramolecular effects that influence the properties of the catalyst.[15-16] In addition, axial ligands with the adequate functionalities have been used to immobilize this class of complexes on conducting solid surfaces.[17-20] At oxidation state II the $[Ru(bda)(N\text{-}Ax)_2]$ complexes have a saturated coordination sphere with a distorted octahedral type of symmetry. As such they are not water oxidation catalysts but actually catalyst precursors. Those complexes enter the catalytic cycle upon coordinating a water molecule and reaching higher oxidation states.[21-22]

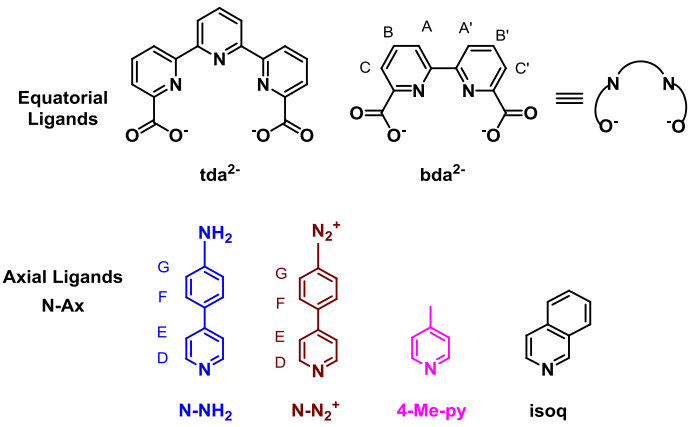

Chart1. Ligands used and discussed in this work together labels for NMR assignment.

The Ru-aqua functionality is important since it provides the capacity to lose protons and electrons in a concerted fashion at relatively low potentials and at the same time provides for an O-O bond formation site. For the particular case where the axial ligand is 4-Methylpyridine (4-Me-py), an X-ray crystal structure of $\{[[Ru^{IV}(OH)(bda\text{-}\kappa\text{-}N^2O^2)(4\text{-}Me\text{-}py)_2](H_2O)]_2(\mu\text{-}H)\}^{3+}$ reveals a *seven coordinate* sphere for the Ru(IV) metal center in a pseudo pentagonal-bipyramid geometry.[23] In sharp contrast, at oxidation state II, the corresponding Ru-aqua complexes are not well characterized. Interestingly, the coordination geometry of the d^6 Ru(II) ion is expected to be octahedral since a seven coordination would imply the violation of the 18 electron rule.[24] Thus, assuming the axial ligands do not detach from the Ru-aqua complex, as evidenced by ^{1}H-NMR spectroscopy, the bda^{2-} ligand must partially decoordinate to generate either a dangling carboxylate or a frustrated coordination site via decoordination of one of Ru-N bonds of the bda^{2-} bipyridyl moiety.[25] The latter is an interesting concept, recently developed, with implications in a variety of processes including heterolytic H_2 splitting.[26-27]

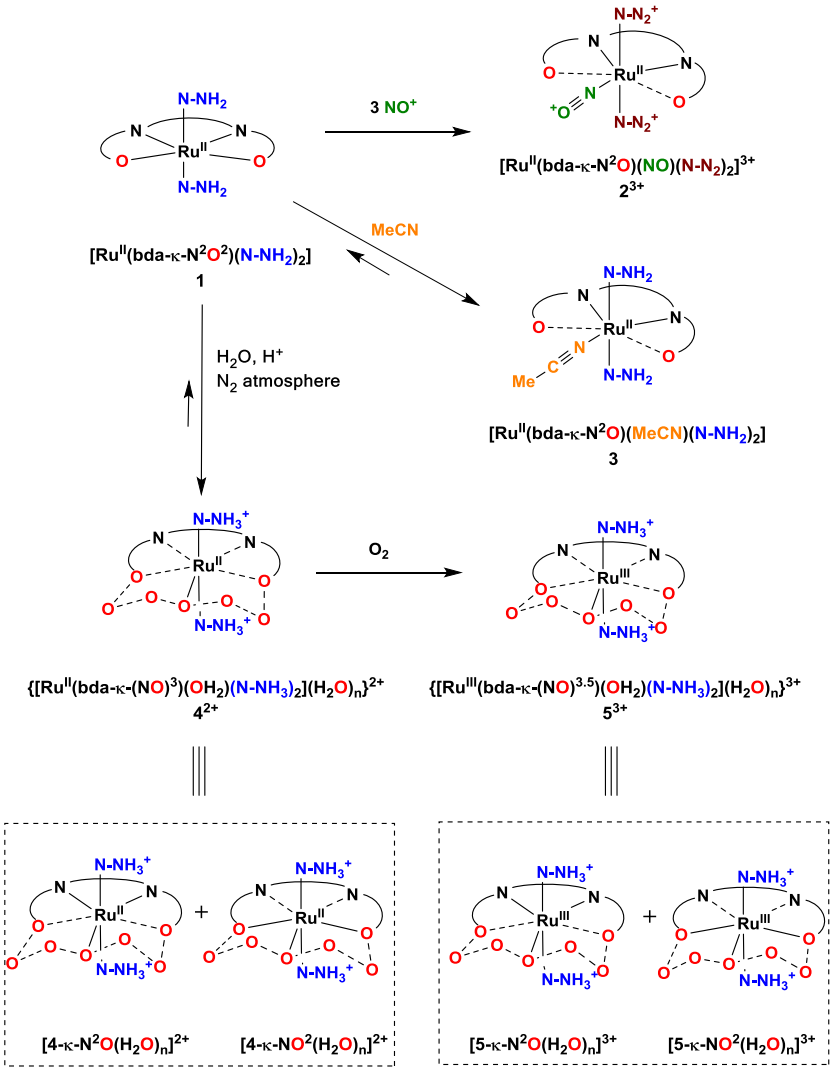

Scheme 1. General synthetic scheme and labels of complexes. The dashed lines at the first coordination sphere of the Ru metal center indicate bonds that are being simultaneously formed and broken. See Chart 1 for the detailed structure of the axial and equatorial ligands. The dashed lines in $\mathbf{4}^{2+}$ and $\mathbf{5}^{3+}$ at the second coordination sphere represent hydrogen bonding from solvent water molecules.

The main goal of the present work is to shed light on the potential coordination modes of the bda^{2-} ligand at low oxidation states (*i.e.,* Ru(II) and Ru(III)) which is

crucial for the aqua ligand coordination that provides the entry into the catalytic cycle. For this purpose, we have prepared a family of Ru-bda complexes (see complexes **1**-**5**$^{3+}$ in Scheme 1) and characterized them by x-ray diffraction and spectroscopic methods as well as by density functional theory (DFT) calculations.

2-Results and Discussion

2·1-Synthesis and solid state structure

We use complex [Ru^{II}(bda-κ-N^2O^2)(N-NH_2)$_2$], **1**, that contains 4-(pyridin-4-yl)aniline (N-NH_2) ligands at axial positions, as the starting material for all the complexes described in this work, following the synthetic strategy depicted in Scheme 1. In this work we selected **1** because of its solubility both in organic solvents and acidic water and because the amino functionality gives an easy synthetic access to the family of Ru-bda complexes depicted in Scheme 1. This family allows to obtain a large variety of spectroscopic properties that analyzed together provide a consistent and comprehensive description of the phenomena occurring in Ru-bda complexes at low oxidation sates. Further, the remote situation of the amino groups does not influence significantly the redox potential of the Ru complex.

The solid-state structure of **1** was analyzed by X-ray diffraction (XRD), Density functional theory (DFT) calculations and X-ray absorption spectroscopy (XAS). Monocrystals of **1** were obtained by slow diffusion of diethyl ether into a methanol solution and an ORTEP drawing of its structure is shown in Figure 1.

The bonding distances and angles found in this structure are similar to related Ru(II) complexes containing similar type of ligands ($d_{Ru-O/Ru-N}$ = 1.9 - 2.1 Å). [28-30] The most interesting feature is the equatorial geometry of the first coordination sphere imposed by the bda^{2-} ligand, generating an ORuO angle of 121.7°.

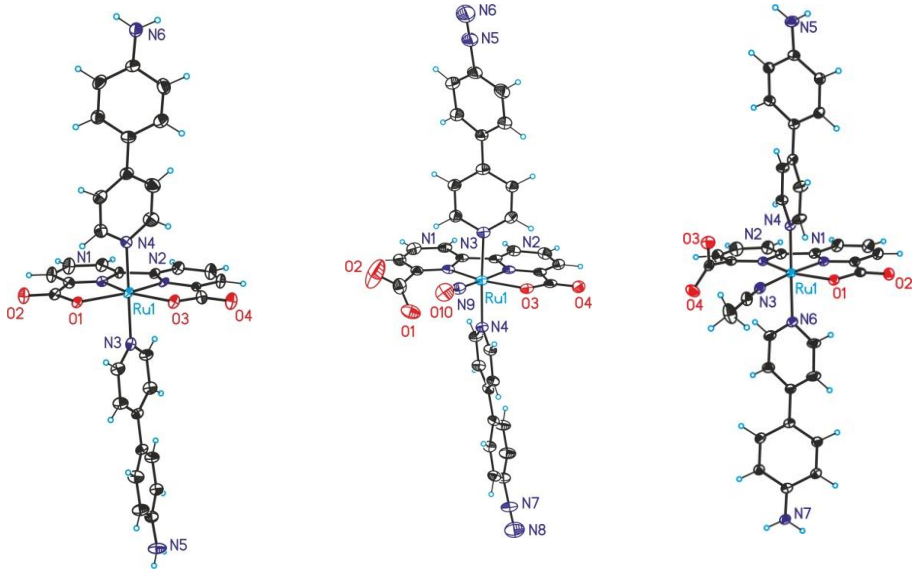

Figure 1. X-ray ORTEP plots (ellipsoids at 50% probability) and labeling scheme of **1** (left), the cationic part of $\mathbf{2}^{3+}$ (center) and **3** (right). Color codes: Ru, cyan; N, blue; O, red; C, black; H, light blue.

III

XAS at the Ru K-edge was carried on a powder of **1**, and the results are reported in Figure 2. The bonding distances obtained by Extended X-ray absorption fine structure (EXAFS) simulation are presented in Table 1 and show very good agreement with the XRD data. Further, DFT calculations were carried out for the geometrical optimization of **1** at the M06 level of theory[31] and the main geometric parameters are also displayed in Table 1, whereas the complete data can be found in the Supporting Information (SI). It is worth noting here the high degree of consistency of all the metric parameters obtained for **1** by these three methodologies bringing a good degree of confidence when used for other related structural characterizations that will be discussed further on.

Table 1. Metric parameters obtained for **1**, $\mathbf{4}^{2+}$ and $\mathbf{5}^{3+}$ from X-ray diffraction (XRD) crystallography, EXAFS and DFT.

	1			***4²⁺***		***5³⁺***		
Distance[a]	XRD	EXAFS (*N*)[b]	DFT[c]	DFT[c] [4-κ-$NO^2(H_2O)_4]^{2+}$	DFT[c] [4-κ-$N^2O(H_2O)_4]^{2+}$	EXAFS (*N*)[b]	DFT[c] [5-κ-$NO^2(H_2O)_4]^{3+}$	DFT[c] [5-κ-$N^2O(H_2O)_4]^{3+}$
Ru-OH_2	--	--	--	2.09	2.18	1.92 (1)	2.03	2.13
Ru-NO	--	--	--	--	--	--	--	--
Ru-N1	1.92	1.92 (2)	1.93	**2.82**	1.94	**2.54** (1)	**2.46**	1.99
Ru-N2	1.93	...	1.93	2.26	2.12	2.11 (3)	**2.32**	2.14
Ru-O1	2.16	2.17 (2)	2.17	2.05	2.12	...	2.03	2.05
Ru-O2	2.18	...	2.17	2.23	**3.45**	...	2.08	**3.06**
Ru-N3	2.07	2.07 (2)	2.08	2.04	2.08	2.01 (2)	2.10	2.11
Ru-N4	2.09	...	2.09	2.06	2.11	...	2.10	2.14
Δ*G* (kcal/mol)				20.3	0.0		2.1	0.0

[a], the labeling scheme is the same as the one used for XRD data of **1** depicted in Figure 1. All distances in Å.
[b], distances between Ru and the atoms in its first and second coordination sphere. In parenthesis, *N*, is the coordination number defined as the number of atoms associated with a particular distance. Additional EXAFS fit parameters (Debye-Waller factors and error sums) are given in Table S1. N and O coordination is indistinguishable in EXAFS analysis as are the locations of ligands in equatorial or axial positions; in the table the distances from EXAFS therefore were ordered to comply with the DFT results.
[c], M06 functional, see SI for details.
[d], in bold are depicted Ru-N or Ru-O distances relevant for the κ-NO^2 vs κ-N^2O isomer discussion.

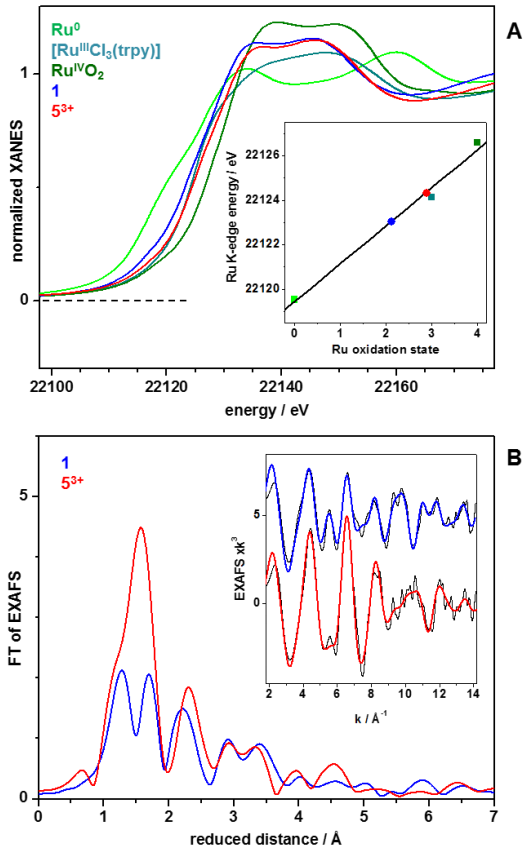

Figure 2. X-ray absorption spectroscopy analysis for **1** and $\mathbf{5}^{3+}$. Data for metallic Ru^0, $Ru^{IV}O_2$, and $[Ru^{III}Cl_3(trpy)]$ is shown for comparison. (A) Ru K-edge spectra. Inset: correlation between K-edge energies (determined at 50 % edge magnitude) and Ru oxidation states. (B) Fourier-transforms (FTs) of EXAFS spectra in the inset. FTs (experimental data) were calculated for k-values of 1.8-14.2 $Å^{-1}$ and using cos^2 windows extending over 10 % at both k-range ends. Spectra were vertically shifted for comparison. Inset, EXAFS oscillations in k-space. Thin black lines are experimental data whereas colored lines are simulations using parameters shown in Table 1 and SI.

Complex **1** reacts with excess NO^+ in acid (generated *in situ* from sodium nitrite)[32] to form complex $[Ru^{II}(bda\text{-}\kappa\text{-}N^2O)(NO)(N\text{-}N_2)_2]^{3+}$, $\mathbf{2}^{3+}$, where the aryl amines of **1** are transformed into diazonium salts ($N\text{-}N_2^+$ = is 4-(pyridin-4-yl)benzenediazonium)). In

addition, a new Ru-NO group is also formed at the equatorial zone according to equation 1. Addition of a saturated solution of KPF_6 allows its isolation as a powdery salt.

$[Ru^{II}(bda\text{-}\kappa\text{-}N^2O^2)(N\text{-}NH_2)_2]$ + 3 NO^+ -> $[Ru^{II}(bda\text{-}\kappa\text{-}N^2O)(NO)(N\text{-}N_2)_2]^{3+}$ + 2 H_2O (Eq.1)

1 **2^{3+}**

Suitable single crystals for x-ray diffraction analysis of **2^{3+}** were obtained by slow evaporation of an acidic aqueous solution of **2^{3+}**. Figure 1 shows the ORTEP representation where the nitrosyl group occupies one of the equatorial positions, while the bda^{2-} exhibits κ-N^2O coordination mode. Such coordination mode releases the geometrical strain in the equatorial plane described in **1**, and produces a dangling carboxylate not bonded to the Ru metal center.

III

The κ-N^2O coordination mode is also favored by the crystal packing of the molecule where the dangling carboxylate interacts with the N atoms of the diazonium groups of another molecule, forming dimers as shown with green dashes in Figure S9. With regard to the Ru-NO^+ group, the near linearity of the Ru-N-O^+ bond (175.8°) and the N-O bond length ($d_{N\text{-}O}$ = 1.13 Å) indicate a N-O triple bond character.

The DFT calculations at the M06 level again gives geometric parameters that are very consistent with those obtained by X-ray diffraction as can be seen in Figure 3 left and Table S2. In particular, **2^{3+}** is assigned as closed-shell singlet with a near lineal Ru-N-O^+ bond (174.7°) and $d_{N\text{-}O}$ = 1.14 Å confirming the Ru^{II}-($N{\equiv}O^+$) nature.

Complex **1** can also react with a coordinating solvent, such as MeCN at room temperature, leading to complex $[Ru^{II}(bda\text{-}\kappa\text{-}N^2O)(MeCN)(N\text{-}NH_2)_2]$, **3**, as shown in equation 2. In this complex, the MeCN coordinates the Ru center in the equatorial plane and again forces the Ru-bda moiety to rearrange its coordination mode by releasing one carboxylate, similar to what is observed for **2^{3+}**.

Single crystals of **3** were obtained by slow diffusion of diethyl ether to a 4:1 MeOH:MeCN solution of **1**, and its ORTEP plot is exhibited in Figure 1. The bda^{2-} ligand coordinates the Ru center in a κ-N^2O fashion with a pendant carboxylate similar to the coordination mode exhibited by $\mathbf{2^{3+}}$. Here again the computational calculations at the M06 level provided geometric parameters for **3** analogous to those obtained by means of XRD (see Table S3).

$$[Ru^{II}(bda\text{-}\kappa\text{-}N^2O^2)(N\text{-}NH_2)_2] + MeCN \rightleftharpoons [Ru^{II}(bda\text{-}\kappa\text{-}N^2O)(MeCN)(N\text{-}NH_2)_2] \quad \text{(Eq. 2)}$$

1 **3**

The coordination of MeCN is subject to an equilibrium where the solvent molecule coordinates and decoordinates the Ru center. This equilibrium can be controlled by the concentration of MeCN solvent. For instance, the addition of a 20% of MeCN to a methanol solution of **1** allows the quantitative generation of **3** as determined by 1D and 2D NMR spectroscopy (see Figures S1-S6). At pH = 1.0, **1** reacts with the water solvent forming complex $\{[Ru^{II}(bda\text{-}\kappa\text{-}(NO)^3)(H_2O)(N\text{-}NH_3)_2](H_2O)_n\}^{2+}$, $\mathbf{4^{2+}}$, as shown in equation 3. Again, the coordination occurs at the equatorial plane with subsequent rearranging of the coordination mode of bda^{2-} ligand. In this case, the modification of the first coordination sphere involves the presence of a network of strongly hydrogen bonded H_2O molecules as a second coordination sphere (see Figures S6-S7). The number of H_2O molecules involved in this network is designated as "*n*" and they are strongly interacting with the Ru-aqua group and the carboxylate moieties of the bda^{2-} ligand. In addition, the amino groups at this pH are protonated forming the corresponding ammonium salts. The proposed label $\mathbf{4^{2+}}$, represents two limit isomeric structures namely $\mathbf{[4\text{-}\kappa\text{-}N^2O(H_2O)_n]^{2+}}$ and $\mathbf{[4\text{-}\kappa\text{-}NO^2(H_2O)_n]^{2+}}$, (denoted as κ-$(NO)^3$) whose relative occurrence will be discussed in the following sections. As observed for **3**, in the solid state the equilibrium shifts towards the more insoluble isomer generating **1** again with no water coordinated at the metal center.

$[Ru^{II}(bda\text{-}\kappa\text{-}N^2O^2)(N\text{-}NH_2)_2]$ + $2H^+$ + (n+1) H_2O ⇌ $\{[Ru^{II}(bda\text{-}\kappa\text{-}(NO)^3)(H_2O)(N\text{-}NH_3)_2](H_2O)_n\}^{2+}$ (Eq. 1)

1 **4^{2+}**

Finally, **4^{2+}** can easily be oxidized by atmospheric oxygen to the paramagnetic d^5 Ru(III) complex $\{[Ru^{III}(bda\text{-}\kappa\text{-}(NO)^{3.5}(H_2O)(N\text{-}NH_3)_2](H_2O)_n\}^{2+}$, **$5^{3+}$**, as presented in Scheme 1 (Figure S8). The fractional value of κ notation here indicates the presence of an additional contact to the pseudo-octahedral geometry of the Ru metal center at we consistently found for these type of complexes. This oxidation has been monitored by UV-vis spectroscopy and takes place with a $t_{1/2}$ of approximately 3.3 minutes at RT according to a first order mechanism (see Figures S10-S11). The complex has been analyzed in solution by Electron Paramagnetic Resonance (EPR) and XAS as it will be described in the following sections and in the SI.

III

2·2-Dynamic behavior in organic solvents

The solution structure of **2^{3+}** and **3** were investigated by VT-NMR in organic solvents and by DFT calculations and the spectra are shown in Figure 4 and in Figures S12-S13. Figure 4 shows the ^{1}H-NMR spectra of **2^{3+}** in acetone-d_6 in the temperature range 273-193 K. At 273 K the ^{1}H-NMR spectrum of **2^{3+}** is not consistent with the κ-N^2O binding mode of the bda^{2-} ligand displayed in the solid state X-ray structure. As the temperature is lowered the resonances due to the bda^{2-} ligand broaden and split, now consistent with the asymmetry observed in the X-ray structure. At 193 K all the resonances are unambiguously assigned based on 2D-NMR spectroscopy (see Figure S12) and in agreement with the DFT calculated chemical shifts (see Figure 4).

The broadening and splitting of the bda^{2-} resonances at lower temperatures points out to the presence of dynamic behavior where the two carboxylates of the bda^{2-} ligand coordinate and decoordinate very fast as graphically shown in Scheme 2. This is further corroborated by the fact that the resonances for protons C and C' contiguous to the carboxylate group, are by far the ones that suffer the largest shift

of more than 0.4 ppm (see Chart 1). An energy of activation of 12.5 kcal/mol is obtained for this process from the spectra (see Figure S14). We also obtained optimized structures for Ru^{II}-NO^{+} complexes via DFT calculations in both κ-N^2O and κ-$(NO)^3$ modes of bda^{2-} ligand and found the latter binding mode, that is proposed to be the transition state in the interconversion, to be higher in energy by 6.2 kcal/mol (see Scheme 2 and Figure 3).

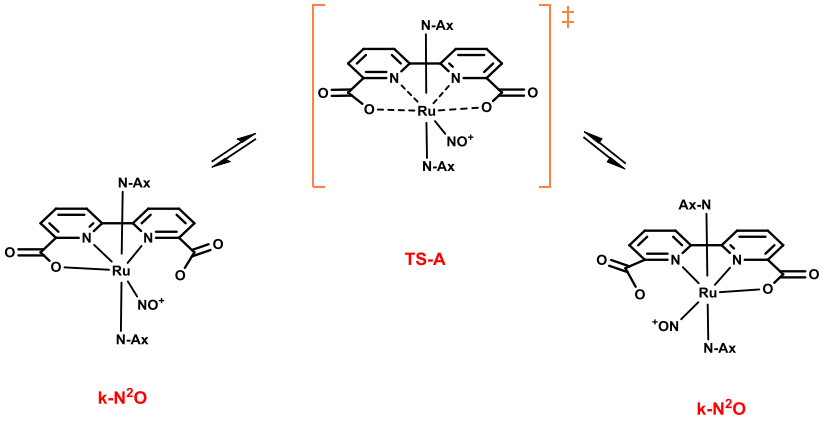

Scheme 2: Species involved in the fast equilibria associated with the dynamic behavior of $\mathbf{2}^{3+}$. Dashed lines indicate the bonds that are simultaneously formed and broken at the transition state TS-A. The DFT calculates TS structure for this complex is depicted in Figure 3 right.

A similar behavior is observed for the Ru^{II}-MeCN complex **3** dissolved in a 1:4 d_3-Acetonitrile:d_4-Methanol mixture but with subtle differences (see Figure S13). At room temperature the main isomer observed is the κ-N^2O that upon heating to temperature close to 320 K, its resonances coalesce. In this case, the energy of activation obtained from the spectra is 15.0 kcal/mol (see Figure S15).

The X-ray structures and VT-NMR results, just described, clearly show the preference for a κ-N^2O coordination mode for the bda^{2-} ligand in $\mathbf{2}^{3+}$ and **3**, in the absence of as second coordination sphere hydrogen bonding. The preference for the κ-N^2O coordination mode for Ru-bda complexes coordinating the MeCN ligand has been observed in related Ru-bda complexes.[33-34] This is in agreement with the

HSAB theory,[35] where Ru at low oxidation states prefers soft π-acceptor ligands such as N-pyridyl over hard O-carboxylate ligands.

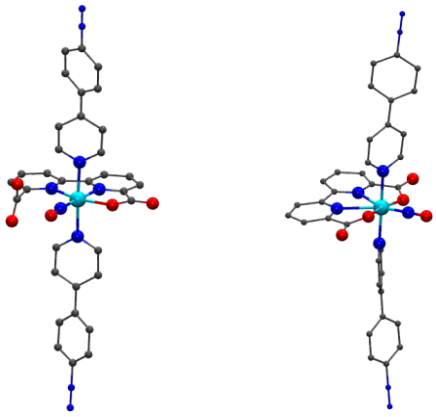

$[2\text{-}\kappa\text{-}N^2O]^{3+}$ **$[2\text{-}\kappa\text{-}(NO)^3]^{3+}$**

Figure 3. Ball and stick representation of the optimized structures at M06 level of theory for **$[2\text{-}\kappa\text{-}N^2O]^{3+}$** and the transition state **$[2\text{-}\kappa\text{-}(NO)^3]^{3+}$** that interconverts the two limiting structures shown in Scheme 2. Color code: Ru, cyan; C, gray; N, blue; O, red, H atoms of the ligands were omitted for clarity.

2·3-Dynamic behavior in acidic aqueous solutions

The ^{1}H-NMR spectrum of **1** was recorded in d_4-Methanol at room temperature and with increasing amounts of a pD = 1.0 solution as indicated in the spectra shown in Figure 5. In pure d_4-Methanol the ^{1}H-NMR spectrum of **1** shows the typical behavior of a six coordinated Ru(II) complex with C_{2v} symmetry. All resonances could be unambiguously assigned based on 2D NMR spectra and also supported by computed NMR chemical shifts at M06 level of theory. However, the addition of CF_3SO_3D dissolved in D_2O, significantly broaden resonances and some of them are strongly shifted as observed in Figure 5. The F labelled protons (Chart I), which are close to the amino group, suffer the highest shift due to the protonation of the amino group.

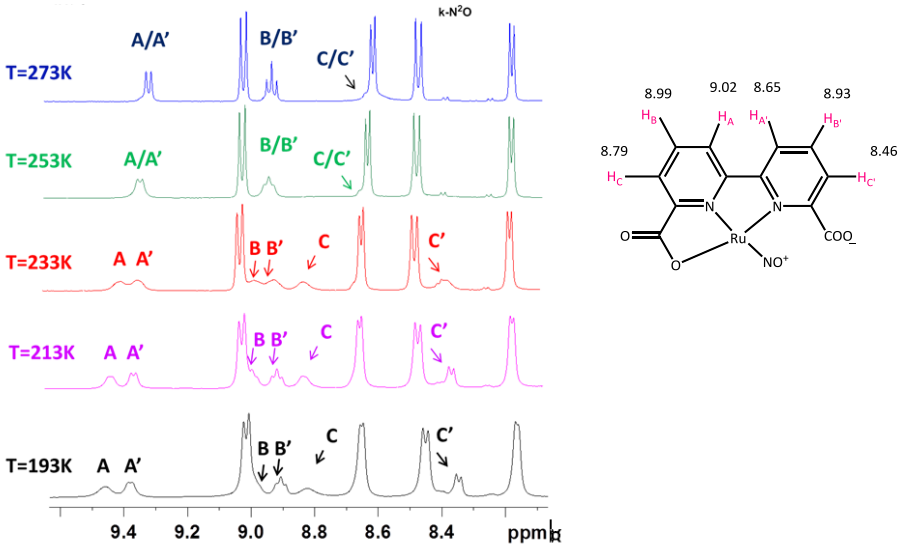

Figure 4. Left, VT -^{1}H-NMR spectra for $\mathbf{2}^{3+}$ in acetone-d_6. Right, computed chemical shifts at M06 level of theory for the bda^{2-} hydrogens in $\mathbf{2}^{3+}$. See Chart 1 for the labeling.

III

The small shift of the D protons indicates that the Ru center is almost unaffected by the protonation of the amines. Further, at 25% of pD = 1.0 solution, we carried out VT-NMR all the way to 240 K where the resonances sharpen again, as shown in Figure 5 (right), consistent with the presence of a single symmetrical isomer.

In contrast to the previous VT-NMR spectra for $\mathbf{2}^{3+}$, now both B and C protons are similarly shifted which advocates for a different type of dynamic behavior where both the Ru-N and Ru-O bonds are simultaneously being formed and broken as proposed in Scheme 3.

Further, the VT-NMR results are consistent with the coordination of a water molecule to the Ru metal center upon addition of an acidic aqueous solution.

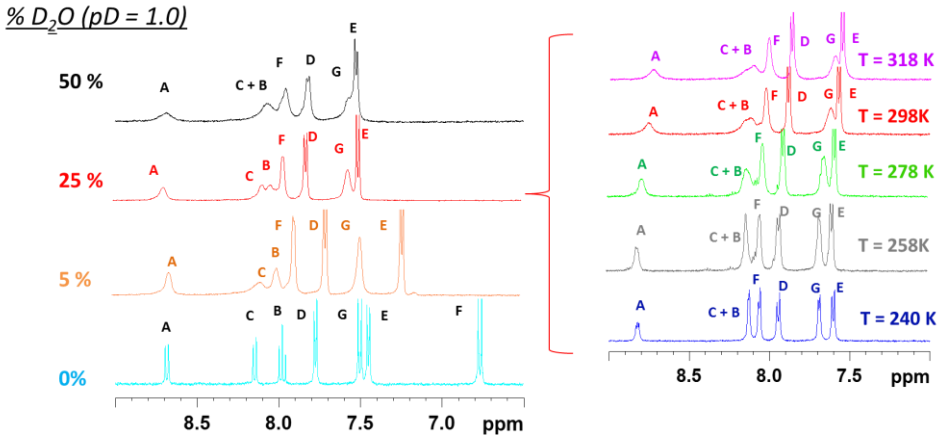

Figure 5. Left, ^{1}H-NMR of **1** in d_4-Methanol (cyan spectrum) and of $\mathbf{4}^{2+}$ with different amounts of a solution of 0.1 M CF_3SO_3D in D_2O (labeled as D_2O, pD = 1.0) at 298 K. Right, VT ^{1}H-NMR of $\mathbf{4}^{2+}$ in d_4-Methanol with 25% D_2O, pD = 1.0. Samples prepared under rigorous N_2 atmosphere. See Chart 1 for the labeling.

III

The formation and braking of the Ru(II)-OH_2 bond occurs simultaneously with a dynamic behavior involving species $\mathbf{[4\text{-}\kappa\text{-}N^2O(H_2O)_n]^{2+}}$ and $\mathbf{[4\text{-}\kappa\text{-}NO^2(H_2O)_n]^{2+}}$, that interconvert through the transition states TS-A, TS-B and TS-C (Scheme 3). The sharpening at low temperature of the ^{1}H resonances is consistent the absence of the coordination/decoordination of water to the Ru center but with all the equilibria indicated in Scheme 3 occurring very fast. In sharp contrast, when **1** is dissolved in neutral aqueous solutions, d_4-Methanol:D_2O (4:1), the VT ^{1}H-NMR experiment reveals that the aqua coordination/decoordination to Ru equilibrium is still present (Figure S16).

The presence of the $\mathbf{[4\text{-}\kappa\text{-}NO^2(H_2O)_n]^{2+}}$ species is favored by solvent H_2O molecules strongly hydrogen bonded to the Ru-H_2O group and the carboxylato moiety of the bda^{2-} ligand. This hydrogen bonding will push the bpy (bipyridyl moiety) part of the bda^{2-} ligand away from the metal center and explains why the intuitively preferred Ru-N coordination mode for a soft low spin d^6 Ru(II) ion is not always favored.

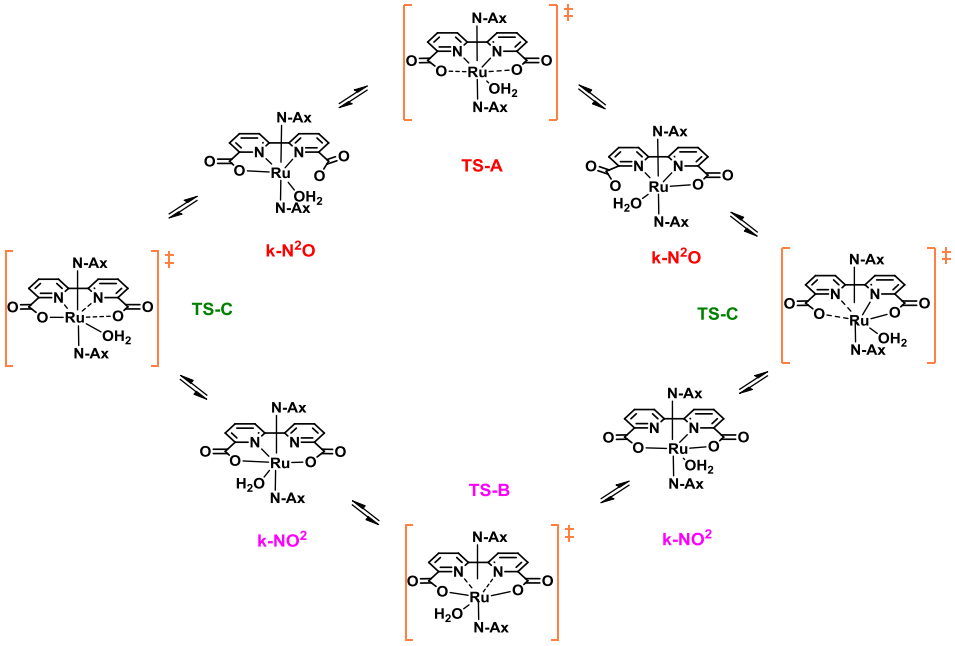

Scheme 3. Reaction pathways leading to a combination of equilibria involved in dynamic behavior of $\mathbf{4}^{2+}$ or $\mathbf{5}^{3+}$ in acidic aqueous solution. The dashed lines indicate bonds that are simultaneously formed and broken in the transition states. Water solvation molecules are not shown for clarity purposes. Three different type of pathways are identified depending on the transition state through which the species are interconverted. Thus path A involves "TS-A" whereas paths B and C involve "TS-B" and "TS-C" respectively.

All the NMR measurements were performed under strict N_2 conditions to avoid the oxidation of $\mathbf{4}^{2+}$ to $\mathbf{5}^{3+}$ (see NMR methods in the SI for further details). In order to further prove that $\mathbf{4}^{2+}$ remains at oxidation state II, we prepared solutions of $\mathbf{4}^{2+}$ identically to those prepared for NMR analysis and carried out EPR measurements. The absence of EPR signal discards the formation of any traces of the one electron oxidized species, $\mathbf{5}^{3+}$, and thus confirms that the nature of the NMR resonance broadening is solely due to the dynamic behavior (Figure S17). The same behavior also occurs in other Ru-bda catalyst such as [Ru(bda-κ-N^2O^2)(isoq)$_2$] (isoq is isoquinoline) under exactly the same conditions as for **1**, as shown in Figure S18 in the supporting information. The comparable shift and broadening of the resonances

observed for the [Ru(bda-κ-N^2O^2)(isoq)$_2$] complex suggests that this is a general phenomenon occurring in Ru-bda complexes.

We carried out DFT calculations for both the **[4-κ-$NO^2(H_2O)_n$]$^{2+}$** and **[4-κ-$N^2O(H_2O)_n$]$^{2+}$** isomers using either two or four solvated water molecules. We have chosen a limited number of water molecules as a model although it is obvious that a much larger number of water molecules will be involved as second and third coordination sphere to the Ru center. The structures with two or four solvated molecules yielded similar results in terms of geometrical features and relative energies of the isomers (see Figures S21-S22 and Tables S4-S5). To simplify the discussion we present only **[4-κ-$NO^2(H_2O)_4$]$^{2+}$** and **[4-κ-$N^2O(H_2O)_4$]$^{2+}$** isomers and the optimized geometries and relevant metric parameters of which are depicted in Figure 6 and Table 1. The first interesting feature of the obtained optimized structures for **[4-κ-$NO^2(H_2O)_4$]$^{2+}$** and **[4-κ-$N^2O(H_2O)_4$]$^{2+}$** is the presence of a hydrogen bonding network between the Ru-aqua group and the carboxylate groups of the bda^{2-} ligand that resembles the crystal structure of {[[Ru^{IV}(OH)(κ-N^2O^2-bda)(4-Me-py)$_2$](H$_2$O)]$_2$(μ-H)}$^{3+}$.

It is also interesting to compare the distances between Ru and the N and O atoms of the bda^{2-} ligand in both isomers. For the **[4-κ-$N^2O(H_2O)_4$]$^{2+}$** isomer these distances are very similar to those of **2^{3+}** with a the characteristic distance between the Ru and the O atom of the dangling carboxylate at 3.45 Å. On the other hand, for **[4-κ-$NO^2(H_2O)_4$]$^{2+}$**, the most unusual distances are the Ru-N that are 2.26 Å and 2.82 Å, which are 0.1 Å and 0.7 Å longer than the typical Ru-N bonds for related complexes.

The computed chemical shifts at M06 level for the optimized structures (Figure S25) are not consistent with either those of the **[4-κ-$N^2O(H_2O)_4$]$^{2+}$** isomer (Path A, Scheme 3) or those of the **[4-κ-$NO^2(H_2O)_4$]$^{2+}$** (Path B, Scheme 3) but with a mixture of all of them. The combination of all these equilibria is depicted in Scheme 3 (Paths A, B and C), where explicit water molecules are not shown for the sake of simplicity.

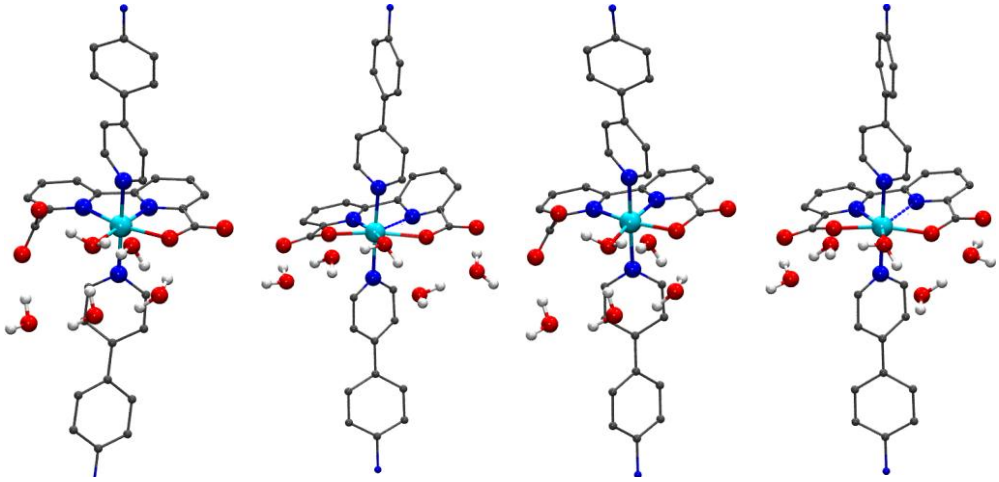

Figure 6. Ball and stick representation of the optimized structures of **[4-κ-N²O(H₂O)₄]²⁺**, **[4-κ-NO²(H₂O)₄]²⁺**, **[5-κ-N²O(H₂O)₄]³⁺** and **[5-κ-NO²(H₂O)₄]³⁺** at M06 level of theory. Dashed line indicates elongated bond. Color code: Ru, cyan; C, gray; N, blue; O, red, H atoms of the ligands were omitted for clarity.

The isomers of the one electron oxidized complex, **[5-κ-N²O(H₂O)₄]³⁺** and **[5-κ-NO²(H₂O)₄]³⁺**, were also optimized at M06 level of theory and the corresponding structures and most relevant geometric parameters are presented in Figure 6 and Table 1.

For the one electron oxidized isomers, the bond distances of the first and second coordination sphere are shortened compared to those found for the **4²⁺** counterparts as expected.[36] However, the most relevant distances for both isomers, Ru-N of 2.46 Å for **[5-κ-NO²(H₂O)₄]³⁺** and the Ru-O distance of 3.06 Å for the dangling carboxylate in **[5-κ-N²O(H₂O)₄]³⁺** remain comparable to its related complex in the oxidation state II. Another very interesting feature of these complexes is their relative energies. While at oxidation sate II, the **[4-κ-N²O(H₂O)₄]²⁺** isomer is favored by 20.3 kcal/mol with regard to the **[4-κ-NO²(H₂O)₄]²⁺** isomer, at oxidation state III this difference is drastically reduced to only 2.1 kcal/mol. While the energy comparison is only indicative because of the possibility of several conformers

associated with solvent molecules hampering a reliable comparison, the trend is certainly significant.

In order to extract further experimental evidence about the potential combination of equilibria acting in the Ru-aqua complexes bearing the bda^{2-} ligand in aqueous solution, we carried out XAS spectroscopy of frozen solutions of $\mathbf{5}^{3+}$. The results obtained are shown in Figure 2 and Table 1 together with those of **1,** $[Ru^{III}Cl_3(trpy)]$ (trpy is 2,2':6',2"-terpyridine) and $Ru^{IV}O_2$ that were used as reference materials.

Table 1 presents the metric parameters $\mathbf{5}^{3+}$, extracted from EXAFS simulations (Figure 2B). As can be observed the EXAFS spectral changes for $\mathbf{5}^{3+}$ compared to **1** involve an overall shortening of the Ru-N/O bond lengths, leading to homogenization of the first coordination sphere of Ru-ligand distances. Very importantly a ~2.54 Å distance was detected that improves the quality of the EXAFS fit by a factor of about 2 (Table S1). This additional distance is thus indicative that the isomer $\mathbf{[5\text{-}\kappa\text{-}NO^2(H_2O)_n]^{3+}}$ is present in the mixture of isomers at this oxidation state. In addition, the metric parameters obtained from EXAFS coincide well with those obtained from the computed structures for $\mathbf{[5\text{-}\kappa\text{-}NO^2(H_2O)_4]^{3+}}$ confirming the presence of these species in frozen aqueous solution (Table 1).

To the best of our knowledge, this is the first time to experimentally demonstrate that the $\kappa\text{-}NO^2$ coordination mode for the bda^{2-} ligands is relevant in the combination of potential isomers involved in Ru-bda type of complexes at low oxidation states, although it had been suggested based on DFT calculations. In addition, we also found a similar distance for the $[Ru(tda)(py)_2]$ catalyst precursor at oxidation state III, where the two isomers, $[Ru^{III}(tda\text{-}\kappa\text{-}N^2O^2)(py)_2]^+$ and $[Ru^{III}(tda\text{-}\kappa\text{-}N^3O)(py)_2]^+$, are found to coexist in the crystal structure.

This counterintuitively behavior on the coordination modes of bda^{2-} in $\mathbf{4}^{2+}$ and $\mathbf{5}^{3+}$, which is different from their homologues to $\mathbf{2}^{3+}$ and **3** in organic solvents, is mainly associated with the strong hydrogen bonding belt along the aqua and carboxylato

ligands. The latter provides the driving force to push away the bpy part of the bda^{2-} ligand producing a decoordination of one of the N-atoms.

3-Conclusions

In summary, our results based on VT-NMR, XAS and DFT calculations provide a detailed description of the nature of the species involved in water oxidation catalysis by Ru-bda type complexes at low oxidation states, where the critical Ru-aqua group that provides access to the catalytic cycle is formed. The results show the fundamental need for a flexible and adaptable ligand, as is the case for bda^{2-}, both from an electronic and geometrical perspective, to comply with the demands of the Ru metal centers at the different oxidation states. Further, for the first time we have shown experimentally the presence of isomers in Ru-bda type of complexes where the ligand acts in a κ-NO^2 fashion.

References

1. Gersten, S. W.; Samuels, G. J.; Meyer, T. J., Catalytic oxidation of water by an oxo-bridged ruthenium dimer. *Journal of the American Chemical Society* **1982,** *104* (14), 4029-4030.
2. Garrido-Barros, P.; Gimbert-Suriñach, C.; Matheu, R.; Sala, X.; Llobet, A., How to make an efficient and robust molecular catalyst for water oxidation. *Chemical Society Reviews* **2017,** *46* (20), 6088-6098.
3. López, I.; Ertem, M. Z.; Maji, S.; Benet-Buchholz, J.; Keidel, A.; Kuhlmann, U.; Hildebrandt, P.; Cramer, C. J.; Batista, V. S.; Llobet, A., A Self-Improved Water-Oxidation Catalyst: Is One Site Really Enough? *Angewandte Chemie International Edition* **2014,** *53* (1), 205-209.
4. Creus, J.; Matheu, R.; Peñafiel, I.; Moonshiram, D.; Blondeau, P.; Benet-Buchholz, J.; García-Antón, J.; Sala, X.; Godard, C.; Llobet, A., A million turnover molecular anode for catalytic water oxidation. *Angewandte Chemie International Edition* **2016,** *55* (49), 15382-15386.
5. Matheu, R.; Moreno-Hernandez, I. A.; Sala, X.; Gray, H. B.; Brunschwig, B. S.; Llobet, A.; Lewis, N. S., Photoelectrochemical behavior of a molecular Ru-based water-oxidation catalyst bound to TiO_2-protected Si photoanodes. *Journal of the American Chemical Society* **2017,** *139* (33), 11345-11348.
6. Duan, L.; Bozoglian, F.; Mandal, S.; Stewart, B.; Privalov, T.; Llobet, A.; Sun, L., A molecular ruthenium catalyst with water-oxidation activity comparable to that of photosystem II. *Nature chemistry* **2012,** *4* (5), 418-423.
7. Richmond, C. J.; Matheu, R.; Poater, A.; Falivene, L.; Benet-Buchholz, J.; Sala, X.; Cavallo, L.; Llobet, A., Supramolecular Water Oxidation with Ru–bda-Based Catalysts. *Chemistry–A European Journal* **2014,** *20* (52), 17282-17286.
8. Wang, L.; Duan, L.; Wang, Y.; Ahlquist, M. S.; Sun, L., Highly efficient and robust molecular water oxidation catalysts based on ruthenium complexes. *Chemical Communications* **2014,** *50* (85), 12947-12950.

9. Schulze, M.; Kunz, V.; Frischmann, P. D.; Würthner, F., A supramolecular ruthenium macrocycle with high catalytic activity for water oxidation that mechanistically mimics photosystem II. *Nature chemistry* **2016,** *8*, 576.
10. Li, F.; Zhang, B.; Li, X.; Jiang, Y.; Chen, L.; Li, Y.; Sun, L., Highly efficient oxidation of water by a molecular catalyst immobilized on carbon nanotubes. *Angewandte Chemie International Edition* **2011,** *50* (51), 12276-12279.
11. Dau, H.; Haumann, M., Eight steps preceding O–O bond formation in oxygenic photosynthesis—A basic reaction cycle of the photosystem II manganese complex. *Biochimica et Biophysica Acta (BBA)-Bioenergetics* **2007,** *1767* (6), 472-483.
12. Cox, N.; Retegan, M.; Neese, F.; Pantazis, D. A.; Boussac, A.; Lubitz, W., Electronic structure of the oxygen-evolving complex in photosystem II prior to OO bond formation. *Science* **2014,** *345* (6198), 804-808.
13. Matheu, R.; Ertem, M. Z.; Benet-Buchholz, J.; Coronado, E.; Batista, V. S.; Sala, X.; Llobet, A., Intramolecular proton transfer boosts water oxidation catalyzed by a Ru complex. *Journal of the American Chemical Society* **2015,** *137* (33), 10786-10795.
14. Matheu, R.; Ertem, M. Z.; Pipelier, M.; Lebreton, J.; Dubreuil, D.; Benet-Buchholz, J.; Sala, X.; Tessier, A.; Llobet, A., The role of seven-coordination in Ru-catalyzed water oxidation. *ACS Catalysis* **2018,** *8* (3), 2039-2048.
15. Duan, L.; Wang, L.; Li, F.; Li, F.; Sun, L., Highly efficient bioinspired molecular Ru water oxidation catalysts with negatively charged backbone ligands. *Accounts of chemical research* **2015,** *48* (7), 2084-2096.
16. Duan, L.; Wang, L.; Inge, A. K.; Fischer, A.; Zou, X.; Sun, L., Insights into Ru-based molecular water oxidation catalysts: Electronic and noncovalent-interaction effects on their catalytic activities. *Inorganic chemistry* **2013,** *52* (14), 7844-7852.
17. Matheu, R.; Francàs, L.; Chernev, P.; Ertem, M. Z.; Batista, V.; Haumann, M.; Sala, X.; Llobet, A., Behavior of the Ru-bda water oxidation catalyst covalently anchored on glassy carbon electrodes. *ACS Catalysis* **2015,** *5* (6), 3422-3429.
18. Gao, Y.; Ding, X.; Liu, J.; Wang, L.; Lu, Z.; Li, L.; Sun, L., Visible light driven water splitting in a molecular device with unprecedentedly high photocurrent density. *Journal of the American Chemical Society* **2013,** *135* (11), 4219-4222.
19. Concepcion, J. J.; Zhong, D. K.; Szalda, D. J.; Muckerman, J. T.; Fujita, E., Mechanism of water oxidation by [Ru(bda)$(L)_2$]: the return of the "blue dimer". *Chemical Communications* **2015,** *51* (19), 4105-4108.
20. Sheridan, M. V.; Sherman, B. D.; Coppo, R. L.; Wang, D.; Marquard, S. L.; Wee, K.-R.; Murakami Iha, N. Y.; Meyer, T. J., Evaluation of chromophore and assembly design in light-driven water splitting with a molecular water oxidation catalyst. *ACS Energy Letters* **2016,** *1* (1), 231-236.
21. Sala, X.; Maji, S.; Bofill, R.; Garcia-Anton, J.; Escriche, L. s.; Llobet, A., Molecular water oxidation mechanisms followed by transition metals: state of the art. *Accounts of chemical research* **2013,** *47* (2), 504-516.
22. Daniel, Q.; Huang, P.; Fan, T.; Wang, Y.; Duan, L.; Wang, L.; Li, F.; Rinkevicius, Z.; Mamedov, F.; Ahlquist, M. S., Rearranging from 6-to 7-coordination initiates the catalytic activity: An EPR study on a Ru-bda water oxidation catalyst. *Coordination chemistry reviews* **2017,** *346*, 206-215.
23. Duan, L.; Fischer, A.; Xu, Y.; Sun, L., Isolated seven-coordinate Ru (IV) dimer complex with $[HOHOH]^-$ bridging ligand as an intermediate for catalytic water oxidation. *Journal of the American Chemical Society* **2009,** *131* (30), 10397-10399.
24. Pyykkö, P., Understanding the eighteen-electron rule. *Journal of organometallic chemistry* **2006,** *691* (21), 4336-4340.
25. Nyhlén, J.; Duan, L.; Åkermark, B.; Sun, L.; Privalov, T., Evolution of O_2 in a Seven-Coordinate RuIV Dimer Complex with a $[HOHOH]^-$ Bridge: A Computational Study. *Angewandte Chemie International Edition* **2010,** *49* (10), 1773-1777.

26. D. W.Stephan, . Eds: Reedijk, J.; Poeppelmeier, K. Elsevier, Oxford, April. *Comp. Inorg. Chem. II.* **2013.**

27. Samuel, P. P.; Mondal, K. C.; Amin Sk, N.; Roesky, H. W.; Carl, E.; Neufeld, R.; Stalke, D.; Demeshko, S.; Meyer, F.; Ungur, L., Electronic structure and slow magnetic relaxation of low-coordinate cyclic alkyl (amino) carbene stabilized iron (I) complexes. *Journal of the American Chemical Society* **2014,** *136* (34), 11964-11971.

28. Di Giovanni, C.; Poater, A.; Benet-Buchholz, J.; Cavallo, L.; Solà, M.; Llobet, A., Dinuclear Ru–Aqua complexes for selective epoxidation catalysis based on supramolecular substrate orientation effects. *Chemistry–A European Journal* **2014,** *20* (14), 3898-3902.

29. Romero, I.; Rodríguez, M.; Llobet, A.; Collomb-Dunand-Sauthier, M.-N.; Deronzier, A.; Parella, T.; Stoeckli-Evans, H., Synthesis, structure and redox properties of a new ruthenium (II) complex containing the flexible tridentate ligand N, N-bis (2-pyridylmethyl) ethylamine, cis-fac-Ru $(bpea)_2^{2+}$, and its homologue attached covalently to a polypyrrole film. *Journal of the Chemical Society, Dalton Transactions* **2000,** (11), 1689-1694.

30. Di Giovanni, C.; Vaquer, L.; Sala, X.; Benet-Buchholz, J.; Llobet, A., New dinuclear ruthenium complexes: Structure and oxidative catalysis. *Inorganic chemistry* **2013,** *52* (8), 4335-4345.

31. Zhao, Y.; Truhlar, D. G., The M06 suite of density functionals for main group thermochemistry, thermochemical kinetics, noncovalent interactions, excited states, and transition elements: two new functionals and systematic testing of four M06-class functionals and 12 other functionals. *Theoretical Chemistry Accounts* **2008,** *120* (1-3), 215-241.

32. Pinson, J.; Podvorica, F., Attachment of organic layers to conductive or semiconductive surfaces by reduction of diazonium salts. *Chemical Society Reviews* **2005,** *34* (5), 429-439.

33. Tong, L.; Duan, L.; Xu, Y.; Privalov, T.; Sun, L., Structural modifications of mononuclear ruthenium complexes: a combined experimental and theoretical study on the kinetics of ruthenium-catalyzed water oxidation. *Angewandte Chemie International Edition* **2011,** *50* (2), 445-449.

34. Alibabaei, L.; Sherman, B. D.; Norris, M. R.; Brennaman, M. K.; Meyer, T. J., Visible photoelectrochemical water splitting into H_2 and O_2 in a dye-sensitized photoelectrosynthesis cell. *Proceedings of the National Academy of Sciences* **2015,** *112* (19), 5899-5902.

35. Pearson, R. G., Hard and soft acids and bases. *Journal of the American Chemical Society* **1963,** *85* (22), 3533-3539.

36. Stynes, H. C.; Ibers, J. A., Effect of metal-ligand bond distances on rates of electron-transfer reactions. Crystal structures of hexaammineruthenium (II) iodide, $[Ru(NH_3)_6]I_2$, and hexaammineruthenium (III) tetrafluoroborate,$[Ru(NH_3)_6][BF_4]_3$. *Inorganic chemistry* **1971,** *10* (10), 2304-2308.

Supporting information

MATERIALS

All the reagents were purchased from Sigma-Aldrich unless indicated differently. $RuCl_3 \cdot 3H_2O$ was supplied by Alfa Aesar. 4-pyridine-4-yl-phenylamine (N-NH_2) was purchased from ChemCollect. $[RuCl_2(dmso)_4]$[1] and $[Ru(bda\text{-}\kappa\text{-}N^2O^2)(isoq)_2]$[2] (isoq is isoquinoline) were prepared according to the literature.

Synthesis of $[Ru(bda\text{-}\kappa\text{-}N^2O^2)(N\text{-}NH_2)_2]$ (1). The preparation of the described compound was carried out by following the reported procedure.[3] A sample of $[RuCl_2(dmso)_4]$ (300 mg, 0.62 mmol), 6,6'-dicarboxylic acid-2,2'-dipyridyl (151 mg, 0.62 mmol) and Et_3N were mixed and degassed in dry methanol (12 mL), refluxed for 3 hours and cooled down to RT. 4-pyridine-4-yl-phenylamine (N-NH_2) (210 mg, 1.24 mmol) was then added to the reaction mixture and the solution was further refluxed for 7 hours. During that time, a brown precipitate appeared and was filtered off and dried under vacuum. The brown solid was then dissolved in a mixture of 2,2,2-Trifluoroethanol (TFE) and dichloromethane (4:100) and added to an alumina column (eluted with 4% TFE, 4% methanol in dichloromethane). The eluent was then reduced to 50 mL and diethyl ether was added to obtain a brown crystalline solid that was filtered on a frit and dried under vacuum (100 mg, 25% yield). The nature and purity of the complex was confirmed by ^{1}H NMR (see Figure 5 in the main section).

Synthesis of $[Ru(bda\text{-}\kappa\text{-}N^2O)(NO)(N\text{-}N_2)][PF_6]_3.KPF_6$ ($2(PF_6)_3$). The preparation of the described compound was carried out by following the reported procedure.[3] A sample of $NaNO_2$ (30 mg, 0.43 g) was dissolved in 0.5 M HCl (2 mL) and added drop wise to a suspension of 1 (100mg, 0.14 mmol) in 0.5 M HCl (24 mL). After stirring for 30 minutes, a saturated solution of KPF_6 in 0.5 M HCl was used to precipitate the product as a powder. The solid was filtered in a frit, washed with water, ethanol and

diethyl ether and dried under vacuum (76 mg, 38% yield). The nature and purity of the complex was confirmed by ^{1}H NMR (see Figure 4 in the main section).

Preparation of a solution of complex [Ru^{II}(bda-κ-N^{2}O)(MeCN)(N-NH$_2$)$_2$] (3). A sample of **1** (2 mg, 2.92 μmol) dissolved in a 1:4 d_3-Acetonitrile: d_4-Methanol mixture (1 mL) and stirred at room temperature (RT) for 5 minutes. ^{1}H-NMR (500 MHz, d_4-Methanol): δ = 6.71 (4H, d, J = 8.6Hz), 7.35 (4H, d, J = 6.5 Hz), 7.44 (4H, d, J = 8.6 Hz), 7.54 (1H, d, J = 6.4 Hz), 7.96 (4H, d, J = 6.5 Hz), 8.02 (3 H, m), 8.37 (1H, dd, J = 6.9 Hz), 8.51 (1H, d, J = 7.7 Hz).^{13}C-NMR (d_4-Methanol): δ = 114.6, 120.2, 121.8, 123.7, 124.4, 124.6, 125.6, 127.6, 133.8, 137.0, 148.4, 150.3, 152.7, 154.2, 157.5, 159.6, 167.8, 169.9, 173.8. The assignment of resonances can be found in Figures S1-S2.

Preparation of a solution of complex {[Ru^{II}(bda-κ-(NO)^{3})(H$_2$O)(N-NH$_3$)$_2$](H$_2$O)$_n$}$^{2+}$, (4^{2+}). The preparation of this solution was performed inside a N_2 filled glovebox and the solutions used were stored, manipulated and added inside the glove box. A sample of **1** (2 mg, 2.92 μmol) was dissolved in methanol (1 mL) and a pH = 1.0 solution was added (330 μL) and stirred at RT for 5 minutes. ^{1}H-NMR (d_4-Methanol): δ = 7.56 (4H, d, J = 8.7 Hz), 7.61 (4H, m), 7.88 (4H, d, J = 8.7 Hz), 8.02 (4H, m), 8.12 (4H, m), 8.75 (1H, m). See Figure 4 in the main section for the assignments.

Preparation of a solution of complex {[Ru^{III}(bda-κ-(NO)$^{3.5}$)(H$_2$O)(N-NH$_3$)$_2$](H$_2$O)$_n$}$^{3+}$ (5^{3+}). A sample of **1** (4 mg, 5.8 μmol) was dissolved in a pH = 1.0 solution (2 mL) under open atmosphere and stirred for 20 min at RT. EPR signals (pD = 1.0): g_x = 2.10, g_y = 2.07 and g_z = 1.96.

Aqueous solutions used for synthesis and NMR/EPR measurements.

pH = 1.0 triflic acid (TA) solution: A sample of neat TA (10 g, 0.0663 mols) was diluted with 662 mL of deionised water.

pD = 1.0 TA solution: A sample of deuterated neat TA (1 g, 0.00663 mols) was diluted with 66.2 mL of deuterated water.

pD = 5.0 ascorbate solution: L(+)-Ascorbic acid sodium salt powder (10 mg, 0.05 mmol) was dissolved in 2 mL of pD = 1.0 solution.

Aqueous Solutions used for XAS measurements.

pH = 0.3 HCl solution. HCl (36 % w/w, 0.41 mL) was diluted up to 10 mL by the use of mili-Q water. The concentration of 5^{3+} in pH = 0.3 HCl solution was higher than in a TA pH = 1.0 solution.

METHODS

NMR methods

Instrument: A Bruker Avance 500 MHz spectrometer equipped with a Cryoprobe™ was used to carry out NMR spectroscopy.

Solutions of **1**, $\mathbf{2}^{2+}$ and **3**: A powder sample of **1**, $\mathbf{2}^{2+}$ or **3** was dissolved in the corresponding organic solvent (~ 3 mM) under open air atmosphere and filtered through a glass microfiber paper (Fisherbrand™ MF 300) to avoid microparticles.

Solutions of 4^{2+} under N_2 atmosphere: A sample of **1** (2 mg, 2.92 μmol) was dissolved in anhydrous d_4-Methanol (1 mL, 99.8 %, Sigma-Aldrich) and filtered through a glass microfiber paper (Fisherbrand™ MF 300). Then, the corresponding volume of the deuterated aqueous solution was added *(see aqueous solutions in the materials section)* to prepare methanoic solutions that contained 5%, 25 % or 50 % of aqueous solution respectively. The solvents and solutions used for the preparation of 4^{2+} were stored, manipulated and added inside a N_2 filled glove box. The tubes with the solutions were taken out of the glovebox, degassed through three cycles of freeze-and-thaw and sealed.

EPR Methods

Instrument: The EPR experiments were carried out at 20 K on frozen solutions by using a X-band spectrometer (Bruker ESP300E) and Oxford cryostat.

Preparation of a solutions of 4^{2+} under N_2 atmosphere: The procedure followed was analogous to the procedure followed in the preparation of the NMR samples. A sample of **1** (2 mg, 2.92 μmol) was dissolved in anhydrous d_4-Methanol (1 mL, 99.8 %, Sigma-Aldrich) and filtered. Then, the corresponding volume of the deuterated aqueous solution was added *(see aqueous solutions in the materials section)* to prepare methanoic solutions that contained 5%, 25 % or 50 % of aqueous solution respectively. The solvents and solutions used for the preparation of $\mathbf{4}^{2+}$ were stored, manipulated and added inside a N_2 filled glove box. The tubes with the solutions were taken out of the glovebox, degassed through three cycles of freeze-and-thaw and sealed.

Preparation of a solution of $\mathbf{5}^{3+}$

A sample of **1** (4 mg, 5.8 μmol) was dissolved in a pD = 1.0 solution (2 mL) and stirred for 20 min at RT. A fraction of the solution (0.2 mL) of the solution was inserted in a EPR tube and degassed through three cycles of freeze and thaw and sealed.

Single Crystal X-ray Diffraction Methods.

Crystal growth

Crystals of **1** were obtained by slow diffusion of ether in a **1** solution in methanol (~ 3 mM). Crystals of $\mathbf{2}(PF_6)_3$ were obtained from the filtrate solution containing $\mathbf{2}(PF_6)_3$ (~ 10 mM). Crystals of **3** were obtained by slow diffusion of ether of a **3** solution (~ 3 mM) in a methanol/acetonitrile mixture (4:1). The measured crystals were prepared under inert conditions immersed in perfluoropolyether as protecting oil for manipulation.

Data collection

Crystal structure determinations for **1**, **2**$(PF_6)_3$ and **3** were carried out using a Apex DUO Kappa 4-axis goniometer equipped with an APPEX 2 4K CCD area detector, a Microfocus Source E025 IuS using MoK_α radiation, Quazar MX multilayer Optics as monochromator and an Oxford Cryosystems low temperature device Cryostream 700 plus (T = -173 °C). Full-sphere data collection was used with ω and φ scans. Programs used: Data collection APEX-2,[4a] data reduction Bruker Saint V/.60A[4b] and absorption correction SADABS.[4c]

Structure Solution and Refinement

Crystal structure solution was achieved using direct methods as implemented in SHELXTL[4d] and visualized using the program SHELXle[4e]. Missing atoms were subsequently located from difference Fourier synthesis and added to the atom list. Least-squares refinement on F^2 using all measured intensities was carried out using the program SHELXTL. All non-hydrogen atoms were refined including anisotropic displacement parameters.

Comments to the structures

1: The asymmetric unit contains one molecule of the metal complex and two and half diethyl ether molecules. The main molecule is connected with neighboring molecules of the crystal array through hydrogen bonds/contacts (O2···N5: 2.965(7) Å, (uncorrected distance O2A···H5B: 2.11 Å), O2···N5': 3.011(7) Å, (uncorrected distance O2···H5A: 2.17 Å), and O4···N6: 2.892(7) Å, (uncorrected distance O4···H6B: 2.05 Å), O4···N6': 2.942(7) Å, (uncorrected distance O4···H6A: 2.10 Å)). One of the diethyl ether molecules is disordered in two positions (ratio 50:50). A second diethyl ether molecule is disordered over a center of inversion and corresponds to a half solvent molecule for asymmetric unit.

$2(PF_6)_3$: The asymmetric unit contains one molecule of the metal complex, three hexafluorophosphate anions and 1.75 water molecules. The hexaflurophosphate anions are localized in four positions with a ratio 1:1:0.5:0.5. One of the hexafluorophosphate anions is located on a twofold axis being shared with the neighboring asymmetric unit. A second hexfluorophosphate anion is disordered sharing its positions with water molecules. The water molecules are located disordered in five positions (ratio 0.5:0.5:0.125:0.25:0.25).

X-ray absorption spectroscopy (XAS) methods.

Preparation of powder samples: Dilutions using Boron Nitride powder were used to prepare samples of **1**, $[Ru(trpy)Cl_3]$ and RuO_2 (4 weight units of Boron Nitride: 1 weight unit of **1**, $[Ru(trpy)Cl_3]$ or RuO_2).

Preparation of a liquid sample of $\mathbf{5}^{3+}$: A sample of **1** (10 mg, 14.5 µmol) was dissolved in a pH = 0.3 (1 mL) solution in open atmosphere, stirred for five minutes, filtered and frozen.

Experimental details: XAS at the ruthenium K-edge was performed at the SuperXAS beamline at Swiss Light Source (SLS at Paul Scherrer Insitute, Villigen, Switzerland) with the storage ring operated in top-up mode (400 mA). Fluorescence-detected XAS spectra were measured with a 12-element energy-resolving Ge-detector (Canberra) shielded by a Mo foil (25 µm) against scattered incident X-rays) on samples held in a liquid-helium cryostat (Oxford) at 20 K using excitation by X-rays from a channel-cut [Si111] monochromator. Harmonics rejection was achieved by a platinum-covered toroidal mirror in grazing incidence. The beam was shaped by slits to a spot size on the sample of about 4x0.5 mm^2. Energy calibration of each scan was done using the peak at 22117 eV in the first derivative of absorption spectra of a Ru–metal powder measured in parallel to the samples.

Computational Methods

All geometries were fully optimized at the M06 level of density functional theory[8] using the Stuttgart [8s7p6d2f | 6s5p3d2f] ECP28MWB contracted pseudopotential basis set[9] on Ru and the 6-31G(d) basis set[10] on all other atoms. Non-analytical integral evaluations made use of a pruned grid having 99 radial shells and 590 angular points per shell. The nature of all stationary points was verified by analytic computation of vibrational frequencies, which were also used for the computation of zero-point vibrational energies and molecular partition functions. Partition functions were used in the computation of 298 K thermal contributions to free energy employing the usual ideal-gas, rigid-rotator, harmonic oscillator approximation.[11] Free energy contributions were added to single-point M06 electronic energies computed with the SDD basis set on ruthenium and 6-311+G(2df,p) basis set on all other atoms to arrive at final, composite free energies. The NMR shifts were also calculated using the same level of theory. Solvation effects associated with water, methanol and acetone as solvents were accounted for using the SMD continuum solvation model.[12] All calculations made use of the *Gaussian09* suite of electronic structure programs.[13]

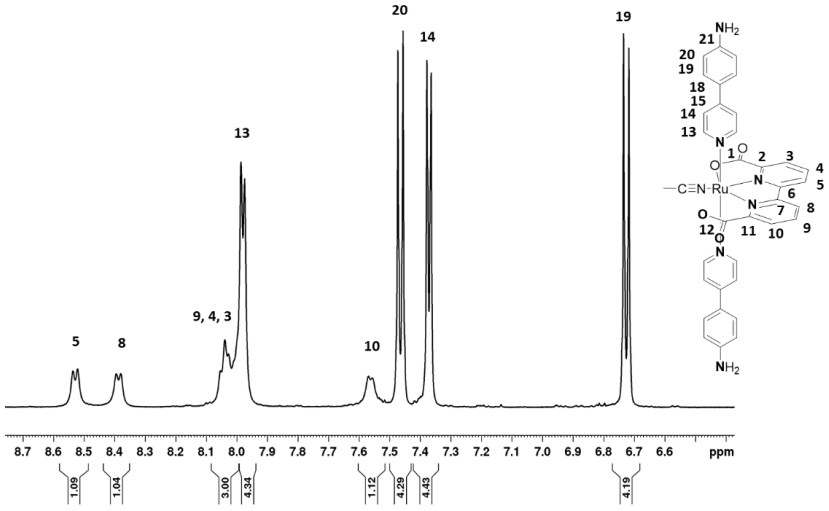

Figure S1. ^{1}H-NMR spectrum of **3** in a d_4-Methanol /acetonitrile-d_3 mixture (4:1) at T = 298K. The assigment of the ^{1}H ressonances was performed according to the 1D and 2D NMR spectra and the computed chemical shifts of the bda^{2-} ligand at M06 level of theory (see Figure S13).

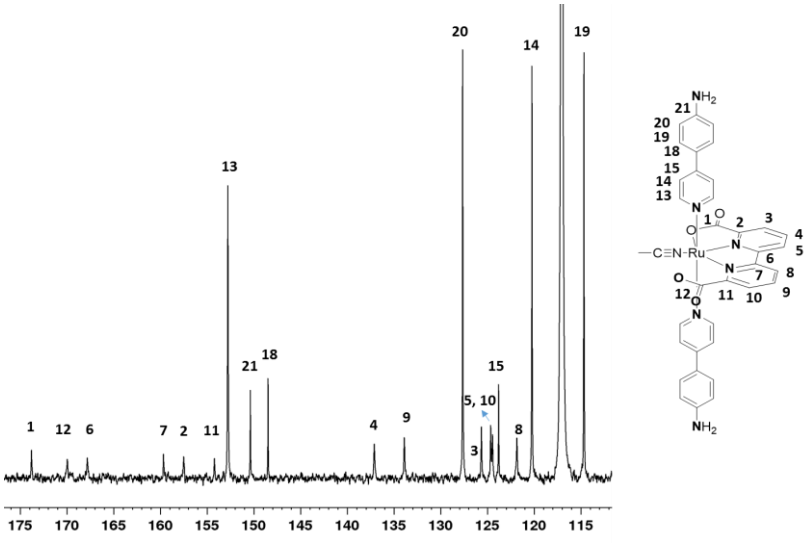

Figure S2. 13C-{H}-NMR spectrum of **3** in a d_4-Methanol /d_3-acetonitrile mixture (4:1) at T=298K.

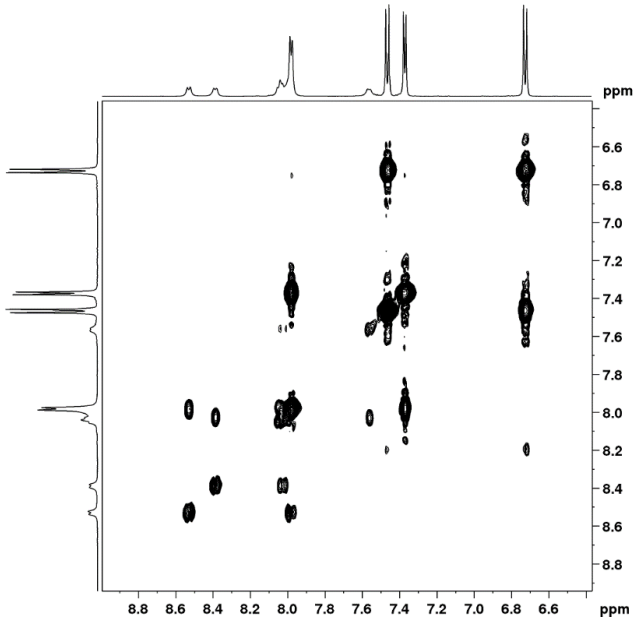

Figure S3. ^{1}H-^{1}H-COSY NMR spectrum of **3** in a d_4-Methanol /d_3-acetonitrile mixture (4:1) at T=298 K.

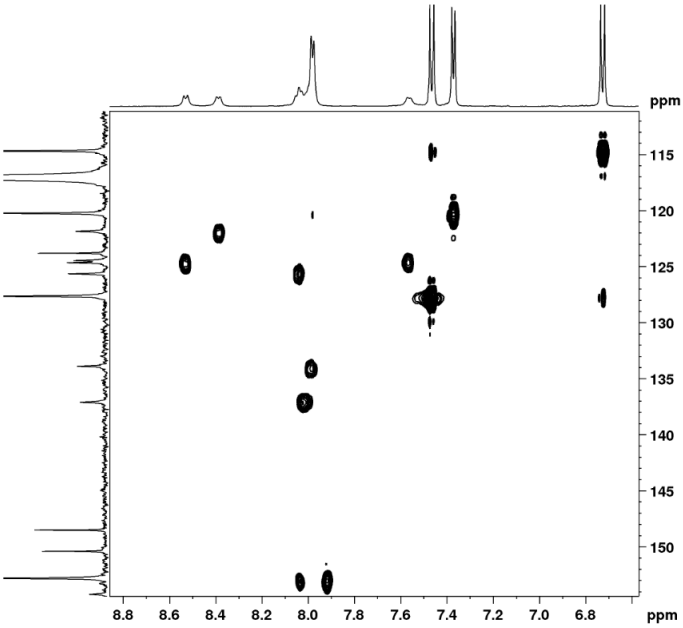

Figure S4. ^{1}H-^{13}C-HSQC NMR spectrum of **3** in a d_4-Methanol /d_3-acetonitrile mixture (4:1), T=298K.

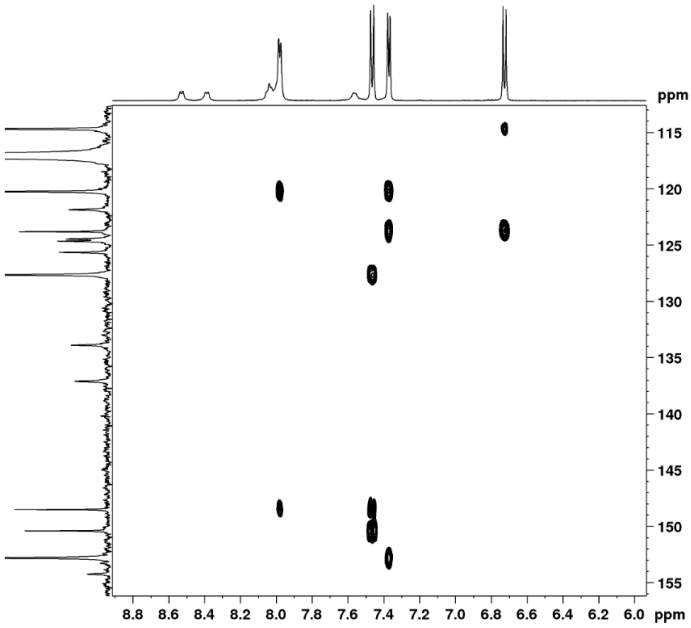

Figure S5. ^{1}H-^{13}C-HMBC NMR spectrum of **3** in a d_4-Methanol /d_3-acetonitrile mixture (4:1), T=298K.

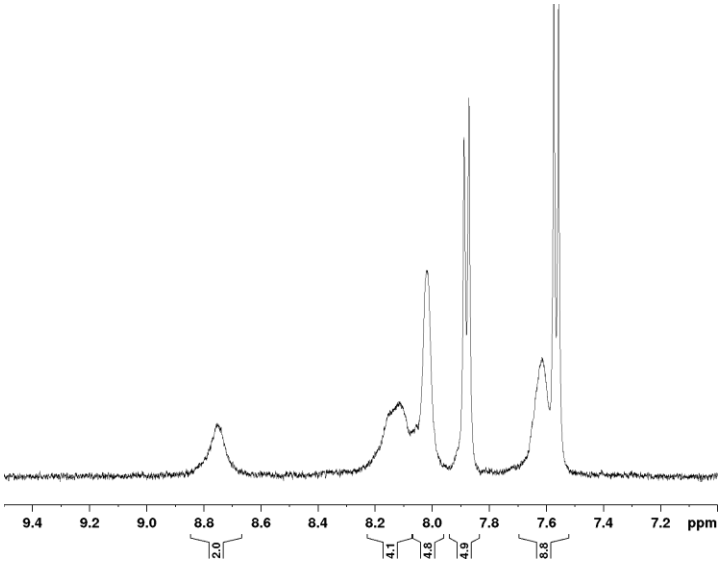

Figure S6. ^{1}H-NMR spectrum of **[4]**$^{2+}$ in a 3:1 d_4-Methanol /pD = 1.0 D_2O mixture at 298 K.

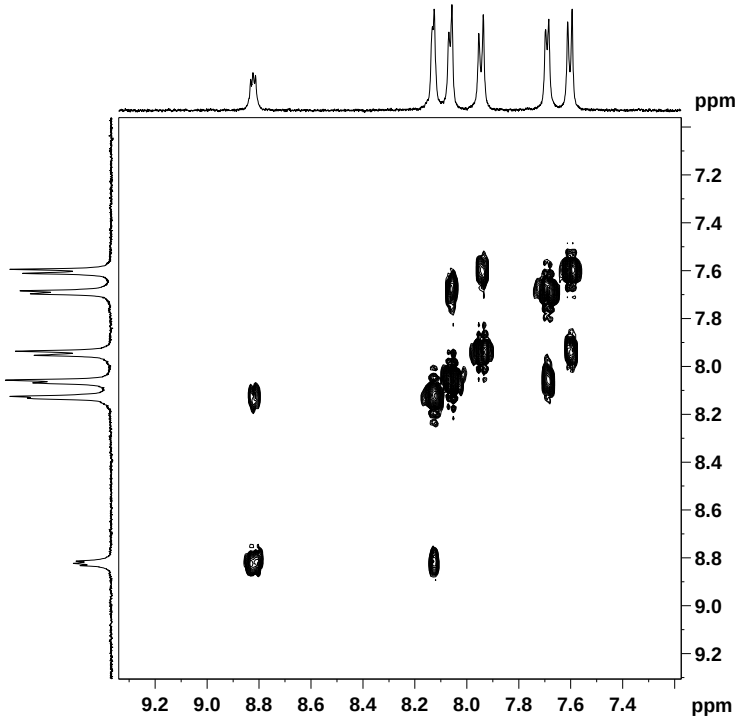

Figure S7. ^{1}H-^{1}H COSY NMR spectrum of **[4]**$^{2+}$ in a 3:1 d_4-Methanol /pD = 1.0 D_2O mixture at 240 K that allows the assignment of the ^{1}H resonances.

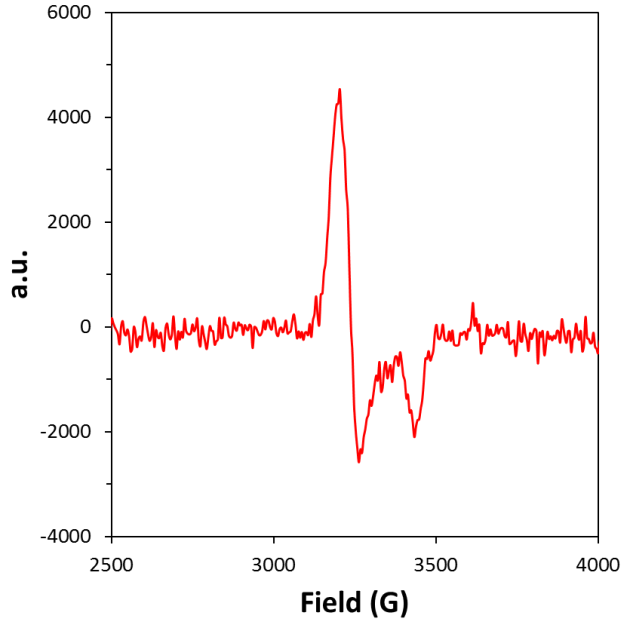

Figure S8. EPR of $\mathbf{5}^{3+}$ at pD = 1.0. EPR signals: g_x = 2.10 (3200 G), g_y = 2.07 (3240 G) and g_z = 1.96 (3430 G). The field was 9.41 GHz.

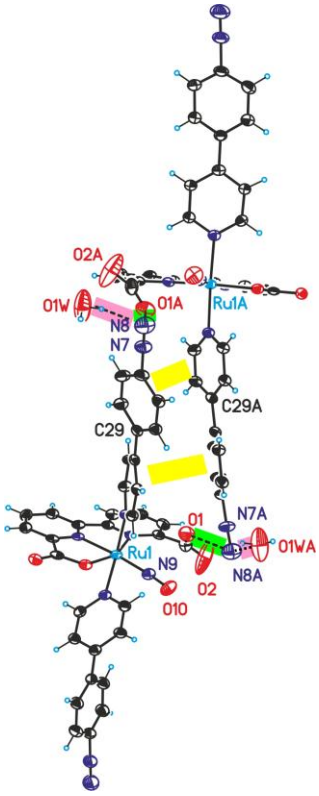

Figure S9. X-ray ORTEP plot (ellipsoids at 50% probability) of the dimers formed by $\mathbf{2}^{3+}$ in the solid state. Coulombic interactions are displayed in green (N8···O1A: 2.9 Å), hydrogen bonding in pink (N8···O1W: 2.8 Å,) and pi-pi staking interactions in yellow (C29···C29A: 3.6 Å, which gives an estimate for the distances between the aromatic rings). Color codes: Ru, cyan; N, blue; O, red; C, black; H, light blue.

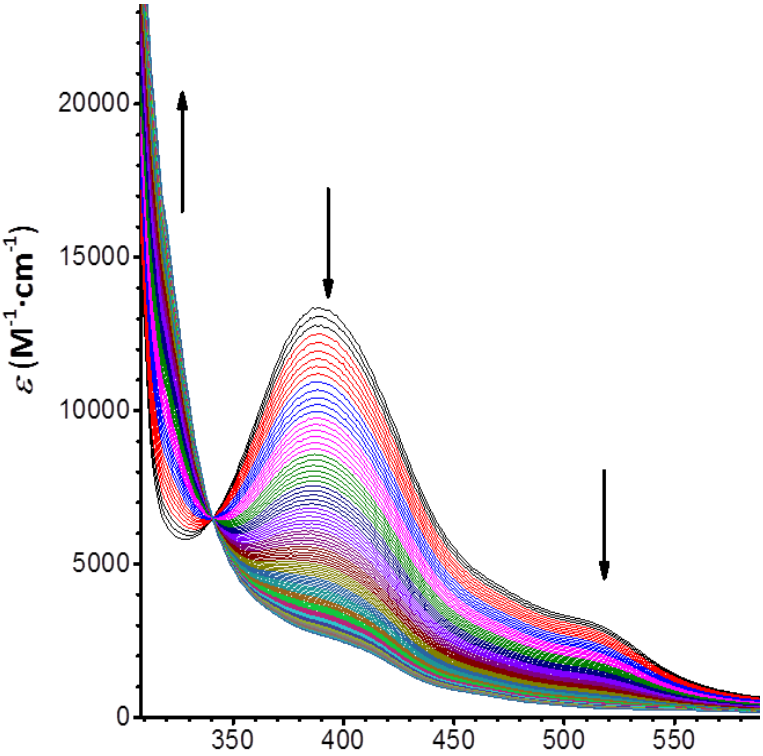

Figure S10. Consecutive UV-Vis spectra of a solution of $\mathbf{4}^{2+}$ that converts into a solution of $\mathbf{5}^{3+}$ at pH = 1.0 for 20 minutes (total number of spectra, 124; spectra frequency, 6.1 min-1). Arrows indicate the trend of the consecutive scans. The solution of $\mathbf{4}^{2+}$ was prepared under N2 and air bubbled for 10 seconds before the measurement. During the whole experiment a flow of air (21% O_2) was maintained in the headspace.

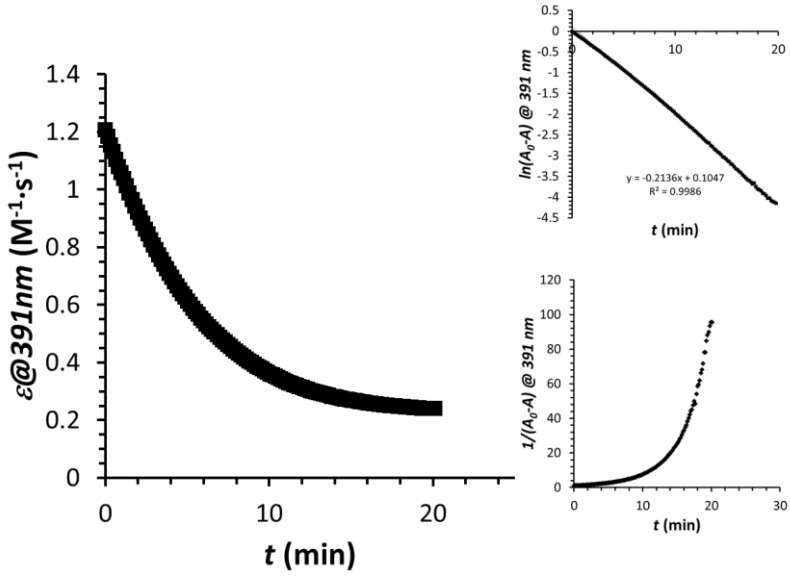

III

Figure S11. Left, molar absorbance at 391 nm upon time of the solution initially containing $\mathbf{4}^{2+}$ at pH = 1.0. The solution of $\mathbf{4}^{2+}$ was prepared under N_2 and was air bubbled for 10 seconds before the measurement and during the whole experiment a flow of air was maintained in the headspace. Top right, kinetic analysis for a first order mechanism (top right) and second order mechanism (bottom right). From the lineal fitting of the first order mechanism, $t_{1/2}$ of 3.3 min was calculated. The formula used was $t_{1/2} = \ln(2)/k$, where k is the slope of the lineal fitting for the first order mechanism.

Table S1. EXAFS simulation parameters for Ru complexes.[a]

	Ru-O	Ru-N	Ru-N	Ru-N	Ru-C	Ru-C	Ru-C	R_F
	N [per Ru] / R [Å] / $2\sigma^2$ x10^3 [Å^2]							[%]
1	2*/2.17/2	2*/1.92/7	2*/2.07/2	-	10*/2.93/32	8*/3.42/26	6*/3.97/7	13.8
5^{3+}	2*/2.14/2	2*/1.98/14	2*/2.04/2	-	10*/2.96/27	8*/3.45/30	6*/3.97/12	21.7
	3*/2.11/4	1*/1.92/6	2*/2.01/2	1*/2.54/4	10*/2.94/26	8*/3.44/30	6*/3.97/13	13.1

[a] The fit error sum (R_F) was calculated for reduced distances of 1-4 Å; *parameters that were fixed in the simulations. The fits furthermore included a multiple scattering shell enhancing the backscattering from C-atoms with N = 6, $2\sigma^2$ = 0.005 Å^2 and projected distances at the Ru center between 1st-sphere N/O- and 2nd-sphere C-ligands of 1.12 Å for **1** and 1.21 Å for **5^{3+}**.

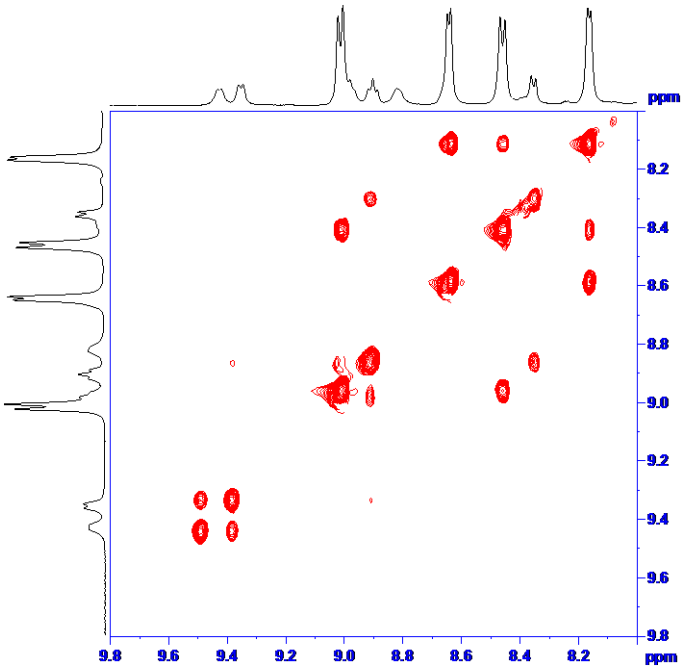

Figure S12. ^{1}H-^{1}H NOESY spectrum of $\mathbf{2}^{3+}$ in acetone-d_4 at 213 K. Note the resonances between the bda protons at 9.4-9.5 ppm and at 8.9-9.0 ppm.

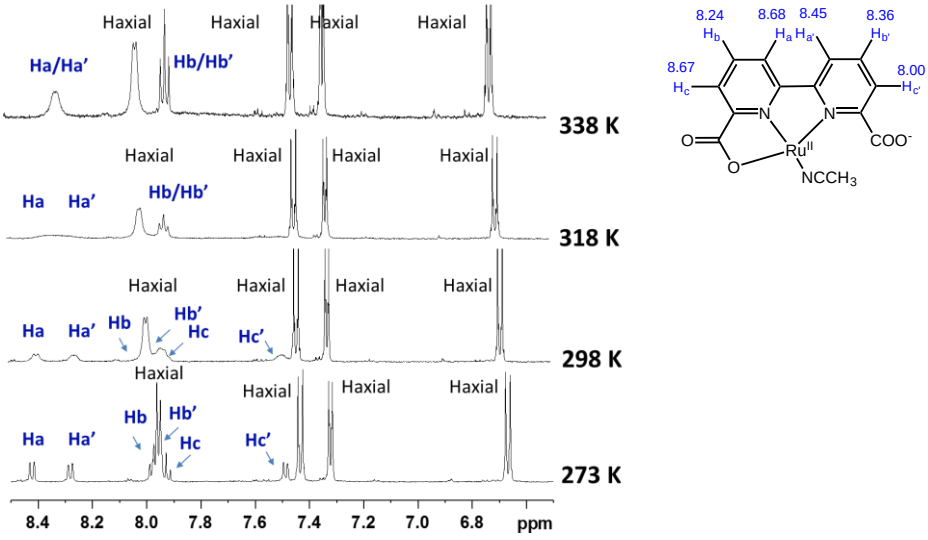

Figure S13. Top, computed chemical shifts for the protons of bda^{2-} ligand in **3** at M06 level of theory. Bottom, VT ^{1}H-NMR of **3** in a d_4-Methanol /d_3-acetonitrile mixture (4:1).

III

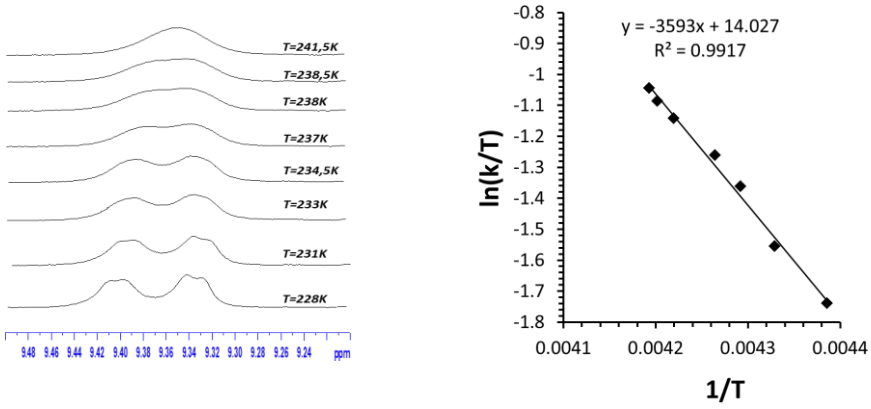

Figure S14. Experimental estimation of the $\Delta G^{\#}$ of $\mathbf{2}^{3+}$ from VT-NMR. Left, ^{1}H NMR spectra of $\mathbf{2}^{3+}$ in acetone in the region of the Hc ressoncance at different temperatures. Right, Eryng plot of the kinetic constants at different temperatures. The kinetic constants (k) at each temperature were estimated by applying the formula $k = \frac{\pi}{\sqrt{2}}\sqrt{(\delta v_0{}^2 - \delta v_d{}^2}$ at temperatures below the coalsence temperature (241.5 K) from the frequency (Hz) of Hc ressonance. Where δv_0 is the difference of frequencies of Hc resonances at 193 K (in the absence of exchange, δv_0=39.1 Hz) and δv_d is the difference of frequencies at each temperature.

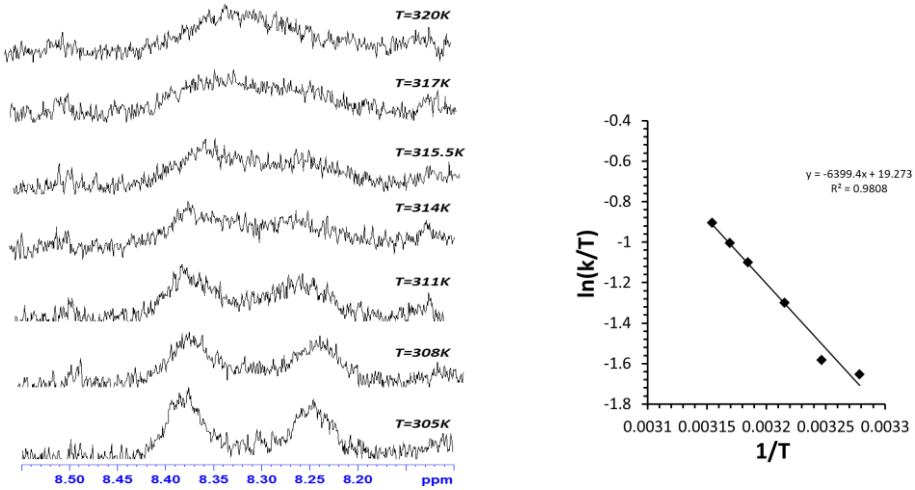

Figure S15. Experimental estimation of the $\Delta G^{\#}$ of **3** from VT-NMR. Left, ^{1}H NMR spectra of **3** in d_4-Methanol/d_3-acetonitrile mixture (4:1) in the region of the Hc ressoncance at different temperatures. Right, Eryng plot of the kinetic constants at different temperatures. The kinetic constants (*k*) at each temperature were estimated by applying the formula $k = \frac{\pi}{\sqrt{2}}\sqrt{(\delta v_0{}^2 - \delta v_d{}^2}$ at temperatures below the coalsence temperature (320 K) from the frequency (Hz) of Hc ressonance. Where δv_0 is the difference of frequencies of Hc resonances at 298 K (in the absence of exchange, δv_0=71.64 Hz) and δv_d is the difference of frequencies at each temperature.

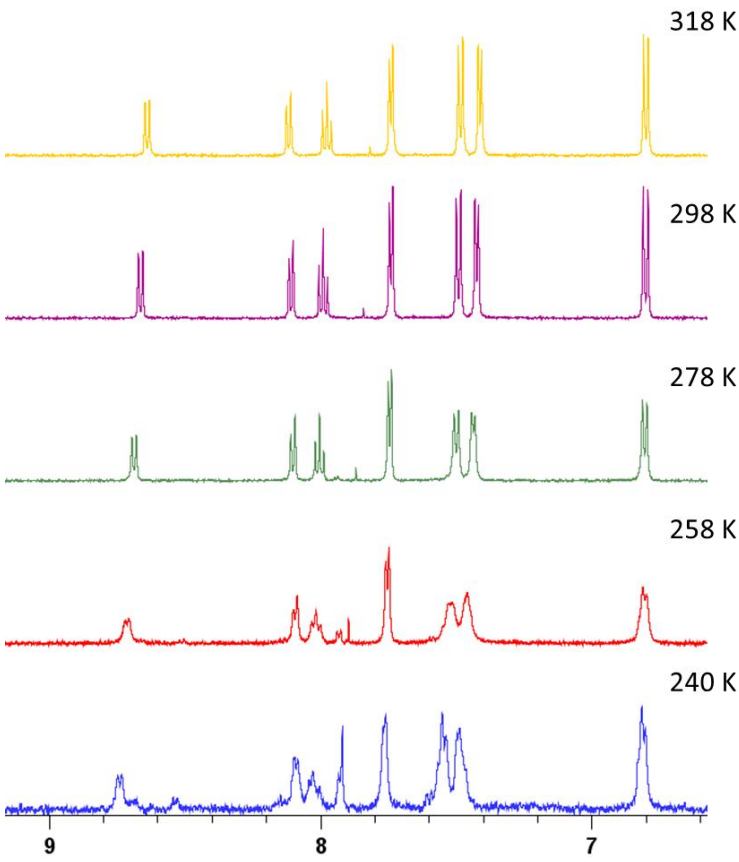

Figure S16. VT ^{1}H-NMR of **1** in a d_4-Methanol /D_2O mixture (4:1). The experiments were carried out initially at 298 K then cooling down to 278, 258, 240 K consecutively, and finally up to 318 K. The temperature decrease produces a broadening and shifting of the resonances in the spectrum together with the generation of new resonances already observable at 258 K and below this temperature (at 258 K see for instance, new resonances at 7.85, 7.89, 8.49 ppm; shoulders at 7.52 ppm etc.). This suggests the presence of an equilibrium between the initial complex **1** and a new complex where the aqua groups binds the Ru metal center.

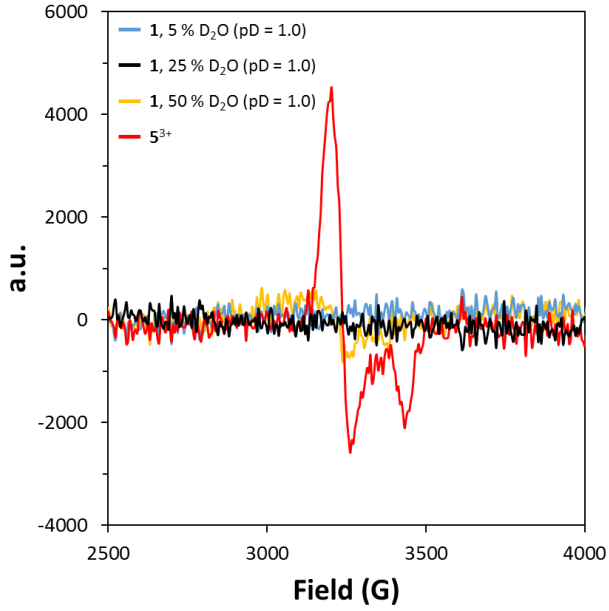

Figure S17. EPR of $\mathbf{4}^{2+}$ in d_4-Methanol with different amounts of a pD = 1.0 solution (blue, 5% of pD = 1.0 solution; black, 25% of pD = 1.0 solution; and yellow, 50% of pD = 1.0 solution) together with a EPR of a solution containing $\mathbf{5}^{3+}$ at pD = 1.0 (red line). All samples were measured under strict N_2 atmosphere (see methods for further details). The experimental conditions used for the preparation of samples containing $\mathbf{4}^{2+}$ in d_4-Methanol containing 5 %, 25 %, and 50 % of a pD = 1.0 solution were identical to those used for the NMR measurements in Figure 4 in the main section.

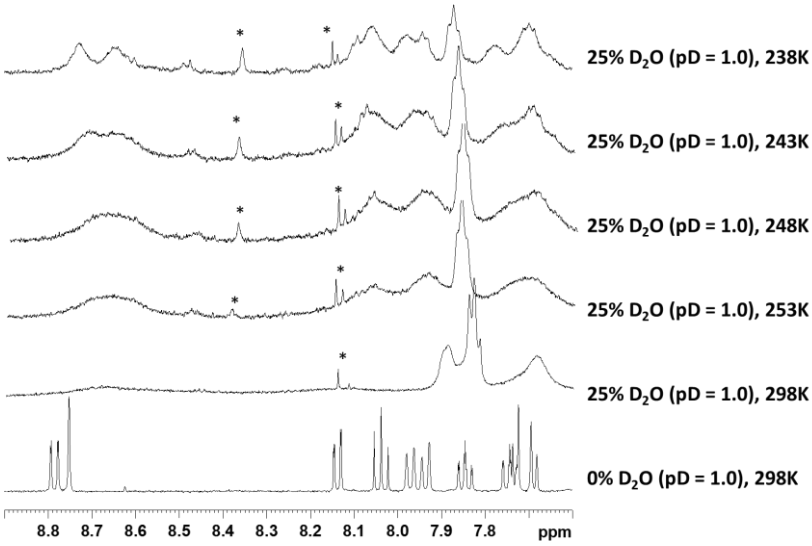

Figure S18. ^{1}H-NMR of [Ru(bda-κ-N^{2}O^{2})(isoq)$_2$] in d$_4$-Methanol (bottom spectrum) and in a 1:3 d$_4$-Methanol /D$_2$O-pD = 1.0 mixture at different temperatures. The resonances with asterisks (*) are due to small impurities not related with the dynamic process.

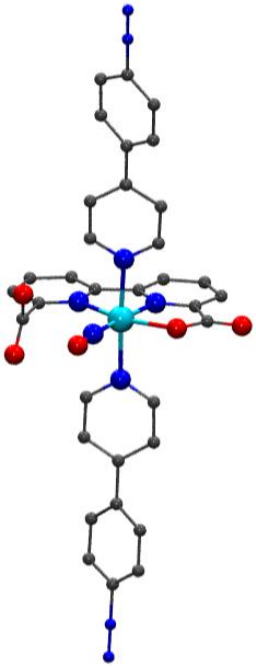

$[Ru^{II}(bda\text{-}\kappa\text{-}N^2O)(NO)(N\text{-}N_2)_2]^{3+}$

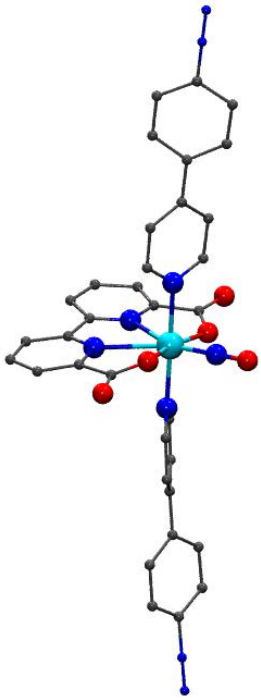

$[Ru^{II}(bda\text{-}\kappa\text{-}N^2O^2)(NO)(N\text{-}N_2)_2]^{3+}$

Figure S19. Ball and stick representation of the optimized structures of $[Ru^{II}(bda\text{-}\kappa\text{-}N^2O)(NO)(N\text{-}N_2)_2]^{3+}$ and $[Ru^{II}(bda\text{-}\kappa\text{-}N^2O^2)(NO)(N\text{-}N_2)_2]^{3+}$. Color code: Ru, cyan; C, gray; N, blue; O, red, H atoms of the ligands were omitted for clarity.

Table S2. Selected bond lengths and angles of the optimized structures of $[Ru^{II}(bda\text{-}\kappa\text{-}N^2O)(NO)(N\text{-}N_2)_2]^{3+}$ and $[Ru^{II}(bda\text{-}\kappa\text{-}N^2O^2)(NO)(N\text{-}N_2)_2]^{3+}$ compared to X-ray data of $\mathbf{2^{3+}}$(see Figure S19).

	$\mathbf{2^{3+}}$ **(X-ray)**	$\mathbf{[Ru^{II}(bda\text{-}\kappa\text{-}N^2O)(NO)(N\text{-}N_2)_2]^{3+}}$	$\mathbf{[Ru^{II}(bda\text{-}\kappa\text{-}N^2O^2)(NO)(N\text{-}N_2)_2]^{3+}}$
Ru–N1 (eq)	2.01	2.03	2.48
Ru–N2 (eq)	2.12	2.14	2.48
Ru–N3 (ax)	2.09	2.15	2.12
Ru–N4 (ax)	2.11	2.16	2.12
Ru–O1	2.05	2.04	2.09
Ru–O2	3.26	3.50	2.09
Ru–N9 (NO)	1.78	1.76	1.70
N9–O10 (NO)	1.12	1.14	1.15
Ru–N9–O10	–	174.7	180.0
ΔG (kcal/mol)	–	0.0	6.2

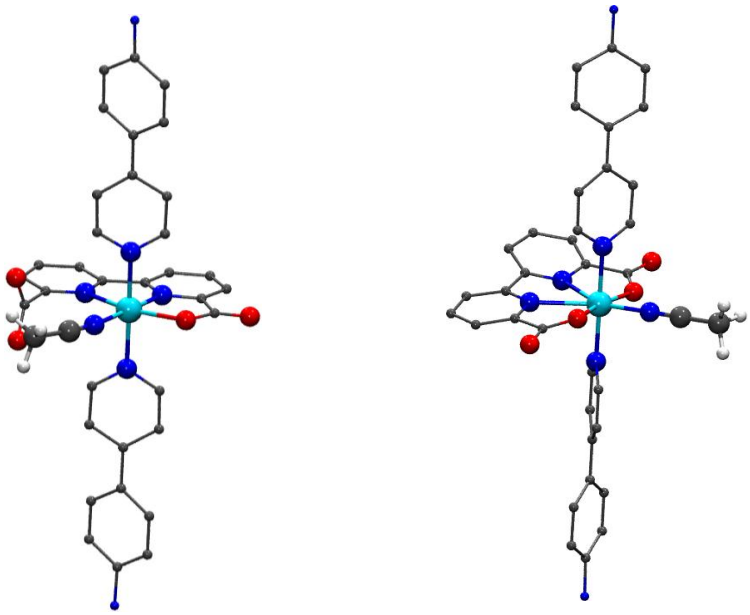

$[Ru^{II}(bda\text{-}\kappa\text{-}N^2O)(NCCH_3)(N\text{-}NH_2)_2]$ **$[Ru^{II}(bda\text{-}\kappa\text{-}NO^2)(NCCH_3)(N\text{-}NH_2)_2]$**

Figure S20. Ball and stick representation of the optimized structures of $[Ru^{II}(bda\text{-}\kappa\text{-}N^2O)(NCCH_3)(N\text{-}NH_2)_2]$ and $[Ru^{II}(bda\text{-}\kappa\text{-}NO^2)(NCCH_3)(N\text{-}NH_2)_2]$. Color code: Ru, cyan; C, gray; N, blue; O, red, H atoms of the ligands were omitted for clarity.

Table S3. Selected bond lengths and angles of the optimized structures of [Ru^{II}(bda-κ-N^2O)($NCCH_3$)($N\text{-}NH_2$)$_2$] and [Ru^{II}(bda-κ-NO^2)($NCCH_3$)($N\text{-}NH_2$)$_2$] (see Figure S20).

	3 (X-ray)	**[Ru^{II}(bda-κ-N^2O)($NCCH_3$)($N\text{-}NH_2$)$_2$]**	**[Ru^{II}(bda-κ-NO^2)($NCCH_3$)($N\text{-}NH_2$)$_2$]**
Ru–N1 (eq)	1.95	1.95	2.43
Ru–N2 (eq)	2.09	2.13	2.76
Ru–N6 (ax)	2.07	2.11	2.09
Ru–N4 (ax)	2.11	2.11	2.08
Ru–O3	3.6	4.05	2.08
Ru–O1	2.11	2.12	2.20
Ru–N3 ($NCCH_3$)	2.05	2.04	1.91
Ru–N3–C1 ($NCCH_3$)	168.16	168.4	180.0
ΔG (kcal/mol)	-	0.0	17.7

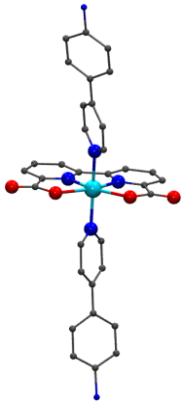

$[Ru^{II}(bda\text{-}\kappa\text{-}N^2O^2)(N\text{-}NH_3)_2]^{2+}$

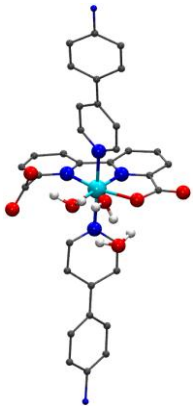

$[Ru^{II}(bda\text{-}\kappa\text{-}N^2O)(OH_2)(N\text{-}NH_3)_2(H_2O)_2]^{2+}$

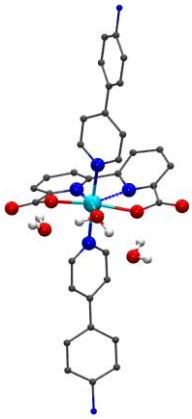

$[Ru^{II}(bda\text{-}\kappa\text{-}NO^2)(OH_2)(N\text{-}NH_3)_2(H_2O)_2]^{2+}$

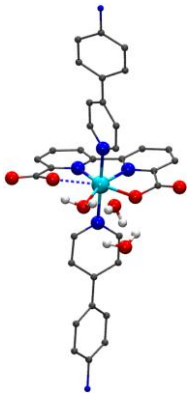

$[Ru^{III}(bda\text{-}\kappa\text{-}N^2O)(OH_2)(N\text{-}NH_3)_2(H_2O)_2]^{3+}$

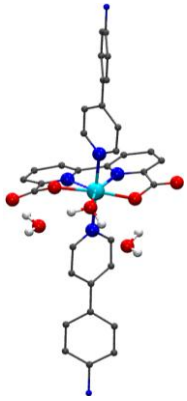

$[Ru^{III}(bda\text{-}\kappa\text{-}NO^2)(OH_2)(N\text{-}NH_3)_2(H_2O)_2]^{3+}$

Figure S21. Ball and stick representation of the optimized structures of $[Ru^{II}(bda\text{-}\kappa\text{-}N^2O^2)(N\text{-}NH_3)_2]^{2+}$, $[Ru^{II}(bda\text{-}\kappa\text{-}N^2O)(OH_2)(N\text{-}NH_3)_2(H_2O)_2]^{2+}$, $[Ru^{II}(bda\text{-}\kappa\text{-}NO^2)(OH_2)(N\text{-}NH_3)_2(H_2O)_2]^{2+}$, $[Ru^{III}(bda\text{-}\kappa\text{-}N^2O)(OH_2)(N\text{-}NH_3)_2(H_2O)_2]^{3+}$ and $[Ru^{III}(bda\text{-}\kappa\text{-}NO^2)(OH_2)(N\text{-}NH_3)_2(H_2O)_2]^{3+}$. Color code: Ru, cyan; C, gray; N, blue; O, red, H atoms of the ligands were omitted for clarity.

Table S4. Selected bond lengths of the optimized structures of $[Ru^{II}(bda\text{-}\kappa\text{-}N^2O^2)(N\text{-}NH_2)_2]^{2+}$, $[Ru^{II}(bda\text{-}\kappa\text{-}N^2O)(OH_2)(N\text{-}NH_3)_2(H_2O)_2]^{2+}$, $[Ru^{II}(bda\text{-}\kappa\text{-}NO^2)(OH_2)(N\text{-}NH_3)_2(H_2O)_2]^{2+}$, $[Ru^{III}(bda\text{-}\kappa\text{-}N^2O)(OH_2)(N\text{-}NH_3)_2(H_2O)_2]^{3+}$ and $[Ru^{III}(bda\text{-}\kappa\text{-}NO^2)(OH_2)(N\text{-}NH_3)_2(H_2O)_2]^{3+}$ (see Figure S21).

	$[Ru^{II}(bda)(N\text{-}NH_3)_2]^{2+}$	$[Ru^{II}(bda)(OH_2)(N\text{-}NH_3)_2(H_2O)_2]^{2+}$		$[Ru^{III}(bda)(OH_2)(N\text{-}NH_3)_2(H_2O)_2]^{3+}$	
	κ-N^2O^2	**κ-N^2O**	**κ-NO^2**	**κ-N^2O**	**κ-NO^2**
Ru–N1 (eq)	1.94	1.94	2.25	2.02	2.22
Ru–N2 (eq)	1.94	2.12	2.83	2.21	2.45
Ru–N3 (ax)	2.07	2.08	2.04	2.11	2.09
Ru–N4 (ax)	2.07	2.09	2.07	2.11	2.11
Ru–O1	2.16	2.12	2.05	2.02	2.02
Ru–O2	2.16	3.37	2.24	2.42	2.10
Ru–O3 (OH_2)	–	2.18	2.12	2.22	2.10
ΔG (kcal/mol)	–	0.0	22.3	0.0	2.6

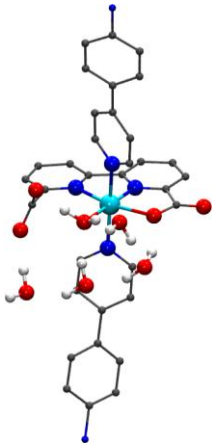

$[Ru^{II}(bda\text{-}\kappa\text{-}N^2O)(OH_2)(N\text{-}NH_3)_2(H_2O)_4]^{2+}$

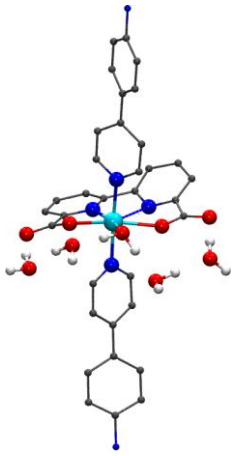

$[Ru^{II}(bda\text{-}\kappa\text{-}NO^2)(OH_2)(N\text{-}NH_3)_2(H_2O)_4]^{2+}$

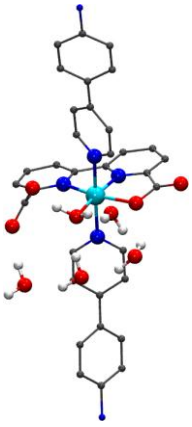

$[Ru^{III}(bda\text{-}\kappa\text{-}N^2O)(OH_2)(N\text{-}NH_3)_2(H_2O)_4]^{3+}$

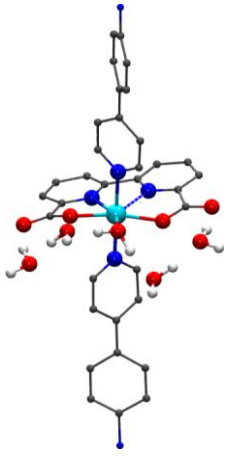

$[Ru^{III}(bda\text{-}\kappa\text{-}NO^2)(OH_2)(N\text{-}NH_3)_2(H_2O)_4]^{3+}$

Figure S22. Ball and stick representation of the optimized structures of $[Ru^{II}(bda\text{-}\kappa\text{-}N^2O)(OH_2)(N\text{-}NH_3)_2(H_2O)_4]^{2+}$, $[Ru^{II}(bda\text{-}\kappa\text{-}NO^2)(OH_2)(N\text{-}NH_3)_2(H_2O)_4]^{2+}$, $[Ru^{III}(bda\text{-}\kappa\text{-}N^2O)(OH_2)(N\text{-}NH_3)_2(H_2O)_4]^{3+}$ and $[Ru^{III}(bda\text{-}\kappa\text{-}NO^2)(OH_2)(N\text{-}NH_3)_2(H_2O)_4]^{3+}$. Color code: Ru, cyan; C, gray; N, blue; O, red, H atoms of the ligands were omitted for clarity.

Table S5. Selected bond lengths of the optimized structures of $[Ru^{II}(bda\text{-}\kappa\text{-}N^2O)(OH_2)(N\text{-}NH_3)_2(H_2O)_4]^{2+}$, $[Ru^{II}(bda\text{-}\kappa\text{-}NO^2)(OH_2)(N\text{-}NH_3)_2(H_2O)_4]^{2+}$, $[Ru^{III}(bda\text{-}\kappa\text{-}N^2O)(OH_2)(N\text{-}NH_3)_2(H_2O)_4]^{3+}$ and $[Ru^{III}(bda\text{-}\kappa\text{-}NO^2)(OH_2)(N\text{-}NH_3)_2(H_2O)_4]^{3+}$ (see Figure S22).

	$[Ru^{II}(bda)(OH_2)(N\text{-}NH_3)_2(H_2O)_4]^{2+}$		**$[Ru^{III}(bda)(OH_2)(N\text{-}NH_3)_2(H_2O)_4]^{3+}$**	
	$\kappa\text{-}N^2O$	**$\kappa\text{-}NO^2$**	**$\kappa\text{-}N^2O$**	**$\kappa\text{-}NO^2$**
Ru–N1 (eq)	1.94	2.26	1.99	2.32
Ru–N2 (eq)	2.12	2.82	2.14	2.46
Ru–N3 (ax)	2.08	2.04	2.11	2.10
Ru–N4 (ax)	2.11	2.06	2.14	2.10
Ru–O1	2.12	2.05	2.00	2.03
Ru–O2	3.45	2.23	3.06	2.08
Ru–O3 (OH_2)	2.18	2.09	2.13	2.03
ΔG (kcal/mol)	0.0	20.3	0.0	2.1

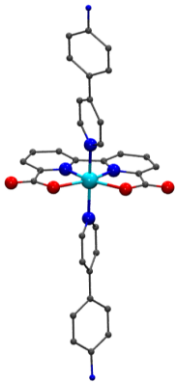

$Ru^{II}(bda\text{-}\kappa\text{-}N^2O^2)(N\text{-}NH_2)_2]$

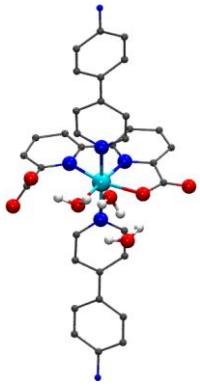

$[Ru^{II}(bda\text{-}\kappa\text{-}N^2O)(OH_2)(N\text{-}NH_2)_2(H_2O)_2]$

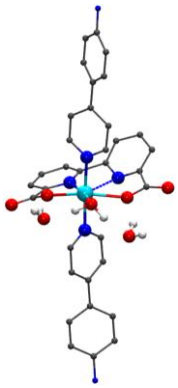

$[Ru^{II}(bda\text{-}\kappa\text{-}NO^2)(OH_2)(N\text{-}NH_2)_2(H_2O)_2]$

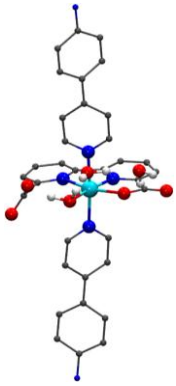

$[Ru^{III}(bda\text{-}\kappa\text{-}N^2O)(OH_2)(N\text{-}NH_2)_2(H_2O)_2]^+$

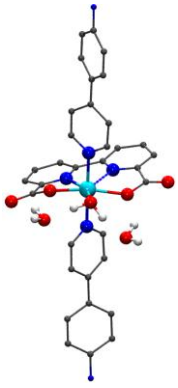

$[Ru^{III}(bda\text{-}\kappa\text{-}NO^2)(OH_2)(N\text{-}NH_2)_2(H_2O)_2]^+$

Figure S23. Ball and stick representation of the optimized structures of $[Ru^{II}(bda\text{-}\kappa\text{-}N^2O^2)(N\text{-}NH_2)_2]$, $[Ru^{II}(bda\text{-}\kappa\text{-}N^2O)(OH_2)(N\text{-}NH_2)_2(H_2O)_2]$, $[Ru^{II}(bda\text{-}\kappa\text{-}NO^2)(OH_2)(N\text{-}NH_2)_2(H_2O)_2]$, $[Ru^{III}(bda\text{-}\kappa\text{-}N^2O)(OH_2)(N\text{-}NH_2)_2(H_2O)_2]^+$ and $[Ru^{III}(bda\text{-}\kappa\text{-}NO^2)(OH_2)(N\text{-}NH_2)_2(H_2O)_2]^+$. Color code: Ru, cyan; C, gray; N, blue; O, red, H atoms of the ligands were omitted for clarity.

Table S6. Selected bond lengths of the optimized structures of $[Ru^{II}(bda\text{-}\kappa\text{-}N^2O^2)(N\text{-}NH_2)_2]$, $[Ru^{II}(bda\text{-}\kappa\text{-}N^2O)(OH_2)(N\text{-}NH_2)_2(H_2O)_2]$, $[Ru^{II}(bda\text{-}\kappa\text{-}NO^2)(OH_2)(N\text{-}NH_2)_2(H_2O)_2]$, $[Ru^{III}(bda\text{-}\kappa\text{-}N^2O)(OH_2)(N\text{-}NH_2)_2(H_2O)_2]^+$ and $[Ru^{III}(bda\text{-}\kappa\text{-}NO^2)(OH_2)(N\text{-}NH_2)_2(H_2O)_2]^+$ (see Figure S23).

	$[Ru^{II}(bda)(N\text{-}NH_2)_2]$	**$[Ru^{II}(bda)(OH_2)(N\text{-}NH_2)_2(H_2O)_2]$**		**$[Ru^{III}(bda)(OH_2)(N\text{-}NH_2)_2(H_2O)_2]^+$**	
	$\kappa\text{-}N^2O^2$	**$\kappa\text{-}N^2O$**	**$\kappa\text{-}NO^2$**	**$\kappa\text{-}N^2O$**	**$\kappa\text{-}NO^2$**
Ru–N1 (eq)	1.93	1.93	2.20	1.98	2.27
Ru–N2 (eq)	1.93	2.12	2.84	2.16	2.45
Ru–N3 (ax)	2.08	2.10	2.07	2.10	2.10
Ru–N4 (ax)	2.09	2.11	2.08	2.11	2.10
Ru–O1	2.17	2.13	2.06	2.03	2.02
Ru–O2	2.17	3.46	2.28	3.32	2.12
Ru–O3 (OH_2)	–	2.17	2.13	2.09	2.08
ΔG (kcal/mol)	–	0.0	19.9	0.0	5.8

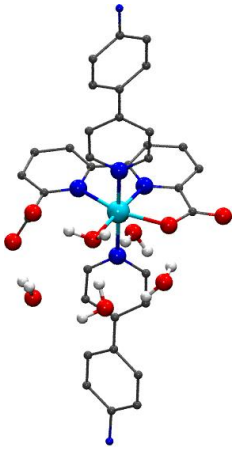

$[Ru^{II}(bda\text{-}\kappa\text{-}N^2O)(OH_2)(N\text{-}NH_2)_2(H_2O)_4]$

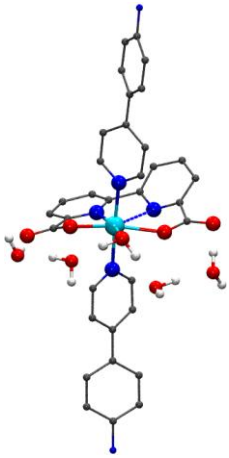

$[Ru^{II}(bda\text{-}\kappa\text{-}NO^2)(OH_2)(N\text{-}NH_2)_2(H_2O)_4]$

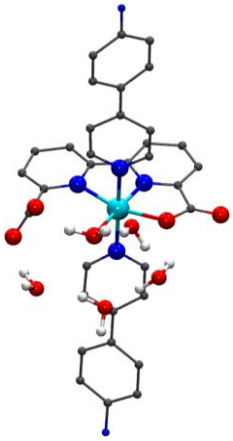

$[Ru^{III}(bda\text{-}\kappa\text{-}N^2O)(OH_2)(N\text{-}NH_2)_2(H_2O)_4]^+$

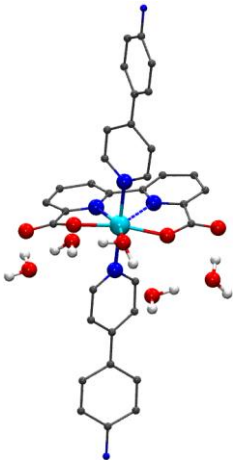

$[Ru^{III}(bda\text{-}\kappa\text{-}NO^2)(OH_2)(N\text{-}NH_2)_2(H_2O)_4]^+$

Figure S24. Ball and stick representation of the optimized structures of $[Ru^{II}(bda\text{-}\kappa\text{-}N^2O)(OH_2)(N\text{-}NH_2)_2(H_2O)_4]$, $[Ru^{II}(bda\text{-}\kappa\text{-}NO^2)(OH_2)(N\text{-}NH_2)_2(H_2O)_4]$, $[Ru^{III}(bda\text{-}\kappa\text{-}N^2O)(OH_2)(N\text{-}NH_2)_2(H_2O)_4]^+$ and $[Ru^{III}(bda\text{-}\kappa\text{-}NO^2)(OH_2)(N\text{-}NH_2)_2(H_2O)_4]^+$. Color code: Ru, cyan; C, gray; N, blue; O, red, H atoms of the ligands were omitted for clarity.

Table S7. Selected bond lengths of the optimized structures of $[Ru^{II}(bda\text{-}\kappa\text{-}N^2O)(OH_2)(N\text{-}NH_2)_2(H_2O)_4]$, $[Ru^{II}(bda\text{-}\kappa\text{-}NO^2)(OH_2)(N\text{-}NH_2)_2(H_2O)_4]$, $[Ru^{III}(bda\text{-}\kappa\text{-}N^2O)(OH_2)(N\text{-}NH_2)_2(H_2O)_4]^+$ and $[Ru^{III}(bda\text{-}\kappa\text{-}NO^2)(OH_2)(N\text{-}NH_2)_2(H_2O)_4]^+$ (see Figure S24).

	$[Ru^{II}(bda)(OH_2)(N\text{-}NH_2)_2(H_2O)_4]$		**$[Ru^{III}(bda)(OH_2)(N\text{-}NH_2)_2(H_2O)_4]^+$**	
	$\kappa\text{-}N^2O$	**$\kappa\text{-}NO^2$**	**$\kappa\text{-}N^2O$**	**$\kappa\text{-}NO^2$**
Ru–N1 (eq)	1.93	2.19	1.98	2.28
Ru–N2 (eq)	2.12	2.82	2.18	2.47
Ru–N3 (ax)	2.11	2.07	2.10	2.09
Ru–N4 (ax)	2.12	2.07	2.11	2.10
Ru–O1	2.12	2.05	2.05	2.03
Ru–O2	3.54	2.28	3.46	2.12
Ru–O3 (OH_2)	2.16	2.10	2.08	2.03
ΔG (kcal/mol)	0.0	19.0	0.0	1.0

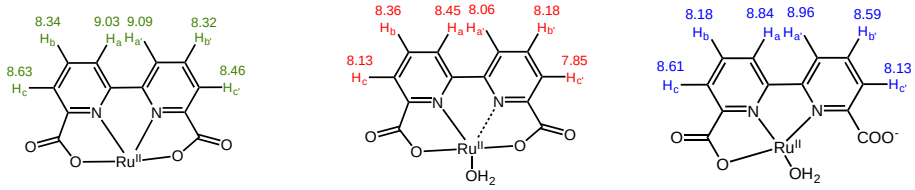

$[Ru^{II}(bda\text{-}\kappa\text{-}N^2O^2)(N\text{-}NH_3)_2]^{2+}$ $[Ru^{II}(bda\text{-}\kappa\text{-}NO^2)(OH_2)(N\text{-}NH_3)_2(H_2O)_4]^{2+}$ $[Ru^{II}(bda\text{-}\kappa\text{-}N^2O)(OH_2)(N\text{-}NH_3)_2(H_2O)_4]^{2+}$

Figure S25. Calculated NMR shifts for hydrogen atoms of bda^{2-} ligand in reference to TMS for $[Ru^{II}(bda\text{-}\kappa\text{-}N^2O^2)(N\text{-}NH_3)_2]^{2+}$, $[Ru^{II}(bda\text{-}\kappa\text{-}N^2O)(OH_2)(N\text{-}NH_3)_2(H_2O)_4]^{2+}$ and $[Ru^{II}(bda\text{-}\kappa\text{-}NO^2)(OH_2)(N\text{-}NH_3)_2(H_2O)_4]^{2+}$ in methanol at M06 level of theory.

References

1. Evans, I.; Spencer, A.; Wilkinson, G., Dichlorotetrakis (dimethyl sulphoxide) ruthenium (II) and its use as a source material for some new ruthenium (II) complexes. *Journal of the Chemical Society, Dalton Transactions* **1973**, (2), 204-209.
2. Duan, L.; Bozoglian, F.; Mandal, S.; Stewart, B.; Privalov, T.; Llobet, A.; Sun, L., A molecular ruthenium catalyst with water-oxidation activity comparable to that of photosystem II. *Nature chemistry* **2012**, *4* (5), 418-423.
3. Matheu, R.; Francàs, L.; Chernev, P.; Ertem, M. Z.; Batista, V.; Haumann, M.; Sala, X.; Llobet, A., Behavior of the Ru-bda water oxidation catalyst covalently anchored on glassy carbon electrodes. *ACS Catalysis* **2015**, *5* (6), 3422-3429.
4. (a) Data collection with APEX II version v2013.4-1. Bruker (**2007**). Bruker AXS Inc., Madison, Wisconsin, USA. (b) Data reduction with Bruker SAINT version V8.30c. Bruker (**2007**). Bruker AXS Inc., Madison, Wisconsin, USA. (c) SADABS: V2012/1 Bruker (**2001**). Bruker AXS Inc., Madison, Wisconsin, USA. Blessing, *Acta Crystallographica* **1995**, A51, 33. (d) Sheldrick G.M. *Acta Crystallographica* **2008**, A64, 112. SHELXTL version V6.14.
5. (a) Vigara, L.; Ertem, M. Z.; Planas, N.; Bozoglian, F.; Leidel, N.; Dau, H.; Haumann, M.; Gagliardi, L.; Cramer, C. J.; Llobet, A., Experimental and quantum chemical characterization of the water oxidation cycle catalysed by $[Ru^{II}(damp)(bpy)(H_2O)]^{2+}$. *Chemical Science* **2012**, *3* (8), 2576-2586; (b) Planas, N.; Christian, G.; Roeser, S.; Mas-Marza, E.; Kollipara, M.-R.; Benet-Buchholz, J.; Maseras, F.; Llobet, A., Substitution Reactions in Dinuclear Ru-Hbpp Complexes: an Evaluation of Through-Space Interactions. *Inorganic chemistry* **2012**, *51* (3), 1889-1901.
6. Dau, H.; Haumann, M., Eight steps preceding O–O bond formation in oxygenic photosynthesis—A basic reaction cycle of the photosystem II manganese complex. *Biochimica et Biophysica Acta (BBA)-Bioenergetics* **2007**, *1767* (6), 472-483.
7. Zabinsky, S.; Rehr, J.; Ankudinov, A.; Albers, R.; Eller, M., Multiple-scattering calculations of X-ray-absorption spectra. *Physical Review B* **1995**, *52* (4), 2995.
8. Zhao, Y.; Truhlar, D. G., The M06 suite of density functionals for main group thermochemistry, thermochemical kinetics, noncovalent interactions, excited states, and transition elements: two new functionals and systematic testing of four M06-class functionals and 12 other functionals. *Theoretical Chemistry Accounts* **2008**, *120* (1-3), 215-241.
9. Andrae, D.; Haeussermann, U.; Dolg, M.; Stoll, H.; Preuss, H., Energy-adjustedab initio pseudopotentials for the second and third row transition elements. *Theoretica chimica acta* **1990**, *77* (2), 123-141.

10. Hehre, W.; Radom, L.; Schleyer, P., v. R.; Pople, JA Ab initio molecular orbital theory. Wiley: New York: **1986**.
11. Cramer, C. J., *Essentials of computational chemistry: theories and models*. John Wiley & Sons: **2013**.
12. Jr., T. H. D., Gaussian basis sets for use in correlated molecular calculations. I. The atoms boron through neon and hydrogen. *The Journal of Chemical Physics* **1989**, *90* (2), 1007-1023.
13. Marenich, A. V.; Cramer, C. J.; Truhlar, D. G., Universal Solvation Model Based on Solute Electron Density and on a Continuum Model of the Solvent Defined by the Bulk Dielectric Constant and Atomic Surface Tensions. *The Journal of Physical Chemistry B* **2009**, *113* (18), 6378-6396.
14. Frisch, M. J.; Trucks, G. W.; Schlegel, H. B.; Scuseria, G. E.; Robb, M. A.; Cheeseman, J. R.; Scalmani, G.; Barone, V.; Mennucci, B.; Petersson, G. A.; Nakatsuji, H.; Caricato, M.; Li, X.; Hratchian, H. P.; Izmaylov, A. F.; Bloino, J.; Zheng, G.; Sonnenberg, J. L.; Hada, M.; Ehara, M.; Toyota, K.; Fukuda, R.; Hasegawa, J.; Ishida, M.; Nakajima, T.; Honda, Y.; Kitao, O.; Nakai, H.; Vreven, T.; Montgomery, J. A.; Peralta, J. E.; Ogliaro, F.; Bearpark, M.; Heyd, J. J.; Brothers, E.; Kudin, K. N.; Staroverov, V. N.; Kobayashi, R.; Normand, J.; Raghavachari, K.; Rendell, A.; Burant, J. C.; Iyengar, S. S.; Tomasi, J.; Cossi, M.; Rega, N.; Millam, J. M.; Klene, M.; Knox, J. E.; Cross, J. B.; Bakken, V.; Adamo, C.; Jaramillo, J.; Gomperts, R.; Stratmann, R. E.; Yazyev, O.; Austin, A. J.; Cammi, R.; Pomelli, C.; Ochterski, J. W.; Martin, R. L.; Morokuma, K.; Zakrzewski, V. G.; Voth, G. A.; Salvador, P.; Dannenberg, J. J.; Dapprich, S.; Daniels, A. D.; Farkas, Ö.; Foresman, J. B.; Ortiz, J. V.; Cioslowski, J.; Fox, D. J. *Gaussian 09, Revision A.02*; Gaussian, Inc.: Wallingford, CT, **2010**.

Chapter 4

Water oxidation catalysis by Ru-bda complexes with isoquinoline axial ligands. Second coordination sphere effects

Abstract

Two new ruthenium complexes with the formula [Ru(bda)(8-isoq-$CO_2H)_2$] (**1**), and [Ru(bda)(8-isoq-$CO_2Me)_2$] (**2**), (where bda: 2,2'-bipyridine-6,6'-dicarboxylate; 8-isoq-CO_2H: 8-isoquinolinecarboxilic acid; 8-isoq-CO_2Me: methyl 8-isoquinolinecarboxilate) are synthesized and thoroughly characterized with spectroscopic, crystallographic and electrochemical techniques. Both compounds are active catalysts for the water oxidation to dioxygen reaction. The behavior of the ester derivative **2** at pH 7 is analogous to the previously reported compound [Ru(bda)$(isoq)_2$], **3**, (isoq: isoquinoline); both follow a bimolecular mechanism in which the O-O bond formation takes place by dimerization of two Ru=O compounds, and it is rate determining. Foot of the wave analysis allowed us to calculate a TOF_{max} = 4.74 s^{-1} (at [Ru] = 70 μM) for catalyst **2**. In sharp contrast, the acid derivative **1** shows an unexpected electrocatalytic profile which does not match with neither a typical bimolecular mechanism nor a unimolecular mechanism. A TOF_{max} = 0.31 s^{-1} (at [Ru] = 0.84 mM) is estimated although an exact value could not be obtained due to the uncertainty of the catalytic pathway. The unique behavior of **1** at pH 7 is attributed to second coordination sphere effects by the acid groups in the axial ligands, which are deprotonated at this pH. A belt of hydrogen bonded water molecules is proposed to stabilize the catalytic intermediates leading to higher kinetic barriers, thus slower catalysis. At pH 1, compounds **1** and **2** show similar activity in both electrochemical water oxidation and chemical water oxidation using cerium (IV) ammonium nitrate as sacrificial electron acceptor with a TOF of 7.4 s^{-1} and 12 s^{-1} (at [Ru] = 2 μM) and TON of 500 and 420, respectively. At this pH, the acid groups of **1** are protonated and are expected to have similar influence on the catalysis than its ester derivative **2**.

1- Introduction

One of the most active family of molecular water oxidation catalysts reported to date are those with the general formula $[Ru(bda)(L)_2]$, where bda is the tetradentate equatorial ligand 2,2'-bipyridine-6,6'-dicarboxylate and L are monodentate pyridine type of ligands, reported first by Sun *et al.* in 2009.[1] Since then, a large family of compounds with different substituents in the axial pyridine ligands and even in the bda equatorial ligand have been reported (Figure 1, top left).[2] Although the introduction of electron-donating or electron-withdrawing groups resulted in shifts of the $Ru^{III/II}$ pre-catalytic redox waves, these changes had little influence on their catalytic performance. A breakthrough in the catalytic activity was achieved in 2012, when the pyridine axial ligands were substituted by π-extended isoquinoline groups (Figure 1, top right, R = H).[3] This catalyst showed a catalytic rate comparable to that of PSII in nature, which represented a 10-fold enhancement compared to the pyridine derivatives. This improvement can be understood from the mechanism of the reaction, which has a dimerization of two Ru^{V}=O species as the rate limiting step of the water oxidation reaction (Figure 1, bottom). The presence of the isoquinoline ligands favors the dimerization step through π-π stacking interactions between the isoquinoline groups of two ruthenium molecules. This effect was further confirmed and even enhanced when a methoxy group was introduced in the axial ligand, achieving rates as fast as 923 s^{-1} at [Ru] = 50 μM.[4]

Despite the important advance in the field with the discovering of the $[Ru(bda)(isoq)_2]$ family, a challenge ahead is the immobilization of molecular catalyst on the surface of electrodes for the construction of anodes for the water oxidation reaction. This is not straightforward for a catalyst that follows a bimolecular mechanism, which will be hindered once anchored on a solid support due to the restricted mobility of the molecule on the surface. Indeed, a kinetic study of a catalyst of the $[Ru(bda)(L)_2]$ family showed a significant detrimental effect on

the catalytic rate of the water oxidation reaction when anchored on a glassy carbon electrode.[5] The lower catalytic activity of the anchored catalyst induced side-reactions leading to the formation of ruthenium oxide on the surface of the electrode. For these reasons, unimolecular mechanisms, where the O-O bond is formed through a nucleophilic attack of a water molecule to the Ru^{V}=O group is preferred for catalysts that are meant to work on surfaces.[6]

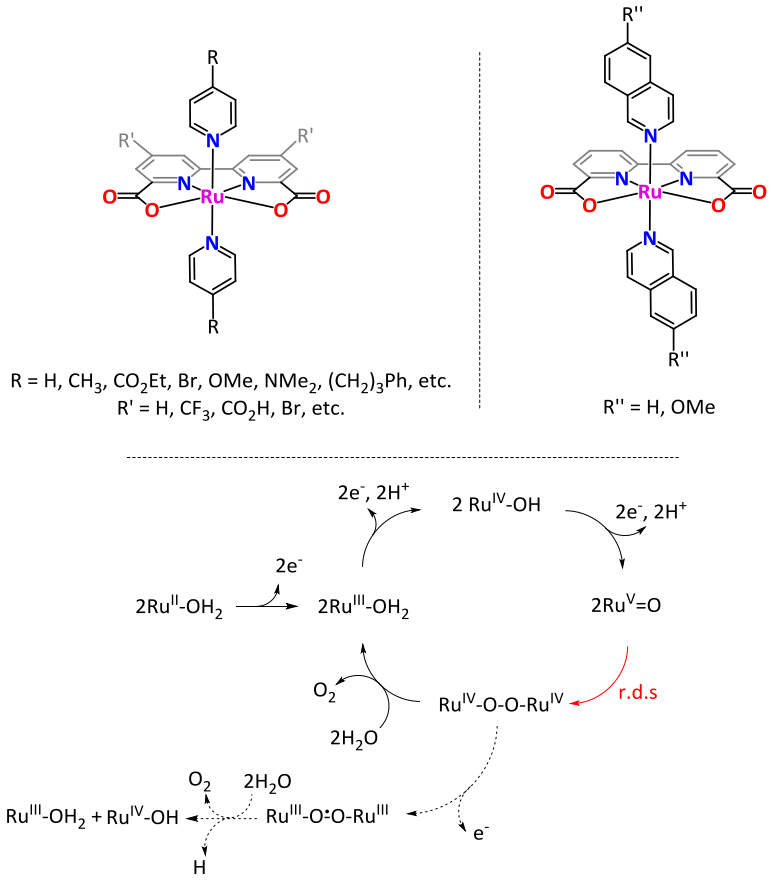

Figure 1. Top) Water oxidation catalysts of the [Ru(bda)(py')$_2$] (left) and [Ru(bda)(isoq)$_2$] (right) families reported in the literature.[2, 7] Bottom) Simplified water oxidation mechanism followed by the [Ru(bda)(py')$_2$] and [Ru(bda)(isoq)$_2$] families at pH 1 based on a bimolecular pathway, in which a dimerization of two Ru^{V}=O groups is often the rate determining step (r.d.s).

In this chapter, second coordination sphere effects in complexes of the family [Ru(bda)(isoq)$_2$] are explored with the aim of studying their influence on the mechanistic pathways. In particular, carboxylic acid groups are strategically placed in the isoquinoline axial ligand, so that they are close enough to the Ru-OH$_2$ catalytic center (Scheme 1). In order to independently assess the electronic and second-coordination sphere effects, an analogous derivative with ester groups is also prepared and studied. Both compounds are thoroughly characterized and tested in electrochemical and chemical water oxidation catalysis.

2- Experimental Section

Materials. $RuCl_3 \cdot 3H_2O$ was purchased from Alfa-Aesar. The precursors $[Ru(DMSO)_4Cl_2]$[8] and 2,2'-bipyridine-6,6'-dicarboxylic acid (H_2bda)[3] were prepared according to literature methods. The other reagents and chemicals were supplied by Sigma-Aldrich and used as received unless indicated differently. When required, solvents were dried by following the standard procedures, distilled under nitrogen and used immediately. High purity de-ionized water used for the electrochemistry experiments was obtained by passing distilled water through an ultrapure Milli-Q water purification system. For other spectroscopic and electrochemical studies, HPLC-grade solvents were used. All synthetic procedures were performed under N_2 atmosphere using Schlenk tubes and vacuum-line techniques.

Instrumentation and Methods. A 500 MHz Bruker Avance II spectrometer was used to carry out NMR spectroscopy. MALDI-TOF-MS experiment was performed on a Bruker Daltonics Autoflex equipped with a nitrogen laser (337 nm) and Mass accuracy in Reflectron mode: 10-50 ppm. ESI-Mass experiment was performed by using micromass Q-TOF mass spectrometer. Elemental analyses were carried out on Perkin-Elmer 240C elemental analyzer. All electrochemical experiments were performed with an IJ-Cambria CHI-730d potentiostat using a three-electrode cell for cyclic voltammetry (CV) and differential pulse voltammetry (DPV). $E_{1/2}$ values

reported in this work were measured from CV experiments as the average of the oxidative and reductive peak potentials ($E_{p,a}$ + $E_{p,c}$)/2 or from DPV. The Reference Electrode (RE) was Hg/Hg_2SO_4 (K_2SO_4 saturated) and potentials were converted to NHE by adding 0.65 V. Glassy carbon disk (ϕ = 0.3 cm, S = 0.07 cm^2), Pt disk, and Hg/Hg_2SO_4 (K_2SO_4 saturated) were used as Working Electrode (WE), Counter Electrode (CE) and Reference Electrode (RE) respectively. Glassy carbon electrodes were polished with 0.05 μm alumina (Al_2O_3) and rinsed with water in every step. Cyclic Voltammograms (CV) were recorded at 100 $mV{\cdot}s^{-1}$ scan rate. The DPV parameters were ΔE= 4 mV, Amplitude = 50 mV, Pulse width = 0.05 s, Sampling width = 0.0167 s, Pulse period = 0.5 s. The pH of the solutions was determined by a pH meter (pH meter Mettler Toledo, SevenCompact™ pH/Ion) calibrated before measurements through a standard solutions at pH= 4.01, 7.00 and 9.21. In aqueous solution the electrochemical experiments were carried out in 0.1 M TA solution for pH 1 and *I* = 0.1 M phosphate buffer solutions with the desired pH. Manometric measurements were performed on a Testo 521 differential pressure manometer with an operating range of 0.1-10 kPa and accuracy within 0.5% of the measurements. The manometer was coupled to thermostatic reaction vessels for dynamic monitoring of the headspace pressure above each reaction solution. The manometer's secondary ports were connected to thermostatic reaction vessels containing the same solvents and headspace volumes as the sample vials. Each measurement for a reaction solution (2.0 mL) was performed at 298 K.

Synthesis of [Ru(bda)(8-isoq-CO_2H)$_2$] (1). A mixture of degassed 2,2′-bipyridine-6,6′-dicarboxylic acid (195 mg, 0.8 mmol) (H_2bda)[3], [$Ru(DMSO)_4Cl_2$][8] (387 mg, 0.8 mmol), triethylamine (0.1 mL, 0.7 mmol) and anhydrous methanol (20 mL) was refluxed overnight under argon. The resulting crude mixture was filtered to get a brown solid, which was washed with methanol and dried (239 mg). 96.8 mg of the aforementioned solid and 8-isoquinolinecarboxilic acid (87 mg, 0.503 mmol) were degassed, dissolved in degassed isopropanol (30 mL) and the mixture refluxed

overnight under argon. The resulting dark-red suspension was filtered; the red solid was washed with diethyl ether and dried. The product was purified by column chromatography on silica gel using dichloromethane:methanol:Et_3N (100:40:2) as eluents. Yield: 49 % (110 mg 0.159 mmol based on $[Ru(DMSO)_4Cl_2]$). ^{1}H NMR (500 MHz, d_4-Methanol:5 µl Et_3N): δ (ppm) = 7.66 (t, *J*= 5.12 Hz, 2 H), 7.74 (d, *J*= 6.52 Hz, 2H), 7.84 (m, *J*= 7.88 Hz, 4H), 7.90 (t, *J*= 7.84, 2 H), 7.95 (d, *J*= 6.92 Hz, 2 H), 8.67 (s, 2 H), 8.75 (d, *J*= 3.96 Hz, 2 H), 8.79 (d, *J*= 6.52 Hz, 2 H). ^{13}C NMR (126 MHz, d_4-Methanol): δ (ppm) = 124.0, 128.6, 128.9, 129.1, 130.4, 131.9, 134.2, 135.1, 138.0, 140.1, 147.7, 156.8, 158.6, 163.4, 175.3, 177.2. UV/Vis λ_{max} (ε) = 227 (24886), 308 (14568), 482 (4158 M^{-1} cm^{-1}). MS (ESI^+): calculated for $[M + H]^+$ *m/z* = 691.0, found: 691.0. Elemental analysis calcd (%) for $C_{32}H_{20}N_4O_8Ru \cdot 1/2CH_2Cl_2 \cdot 5H_2O$ ($C_{32.5}H_{31}ClN_4O_{13}Ru$): C 47.48, H 3.8, N 6.81. Found C 47.88, H 3.36, N 7.15.

Synthesis of 8-isoq-CO_2Me. 8-isoquinolinecarboxilic acid (200 mg, 1.15 mmol) was dissolved in anhydrous methanol (10 ml), which will act not only as a solvent but also as an esterification agent. The solution was cooled inside an ice bath and 0.5 mL of $SOCl_2$ were added slowly. Afterwards, the ice bath was removed and the temperature increased to reflux and stirred at this temperature overnight. To the resulting yellow solution diethyl ether was added inducing the precipitation of a white solid that was filtered and washed with more diethyl ether. Yield: 85% (0.978 mmol, 183 mg). ^{1}H NMR (500 MHz, d_4-Methanol): δ (ppm) = 4.18 (s , 3 H), 8.39 (t, *J*= 7.85 Hz, 3 H), 8.64 (d, *J*= 8.4 Hz, 1 H), 8.72 (d, *J*= 6.45 Hz, 1 H), 8.81 (m, 2 H), 10.73 (s, 1 H).^{13}C NMR (126 MHz, d_4-Methanol): δ (ppm) = 52.35, 125.53, 126.34, 128.85, 131.84, 132.59, 134.91, 135.59, 139.84, 145.77, 165.34 ppm.

Synthesis of [Ru(bda)(8-isoq-CO_2Me)$_2$] (2). A mixture of degassed H_2bda (195 mg, 0.8 mmol), $[Ru(DMSO)_4Cl_2]$ (387 mg, 0.8 mmol), triethylamine (0.1 mL, 0.71 mmol) and anhydrous methanol (20 mL) was refluxed overnight under argon. The resulting crude mixture was filtered to get a brown solid, which was washed with methanol

and dried (239 mg). 48.5 mg of the aforementioned solid, methyl isoquinoline-8-carboxylate (46.75 mg, 0.25 mmol) and sodium L-ascorbate (41.6 mg, 0.21 mmol) were degassed, dissolved in degassed methanol (15 mL) and the mixture refluxed overnight under argon. The resulting dark-red suspension was filtered and the resulting red solid was washed with diethyl ether and dried. The product was purified by column chromatography on silica gel using dichloromethane:methanol:Et_3N (100:1:0.5) as eluent. The column chromatography was performed under ambient conditions and solvents were purged with N_2 beforehand. Yield: 36 % (0.0612 mmol, 44 mg, based on $[Ru(dmso)_4Cl_2]$). ^1H NMR (500 MHz, d_4-Methanol): δ (ppm) = 7.80 (m, 2 H), 7.97 (t, *J*= 7.93 Hz, 1 H), 8.09 (m, 2 H), 8.30 (dd, *J*= 1.1, 7.36 Hz, 1 H), 8.71 (d, *J*= 8.05 Hz, 1 H), 8.80 (d, *J*= 6.50 Hz, 1 H), 9.02 ppm (s, 1 H). ^{13}C NMR (126 MHz, d_4-Methanol): δ (ppm) = 121.56, 124.87, 125.68, 125.94, 126.15, 130.73, 131.94, 132.57, 135.32, 145.65, 152.55, 156.45, 160.10, 165.77, 173.73 ppm. UV/Vis λ_{max} (ε) = 227 (47600), 306 (34000), 471 (18400 M^{-1} cm^{-1}). MALDI$^+$: calculated for M^+ *m/z*: 718.06; found: 718.1. Elemental analysis calcd (%) for $C_{34}H_{24}N_4O_8Ru \cdot 1/4CH_2Cl_2 \cdot 1/4CH_3OH$ ($C_{34.5}H_{25.5}Cl_{0.5}N_4O_{8.25}Ru$): C 55.48, H 3.44, N 7.50. Found C 55.59, H 3.02, N 7.45.

Synthesis of $[Ru(bda)(isoq)_2]$ (3). A mixture of degassed 2,2'-bipyridine-6,6'-dicarboxylic acid (195 mg, 0.8 mmol) (H_2bda), $[Ru(DMSO)_4Cl_2]$ (387 mg, 0.8 mmol), triethylamine (0.1 mL, 0.71 mmol) and methanol (20 mL) was refluxed overnight under argon. The resulting crude mixture was filtered to get a brown solid, which was washed with methanol and dried (239 mg). 30 mg of this solid, and isoquinoline (67 mg, 0.52 mmol) were degassed, dissolved in degassed methanol (15 mL) and the mixture refluxed overnight under argon. The solvent was removed and the residual solid was purified by column chromatography on silica gel using dichloromethane : methanol (1:0 to 10:1, v:v) as eluents. Compound **3** was isolated as a red solid. Yield: 42% yield (0.025 mmol, 15.6 mg, based on $[Ru(dmso)_4Cl_2]$). Spectroscopic data matched with that reported for the same compound.[3]

Single Crystal X-Ray Diffraction. Data collection: Crystal structure determination for samples **1, 2** and **3** were carried out using a Apex DUO Kappa 4-axis goniometer equipped with an APPEX 2 4K CCD area detector, a Microfocus Source E025 IuS using MoK_{α} radiation, Quazar MX multilayer Optics as monochromator and an Oxford Cryosystems low temperature device Cryostream 700 plus (T = -173 °C). Crystal structure determination for samples Full-sphere data collection was used with ω and φ scans. *Programs used:* Data collection APEX-2,[9] data reduction Bruker Saint[10] V/.60A and absorption correction SADABS.[11] **Structure Solution and Refinement**: Crystal structure solution was achieved using the computer program SHELXT[12]. Visualization was performed with the program SHELXle.[13] Missing atoms were subsequently located from difference Fourier synthesis and added to the atom list. Least-squares refinement on F^2 using all measured intensities was carried out using the program SHELXL 2015.[14] All non-hydrogen atoms were refined including anisotropic displacement parameters. **Crystal preparation:** Crystals of [Ru(bda)(isoq-8-CO_2H)$_2$] (**1**), [Ru(bda)(isoq-8-CO_2Me)$_2$] (**2**) and [Ru(bda)(isoq)$_2$] (**3**) were grown by slow diffusion of Et_2O in methanol:Et_3N 30:1, methanol:DCM 1:2, and methanol:$CDCl_3$ 1:1 respectively. The crystals used for structure determination were selected using a Zeiss stereomicroscope using polarized light and prepared under inert conditions immersed in perfluoropolyether as protecting oil for manipulation. **Comments to the structures: Structure 1:** The asymmetric unit contains a half molecule of the metal complex, a triethyl ammonium cation and a half methanol molecule. In total there are two triethyl ammonium cations for each metal complex molecule. The metal complex shows a *C*s molecule symmetry (mirror plane), although the isoquinoline ligands are breaking this symmetry showing a disorder in two orientations. The methanol molecule is disordered around the mirror plane in two orientations. One of the ethyl groups of the ammonium cation is also disordered in two orientations. **Structure 2:** The asymmetric unit contains one molecule of the metal complex disordered in two orientations (ratio 60:40).

Structure 1: The asymmetric unit contains one molecule of the metal complex and one disordered methanol molecule (disorder ratio: 51:49).

3-Results and Discussion

3·1-Synthesis, spectroscopic and crystallographic characterization of 1 and 2

The synthesis of compounds **1** and **2** is straightforward following an adapted procedure reported for compound **3** with the non-functionalized isoquinoline group (Scheme 1).[3] It consists of a two-step synthesis starting from $[Ru(DMSO)_4Cl_2]$ and 2,2'-bipyridine-6,6'-dicarboxylic acid (H_2bda), that produces an intermediate species isolated as a brown solid, whose exact composition is unknown but that serves as an excellent precursor for $[Ru(bda)(py)_2]$ type of complexes.[15] This intermediate compound is used to react with a slight excess of the corresponding isoquinoline to give the final products in moderate yields for the two steps (36-49 %, Scheme 1).

Both compounds are air sensitive, particularly in solution, and need to be handled under inert atmosphere. This is clearly shown by UV-Vis spectroscopy at pH 1 solution that gives a kinetic constants for the Ru(II) to Ru(III) oxidation of 2.3×10^{-6} s^{-1} and 2.5×10^{-6} s^{-1} for **1** and **2**, respectively (Figure S23). The ^1H NMR spectra of **1** and **2** in organic solvents show the typical resonances for a C_{2v} type of symmetry, as expected for these type of compounds (Figures S1-S15).

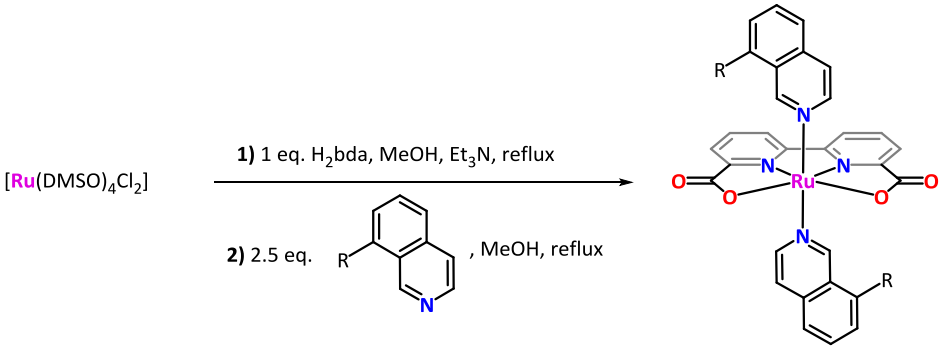

R= CO_2H, [Ru (bda)(isoq-8-$CO_2H)_2$], **1**, 49 %
R= CO_2Me, [Ru(bda)(isoq-8-$CO_2Me)_2$], **2**, 36 %
R= H [Ru(bda)$(isoq)_2$], **3**, 42 %

Scheme 1. Synthetic scheme for the two-step preparation of [Ru(bda)(isoq-8-$CO_2H)_2$] (**1**), [Ru(bda)(isoq-8-$CO_2Me)_2$] (**2**) and [Ru(bda)$(isoq)_2$] (**3**).

Single crystals suitable for x-ray diffraction analysis were obtained for both complexes and their ORTEP plots are shown in Figure 2, together with that of compound **3** that has already been reported before.[16] Bond distances and angles are unexceptional in the expected range for similar compounds.[4, 16]

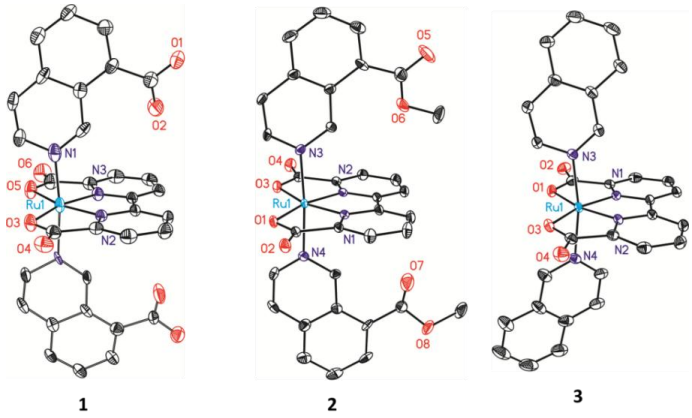

Figure 2. ORTEP plots at 50% probability of complexes **1**, **2** and **3**. H atoms are omitted for clarity.

3·2-Electrochemistry of 1 and 2

The electrochemical properties of complexes **1** and **2** were investigated in aqueous solution at pH 1 and pH 7 by means of cyclic voltammetry (CV) and differential pulse

voltammetry (DPV). In this chapter all potentials are reported vs the normal hydrogen electrode (NHE). Due to the limited solubility of the ester derivative **2**, trifluoroethanol (TFE) or acetonitrile (ACN) were added to the electrolytic solution. The former is preferred because ACN is known to coordinate to the ruthenium center of [Ru(bda)(L)$_2$] type of complexes, particularly at low oxidation states as reported before and discussed in detail below.[17] Cyclic voltammetry experiments at pH 1 are presented in Figure 3 for **1** and **2**. They both show very similar profiles with two reversible one-electron waves at $E_{1/2}$ = 0.74 V (ΔE = 60 mV) and 1.23 V (ΔE = 138 mV) for **1** in black and at $E_{1/2}$ = 0.71 V (ΔE = 70 mV) and 1.17 V (ΔE = 123 mV) for **2** in red, corresponding to the $Ru^{III/II}$ and $Ru^{IV/III}$ redox couples, respectively.

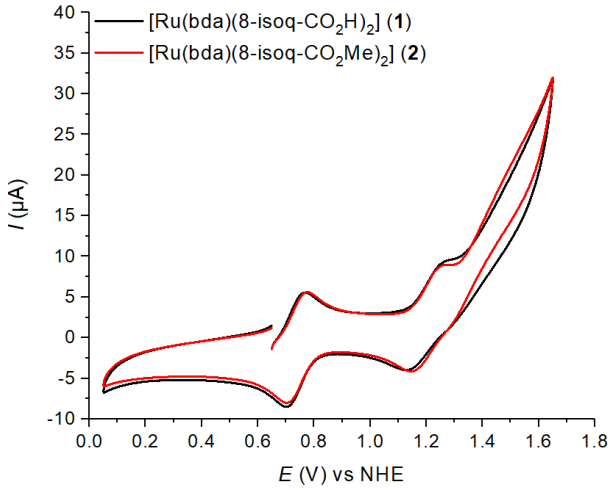

Figure 3. CVs of **1** and **2** at pH 1 CF_3CH_2OH/Triflic acid (TA) (1:2). [Cat] = 1 mM, v = 100 mV s^{-1}, working electrode = glassy carbon (0.07 cm^2), counter electrode = Pt and reference electrode = Hg/Hg_2SO_4.

The $Ru^{III/II}$ and $Ru^{IV/III}$ couples are slightly anodically shifted (80-140 mV) in respect to the non-functionalized compound **3** ($Ru^{III/II}$ = 0.63 V, $Ru^{IV/III}$ = 1.09 V), due to the electron-withdrawing effect of the carboxylic acid and methyl ester groups in the axial ligands of **1** and **2**, respectively (see Table S1 and Figure S17).[7]

Upon scanning to higher potentials, an irreversible wave associated with the $Ru^{V/IV}$ redox couple followed by water oxidation catalysis is observed at E_{onset} ≈ 1.35 V for both complexes. The catalytic activity of **1** and **2** at pH 1 is significantly lower than that of **3**, indicating a detrimental effect of the substituents in the isoquinoline axial ligand in the catalytic process (Figure S17). In sharp contrast, cyclic voltammetry experiments at pH 7 show a completely different scenario for **1** and **2** (Figure 4). While the first two pH dependent redox waves appear in similar positions for the two complexes ($E(Ru^{III/II})_{1/2}$ = 0.67 (ΔE = 61 mV) and 0.71 V (ΔE = 50 mV); $E(Ru^{IV/III})_{1/2}$ = 0.88 (ΔE = 60 mV) and 0.87 V (ΔE= 59 mV) respectively), the catalytic wave for the ester is about 7 times higher than that of the acid derivative. A similar phenomenon has been observed with structurally related complexes containing phosphonic acid or phosphonic ester groups.[2b] The performance of compound **2** is comparable to that of derivative **3** as shown in Figure S18.

Here, the net charge of the complexes could play a role as catalysts **2** and **3** are neutral compounds while catalyst **1** is a doubly-charged species at pH 7 due to the deprotonation of the carboxylic acid of the axial ligands at this pH. However, this wouldn't explain why the ester derivative has such a significant change in activity between pH 1 and pH 7. Hydrolysis of the ester to the acid at acidic pHs was ruled out by electrochemical experiments as follows. First, a CV experiment at pH 1 was done for the two complexes in exactly the same conditions. Then, the same solution was basified to pH 7 and submitted to a new CV experiment. As shown in Figure S19, the activity at pH 7 is higher for ester, reproducing the same trends observed in Figures 3 and 4 and ruling out the hydrolysis of the ester.

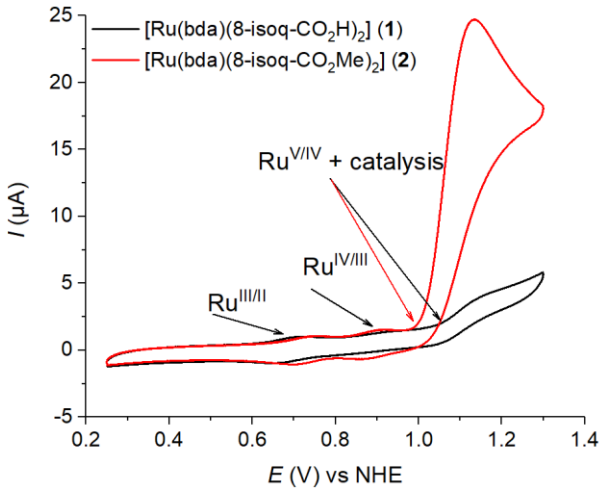

Figure 4. CVs of **1** and **2** at pH 7 phosphate buffer aqueous solution with 25 % TFE. [Cat] = 0.07 mM, v = 100 mV s^{-1}, working electrode = glassy carbon (0.07 cm^2), counter electrode = Pt and reference electrode = Hg/Hg_2SO_4.

IV

Pourbaix diagrams of **1** and **2** are shown in Figures 5 and 6 and are analogous to that of previously reported catalyst **3** and other related compounds.[3, 17b]

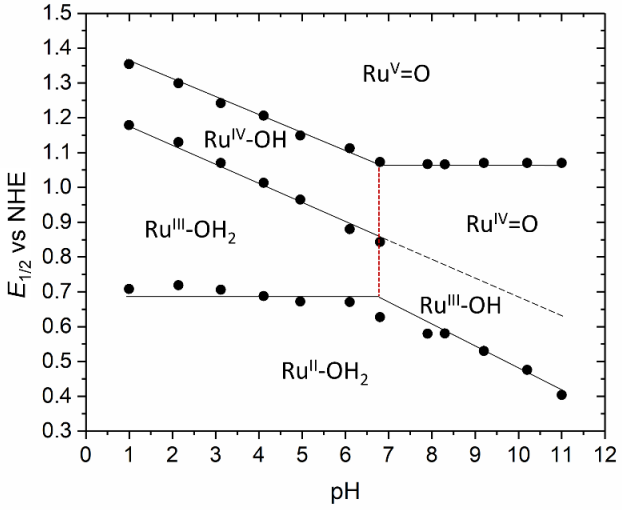

Figure 5. Pourbaix diagram of **1**. The black solid lines indicate trends in data. The pK_a value of the Ru^{III}-OH_2/Ru^{III}-OH and Ru^{IV}-OH/Ru^{IV}=O acid-base couples are indicated by the dotted red vertical line.

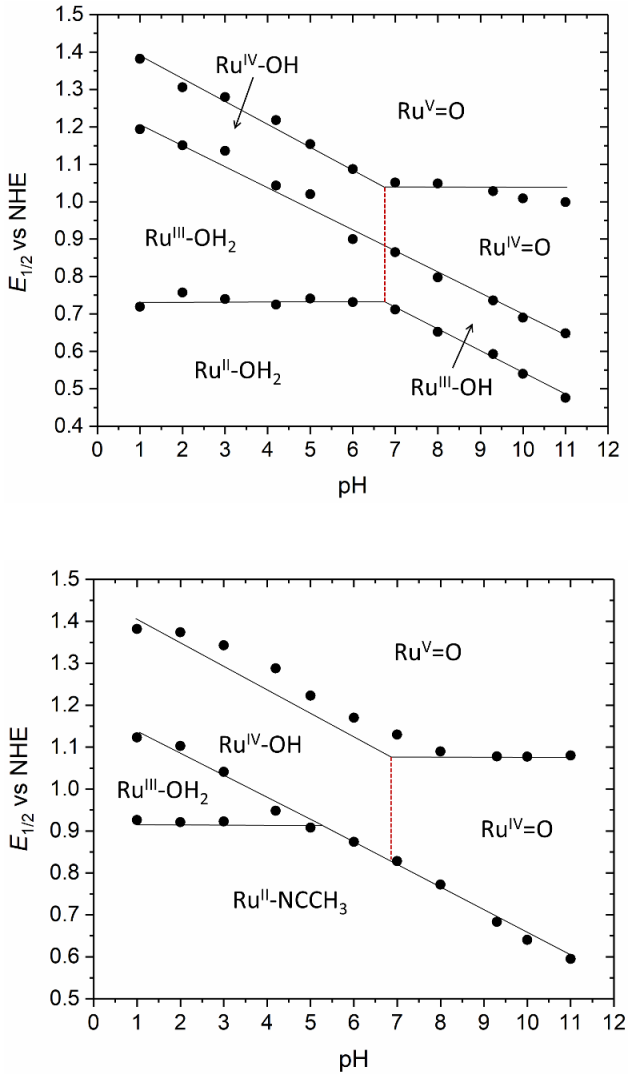

Figure 6. Pourbaix diagrams of **2** in the absence (top) and in the presence of 10% ACN (bottom). The black solid lines indicate trends in data. See Equations 1-7 for detailed description of the processes taking place in Figure 6, bottom. The pK_a value of the Ru^{III}-OH_2/Ru^{III}-OH and Ru^{IV}-OH/Ru^{IV}=O acid-base couples are indicated by the dashed red vertical line.

They illustrate the range of stability of the different species at the different pH ranges and their degree of protonation. At oxidation state II, they all exist in the

Ru^{II}-OH_2 form in the whole pH range (pH 1-11). They undergo a single electron transfer from pH 1 to pH 6.8, beyond this pH a proton coupled electron transfer (PCET) process to give the corresponding Ru^{III}-OH takes place, as indicated by the Nernstian behavior of the waves which show a *ca.* -59 mV/pH slope. The pK_a value of the Ru^{III}-OH_2/Ru^{III}-OH and Ru^{IV}-OH/Ru^{IV}=O acid-base couples are identical and are indicated by the dashed red vertical lines. Interestingly, there is no evident involvement of the carboxylic acid groups in the redox chemistry of complex **1**, although some deviation from the ideal slope of 0 or -59 mV/pH in the pH range from 1 to 6 could be attributed to their influence.

Compound **2** is not soluble in pure aqueous conditions and mixtures of aqueous buffers with organic solvents were used to reach optimum solubility. In this regard, it is important to highlight that in the presence of coordinating solvents such as acetonitrile, the coordination of the solvent occurs as indicated in Equation 1. This is evident from the Pourbaix diagram in the bottom of Figure 6 measured in the presence of acetonitrile, which accounts for a shift of 200 mV for the $Ru^{III/II}$ couple in the range of pH 1-5.5 (see also Figure 7). Upon oxidation, the aquo ligand is preferred and the acetonitrile leaves (Equations 2-4). As a consequence, the redox behavior of compound **2** in the absence and in the presence of acetonitrile is identical at high oxidation states (Equations 5-7, compare top and bottom of Figure 6).

$$[Ru^{II}] + CH_3CN \rightarrow [Ru^{II} - NCCH_3] \quad \text{Eq. 1}$$

$$[Ru^{II} - NCCH_3] + H_2O \rightarrow [Ru^{III} - OH_2] + CH_3CN + 1e^- \quad (\text{at pH} < 5.5) \quad \text{Eq. 2}$$

$$[Ru^{II} - NCCH_3] + H_2O \rightarrow [Ru^{IV} - OH] + CH_3CN + 2e^- + H^+ \quad (\text{at } 5.5 < \text{pH} < 6.8) \quad \text{Eq. 3}$$

$$[Ru^{II} - NCCH_3] + H_2O \rightarrow [Ru^{IV} - O] + CH_3CN + 2e^- + 2H^+ \quad (\text{at pH} > 6.8) \quad \text{Eq. 4}$$

$$[Ru^{III} - OH_2] \rightarrow [Ru^{IV} - OH] + 1e^- + 1H^+ \quad (\text{at pH} < 5.5) \quad \text{Eq. 5}$$

$$[Ru^{IV} - OH] \rightarrow [Ru^{V} - O] + 1e^- + 1H^+ \quad (\text{at pH} < 6.8) \quad \text{Eq. 6}$$

$$[Ru^{IV} - O] \rightarrow [Ru^{V} - O] + 1e^- \quad (\text{at pH} > 6.8) \quad \text{Eq. 7}$$

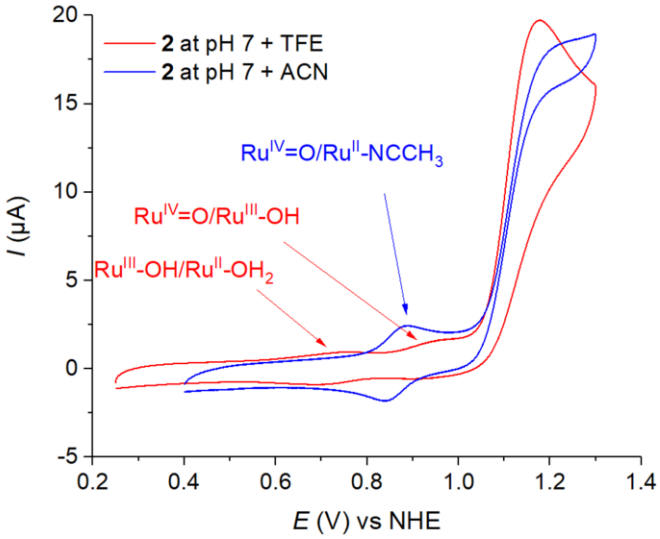

Figure 7. CVs of **2** at pH 7 in phosphate buffer containing 25% TFE (red) and in phosphate buffer containing 10% ACN (blue).

3·3-Foot of the wave analysis at pH 7

IV

Foot of the wave analysis (FOWA) is a powerful electrochemical tool that allows us not only to calculate the maximum turnover frequency (TOF_{max}) of a given catalyst, but also to investigate their catalytic mechanism.[5c, 18] One of the key features of FOWA is that it analyzes only the first points of a catalytic wave, as opposed to the maximum limiting current, used in more traditional methods.[5c] This is very important because it allows to analyze electrocatalytic processes in the absence of a perfect S-shape catalytic wave, and to get reliable rate constants even if side-reactions take place at the studied potential range. A clear example is given in Figure 7, for the CV of **2** in the presence of either TFE or ACN. Although the catalytic wave has a significantly different shape in both experiments, a careful look at the foot of wave suggests that the rate of the catalysis is the same in both cases (Figure 7).

As described in detailed in chapter 1, the O-O bond formation in molecular water oxidation catalysis can occur in two ways for mononuclear complexes. The first one

is a unimolecular mechanism, in which a solvent water molecule attacks a high-valent Ru=O group (WNA). The second possibility is that two Ru^{V}=O groups dimerize to form a peroxo intermediate species (I2M). If the latter step is rate determining, the order of the reaction should be second order.

Unimolecular and bimolecular mechanisms can be elucidated using FOWA by applying Equations 8 and 9, respectively.

$$\frac{i}{i_p} = \frac{4*2.24*\sqrt{\frac{RTk_{obs}}{Fv}}}{1+\exp(\frac{F(E°-E)}{RT})} \quad \text{Eq. 8} \qquad \frac{i}{i_p} = \frac{4*2.24*\sqrt{\frac{RTC°_{cat}\,k_D}{3Fv}}}{1+\exp(\frac{F(E°-E)}{RT})^{1.5}} \quad \text{Eq. 9}$$

Where i is the current intensity in the presence of substrate, i_p is the current intensity in the absence of substrate (we approximate this current to the current associated with the $Ru^{III/II}$ couple), E° is the standard potential for the redox couple that starts the catalysis (extracting from the DPV), E (V) stands for the operating potential in CV, F is the Faraday constant, v is the scan rate, R is gas constant, C°_{cat} is initial bulk concentration of catalyst, k_{obs} is apparent WNA pseudo-rate constant ($k_1[H_2O]$), k_D is apparent dimerization constant and can be extracted from the plot of i/i_p vs $1/(1 + \exp[(F/RT)(E^{\circ}-E)])$, and TOF_{max} stands for maximum turnover frequency which can be calculated from k_D and catalyst concentration.

Figures 8 and 9 depict the FOWA at pH 7 for catalysts **1** and **2** respectively. For catalyst **1**, a TOF_{max} of 0.45 s^{-1} is calculated for a WNA and 0.3 s^{-1} for a I2M mechanism (at [Ru] = 0.84 mM), while a TOF_{max} of 2.24 s^{-1} (WNA) and 4.74 s^{-1} (I2M) is calculated for **2** (at [Ru] = 0.07 mM). These values manifest the greater performance of catalyst **2** compared to **1**, as already suggested by cyclic voltammetry experiments performed under the same experimental conditions (Figure 4).

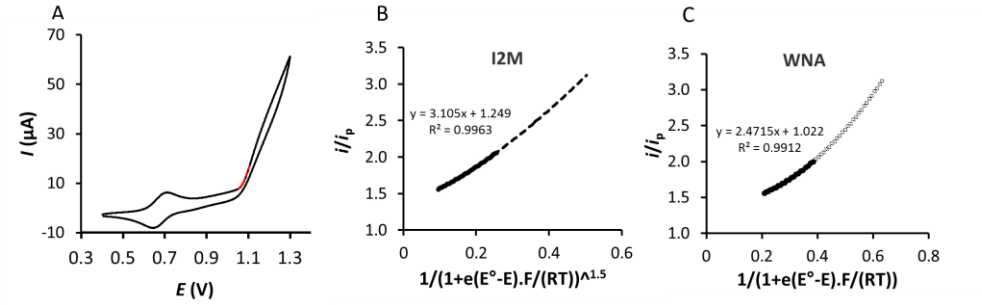

Figure 8. (A) Black solid line shows a CV of **1** (0.84 mM) at pH 7. The red dashed line indicates the data points used for the FOWA. (B) i/i_p vs $1/(1+e[(E°\text{-}E)(F/RT)])^{\wedge 1.5}$ plot assuming a I2M mechanism. (C) i/i_p vs $1/(1+e[(E°\text{-}E)(F/RT)])$ plot assuming a WNA mechanism. The fitting points for the extraction of rate constants at the foot of the wave are represented as a black solid line in graphs B and C.

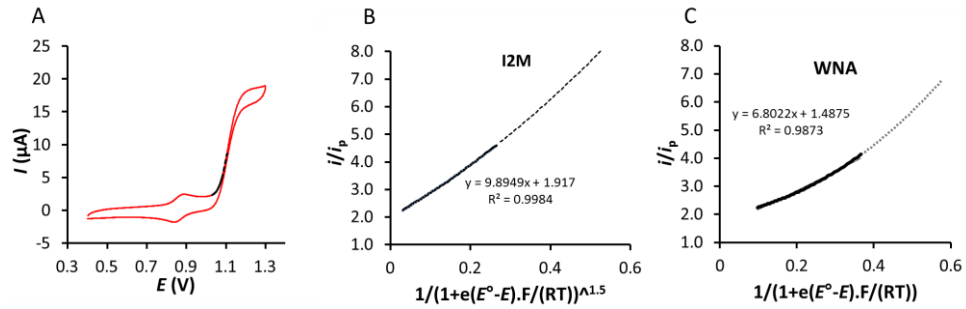

Figure 9. (A) Red solid line shows a CV of **2** (0.07 mM) at pH 7, 10% ACN was added to make the complex soluble. (B) i/i_p vs $1/(1+e[(E°\text{-}E)(F/RT)])^{\wedge 1.5}$ plot assuming a I2M mechanism. (C) i/i_p vs $1/(1+e[(E°\text{-}E)(F/RT)])$ plot assuming a WNA mechanism. The fitting points for the extraction of rate constants at the foot of the wave are represented as a black solid line in the three graphs.

In order to obtain more information about the catalytic pathway (WNA vs I2M) followed by **1** and **2**, a thorough FOWA at different concentration of catalyst was performed (Figures 10 and 11). A plot of the k_{WNA} and k_D vs catalyst concentration is the figure of merit that reveals the mechanistic features of specific catalyst. While interpretation of the results for **2** are straightforward (Figure 11C), clearly indicating that an I2M mechanism is playing with a constant k_D = 210 x 10^3 $M^{-1}s^{-1}$ over the

whole concentration range, the results for catalyst **1** are certainly puzzling. As shown in Figure 10C, neither k_{WNA} nor k_D follow the expected trend and therefore, the mechanism followed by catalyst **1** cannot be described with the models given for the FOWA Equations 8 and 9.

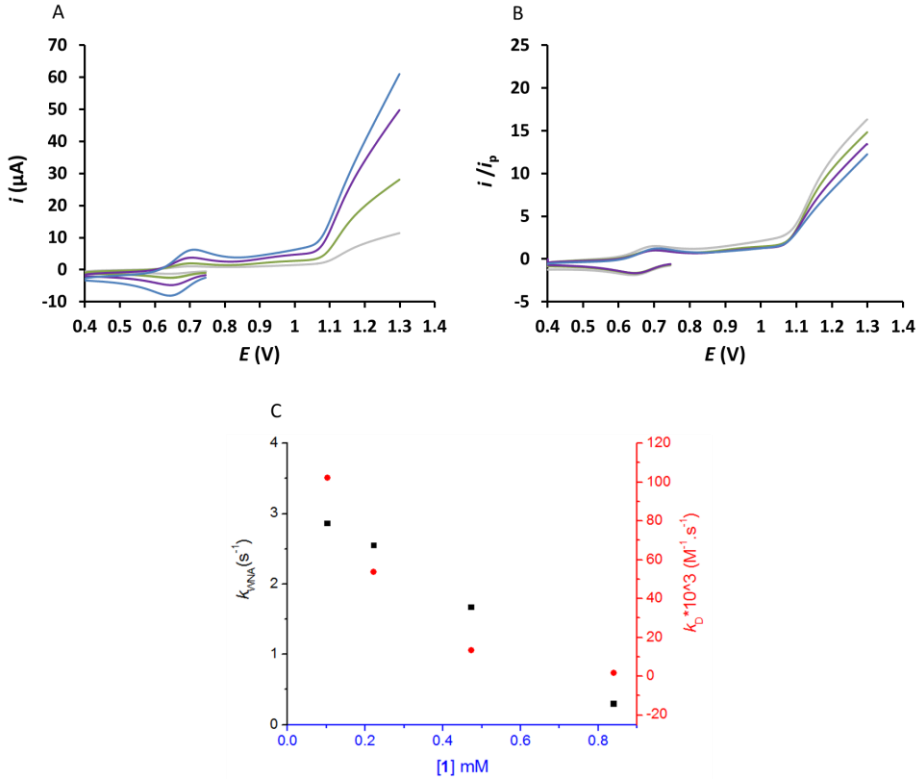

Figure 10. A) CVs of **2** at pH 7 at different concentrations (Blue solid line: 1mm; violet solid line: 0.9 mm; green solid line: 0.5 mm; and gray solid line: 0.2 mm. B) i_p normalized CVs. C) k_D and k_{WNA} vs [**1**].

Although these results does not shed light into the exact mechanism followed by **1**, they give some hints towards a special behavior of this catalyst at pH 7 that distinguish it from catalyst **2** and most of [Ru(bda)(L)$_2$] type of complexes described in the literature.[2-4, 5c]

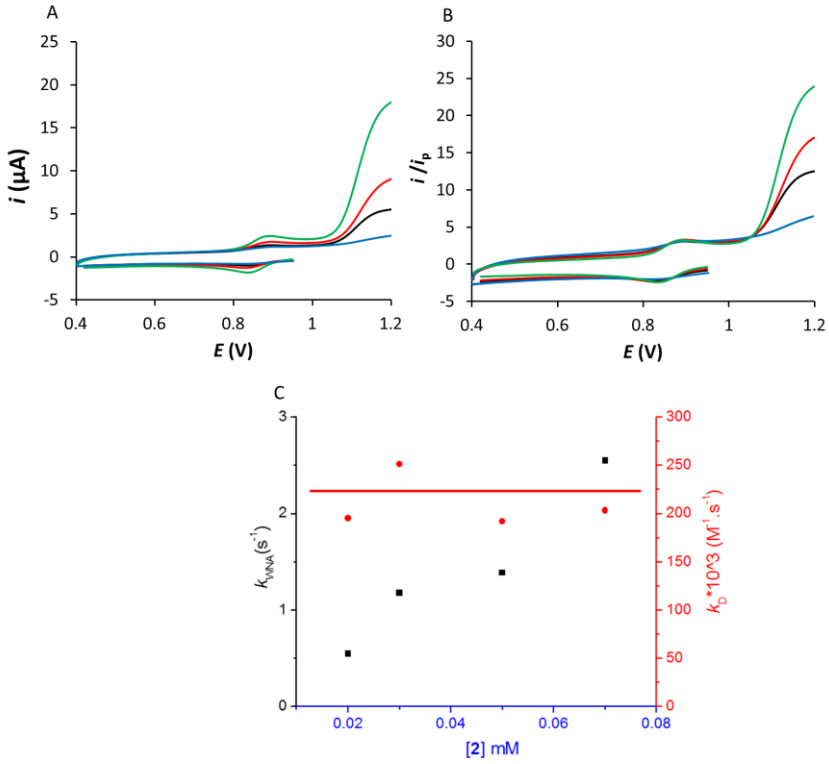

Figure 11. (A) CVs of **2** at different concentrations at pH 7, 10% ACN was added to make the complex soluble (Green solid line: 0.07 mm; red solid line: 0.05 mm; black solid line: 0.03 mm, and blue solid line: 0.01mm) (B) i_p normalized CVs. C) k_D and k_{WNA} vs [**2**]. The solid red line shows the trend for the I2M mechanism.

3·4-Chemical water oxidation by 1 and 2 at pH 1

The ability of **1** and **2** to oxidize water to dioxygen was explored using cerium(IV) ammonium nitrate (Ce^{IV} hereafter) as sacrificial agent at pH 1. The evolved gas was monitored using manometry measurements and the results are shown in Figure 12, together with those of catalyst **3** for comparison purposes. Compounds **1**, **2** and **3** are all very fast and efficient catalysts with TOF_{max} = 7.74 s^{-1}, 12 s^{-1} and 14 s^{-1}, and turnover numbers of TON = 500, 420 and 315, respectively. The latter account for chemical efficiencies of 80 %, 67% and 50%, respectively, in the same range of previously reported catalysts of the $[Ru(bda)(L)_2]$ family.

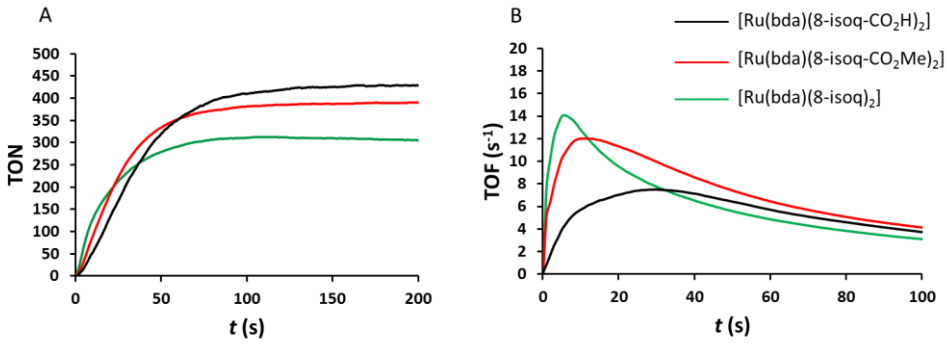

Figure 12. A) Oxygen evolution profile for chemical water oxidation catalysis by **1**, **2** and **3**. $[Cat]_o$ = 2 µM and $[Ce]_o$ = 5 mM, in 0.1 M CF_3SO_3H solution with 6% TFE. B) Plot of TOF vs time.

4-Discussion

The addition of electron withdrawing groups in the isoquinoline axial ligands of complexes of the $[Ru(bda)(L)_2]$ family have a small influence in the electronic density on the metal center as demonstrated by cyclic voltammetry experiments of **1**-**3**. Maximum anodic shifts of 110 mV and 140 mV have been observed for the $Ru^{III/II}$ and $Ru^{IV/III}$ couples, respectively (Table S1). On the other hand, the addition of these groups has had a huge impact in their respective catalytic rate under electrochemically induced catalysis. At pH 1, compounds **1** and **2** show analogous activity, which is significantly lower than that of the non-functionalized complex **3** (Figure S17). In sharp contrast, at pH 7, compound **2** performs as well as **3** while catalyst **1** remains a weaker catalyst (Figure S18). The contrasting results obtained for **2** at pH 1 and pH 7, rule out electronic or steric effects of the ester group in its catalytic performance. Instead, we attribute this unique behavior to second coordination sphere effects induced by the presence of the acids and esters groups in **1** and **2**, in close proximity to the metal active center. At pH 1, both catalysts are neutral compounds at oxidation state Ru^{II} and Ru^{IV} and we expect a similar performance as experimentally proven and already discussed. On the other hand, at pH 7, the carboxylic acid groups in **1** are deprotonated leading to a doubly charged species at oxidation state Ru^{II} and Ru^{IV}. In this scenario, the second coordination

sphere effects between **1** and **2** are expected to be different, leading to different catalytic results.

FOWA analysis at pH 7, reveal that catalyst **2** follows an I2M mechanism in which the dimerization of two Ru^{V}=O molecules is the rate determining step, analogous to that reported for **3** (Figure 1, bottom). In contrast, no conclusive results were obtained for **1** which did not follow the expected behavior for neither a WNA nor a I2M mechanism. Thus, the catalytic performance **1**, is strongly influenced by the second coordination sphere of the deprotonated acids.

With all these results in hand, we propose that a network of H-bonded molecules growing around the Ru-OH_2 center of catalysts **1** and **2** is responsible for the unexpected and contrasting catalytic behavior of these two new catalysts. This network is assisted by the acid and ester groups strategically situated close the metallic center (at pH 1) and only observed for the deprotonated acid at pH 7 (Figure 13). This network would stabilize intermediate species of the water oxidation catalysis leading to higher activation energies for the O-O bond formation, which is usually the rate determining step. A similar second coordination sphere effect has also been proposed for a Ru complex containing the ligand 6,6'-difluoro-2,2'-bipyridine, in which the fluoro substituent in the ortho position of the bipyridine group would interact with the Ru-OH_2 group stabilizing catalytic intermediates, in this case with no need of hydrogen-bonded molecules due to the closer proximity if the fluoro group.[19]

Alternatively, slow electron transfer of the $Ru^{V/IV}$ couple on the surface of the electrode could be responsible for the lower reactivity of **1** and **2** under electrocatalytic conditions with a glassy carbon electrode at pH 1, due to the higher hydrophilicity of these two compounds compared to **3**. In this scenario, the rate determining step of the reaction would change from the O-O bond formation to the previous $Ru^{V/IV}$ oxidation step (see Figure 1, bottom). This effect is enhanced for complex **1** at pH 7, which is charged and thus even more hydrophilic. This

phenomenon would also explain why the catalytic behavior of **1** and **2** under electrochemical and chemical conditions are significantly different (compare Figure 3, Figure S17 and Figure 12).

Although both hypothesis are speculative at this stage, they give good explanations for the experimental results obtained until now. Further experiments and calculations are certainly necessary to confirm or rule out these proposals.

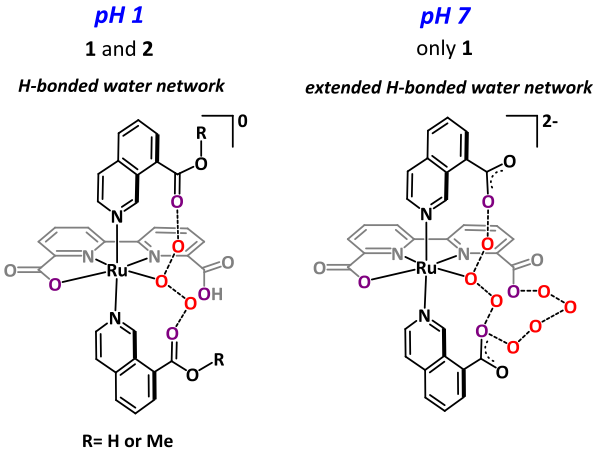

Figure 13. Representative second coordination sphere effects in complexes **1** and **2** at oxidation state II. The formation of a network of H-bonded water molecules is proposed to stabilize these complexes at low and high oxidation states. At pH 1, both complexes experience the same stabilization (left) while at pH 7, only **1** shows enhanced stability induced by the deprotonation of the carboxylic acid groups that can lead to extended networks (right). Oxygen atoms in red represent water molecules involved in the network and dashed black lines represent the bonding between them. Oxygen atoms in purple depict carboxylates that may be involved in the same network.

Despite the superior performance observed for **3** compared to the new catalysts **1** and **2** in terms of catalytic rate under electrochemically induced catalysis at pH 1 (Figure S17), they show comparable turnover frequencies under chemically induced catalysis using Ce^{IV} as sacrificial agent at the same pH (7.7 to 14 s^{-1}, Figure 12). These results highlights the importance of thorough catalytic assessment in different

conditions (electrochemical vs chemical) to be able to fully understand all the factors influencing the catalytic activity of a specific catalyst.

5-Conclusions

Two new catalysts of the [Ru(bda)$(L)_2$] family have been prepared, characterized and assessed in water oxidation catalysis. They have functionalized isoquinoline groups (8-isoq-CO_2H and 8-isoq-CO_2Me). They are powerful catalysts, with unique electrocatalytic performance that is tentatively attributed to second coordination sphere effects induced by the acid and ester groups in the isoquinoline ligands. A network of H-bonded water molecules, favored by the presence of these groups is proposed to be responsible of the different behaviors at pH 1 and pH 7. In addition, slow electron transfer of the $Ru^{V/IV}$ couple is proposed for both catalysts at pH 1 due to the higher hydrophilicity provided by the polar acid and ester group. Further experiments and calculations should give more insights into the actual role of both the acid and ester groups in **1** and **2**, respectively, in their catalytic performance.

References

1. Duan, L.; Fischer, A.; Xu, Y.; Sun, L., Isolated seven-coordinate Ru (IV) dimer complex with $[HOHOH]^-$ bridging ligand as an intermediate for catalytic water oxidation. *Journal of the American Chemical Society* **2009,** *131* (30), 10397-10399.

2. (a) Shaffer, D. W.; Xie, Y.; Szalda, D. J.; Concepcion, J. J., Manipulating the rate-limiting step in water oxidation catalysis by ruthenium bipyridine–dicarboxylate complexes. *Inorganic chemistry* **2016,** *55* (22), 12024-12035; (b) Kamdar, J. M.; Marelius, D. C.; Moore, C. E.; Rheingold, A. L.; Smith, D. K.; Grotjahn, D. B., Ruthenium Complexes of 2, 2′-Bipyridine- 6, 6′-diphosphonate Ligands for Water Oxidation. *ChemCatChem* **2016,** *8* (19), 3045-3049; (c) Li, T.-T.; Zhao, W.-L.; Chen, Y.; Li, F.-M.; Wang, C.-J.; Tian, Y.-H.; Fu, W.-F., Photochemical, Electrochemical, and Photoelectrochemical Water Oxidation Catalyzed by Water-Soluble Mononuclear Ruthenium Complexes. *Chemistry – A European Journal* **2014,** *20* (43), 13957-13964; (d) Liu, Z.; Gao, Y.; Yu, Z.; Zhang, M.; Liu, J., Effects of Br substituent on catalytic performance of Ru-bda (H_2bda = 2,2'-bipyridine-6,6'-dicarboxylic acid) catalysts for water oxidation. *Chinese Journal of Catalysis* **2015,** *36* (10), 1742-1749.

3. Duan, L.; Bozoglian, F.; Mandal, S.; Stewart, B.; Privalov, T.; Llobet, A.; Sun, L., A molecular ruthenium catalyst with water-oxidation activity comparable to that of photosystem II. *Nature chemistry* **2012,** *4* (5), 418-423.

4. Richmond, C. J.; Matheu, R.; Poater, A.; Falivene, L.; Benet-Buchholz, J.; Sala, X.; Cavallo, L.; Llobet, A., Supramolecular Water Oxidation with Ru–bda-Based Catalysts. *Chemistry–A European Journal* **2014,** *20* (52), 17282-17286.

5. (a) Garrido-Barros, P.; Matheu, R.; Gimbert-Suriñach, C.; Llobet, A., Electronic, mechanistic, and structural factors that influence the performance of molecular water oxidation catalysts anchored on electrode surfaces. *Current Opinion in Electrochemistry* **2019,** *15*, 140-147; (b) Matheu, R.; Francàs, L.; Chernev, P.; Ertem, M. Z.; Batista, V.; Haumann, M.; Sala, X.; Llobet, A., Behavior of the Ru-bda water oxidation catalyst covalently anchored on glassy carbon electrodes. *ACS Catalysis* **2015,** *5* (6), 3422-3429; (c) Matheu, R.; Neudeck, S.; Meyer, F.; Sala, X.; Llobet, A., Foot of the Wave Analysis for Mechanistic Elucidation and Benchmarking Applications in Molecular Water Oxidation Catalysis. *ChemSusChem* **2016,** *9* (23), 3361-3369.

6. (a) Creus, J.; Matheu, R.; Peñafiel, I.; Moonshiram, D.; Blondeau, P.; Benet-Buchholz, J.; García-Antón, J.; Sala, X.; Godard, C.; Llobet, A., A million turnover molecular anode for catalytic water oxidation. *Angewandte Chemie International Edition* **2016,** *55* (49), 15382-15386; (b) Grau, S.; Berardi, S.; Moya, A.; Matheu, R.; Cristino, V.; Vilatela, J. J.; Bignozzi, C. A.; Caramori, S.; Gimbert-Suriñach, C.; Llobet, A., A hybrid molecular photoanode for efficient light-induced water oxidation. *Sustainable Energy & Fuels* **2018,** *2* (9), 1979-1985.

7. Duan, L.; Wang, L.; Inge, A. K.; Fischer, A.; Zou, X.; Sun, L., Insights into Ru-based molecular water oxidation catalysts: Electronic and noncovalent-interaction effects on their catalytic activities. *Inorganic chemistry* **2013,** *52* (14), 7844-7852.

8. Evans, I. P.; Spencer, A.; Wilkinson, G., Dichlorotetrakis(dimethyl sulphoxide)ruthenium(II) and its use as a source material for some new ruthenium(II) complexes. *Journal of the Chemical Society, Dalton Transactions* **1973,** (2), 204-209.

9. Data collection with APEX II version v2013.4-1. Bruker (**2007**). Bruker AXS Inc., Madison, Wisconsin, USA.

10. Data reduction with Bruker SAINT version V8.30c. Bruker (**2007**). Bruker AXS Inc., Madison, Wisconsin, USA.

11. SADABS: V2012/1 Bruker (2001). Bruker AXS Inc., Madison, Wisconsin, USA. Blessing,. *Acta Crystallographica* **1995,** *A51*, 33-38.

12. SHELXT; V2014/4 (Sheldrick 2014). Sheldrick, G. M., *Acta Crystallographica* **2015,** *A71*, 3-8.

13. SHELXle; C.B. Huebschle, G. M. S., B. Dittrich, SHELXle;. *Journal of Applied Crystallography* **2011,** *44*, 1281-1284.

14. SHELXL; SHELXL-2014/7 (Sheldrick 2014). Sheldrick, G. M., *Acta Crystallographica* **2015,** *C71*, 3-8.

15. The exact composition of this intermediate in the solid state is not fully elucidated through elemental analysis. It is only soluble in DMSO solvent giving pure [Ru(bda)$(DMSO)_2$] that is the result of the substitution of X by DMSO.

16. Concepcion, J. J.; Zhong, D. K.; Szalda, D. J.; Muckerman, J. T.; Fujita, E., Mechanism of water oxidation by [Ru(bda)$(L)_2$]: the return of the "blue dimer". *Chemical Communications* **2015,** *51* (19), 4105-4108.

17. (a) Song, N.; Concepcion, J. J.; Binstead, R. A.; Rudd, J. A.; Vannucci, A. K.; Dares, C. J.; Coggins, M. K.; Meyer, T. J., Base-enhanced catalytic water oxidation by a carboxylate–bipyridine Ru (II) complex. *Proceedings of the National Academy of Sciences* **2015,** *112* (16), 4935-4940; (b) Matheu, R.; Ghaderian, A.; Francàs, L.; Chernev, P.; Ertem, M. Z.; Benet-Buchholz, J.; Batista, V. S.; Haumann, M.; Gimbert-Suriñach, C.; Sala, X.; Llobet, A., Behavior of Ru–bda Water-Oxidation Catalysts in Low Oxidation States. *Chemistry – A European Journal* **2018,** *24* (49), 12838-12847.

18. Costentin, C.; Drouet, S.; Robert, M.; Savéant, J.-M., Turnover numbers, turnover frequencies, and overpotential in molecular catalysis of electrochemical reactions. Cyclic voltammetry and preparative-scale electrolysis. *Journal of the American Chemical Society* **2012,** *134* (27), 11235-11242.

19. Maji, S.; López, I.; Bozoglian, F.; Benet-Buchholz, J.; Llobet, A., Mononuclear ruthenium–water oxidation catalysts: discerning between electronic and hydrogen-bonding effects. *Inorganic chemistry* **2013,** *52* (7), 3591-3593.

Supporting information

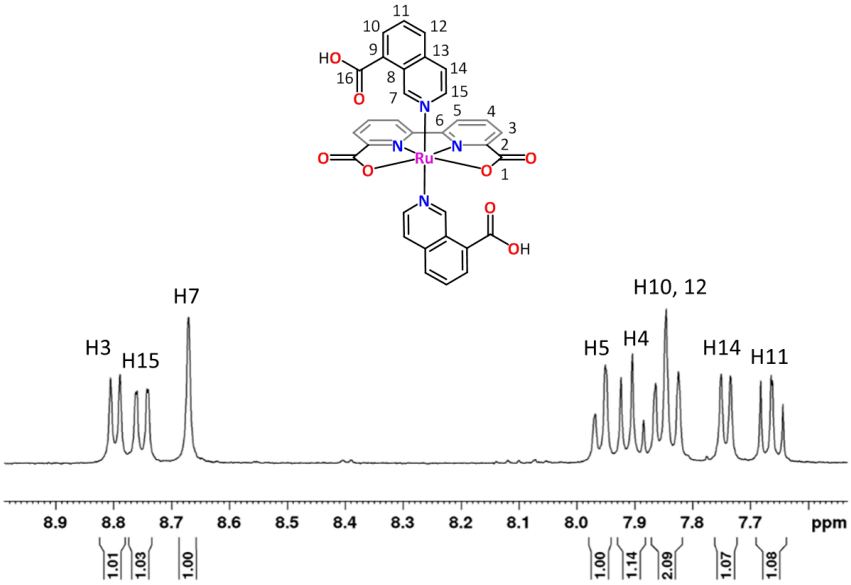

Figure S1. ^{1}H NMR of **1** in d_4-Methanol mixed with 5 microliters Et_3N.

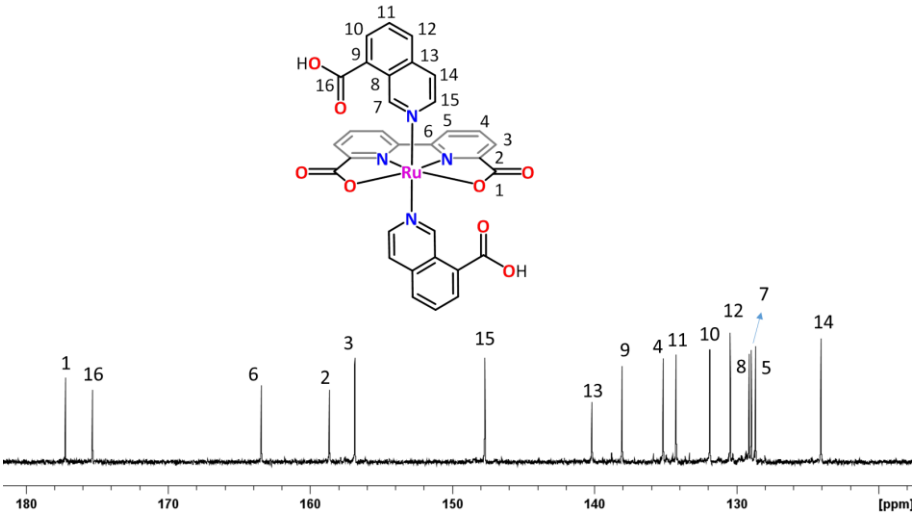

Figuer S2. ^{13}C NMR of **1** in d_4-Methanol.

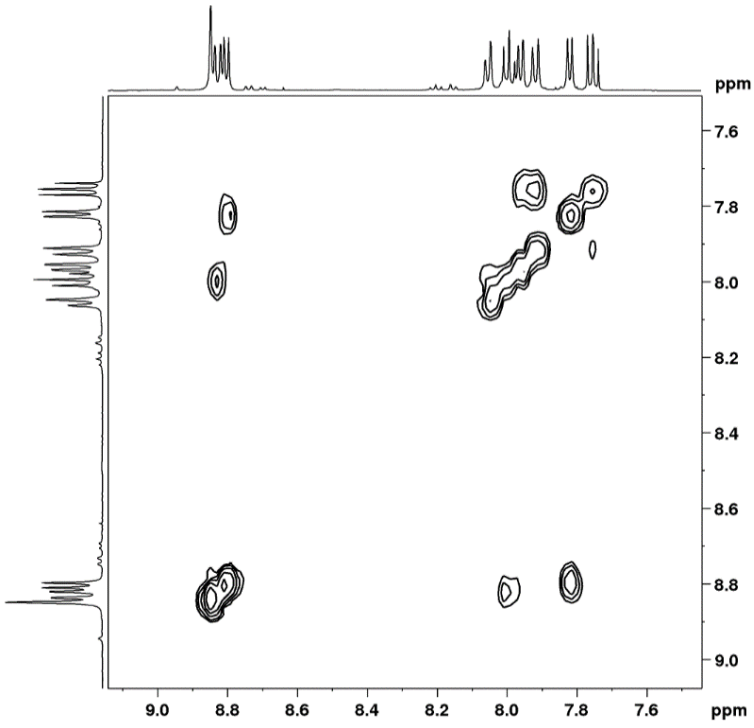

Figure S3. ^{1}H-H COSY of **1** in d_4-Methanol.

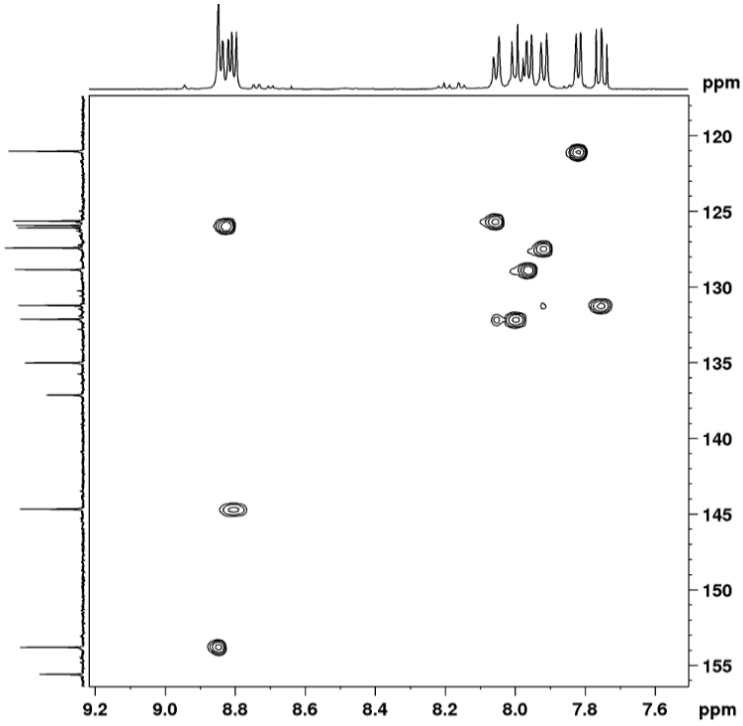

Figure S4. ^{1}H-^{13}C HSQC of **1** in d_4-Methanol.

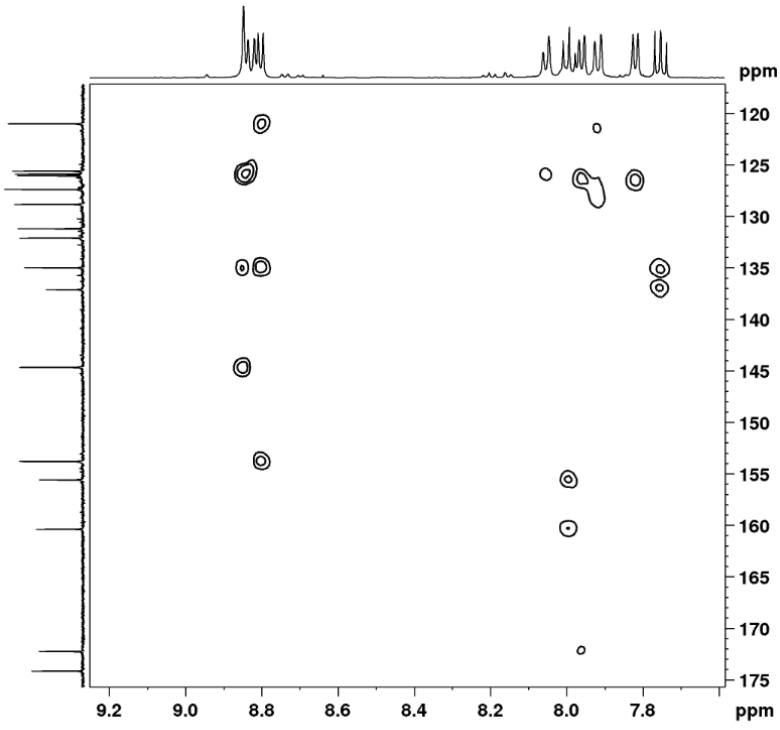

Figure S5. ^{1}H-^{13}C HMBC of **1** in d_4-Methanol.

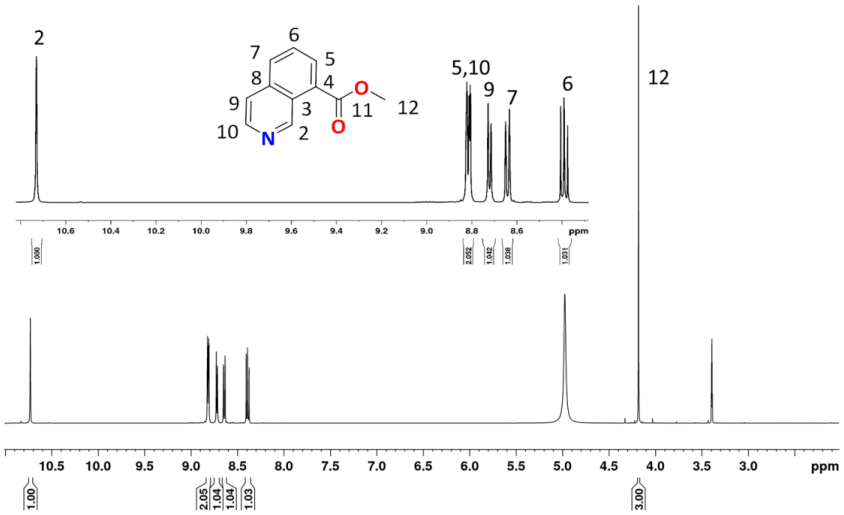

IV

Figure S6. ^{1}H NMR of 8-isoq-CO_2Me in d_4-Methanol.

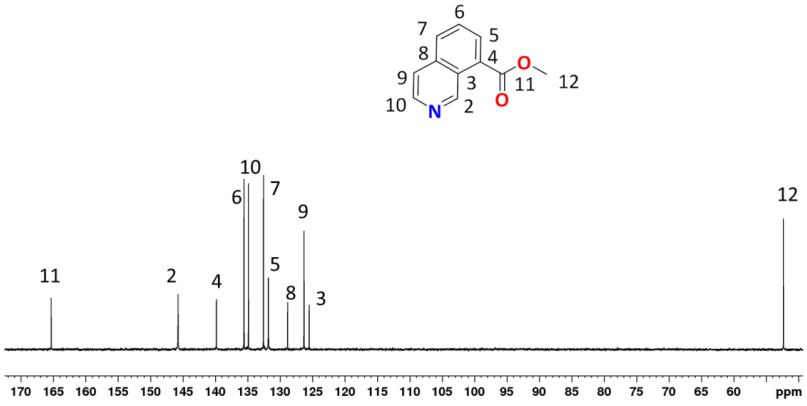

Figure S7. ^{13}C {H} NMR of 8-isoq-CO_2Me in d_4-Methanol.

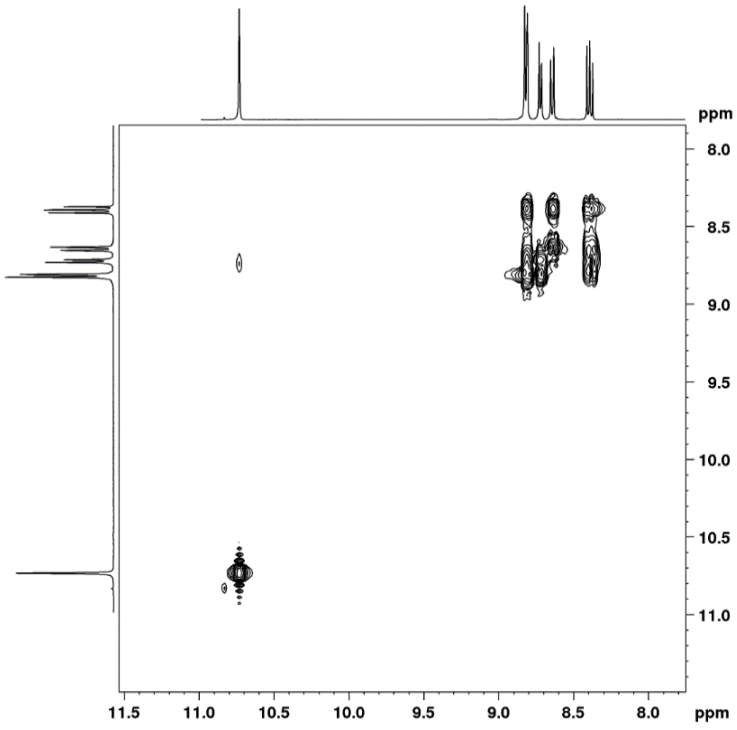

Figure S8. ^{1}H-H COSY NMR of 8-isoq-CO_2Me in d_4-Methanol.

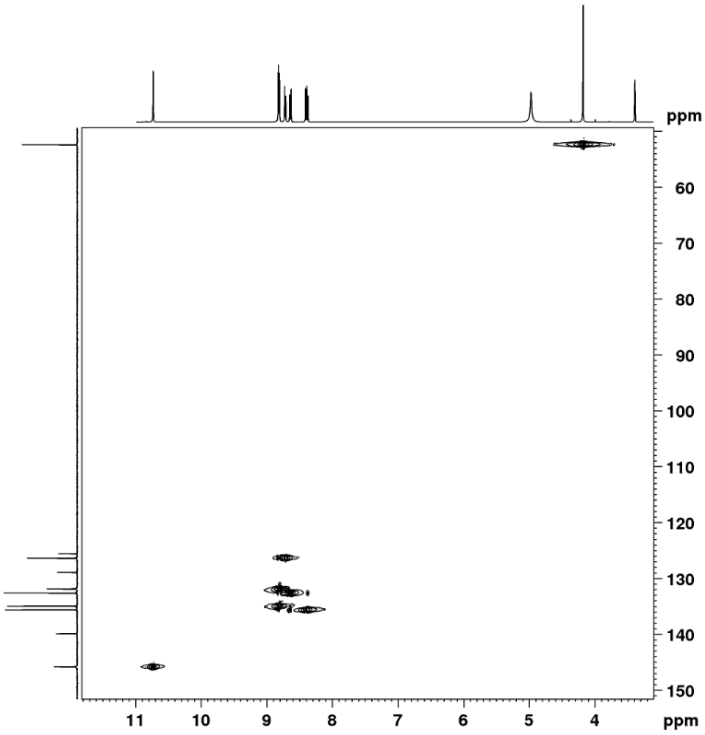

Figure S9. ^{1}H-^{13}C HSQC NMR of 8-isoq-CO_2Me in d_4-Methanol.

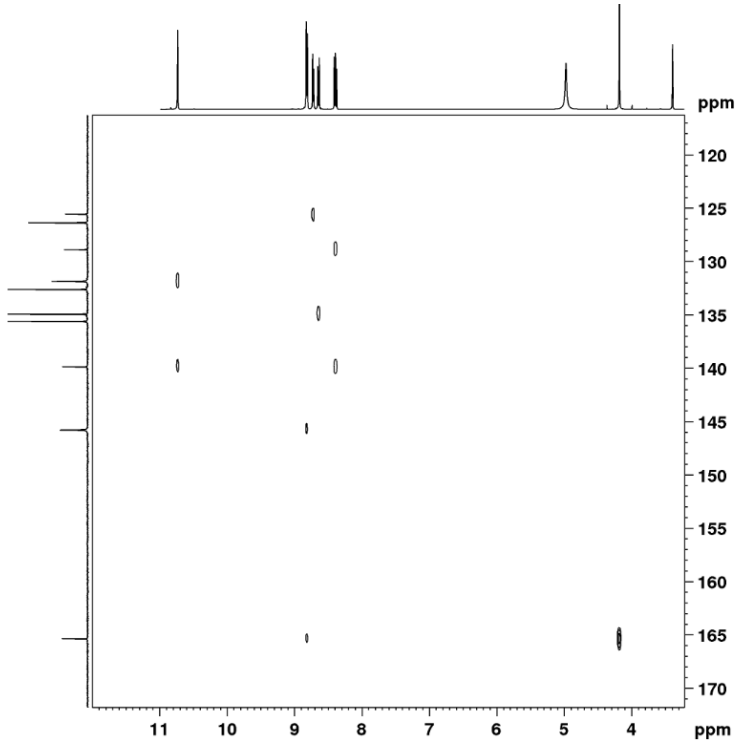

Figure S10. ^{1}H-^{13}C HMBC NMR of 8-isoq-CO_2Me in d_4-Methanol.

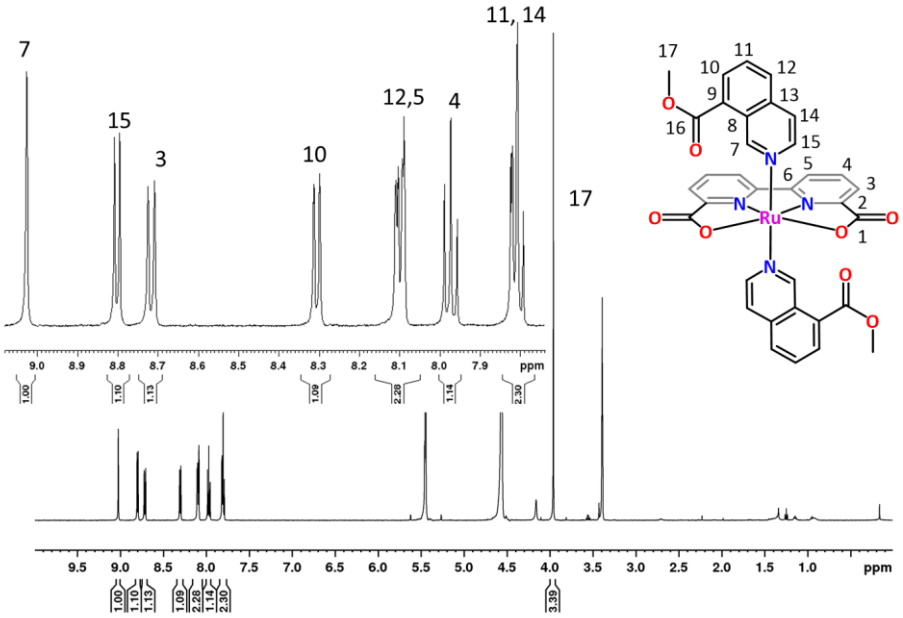

Figure S11. ^{1}H NMR of **2** in d_4-Methanol/CD_2Cl_2 (1:2).

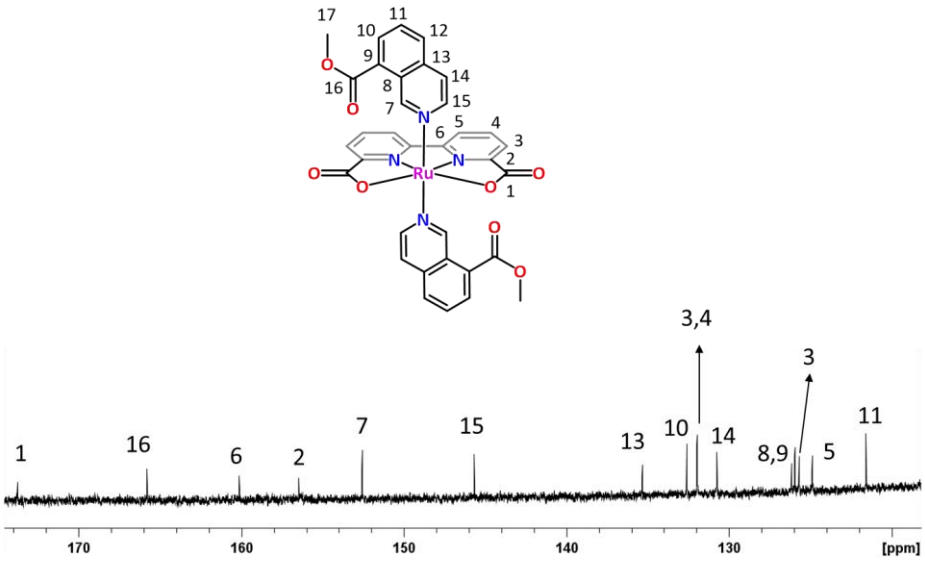

Figure S12. ^{13}C {H} NMR of **2** in d_4-Methanol/CD_2Cl_2 (1:2).

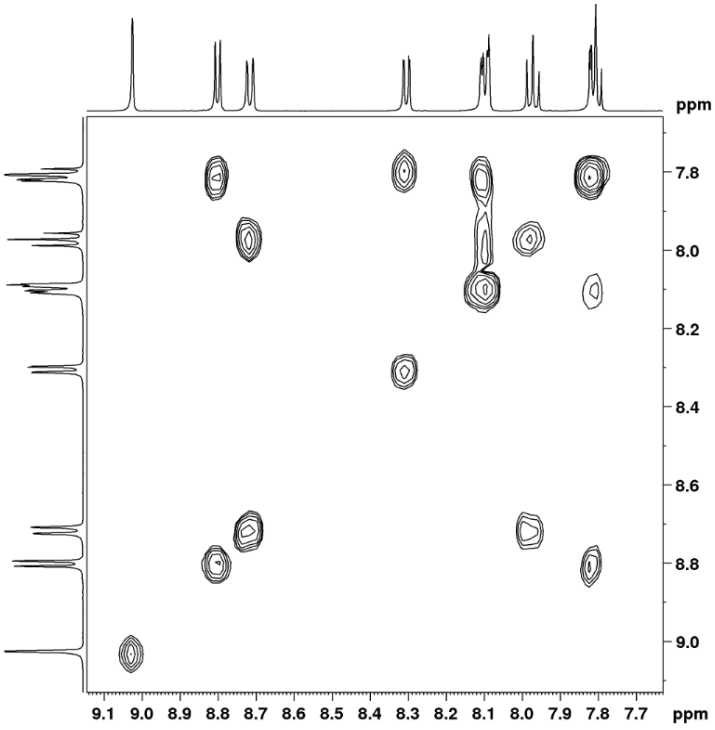

Figure S13. ^{1}H-H COSY NMR of **2** in d_4-Methanol/CD_2Cl_2 (1:2).

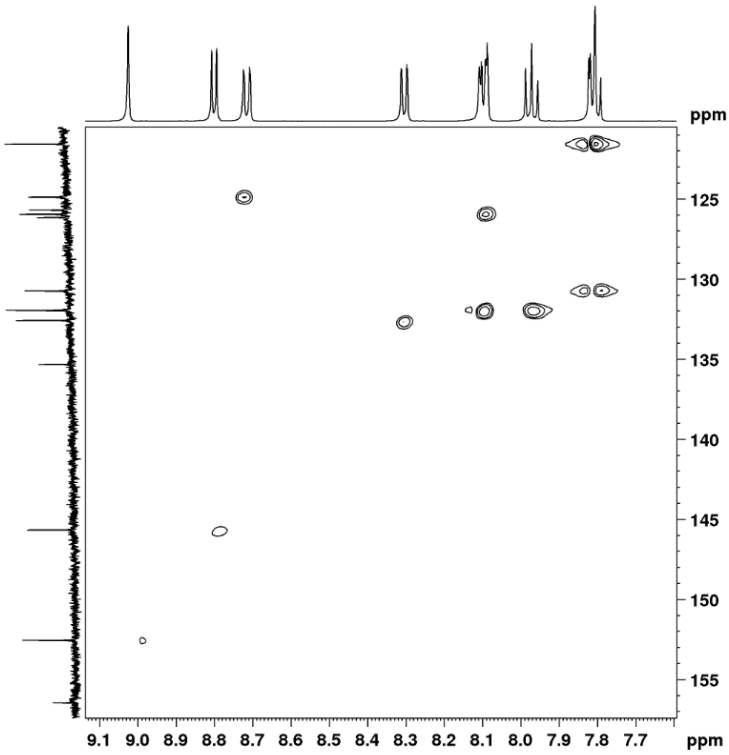

Figure S14. ^{1}H-^{13}C HSQC NMR of **2** in d_4-Methanol/CD_2Cl_2 (1:2).

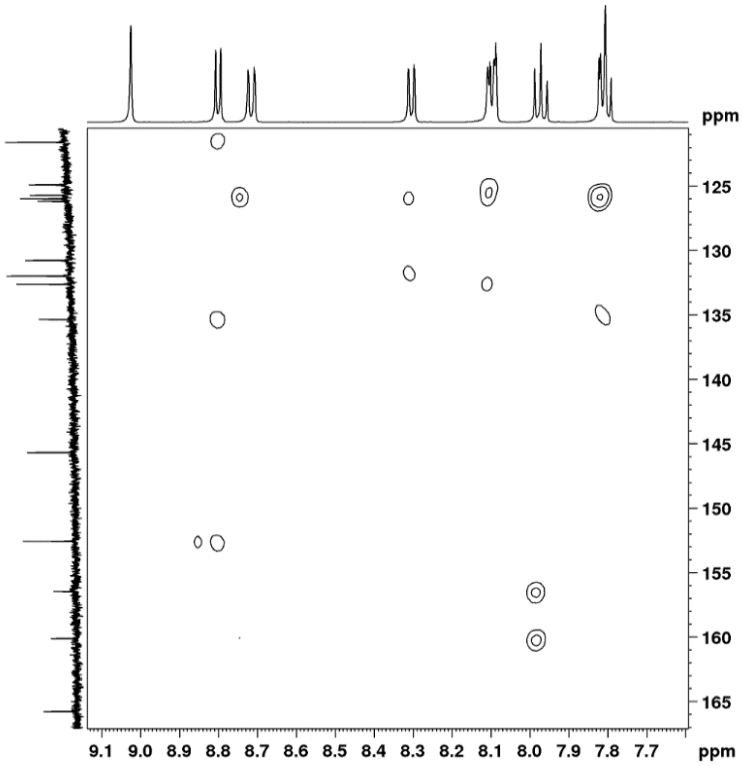

Figure S15. ^{1}H-^{13}C HMBC NMR of **2** in d_4-Methanol/CD_2Cl_2 (1:2).

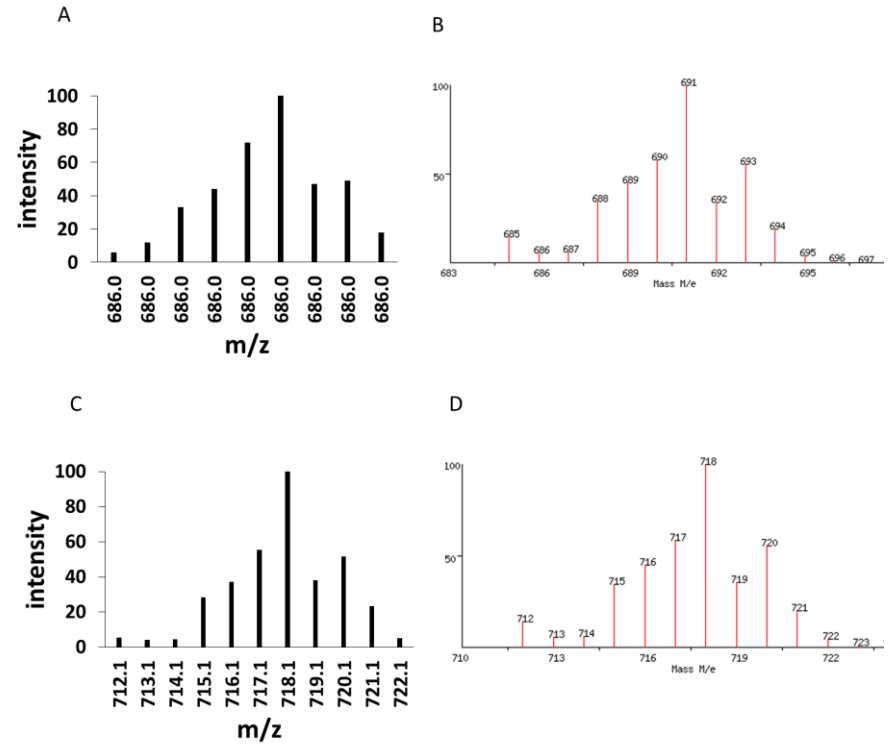

Figure S16. A) Mass spectrum of **1** was performed in direct injection in methanol and ESI^+ as ionization mode. The molecular peak was found as $[\mathbf{1}+H]^+$. B) Simulated isotopic pattern for [**1**+H]. C) Mass Spectrum of **2** in a $MALDI^+$ dctb matrix. The molecular peak was found as $[\mathbf{2}+H]^+$. D) Simulated isotopic pattern for $[\mathbf{2}+H]^+$.

Table S1. The redox potentials of **1**, **2** and **3** at pH 1 and 7.

Complex	$E_{1/2}$ (pH 1)[a]			$E_{1/2}$ (pH 7)[b]		
	III/II	IV/III	V/IV	III/II	IV/III	V/IV
1	0.74	1.23	1.40	0.67	0.88	1.06
2	0.71	1.17	1.33	0.71	0.87	1.05
3[c]	0.63	1.09	1.27	0.52	0.82	1.1

a) Conditions: **[Cat] = 1 mM**, pH 1 solution (TFE/TA (1:2)). b) Conditions: **[Cat] = 0.1 mM**, 25% TFE was added in a phosphate buffer aqueous solution at pH 7, because of poor solubility of complex **2** and comparing redox potential of **1** and **2** in the same condition. v= 100 mV s^{-1}, working electrode = glassy carbon (0.07cm^2), counter electrode = Pt, and reference electrode = Hg/Hg_2SO_4. c) These data is extracted from the literature.[1]

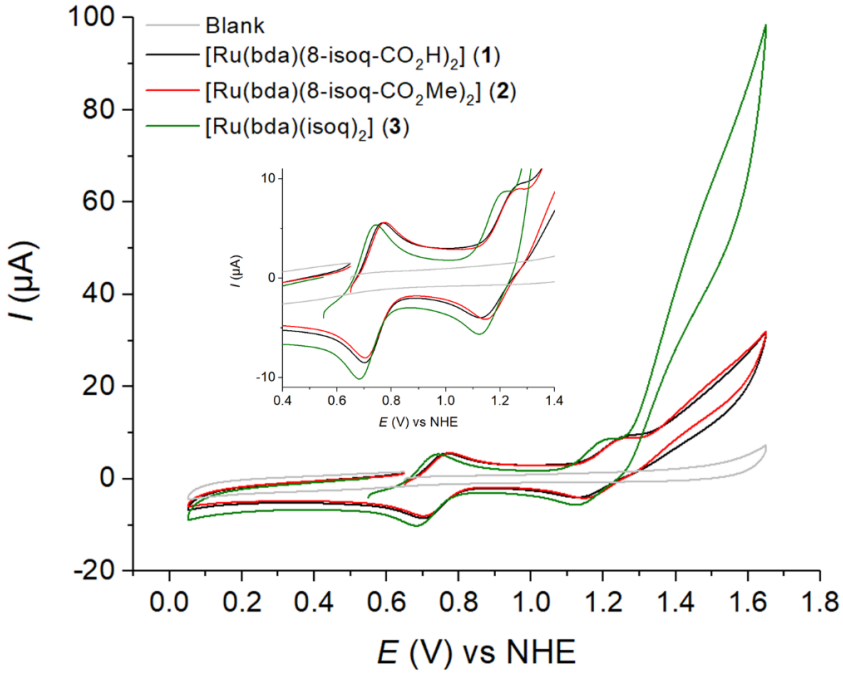

IV

Figure S17. CVs of **1**, **2**, and **3** at pH 1 [Cat] = 1 mM, v= 100 mV s^{-1}, working electrode = glassy carbon (0.07 cm^2), counter electrode = Pt and reference electrode = Hg/Hg_2SO_4.

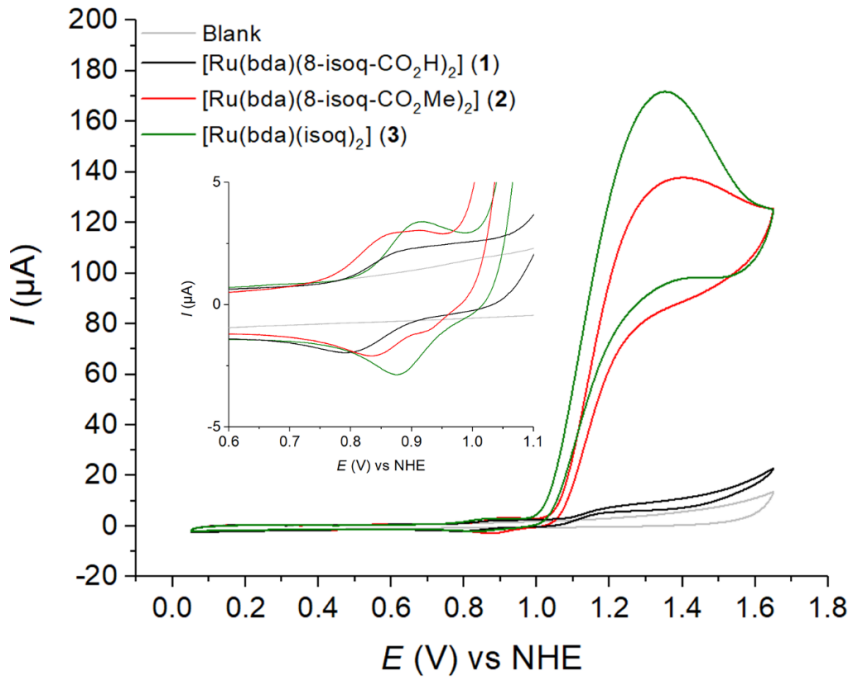

Figure S18. CVs of **1**, **2**, and **3** at pH 7 phosphate buffer mixed with 10% CH_3CN. [Cat] = 0.1 mM, ν= 100 mV s^{-1}, working electrode = glassy carbon (0.07 cm^2), counter electrode= Pt and reference electrode = Hg/Hg_2SO_4.

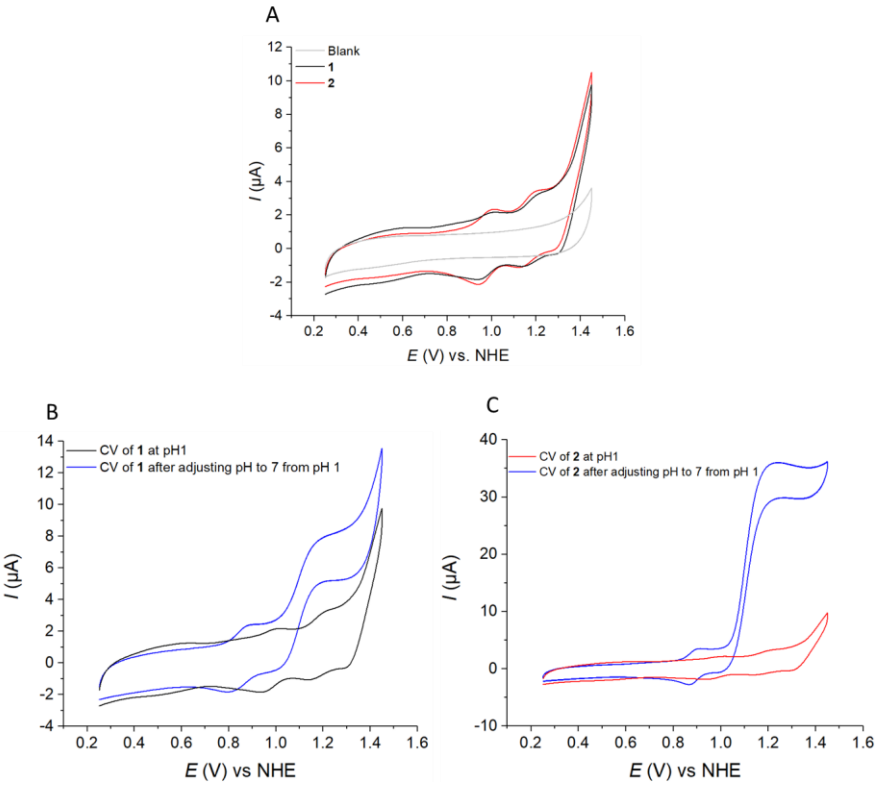

Figure S19. A) CVs of 0.1mM solutions of **1** (black) and **2** (red) at pH1 TA (10% ACN). B) CV of **1** after basifying the solution used in the CV of Figure S19A up to pH 7 by adding a concentrated NaOH solution, the CV at pH 1 is also given in dotted line for comparison. C) CV of **2** after basifying the solution used in the CV of Figure S19A up to pH 7 by adding a concentrated NaOH solution, the CV at pH 1 is also given in dotted line for comparison.

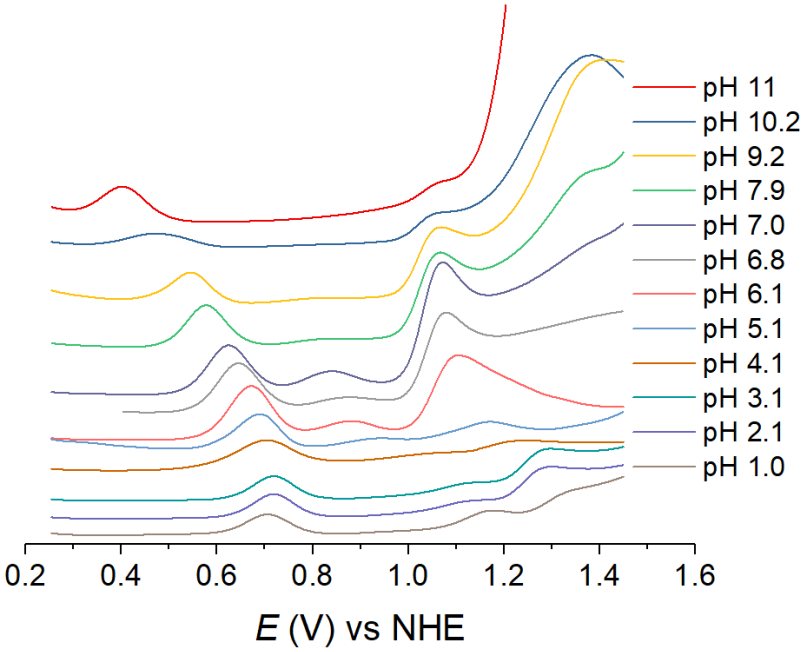

Figure S20. DPVs of **1** at different pHs.

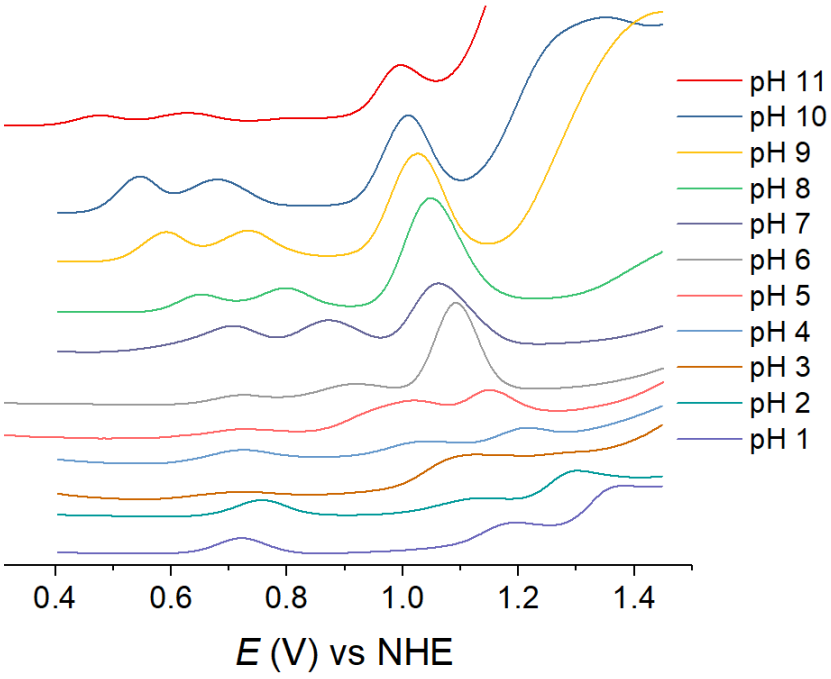

IV

Figure S21. DPVs of **2** at different pHs with 25% TFE.

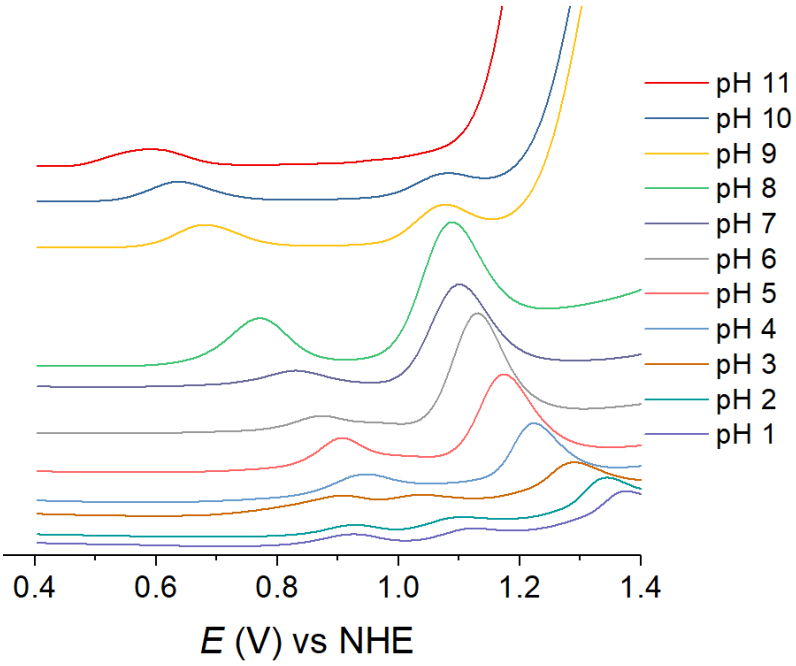

Figure S22. DPVs of **2** at different pHs with 10 % ACN.

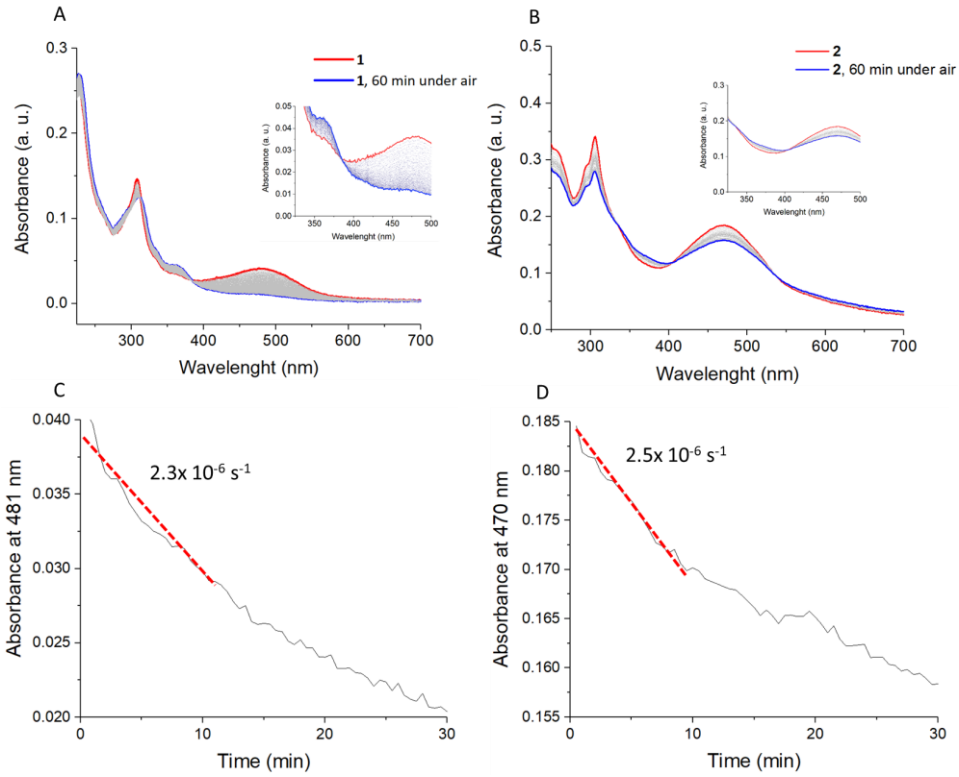

Figure S23. A and B) UV-Vis spectra of 50 µM solutions of **1** and **2** in in TA with 25% CF_3CH_2OH, respectively and their evolution upon exposure to air. C and D) Kinetics of the oxidation of Ru^{II} to Ru^{III} under air.

Reference

1. Song, N.; Concepcion, J. J.; Binstead, R. A.; Rudd, J. A.; Vannucci, A. K.; Dares, C. J.; Coggins, M. K.; Meyer, T. J., Base-enhanced catalytic water oxidation by a carboxylate–bipyridine Ru (II) complex. *Proceedings of the National Academy of Sciences* **2015,** *112* (16), 4935-4940.

Chapter 5

A Ru-bda complex with a dangling carboxylate group: synthesis and electrochemical properties

Abstract

Ruthenium complexes containing the tetradentate 2,2'-bipyridine-6,6'-dicarboxylato (bda^{2-}) equatorial ligand and ortho-subsituted pyridines in the axial position have been prepared and characterized using spectroscopic, crystallographic and electrochemical techniques. Complexes [Ru(Hbda)(DMSO)(pyC)] (**1**) and [Ru(bda)(DMSO)(pyA)] (**2**) (where pyC is 2-pyridinecarboxylate, pyA is pyridine-2-ylmethanol and DMSO is dimethylsulfoxide) have been isolated in moderate to high yields. The solid state structures of (**1**-H)$^{-}$ and **2** reveal the strong chelate effect of the axial pyridine ligand that coordinates in a bidentate fashion leaving the bda^{2-} equatorial ligand coordinating in a tridentate mode. In solution, compound **2** shows a dynamic equilibrium between different coordination modes of the bda^{2-} and pyA ligands. This phenomenon does not occur for **1** because the carboxylate binds stronger than the labile alcohol in **2**. Cyclic voltammetry analysis of **1** reveal a pH independent two-electron wave at $E_{1/2}$ = 1.12 V associated with the $Ru^{IV/II}$ couple. In sharp contrast, complex **2** shows a pH dependent one-electron wave at $E_{1/2}$ = 0.83 V (pH 1), assigned to the proton couple electron transfer process of the $Ru^{III/II}$ couple and a pH independent wave at $E_{1/2}$ = 1.06 V assigned to the $Ru^{IV/III}$ couple. Compound **2** was used to prepare complex [Ru(bda)(pic)(pyA)] (**4**). This complex is air sensitive and converts to complex [Ru(bda)(pic)(pyE)] (**5**) (where pyE is methyl 2-pyridine carboxylate) in the presence of methanol. This oxidation also occurs by applying a positive potential to an aqueous solution of **4**, producing the derivative [Ru(bda)(pic)(pyC)] (**3**). Cyclic voltammetry of **3** shows two pH independent one-electron oxidation waves at $E_{1/2}$ = 0.64 V and $E_{1/2}$ = 1.0 V, corresponding to the $Ru^{III/II}$ and $Ru^{IV/III}$ couples, respectively. In addition, a water oxidation catalytic wave appears at E_{onset} ≈ 1.3 V. Foot of the wave analysis of this catalytic wave based on a water nucleophilic attack accounts for a TOF_{max} = 3.1 s^{-1}.

1-Introduction

In the field of water oxidation to dioxygen catalysis, ruthenium complexes have played an important role not only allowing the elucidation of catalytic mechanisms but also generating the fastest and most rugged molecular catalysts reported to date.[1] The recent advances have allowed the scientific community to identify a series of features that are crucial to reach turnover frequencies (TOFs) above 10^4 s^{-1} and stabilities beyond millions of turnover numbers (TONs).[2] Among them it is important to highlight the ligand robustness, the possibility to reach seven coordination number at high metal oxidation states and second coordination sphere effects. There are two families of complexes that comply with these requirements and are characterized by containing an equatorial polypyridine ligand with one or two carboxylate groups bound to the metal center. In particular, ruthenium complexes containing the tetradentate bda^{2-} (2,2'-bipyridine-6,6'-dicarboxylato) ligand and pentadentate tda^{2-} ([2,2':6',2''-terpyridine]-6,6''-dicarboxylato) ligand are those showing record rates and stabilities (see Figure 1 for catalyst precursors).[3] The former bda family of complexes are known to follow a bimolecular mechanism in respect to Ru where two Ru-oxo groups react in the key O-O bond formation step (I2M) while the latter tda family of catalysts follows a water nucleophilic attack mechanism (WNA) assisted by the dangling carboxylate group in the equatorial ligand. The κ-N^2O^2 coordination fashion of the bda^{2-} ligands provides high electron density to the metal center mainly due to the two carboxylate groups that results in the lowest overpotential for water oxidation reaction based on ruthenium molecular complexes reported until now. On the other hand, the κ-N^3O^1 coordination mode of the tda^{2-} ligand, with only one carboxylate group bound to the metal center results in higher overpotential. However, the presence of a dangling carboxylate group in the tda^{2-} is key to provide fast catalysis through a WNA mechanism, and to incorporate such catalytic centers in conductive and semiconductive solid supports.[2a, 4] This is not straightforward with the bda family of

complexes that follow an I2M mechanism, for which the incorporation into electrodes results in decomposition to ruthenium oxide due to the restricted mobility of the ruthenium centers once attached on a surface.[5]

In this work, we take inspiration from the best features of the bda and tda family of complexes and explore the synthesis of the complex [Ru^{III}(bda)(pic)(pyC)] where pic is 4-methylpyridine and pyC is 2-pyridinecarboxylate (Figure 1, right). The complex has a similar coordination sphere around the metal center to that of the bda family (Figure 1, left), this means, 4 neutral pyridine ligands and 2 anionic carboxylate ligands. The main difference is that the second coordinated carboxylate group is provided by an axial pyridine ligand instead of the equatorial bda^{2-} ligand. At the same time, the target complex has a dangling carboxylate that may assist a water nucleophilic attach to the high valent Ru-oxo species, in a similar fashion to that of the tda complex (Figure 1, middle).

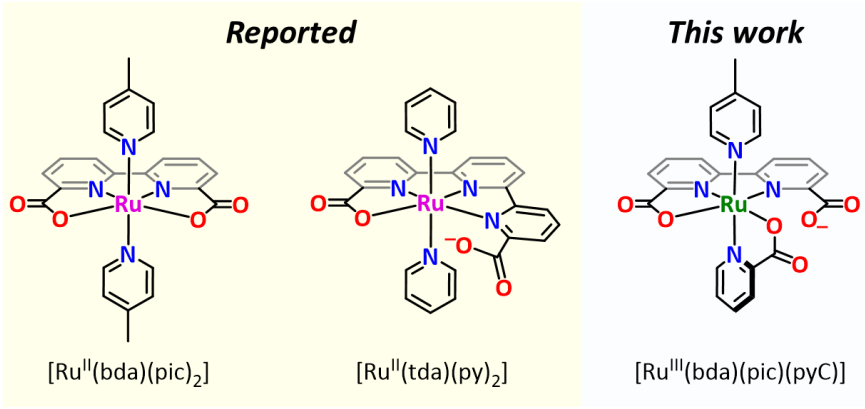

Figure 1. Left) Ruthenium complexes that are precursors of water oxidation to dioxygen catalysts. Right) Catalyst designed in this work. Abbreviations: bda^{2-} is 2,2'-bipyridine-6,6'-dicarboxylato, tda^{2-} is [2,2':6',2''-terpyridine]-6,6''-dicarboxylato, pic is 4-methylpyridine, py is pyridine and pyC is 2-pyridinecarboxylato.

2-Experimental Section

Synthetic materials: The bda^{2-} ligand 2,2'-bipyridine-6,6'-dicarboxylato[3a] and the ruthenium precursor $[Ru(DMSO)_4Cl_2]$[6] and intermediate [Ru(bda)(DMSO)(X)] (where X = MeOH or DMSO)[7] were prepared according to the literature. The ortho-functionalized pyridines 2-pyridinecarboxylic acid (HpyC), pyridine-2-ylmethanol (pyA) and other reagents including 4-picoline (pic) were obtained from Sigma-Aldrich and used as received. When required, solvents were dried by following the standard procedures, distilled under nitrogen and used immediately. High purity de-ionized water used for the electrochemistry experiments was obtained by passing distilled water through a nanopure Milli-Q water purification system. For other spectroscopic and electrochemical studies, HPLC-grade solvents were used. **Instrumentation and methods:** A 500 MHz Bruker Avance II spectrometer was used to carry out NMR spectroscopy. ESI-Mass experiments were performed by using micromass Q-TOF mass spectrometer. UV/Vis spectroscopy was performed on a Cary 50 (Varian) UV/Vis spectrophotometer in 0.1 cm quartz cuvettes. Elemental analyses were carried out on Perkin-Elmer 240C elemental analyzer. The pH of the electrolytic solutions was determined by a pH meter (CRISON, Basic 20+) calibrated before measurements through a standard solutions at pH 4.01, 7.00 and 9.21. Manometric measurements were performed on a Testo 521 differential pressure manometer with an operating range of 0.1-10 kPa and accuracy within 0.5% of the measurements. The manometer was coupled to thermostatic reaction vessels for dynamic monitoring of the headspace pressure above each reaction solution. **Electrochemical techniques and materials:** all electrochemical experiments were performed with an IJ-Cambria CHI-660 potentiostat using a one-compartment three-electrode cell for cyclic voltammetry (CV) and differential pulse voltammetry (DPV) or two compartment cell for bulk electrolysis. $E_{1/2}$ values reported in this work were estimated from CV experiments as the average of the oxidative and reductive peak potentials ($E_{p,a}$ + $E_{p,c}$)/2 or from DPV. All the potentials reported in this work

were measured vs Hg/Hg_2SO_4 (K_2SO_4 saturated) as reference electrode (unless indicated), and converted to NHE by adding 0.648 V. Glassy carbon disk (ϕ = 0.3 cm, S = 0.07 cm^2) and Pt disk were used as Working Electrode (WE) and Counter Electrode (CE), respectively, unless explicitly mentioned. Glassy carbon electrodes were polished with 0.05 µm alumina (Al_2O_3) and rinsed with water. CVs and DPs were *i*R compensated at 85%. Cyclic Voltammograms (CV) were recorded at 100 $mV{\cdot}s^{-1}$ scan rate, unless explicitly metnioned. The DPV parameters were Δ*E*= 4 mV, Amplitude = 50 mV, Pulse width = 0.05 s, Sampling width = 0.0167 s, Pulse period = 0.5 s. The electrolytes used in the electrochemical experiments were 0.1 M triflic acid (TA) solution for pH 1 and *I* = 0.1 M phosphate buffer solutions with desired the pH. For routine bulk electrolysis experiments, a Pt mesh (cylindrical Pt mesh electrode, ø: 10 mm) was used as a WE, another Pt grid (square Pt mesh 20*20 mm) as a CE and a Hg/Hg_2SO_4 (K_2SO_4 saturated) as a RE.

Synthesis of the [Ru(Hbda)(DMSO)(pyC)] (1). [Ru(bda)(DMSO)(X)] (X = MeOH or DMSO) (150 mg, 0.3 mmol) and pyridine-2-carboxylic acid (HpyC) (40 mg, 0.32 mmol) were dissolved in anhydrous MeOH (200 mL) and stirred (600 rpm) at room temperature overnight under Ar. The product precipitated as a red powder, which was filtered off and washed with acetone (1 x 5 mL), Et_2O (3 x 5 mL) and dried under vacuum (0.165 mmol, 55% yield). ^{1}H NMR (500 MHz, D_2O): δ (ppm) = 2.47 (s, 3 H), 2.67 (s, 3 H), 7.49 (d, *J*= 7.72 Hz, 1 H), 7.76 (dd, *J*= 4.93, 9.94 Hz, 1 H), 8.04 (d, *J*= 4.24 Hz, 2 H), 8.09 (t, *J*= 7.96 Hz, 1 H), 8.14 (d, *J*= 7.72, 1 H), 8.22 (t, *J*= 7.98 Hz, 1 H), 8.40 (d, *J*= 7.36, Hz 1 H), 8.56 (d, *J*= 8.08 Hz, 1 H), 9.76 (d, *J*= 5.52 Hz, 1 H). ^{13}C NMR (500 MHz, d_4-Methanol): δ= 42.27, 43.37, 124.20, 125.46, 126.27, 126.59, 127.31, 128.23, 138.26, 138.32, 139.94, 151.94, 155.22, 157.80, 157.89, 161.52, 167.27, 174.62, 174.93. UV/Vis [λ_{max}, nm (ε, M^{-1} cm^{-1})]: 256 (14698), 296 (20017), 396 (6083). Dark red single crystals of Na[Ru(bda)(DMSO)(pyC)], Na[**1**-H], suitable for X-ray diffraction studies formed after dissolving **1** in the minimum amount of MeOH at room temperature and left it in the fridge overnight, as a result of deprotonation

of the carboxylic acid in **1** and precipitation with sodium countercation from traces of inorganic salts. Elemental analysis calcd (%) for $C_{20}H_{16}N_3O_7RuS^{-}\cdot Na^{+}\cdot 2H_2O\cdot MeOH$ ($C_{21}H_{24}N_3NaO_{10}RuS$): C 39.75, H 3.81, N 6.62. Found C 39.02, H 3.93, N 6.83. MS (ESI, positive mode, MeOH): m/z^{+} = 589.95 ($M + 2Na^{+}$).

Synthesis of the [Ru(bda)(DMSO)(pyA)] (2). [Ru(bda)(DMSO)(X)] (X = MeOH or DMSO) (200 mg, 0.4 mmol) and pyridine-2-ylmethanol (pyA) (60.6 µl, 0.8 mmol) were dissolved in anhydrous MeOH (20 mL) and heated to reflux for 3 h under Ar. A red solid formed, which was filtered to remove unreacted solid ruthenium precursor. The filtered solution was concentrated by rotary evaporator and diethyl ether added inducing precipitation of compound **2**, which was filtered and washed with additional diethyl ether (0.38 mmol, 95% yield). Single crystals of **2** were obtained by dissolving it in the minimum amount of degassed methanol at room temperature and left in the fridge overnight. ^{1}H NMR (500 MHz, d_4-Methanol): δ (ppm) = 3.09 (s, 6 H), 5.43 (s, 2 H), 7.23 (t, *J*= 6.32 Hz, 1 H), 7.29 (d, *J*= 5.08 Hz, 1 H), 7.67 (d, *J*= 7.84 Hz, 1 H), 7.92 (t, *J*= 3.35 Hz, 1 H), 8.06 (d, *J*= 7.64, 2 H), 8.23 (t, *J*= 7.92 Hz, 2 H), 8.71 (d, *J*= 8.00 Hz, 2 H). ^{13}C NMR (500 MHz, d_4-Methanol): δ= 42.65, 69.56, 120.70, 124.78, 126.83, 137.05, 138.53, 139.06, 147.96, 158.80, 161.92, 172.09 ppm. UV/Vis [λ_{max}, nm (ε, M^{-1} cm^{-1})]: 242 (12018), 296 (26221), 407 (3691). Elemental analysis calcd (%) for $C_{20}H_{19}N_3O_6RuS\cdot 2H_2O$ ($C_{20}H_{23}N_3O_8RuS$): C 42.40, H 4.09, N 7.42. Found C 42.84, H 3.84, N 7.39. MS (ESI, positive mode, MeOH): m/z^{+} = 553.9 ($M + Na^{+}$).

Synthesis of the [Ru(bda)(pic)(pyA)] (4). [Ru(bda)(DMSO)(pyA)] (**2**) (151 mg, 0.27 mmol) and 4-methylpyridine (pic) (0.3 ml, 3 mmol) were dissolved in anhydrous MeOH (20 mL) and heated to reflux overnight under Ar. A dark-red solution appeared which was evaporated to dryness. The residual solid was purified by column chromatography on silica gel using DCM/MeOH (100:17) as eluents. Compound **4** was isolated as a red solid (0.042 mmol, 15% yield). ^{1}H NMR (500 MHz, d_4-Methanol): δ (ppm) = 2.40 (s, 3 H), 4.72 (s, 2 H), 7.21 (d, *J*= 6.10 Hz, 2 H), 7.47 (m,

2 H), 7.83 (d, *J*= 7.60 Hz, 2 H), 8.00 (t, *J*= 3.15 Hz, 1 H), 8.06 (t, *J*= 7.90 Hz, 1 H), 8.16 (d, *J*= 6.60, 2 H), 8.37 (t, *J*= 7.85 Hz, 1 H), 8.60 (d, *J*= 4.02 Hz, 2 H). ^{13}C NMR (500 MHz, MeOD): δ=19.36, 55.96, 123.34, 124.93, 125.86, 127.44, 129.63, 134.81, 136.70, 149.71, 150.30, 151.44, 151.58, 159.10, 171.31, 173.31. UV/Vis [λ_{max}, nm (ε, M^{-1} cm^{-1})]: 255 (15100), 301 (22998), 346 (6430), 419 (5325), 422 (5591). Elemental analysis calcd (%) for $C_{24}H_{20}N_4O_5Ru{\cdot}H_2O{\cdot}MeOH{\cdot}DCM$ ($C_{26}H_{28}Cl_2N_4O_7Ru$): C 45.89, H 4.15, N 8.23. Found C 45.79, H 3.65, N 8.56. MS (ESI, positive mode, MeOH): m/z^+ = 575.9 [M-H^++MeO]. Single crystals of derivative **5** were grown by dissolving **4** in DCM/Methanol and by diffusion of diethyl ether under air. Compound **5** is the result of the oxidation of the benzylic alcohol in compound **4** to give the corresponding methyl ester group, see main text for discussion.

X-ray Crystallography. Data collection: Crystal structure determination for compounds **1** and **Na_2[Ru(bda)$_2$]** were carried out using a Rigaku diffractometer equipped with a Pilatus 200K area detector, a Rigaku MicroMax-007HF microfocus rotating anode with MoK_α radiation, Confocal Max Flux optics and an Oxford Cryosystems low temperature device Cryostream 700 plus (*T* = -173 °C). Full-sphere data collection was used with ω and φ scans. *Programs used:* Data collection and reduction with CrysAlisPro[8] V/.60A and absorption correction with Scale3 Abspack scaling algorithm.[9] Crystal structure determination for compounds **2** and **5** were carried out using a Apex DUO Kappa 4-axis goniometer equipped with an APPEX 2 4K CCD area detector, a Microfocus Source E025 IuS using MoK_α radiation, Quazar MX multilayer Optics as monochromator and an Oxford Cryosystems low temperature device Cryostream 700 plus (*T* = -173 °C). Crystal structure determination for samples Full-sphere data collection was used with ω and φ scans. *Programs used:* Data collection APEX-2[8], data reduction Bruker Saint[9] V/.60A and absorption correction SADABS.[10] **Structure Solution and Refinement**: Crystal structure solution was achieved using the computer program SHELXT[11]. Visualization was performed with the program SHELXle.[12] Missing atoms were

subsequently located from difference Fourier synthesis and added to the atom list. Least-squares refinement on F^2 using all measured intensities was carried out using the program SHELXL 2015.[13] All non-hydrogen atoms were refined including anisotropic displacement parameters. **Comments to the structures: $Na_2[Ru(bda)_2]$:** The asymmetric unit contains one molecule of the metal complex, two sodium cations, 1.65 molecules of water (partially disordered) and 4.60 molecules of methanol (partially disordered). The distance between the two independent sodium cations is of 3.42 Å and they are additionally connected through oxygen bridges coming from the dimethyl sulfoxide groups. **1:** The asymmetric unit contains one molecule of the metal complex, a sodium cation, two water molecules and a methanol molecule. The sodium cation is coordinated to the metal complex through the dimethylsulfoxide group and two carboxylates. Additionally the sodium cation is coordinated to the two water molecules and forms a dimer with another sodium cation. The distance between sodium atoms is of 3.7 Å and they are connected through oxygen bridges coming from the dimethyl sulfoxide groups. The dimer formed by the sodium cations has *C*i symmetry. **2:** The asymmetric unit contains two independent molecules of the metal complex and highly disordered solvent molecules. A diethyl ether molecule with an occupancy of 50 % is disordered around an inversion center shared with the neighboring unit cell and could be refined properly. A second highly disordered solvent molecule, which could contain diethyl ether or ethanol, could not be refined properly. In order to avoid these highly disordered solvent molecule the program SQUEEZE[14] was applied to remove it from the electron density. **5:** The asymmetric unit contains one independent molecule of the metal complex, one methanol molecule and half water molecule disordered in two positions (occupancy 0.3:0.2).

3-Results

3·1-Preparation and characterization of compounds 1-4

The synthesis of complexes with general formula [Ru(bda)(py')(py'')] where py' and py'' are two different monodentate pyridine ligands can be achieved by two consecutive substitution reactions from [Ru(bda)(DMSO)(X)] where X is MeOH or DMSO (Scheme 1).[16,7] The intermediate [Ru(bda)(DMSO)(X)] was obtained as a brown solid with a yield of *ca.* 67 %, along with a side product identified as the bis-substituted bda complex $[Ru(bda)_2]^{2-}$ (*ca.* 5-7 %). The latter compound has never been reported before, it has been fully characterized by NMR spectroscopy, single crystal x-ray diffraction (XRD) and elemental analysis as described in detail in the experimental section and the supporting information.

The reaction of [Ru(bda)(DMSO)(X)] with 2-pyridinecarboxylic acid (HpyC) affords complex **1** in 55 % yield, which has been fully characterized by spectroscopic, analytic and electrochemical techniques. Single crystals suitable for XRD studies were obtained and the ORTEP plot of the anionic complex [Ru(bda)(DMSO)(pyC)], (**1**-H)$^-$, is shown in Figure 2. Compound (**1**-H)$^-$ is a Ru^{II} complex with pseudo-octahedral geometry with Ru-N, Ru-O and Ru-S bond distances similar to those of other Ru complexes of the bda family.[17] Interestingly, the bda^{2-} ligand coordinates in a κ-N^2O^1 fashion while the pyC ligand acts as a bidentate ligand with the carboxylate occupying the fourth equatorial position. As a consequence, the angle O-Ru-O formed by the equatorial ligand is 93.72°, close to the 90° expected for a perfect octahedral geometry. This is in sharp contrast to Ru complexes, where the bda^{2-} coordinates in a κ-N^2O^2 mode resulting in broad O-Ru-O angles in the range of 121° to 124°.[17a, 18, 19] The axial positions in **1** are occupied by DMSO and the pyridine of the pyC ligand. The ^{1}H NMR spectrum of **1** in deuterated water shows a non-symmetric nature of the two pyridine rings of the bda^{2-} ligand, even at high temperature, and indicates that the structure just described in the solid state is maintained in solution (Figure S7 and Figure S12).

The reaction of **1** with 4-picoline (pic) to afford the targeted compound $[Ru(bda)(pic)(pyC)]^-$, **3**, was not possible after several attempts at high temperature, long reaction times and different combination of solvents. The main products observed after reaction were the starting materials, [Ru(bda)(pic)(DMSO)] and $[Ru(bda)(pic)_2]$.

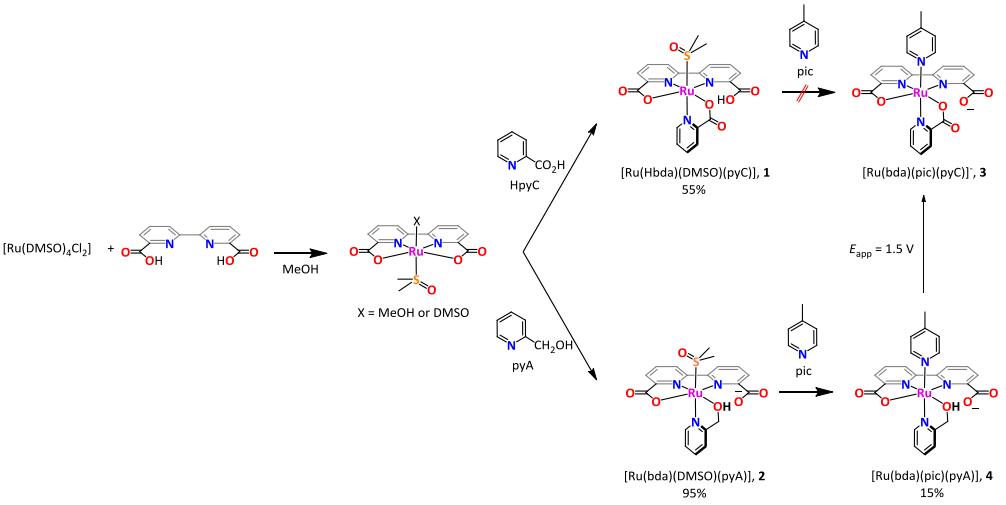

Scheme 1. Synthetic scheme for the preparation of [Ru(Hbda)(DMSO)(pyC)] (**1**), [Ru(bda)(DMSO)(pyA)] (**2**), $[Ru(bda)(pic)(pyC)]^-$ (**3**), and [Ru(bda)(pic)(pyA)] (**4**).

In view of the unsuccessful reaction to prepare **3** using **1** as precursor, an alternative route was designed, based on the intermediate [Ru(bda)(DMSO)(pyA)], **2** in Scheme 1, that contains an hydroxymethyl group in the orto position of the axial pyridine. Compound **2** was prepared in 95 % yield starting from precursor [Ru(bda)(DMSO)(X)] (where X = MeOH or DMSO). The solid state structure of the neutral complex **2** was determined by single crystal XRD and its ORTEP plot is shown in Figure 2. The alcohol in the axial ligand is coordinating the metal center leaving a dangling carboxylate of the bda^{2-} ligand, that binds in a $\kappa\text{-}N^2O^1$ mode. It shows an analogous geometry to that of compound **1** with similar bond distances and angles.

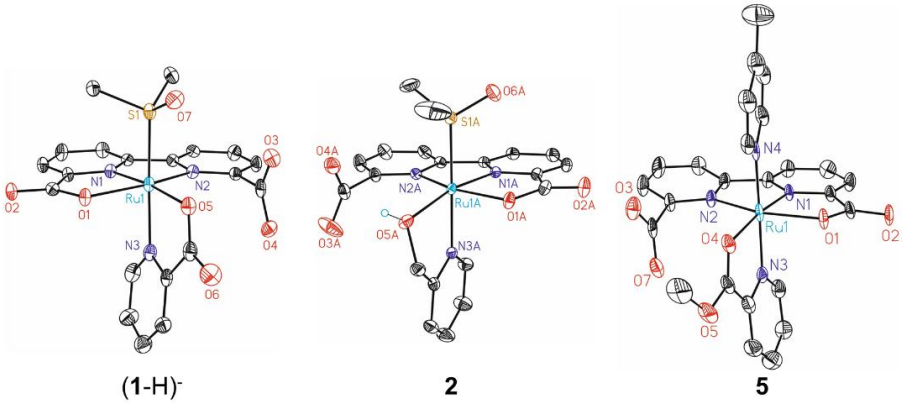

Figure 2. ORTEP plots at 50% probability for (**1**-H)$^{-}$, **2** and **5**. H atoms are omitted for clarity except for the H atom coordinated to oxygen atom in **2**.

On the other hand, NMR characterization of **2** in methanol at room temperature shows only one set of resonances for the two pyridines of the bda^{2-} ligand, indicative of a symmetric geometry as opposed to what we observed in the solid state (Figure 3, blue spectrum). By lowering the temperature to 223 K, the bda^{2-} ligand resonances become broad suggesting a fast equilibrium between species with different connectivity as indicated in the sequence of reactions in the top of Figure 3. These type of equilibria have been observed before for ruthenium complexes containing the bda^{2-} and tda^{2-} equatorial ligands.[3b, 20] In addition, the characteristic benzylic resonance at δ = 5.43 ppm split upon lowering the temperature, supporting the involvement of this group in the fast equilibria (Figures S18 and S19).

These results highlight a crucial difference between **1** and **2**. While the carboxylate group in the axial pyridine of **1** binds very strongly to the ruthenium, the alcohol in **2** is more labile and can coordinate and decoordinate easily at room temperature.

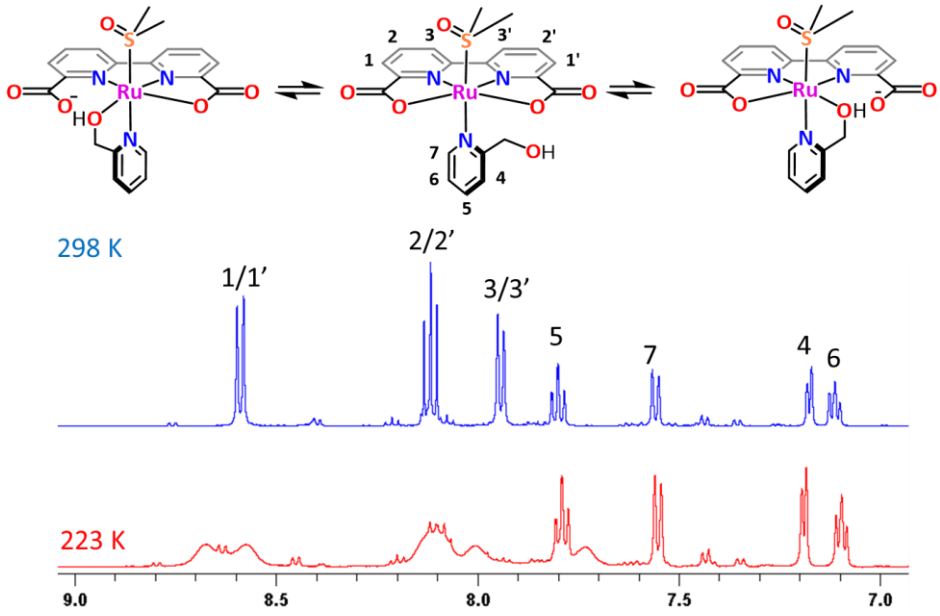

Figure 3. Zoom of the aromatic region of a ^{1}H-NMR of **2** in d_4-Methanol at 223 K (Red) and 298 K (blue).

Compound **2** is also more reactive than **1**, as it was possible to substitute the DMSO axial ligand for a pic ligand to give compound [Ru(bda)(pic)(pyA)], **4**, as indicated in Scheme 1. Compound **4** is fairly air sensitive and gets oxidized to its Ru^{III} derivative leading to further decomposition when exposed to open atmosphere for prolonged times. It was fully characterized by spectroscopic and analytical techniques as described in detail in the experimental section. The ^{1}H NMR spectrum of **4** shows a symmetric bda^{2-} backbone, indicating that in solution this compound is involved in a fast dynamic behavior analogous to that of its parent compound **2** (Figures S20-S25). In an attempt to crystallize compound **4**, we obtained the derivative product **5** in Figure 2 which is the result of the oxidation of the benzylic alcohol to a methyl ester group. Indeed, benzylic groups are prone to oxidation, which could be a consequence of the nucleophilic attack of a methanol solvent molecule used in the crystallization mixture, to the electrophilic carbon of the coordinated alcohol group. Alternatively, the close proximity of the methylene group in **4** to a putative high

valent and strongly oxidizing Ru-OH or Ru=O group could also be responsible of the oxidation to a carboxylic acid that esterifies in the presence of methanol .[21] The formation of the Ru-OH or Ru=O reactive species implies i) oxidation of the initial Ru^{II} by air and ii) the coordination of an aquo ligand coming from moisture in the crystallization solvent.

3·2-Electrochemistry of 1 and 2

The electrochemical properties of complexes **1** and **2** were investigated in aqueous solution at pH 1 and pH 7 by means of cyclic voltammetry (CV) and differential pulse voltammetry (DPV). In this manuscript all potentials are reported vs the normal hydrogen electrode (NHE).

The cyclic voltammetry of compound **1** at pH 1 is shown in Figure 4. In the anodic scan, it shows a reversible wave at $E_{1/2}$ = 1.12 V with a very low peak to peak separation (ΔE < 59 mV) suggesting a two electron process is taking place at this potential (E^1 and E^2 in Scheme 2, where $E^2 < E^1$). In the reverse cathodic scan, a new wave appears at $E^3_{1/2}$ = 0.54 V (ΔE = 59 mV), that we attribute to a putative Ru-OH_2/Ru-OH complex, that is formed upon substitution of one of the carboxylate groups by a water solvent molecule at high oxidation states (Scheme 2, bottom). This substitution is common in Ru-bda type of complexes.[20]

Three weak additional redox processes at $E \approx 0.26$ V, $E \approx 0.98$ V and $E \approx 1.40$ V also appear after the first scan (see also Figure S26). We attribute them to side-products derived from DMSO ligand oxidation or to isomers of complex **1** that differ in the coordination modes of the bda^{2-}, pyC or DMSO ligands. The intensities of these waves are higher at pH 7 (Figures S26 and S27). At this pH, the redox wave at $E^1_{1/2}$ = 1.12 V is not fully reversible, consistent with the presence of higher amount of side-products. In addition, a redox wave appears at $E_{1/2}$ = 0.30 V (ΔE = 80mV) at pH 7 after sweeping the cycle to the second wave, that we attribute to the pH dependent wave associated with the Ru-OH_2/Ru-OH complex in the bottom of Scheme 2.

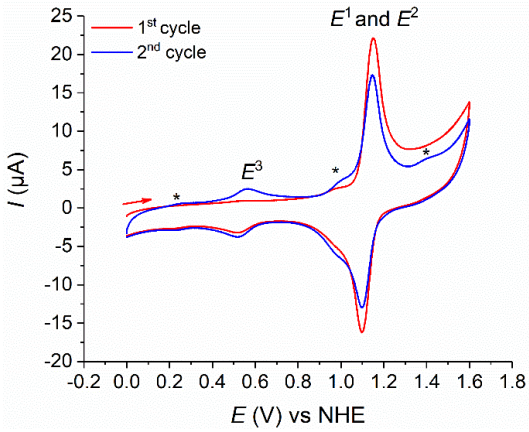

Figure 4. Two consecutive CV cycles of **1** at pH 1 (TA = 0.1 M), v = 100 mV/s. [Ru]: 1mM, WE: glassy carbon electrode; CE: platinum electrode; RE: Hg/Hg_2SO_4. Asterisks (*) show unidentified redox waves.

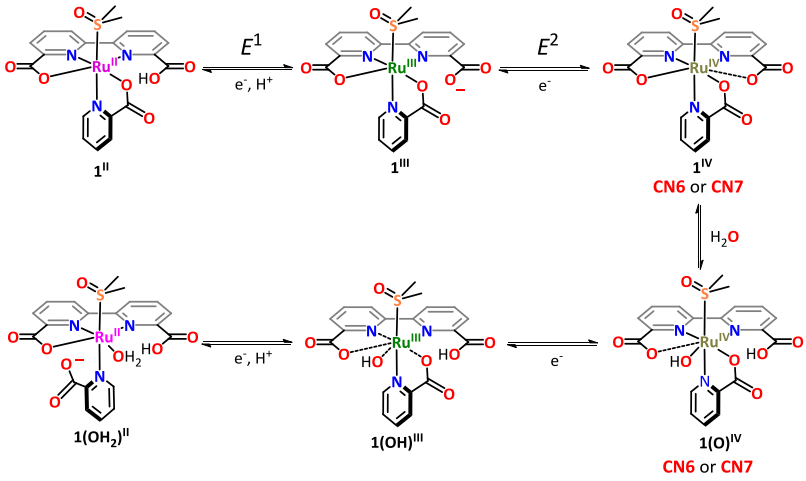

Scheme 2. Reactions involved in the redox chemistry of **1**.

Despite the similarities in the coordination environment of complexes **1** and **2** in the solid state structures depicted in Figure 2, the cyclic voltammetry of **2** shows a very different redox profile when compared to that of **1**. In the first anodic scan of a cyclic voltammetry at pH 1 compound **2** shows two redox processes at $E^4_{1/2}$ = 0.83 V ($\Delta E \approx 127$ mV) and $E^5_{1/2}$ = 1.06 V ($\Delta E \approx 262$ mV) associated with the $Ru^{III/II}$ and $Ru^{IV/III}$ couples respectively (red trace in Figure 5). The first wave is pH dependent and

appears at $E^4_{1/2}$ = 0.51 V (ΔE = 95 mV) at pH 7 (blue trace in Figure 5). The Nernstian behavior of the first wave E^4 is a clear indication that a proton coupled electron transfer (PCET) process is taking place.[22] As shown in Scheme 3, this PCET is attributed to the $Ru^{III/II}$ couple with concomitant proton loss from the coordinated alcohol.

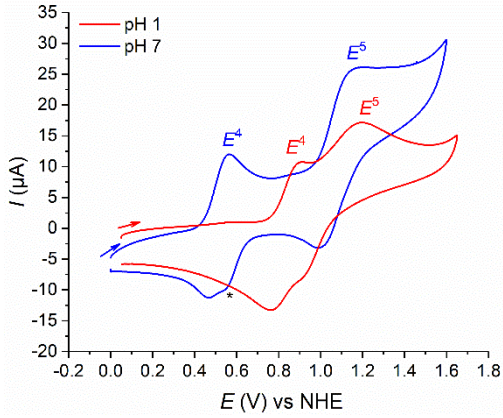

Figure 5. CV of **2** at pH 1 (blue) and pH 7 (red). Conditions: pH 1 (TA= 0.1 M), pH 7 (phosphate buffer aqueous solution), v = 100 mV/s. [Cat]: 1mM, WE: glassy carbon electrode; CE: platinum electrode; RE: Hg/Hg_2SO_4. Arrows show the scan direction. Asterisk (*) shows unidentified redox wave that appears only after scanning the second oxidation wave.

The $Ru^{IV/III}$ oxidation wave of **2** is pH independent and appears at $E^5_{1/2}$ = 1.06 V (ΔE = 141 mV) at pH 7. In the cathodic scan of the cyclic voltammetry of **2** at pH 7 solution, a new redox wave appears at $E \approx 0.55$ V only when the anodic scan is swept beyond the second oxidation at pH 7 while the first wave at $E^4_{1/2}$ = 0.51 V decreases in intensity (see also Figures S28 and S29). This phenomenon also occurs at pH 1 and is progressive upon cycling (Figure S30). These results suggest that **2** converts to a new species that we attribute to DMSO ligand oxidation, to the oxidation of the pyA ligand to give the corresponding carboxylic acid pyC ligand or both. Indeed, the new oxidation potential appearing upon scanning appears in a very similar potential to that observed for compound **1**.

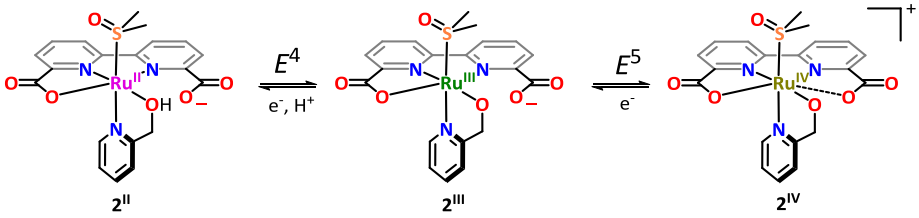

Scheme 3. Reactions involved in the redox chemistry of **2**.

3·3-Electrochemistry of 4 and its transformation to a water oxidation catalyst

The electrochemical properties of complex **4** were investigated in aqueous solution at pH 7 by means of CV, DPV and bulk electrolysis experiments.

The first CV scan of a solution of **4** at pH 7 shows a complex behaviour with five waves appearing at $E^6_{1/2}$ = 0.64 V (ΔE ≈ 66 mV), $E^7_{1/2}$ = 0.86 V (ΔE ≈ 89 mV), $E^8_{1/2}$ = 1.0 V (ΔE ≈ 74 mV), $E^9_{p,a}$ = 1.33 V and $E^{10}_{p,a}$ = 1.42 V (Figure 6, left). Upon cycling in the potential range from 0.1 V to 1.6 V, the CV profile simplifies leaving only the reversible waves E^6 and E^8 (Figure 6, right and Figure S31).

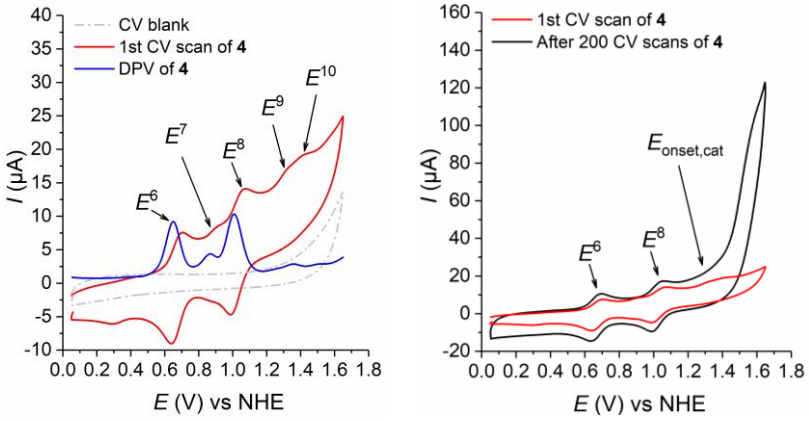

Figure 6. Left) First CV scan of **4** in a phosphate buffer aqueous solution at pH 7. Right) Comparison of CV of **4** before (red) and after 200 cycles (black). [Ru]: 1mM, v = 100 mV/s, WE: glassy carbon electrode; CE: platinum electrode; RE: Hg/Hg_2SO_4.

In addition, the appearance of a very intense, irreversible wave at E_{onset} ≈ 1.3 V appears upon cycling, that we tentatively attribute to water oxidation catalysis. Indeed, a bulk electrolysis experiment of a solution of **4**, shows a steady current vs time profile upon applying a potential of E_{app}= 1.5 V, indicative of a catalytic process (Figure 7 and Figure S34). Importantly, the two reversible waves at E^6 and E^8 are fully recovered after the catalytic wave, a proof of the integrity of the complex upon turnover. These two waves are pH independent and are consistent with two successive one-electron oxidations from Ru^{II} to Ru^{IV} of a complex that do not contain a Ru-OH_2 group (Figure S32). Thus, the aquo ligand must coordinate at the Ru^{IV} or Ru^{V} oxidation states to form a Ru-oxo/hydroxo species responsible of triggering the catalysis. A foot of the wave analysis (FOWA) of a cyclic voltammetry containing the catalytic species gives a maximum turnover frequency (TOF_{max}) of 3.1 s^{-1} (Figure S33).

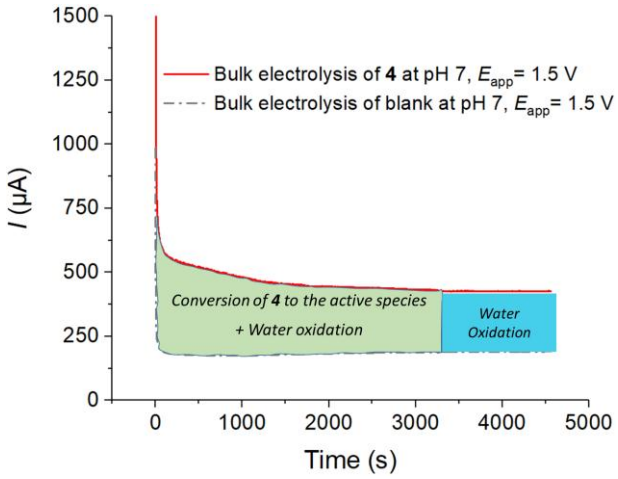

Figure 7. Bulk electrolysis of **4** in a phosphate buffer solution at pH 7 solution at E_{app}= 1.5 V. During the first 55 minutes, complex **4** converts to an active complex (green area). From this time, the current passed is attributed to the water oxidation catalysis process by the active species, giving a TON = 2990, based on the active catalyst on the surface, see supporting information.[22]

4-Discussion

The first attempt towards the synthesis of the target compound [Ru(bda)(pic)(pyC)], **3**, from the intermediate [Ru(Hbda)(DMSO)(pyC)], **1**, by substitution of the DMSO ligand by pic was unsuccessful due to the low reactivity of **1**. Thus, an alternative route based on the intermediate [Ru(bda)(pic)(pyA)], **4**, successfully prepared from [Ru(bda)(DMSO)(pyA)], **2**, was pursued. The distinct reactivity towards DMSO substitution of related compounds **1** and **2** can be understood from their respective unique structural and electronic features. While the carboxylate group of the axial pyC ligand is strongly bound to the ruthenium, the alcohol group in the pyA ligand is labile and is involved in a dynamic behaviour in solution. This is demonstrated by low temperature ^{1}H NMR experiments that show a non-symmetric nature of the bda^{2-} ligand while analogous experiments done at room temperature show a perfectly symmetric compound, a result of an averaged of all the species involved in the equilibrium (Figure 3). In addition, the electrochemical behaviour of **1** and **2** are radically different. Compound **2** shows two consecutive one-electron oxidation, as expected for this type of complexes. In sharp contrast, complex **1** undergoes a single two-electron oxidation event, likely a consequence of the favored seven coordination (CN7) environment around the metal center upon oxidation (Scheme 2).[1, 23]

The benzylic alcohol in **4** is susceptible to oxidation, and upon exposure to the air in a methanolic solution it produces the ester derivative **5** in Figure 2. This is the first indication of the feasibility of preparing the desired complex **3** by oxidation of the alcohol precursor **4** in the absence of an esterification agent. Indeed, the methylene group in the ortho-position of the pyridine ligand pyA is situated in a very close proximity to the ruthenium centre, which can catalyse the reaction. This oxidation can be accelerated electrochemically, by cycling towards oxidative potentials to produce a high valent ruthenium complex, which can coordinate a solvent water molecule generating compound $\mathbf{4^{IV}(O)}$ in Scheme 4. This Ru^{IV}=O species is very

reactive and can undergo the oxidation of the alcohol to carboxylic acid through an oxygen transfer reaction that would produce the target compound **3**.[20]

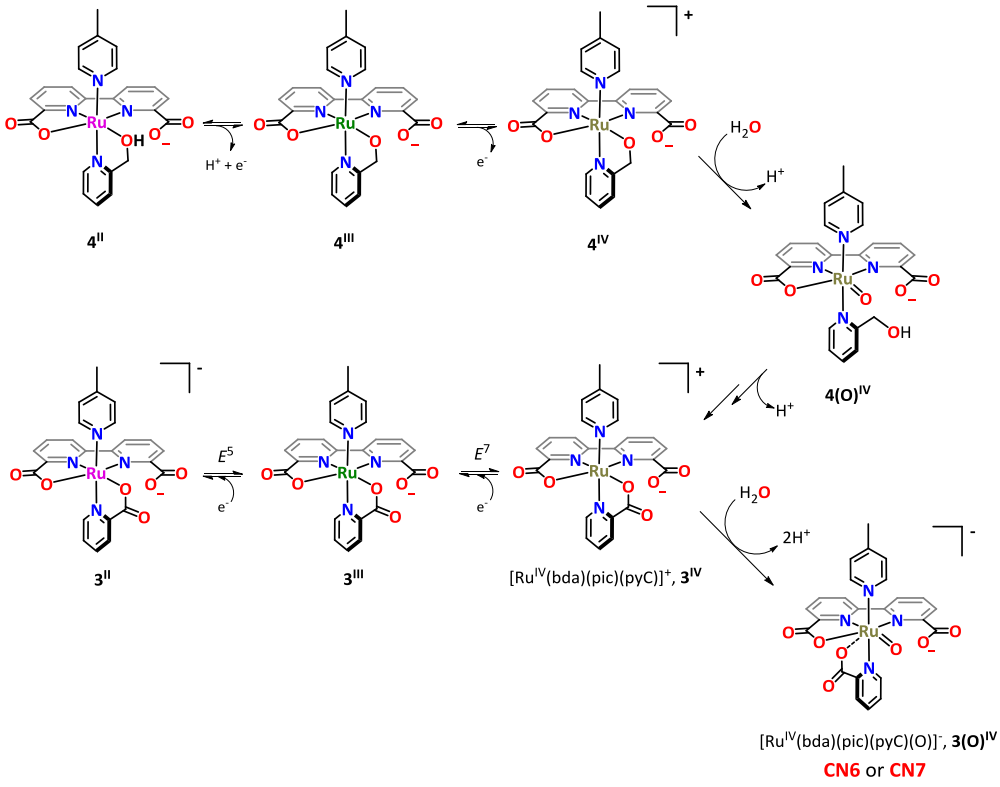

Scheme 4. Putative mechanism to form the active water oxidation catalyst, **3**, after bulk electrolysis of **4** in a phosphate buffer solution at pH 7 and at E_{app}= 1.5 V.

This hypothesis is supported by the electrochemical behaviour of **4** in water, summarized in Figure 6. While the first scan of a cyclic voltammetry experiment shows a complex profile with five redox waves, indicative of a mixture of species present in solution, it progressively evolves towards a much simpler profile. As shown in the black trace of Figure 6 (right), only two consecutive pH independent one-electron oxidation waves are observed, attributed to the $Ru^{III/II}$ and $Ru^{IV/III}$ redox couples, followed by a catalytic process with E_{onset} = 1.3 V. This behaviour is fully consistent with complex **3**, which at low oxidation state, does not coordinate any

aqua ligand due to the strong binding of the carboxylate of the axial pyC ligand leading to two pH independent redox events (Scheme 4, bottom, and Table 1). However, at high oxidation states, the possibility to reach CN7 facilitates the coordination of a water molecule producing the Ru-oxo species **3(O)^{IV}**. This species is further oxidized to **3(O)^{V}**, which will be directly involved in the O-O formation step toward the production of oxygen.

Foot of the wave analysis of the cyclic voltammetry of a solution containing electrogenerated **3** accounts for a TOF_{max}= 3.1 s^{-1} assuming a water nucleophilic attack mechanism. This value is comparable to that of the widely used [Ru(bda)(pic)$_2$] complex with TOF_{max}= 11 s^{-1} based on a mechanism involving the interaction of two M=O groups (Table 1).[3a,24] Complexes **3** and [Ru(bda)(pic)$_2$] have a similar coordination sphere with four pyridine type of ligands and two carboxylate groups. However, they have a significantly different geometry; while compound [Ru(bda)(pic)$_2$] shows a highly distorted octahedral geometry due to the wide O-Ru-O angle around 124° provided by the bda^{2-} ligand, complex **3** is expected to be close to the ideal octahedral coordination with a O-Ru-O around 90°, as suggested by the XRD structures of (**1**-H)$^-$ and **5** in Figure 2. This is a consequence of the chelate effect of the axial pyC ligand, that strongly binds to the ruthenium leaving a carboxylate of the bda^{2-} ligand dangling. This key feature can determine the final geometry of the reactive **3(O)^{V}**, which can be either six or seven coordinated, influencing the overpotential of the reaction.[25]

Another key feature of **3** that differs from compound [Ru(bda)(pic)$_2$] is the presence of a dangling carboxylate group if the active **3(O)^{V}** is CN7 or even two dangling carboxylate groups if it has CN6 (Scheme 4). Interestingly, this is not enough to outperform the high catalytic activity of the fastest molecular water oxidation catalyst reported to date [Ru(tda)(py)$_2$] with TOF_{max} = 7700 s^{-1} (Table 1).[3b] The latter is characterized by a unique mechanism based on a water nucleophilic attack

assisted by the well positioned dangling carboxylate group of the equatorial ligand (Table 1).

Table 1. Electrochemical and water oxidation data at pH 7 for complex **3** and structurally related compounds $[Ru(bda)(pic)_2]$ and $[Ru(tda)(py)_2]$ reported in the literature.

Ru complex	$E_{1/2}$ in volts vs NHE at pH 7			TOF_{max} [a] (s^{-1})	*Ref.*
	$Ru^{III/II}$	$Ru^{IV/III}$	$E_{cat,onset}$		
$[Ru^{III}(\kappa\text{-}N^2O^1\text{-bda})(pic)(\kappa\text{-}N^1O^1\text{-pyC})]$, **3**	0.65[b]	1.01[b]	1.3[c]	3.1	This work
$[Ru^{II}(\kappa\text{-}N^2O^2\text{-bda})(pic)_2]$	0.55	0.82	1.1	11	3a, 26
$[Ru^{II}(\kappa\text{-}N^3O^1\text{-tda})(py)_2]$	0.55[b]	1.10[b]	1.3[c]	7700	3b, 26

[a] Calculated using the FOWA method[26] and assuming a mechanism based on the interaction between two M=O groups (I2M) for $[Ru^{II}(\kappa\text{-}N^2O^2\text{-bda})(pic)_2]$ and a water nucleophilic attack mechanism (WNA) for **3** and $[Ru^{II}(\kappa\text{-}N^3O^1\text{-tda})(py)_2]$. [b] Data for the complex with no hydroxo/oxo coordinated to the ruthenium. [c] Data for the ruthenium oxo species that forms only at high oxidation states.

V

5-Conclusions

An intramolecular oxidation of the benzylic alcohol of complex [Ru(bda)(pic)(pyA)], **4**, allowed us to prepare the corresponding carboxylic acid complex [Ru(bda)(pic)(pyC)], **3**, *in situ* by electrochemical techniques. Compound **3** is a precursor of a water oxidation catalyst that has similar coordination sphere to those of well-known $[Ru(bda)(pic)_2]$ and $[Ru(tda)(py)_2]$ complexes, which are very active catalysts.

While the catalytic results obtained for **3** are amongst the best reported to date, with TOF_{max} = 3.1 s^{-1} at an onset potential of 1.3 V, it does not overcome the results obtained for $[Ru(bda)(pic)_2]$ and $[Ru(tda)(py)_2]$ under the same experimental conditions (TOF_{max} = 11 s^{-1} at 1.1 V and TOF_{max} = 7700 s^{-1} at 1.3 V, respectively). We attribute the lower performance of **3** to the different geometrical requirements of

the equatorial and axial ligands. In particular, to the stabilization effect of the pyridine-2-carboxylate ligand (pyC) in **3** that binds in a bidentate fashion and leaves a dangling carboxylate from the bda^{2-} axial ligand. As a consequence, **3** adopts a coordination sphere that is close to a perfect octahedral geometry with angles around 90°, as observed for the related compounds [Ru(bda)(DMSO)(pyC)], (**1**-H)$^{-}$, and **5** in Figure 2, that were studied in the solid state. In sharp contrast, the axial ligands in $[Ru(bda)(pic)_2]$ and $[Ru(tda)(py)_2]$ are monodentate, thus the equatorial ligands bda^{2-} and tda^{2-} act as tetradentate ligands, forcing a distorted octahedral geometry with O-Ru-O and N_{eq}-Ru-O angles of 124° and 141° at oxidation state Ru^{II}, respectively. In addition, the tda^{2-} ligand can act as a pentadentate ligand at Ru^{IV} forming a CN7 complex. These characteristics together with additional second coordination sphere effects, provide the optimum electronic and geometric features to undergo fast water oxidation catalysis.

This work highlights the importance of geometry around the ruthenium metal center in complexes that are active for the water oxidation catalysis. It also provides evidence of the reactivity of Ru towards intramolecular oxidation of neighboring benzylic groups.

V

References

1. (a) Matheu, R.; Ertem, M. Z.; Gimbert-Suriñach, C.; Sala, X.; Llobet, A., Seven Coordinated Molecular Ruthenium–Water Oxidation Catalysts: A Coordination Chemistry Journey. *Chemical Reviews* **2019,** *119* (6), 3453-3471; (b) Matheu, R.; Garrido-Barros, P.; Gil-Sepulcre, M.; Ertem, M. Z.; Sala, X.; Gimbert-Suriñach, C.; Llobet, A., The development of molecular water oxidation catalysts. *Nature Reviews Chemistry* **2019,** *3* (5), 331-341; (c) Tong, L.; Thummel, R. P., Mononuclear ruthenium polypyridine complexes that catalyze water oxidation. *Chemical Science* **2016,** *7* (11), 6591-6603.

2. (a) Creus, J.; Matheu, R.; Peñafiel, I.; Moonshiram, D.; Blondeau, P.; Benet-Buchholz, J.; García-Antón, J.; Sala, X.; Godard, C.; Llobet, A., A Million Turnover Molecular Anode for Catalytic Water Oxidation. *Angewandte Chemie International Edition* **2016,** *55* (49), 15382-15386; (b) Richmond, C. J.; Matheu, R.; Poater, A.; Falivene, L.; Benet-Buchholz, J.; Sala, X.; Cavallo, L.; Llobet, A., Supramolecular Water Oxidation with Ru–bda-Based Catalysts. *Chemistry – A European Journal* **2014,** *20* (52), 17282-17286.

3. (a) Duan, L.; Bozoglian, F.; Mandal, S.; Stewart, B.; Privalov, T.; Llobet, A.; Sun, L., A molecular ruthenium catalyst with water-oxidation activity comparable to that of photosystem II. *Nature chemistry* **2012,** *4* (5), 418-423; (b) Matheu, R.; Ertem, M. Z.; Benet-Buchholz, J.; Coronado, E.; Batista,

V. S.; Sala, X.; Llobet, A., Intramolecular proton transfer boosts water oxidation catalyzed by a Ru complex. *Journal of the American Chemical Society* **2015,** *137* (33), 10786-10795.

4. (a) Matheu, R.; Moreno-Hernandez, I. A.; Sala, X.; Gray, H. B.; Brunschwig, B. S.; Llobet, A.; Lewis, N. S., Photoelectrochemical Behavior of a Molecular Ru-Based Water-Oxidation Catalyst Bound to TiO2-Protected Si Photoanodes. *Journal of the American Chemical Society* **2017,** *139* (33), 11345-11348; (b) Grau, S.; Berardi, S.; Moya, A.; Matheu, R.; Cristino, V.; Vilatela, J. J.; Bignozzi, C. A.; Caramori, S.; Gimbert-Suriñach, C.; Llobet, A., A hybrid molecular photoanode for efficient light-induced water oxidation. *Sustainable Energy & Fuels* **2018,** *2* (9), 1979-1985.

5. Matheu, R.; Francàs, L.; Chernev, P.; Ertem, M. Z.; Batista, V.; Haumann, M.; Sala, X.; Llobet, A., Behavior of the Ru-bda water oxidation catalyst covalently anchored on glassy carbon electrodes. *ACS Catalysis* **2015,** *5* (6), 3422-3429.

6. Evans, I. P.; Spencer, A.; Wilkinson, G., Dichlorotetrakis(dimethyl sulphoxide)ruthenium(II) and its use as a source material for some new ruthenium(II) complexes. *Journal of the Chemical Society, Dalton Transactions* **1973,** (2), 204-209.

7. (a) Wang, L.; Mirmohades, M.; Brown, A.; Duan, L.; Li, F.; Daniel, Q.; Lomoth, R.; Sun, L.; Hammarström, L., Sensitizer-catalyst assemblies for water oxidation. *Inorganic chemistry* **2015,** *54* (6), 2742-2751; (b) The exact composition of this intermediate in the solid state is not fully elucidated through elemental analysis. It is only soluble in DMSO solvent giving pure [Ru(bda)$(DMSO)_2$] that is the result of the substitution of X by DMSO.

8. Data collection with APEX II version v2013.4-1. Bruker (**2007**). Bruker AXS Inc., Madison, Wisconsin, USA.

9. Data reduction with Bruker SAINT version V8.30c. Bruker (**2007**). Bruker AXS Inc., Madison, Wisconsin, USA.

10. SADABS: V2012/1 Bruker (**2001**). Bruker AXS Inc., Madison, Wisconsin, USA. Blessing,. *Acta Crystallographica* **1995,** *A51*, 33-38.

11. SHELXT; V2014/4 (Sheldrick **2014**). Sheldrick, G. M., *Acta Crystallographica* **2015,** *A71*, 3-8.

12. SHELXle; C.B. Huebschle, G. M. S., B. Dittrich, SHELXle;. *Journal of Applied Crystallography* **2011,** *44*, 1281-1284.

13. SHELXL; SHELXL-2014/7 (Sheldrick **2014**). Sheldrick, G. M., *Acta Crystallographica* **2015,** *C71*, 3-8.

14. (a) Spek, A. L., SQUEEZE implemented in Platon. Platon:. *Journal of Applied Crystallography* **2003,** *36*, 7-13; (b) A.L., S., SQUEEZE: . *Acta Crystallographica* **2015,** *C71*, 9-18.

15. Wang, L.; Mirmohades, M.; Brown, A.; Duan, L.; Li, F.; Daniel, Q.; Lomoth, R.; Sun, L.; Hammarström, L., Sensitizer-Catalyst Assemblies for Water Oxidation. *Inorganic chemistry* **2015,** *54* (6), 2742-2751.

16. (a) Duan, L.; Fischer, A.; Xu, Y.; Sun, L., Isolated Seven-Coordinate Ru(IV) Dimer Complex with [HOHOH]− Bridging Ligand as an Intermediate for Catalytic Water Oxidation. *Journal of the American Chemical Society* **2009,** *131* (30), 10397-10399; (b) Wang, L.; Duan, L.; Stewart, B.; Pu, M.; Liu, J.; Privalov, T.; Sun, L., Toward Controlling Water Oxidation Catalysis: Tunable Activity of Ruthenium Complexes with Axial Imidazole/DMSO Ligands. *Journal of the American Chemical Society* **2012,** *134* (45), 18868-18880.

17. (a) Tong, L.; Duan, L.; Xu, Y.; Privalov, T.; Sun, L., Structural modifications of mononuclear ruthenium complexes: a combined experimental and theoretical study on the kinetics of ruthenium-catalyzed water oxidation. *Angewandte Chemie International Edition* **2011,** *50* (2), 445-449; (b) Duan, L.; Wang, L.; Inge, A. K.; Fischer, A.; Zou, X.; Sun, L., Insights into Ru-based molecular water oxidation catalysts: Electronic and noncovalent-interaction effects on their catalytic activities. *Inorganic chemistry* **2013,** *52* (14), 7844-7852.

18. Matheu, R.; Ghaderian, A.; Francàs, L.; Chernev, P.; Ertem, M. Z.; Benet-Buchholz, J.; Batista, V. S.; Haumann, M.; Gimbert-Suriñach, C.; Sala, X.; Llobet, A., Behavior of Ru–bda Water-Oxidation Catalysts in Low Oxidation States. *Chemistry – A European Journal* **2018,** *24* (49), 12838-12847.

19. Garrido-Barros, P. F., I.; Farràs, P.; Gimbert-Suriñach, C.; Maseras, F.; Llobet, A, Water as an oxygen source for oxidation reactions from "Catalytic oxidation in organic synthesis". *Edited by Muñiz, K. Thieme Chemistry - Stuttgart* **2017**, 63-77.
20. Weinberg, D. R.; Gagliardi, C. J.; Hull, J. F.; Murphy, C. F.; Kent, C. A.; Westlake, B. C.; Paul, A.; Ess, D. H.; McCafferty, D. G.; Meyer, T. J., Proton-coupled electron transfer. *Chemical Reviews* **2012,** *112* (7), 4016-4093.
21. (a) Costentin, C.; Drouet, S.; Robert, M.; Savéant, J.-M., Turnover numbers, turnover frequencies, and overpotential in molecular catalysis of electrochemical reactions. Cyclic voltammetry and preparative-scale electrolysis. *Journal of the American Chemical Society* **2012,** *134* (27), 11235-11242; (b) Zhang, T.; Wang, C.; Liu, S.; Wang, J.-L.; Lin, W., A biomimetic copper water oxidation catalyst with low overpotential. *Journal of the American Chemical Society* **2013,** *136* (1), 273-281.
22. Hoque, M. A.; Benet-Buchholz, J.; Llobet, A.; Gimbert-Suriñach, C., Catalytic Oxidation of Water to Dioxygen by Mononuclear Ru Complexes Bearing a 2,6-Pyridinedicarboxylato Ligand. *ChemSusChem* **2019,** *12* (9), 1949-1957.
23. Matheu, R.; Ertem, M. Z.; Gimbert-Suriñach, C.; Benet-Buchholz, J.; Sala, X.; Llobet, A., Hydrogen Bonding Rescues Overpotential in Seven-Coordinated Ru Water Oxidation Catalysts. *ACS Catalysis* **2017,** *7* (10), 6525-6532.
24. Matheu, R.; Neudeck, S.; Meyer, F.; Sala, X.; Llobet, A., Foot of the Wave Analysis for Mechanistic Elucidation and Benchmarking Applications in Molecular Water Oxidation Catalysis. *ChemSusChem* **2016,** *9* (23), 3361-3369.

Supporting information

Preparation of [Ru(bda)(DMSO)(X)] and characterization of side-product $Na_2[Ru(bda)_2]$

Synthesis of [Ru(bda)(DMSO)(X)] and $Na_2[Ru(bda)_2]$. The [Ru(bda)(DMSO)(X)] where X = MeOH or DMSO was prepared according to a reported method from the ruthenium precursor $[Ru(DMSO)_4Cl_2]$ and H_2bda in the presence of triethylamine.[1] The product was obtained as a brown solid after filtration (325 mg, aprox. 67% yield). ^{1}H NMR (500 MHz, DMSO-*d6*): δ= 6.99 (d, *J*= 2.96 Hz, 2 H), 7.77 (t, *J*= 7.82 Hz, 2 H), 8.06 (t, *J*= 7.86 Hz, 2 H), 8.14 (d, *J*= 2.84 Hz, 2 H), 8.38 (d, *J*= 3.12 Hz, 2 H), 8.67 ppm (d, *J*= 2.97, 2 H). The filtered solution was purified by column chromatography on silica gel using DCM : Methanol (2:8) as eluent, the red fraction was evaporated to dryness to give a bright red solid identified as **$Na_2[Ru(bda)_2]$** (10 mg, 7% yield). Single crystals were grown by dissolving the resulting solid in methanol and diffusing diethyl ether. ^{1}H NMR (500 MHz, d_4-Methanol): δ= 6.99 (d, *J*= 2.96 Hz, 2 H), 7.77 (t, *J*= 7.82 Hz, 2 H), 8.06 (t, *J*= 7.86 Hz, 2 H), 8.14 (d, *J*= 2.84 Hz, 2 H), 8.38 (d, *J*= 3.12 Hz, 2 H), 8.67 ppm (d, *J*= 2.97, 2 H). ^{13}C NMR (500 MHz, d_4-Methanol): δ= 119.95, 121.58, 123.24, 123.87, 132.24, 135.35, 153.15, 157.97, 160.05, 165.97, 168.63, 174.98. UV/Vis [λ_{max}, nm (ε, M^{-1} cm^{-1})]: 253 (16791), 303 (38259), 359 (4484), 486 (9700). Elemental analysis calcd (%) for $C_{24}H_{12}N_4O_8Ru{\cdot}4H_2O{\cdot}CH_2Cl_2$ ($C_{25}H_{22}Cl_2N_4O_{12}Ru$): C 40.44, H 2.99, N 7.55. Found C 40.27, H 2.21, N 7.52. MS (ESI, negative mode, methanol): m/z^- = 586.95 ($M + H^+$).

a) b)

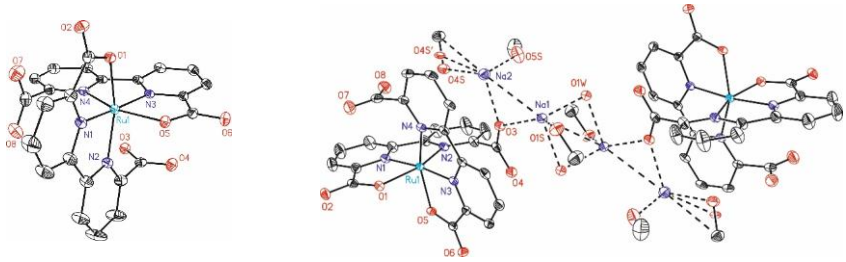

Figure S1. ORTEP plots at 50% probability for the anionic **$[Ru(bda)_2]^{2-}$** structure (a) and dimeric structure derived from **$Na_2[Ru(bda)_2]$** (b).[2]

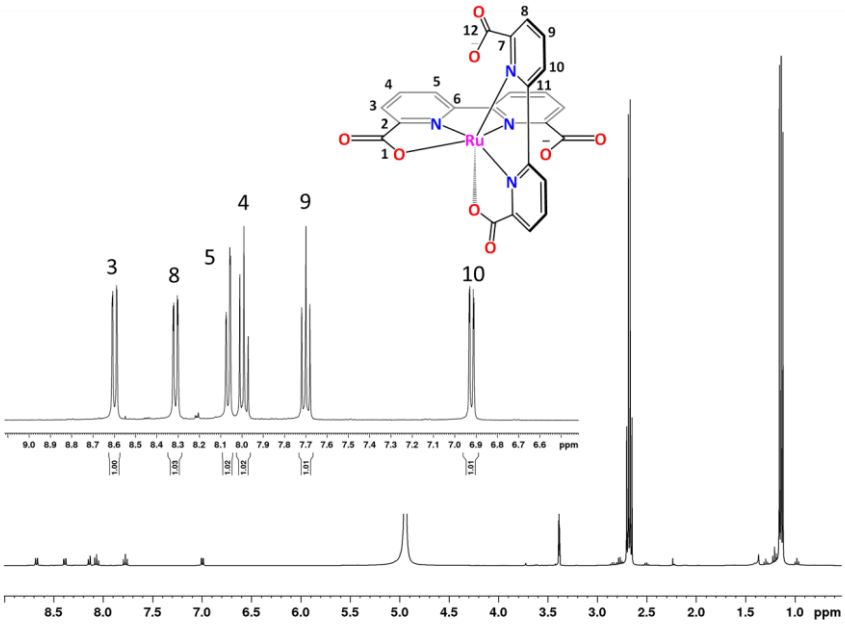

Figure S2. ^{1}H NMR spectrum of **$Na_2[Ru(bda)_2]$** in d_4-Methanol with 5 µl Et_3N at T= 298K. Inset: the magnification of the aromatic region.

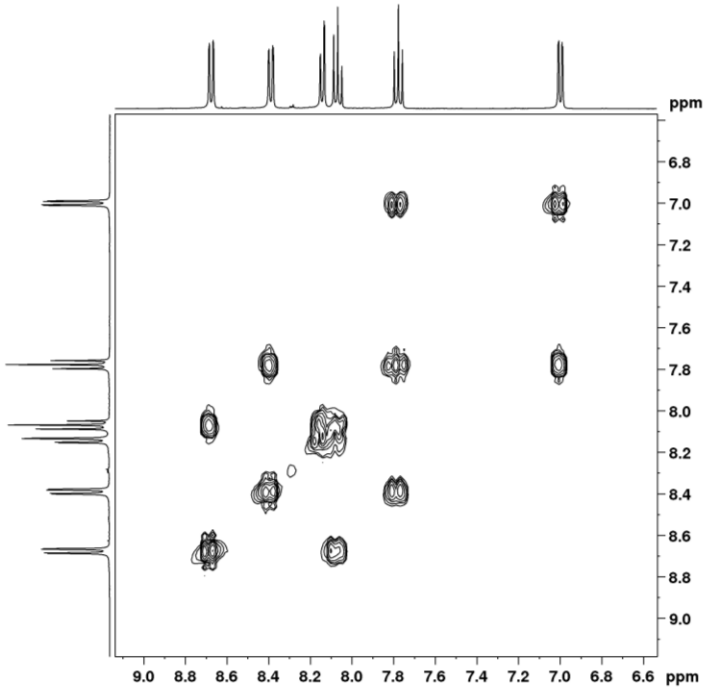

V

Figure S3. ^{1}H-^{1}H COSY of **$Na_2[Ru(bda)_2]$** in d_4-Methanol with 5 µl Et_3N at T= 298K.

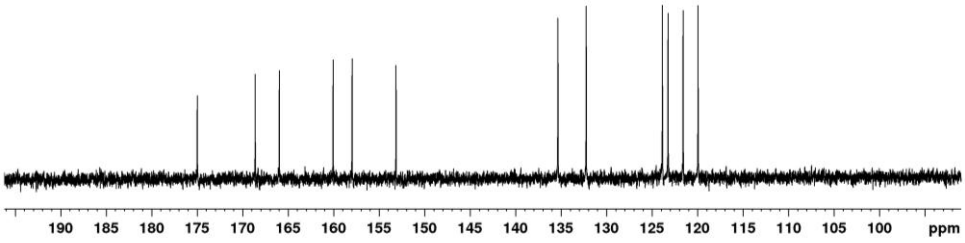

Figure S4. ^{13}C NMR of **$Na_2[Ru(bda)_2]$** in d_4-Methanol with 5 µl Et_3N at T= 298K.

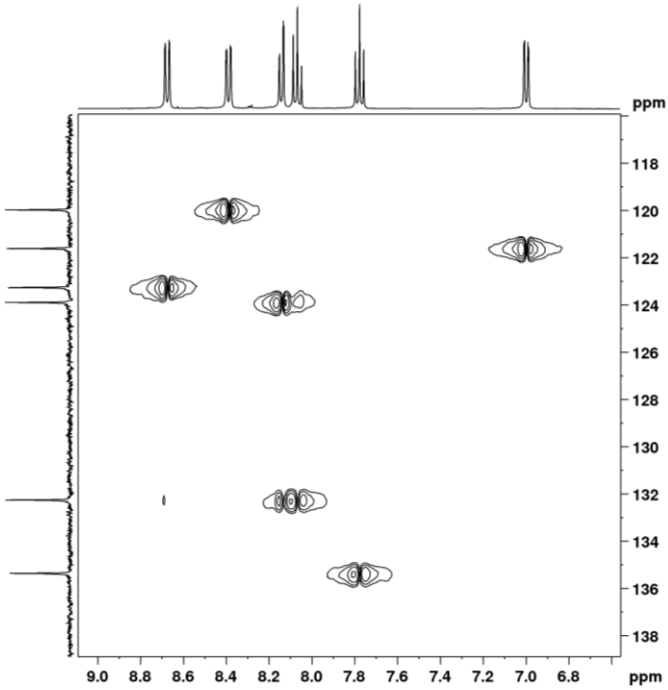

V

Figure S5. ^{1}H-^{13}C HSQC NMR of **$Na_2[Ru(bda)_2]$** in d_4-Methanol with 5 µl Et_3N at T= 298K.

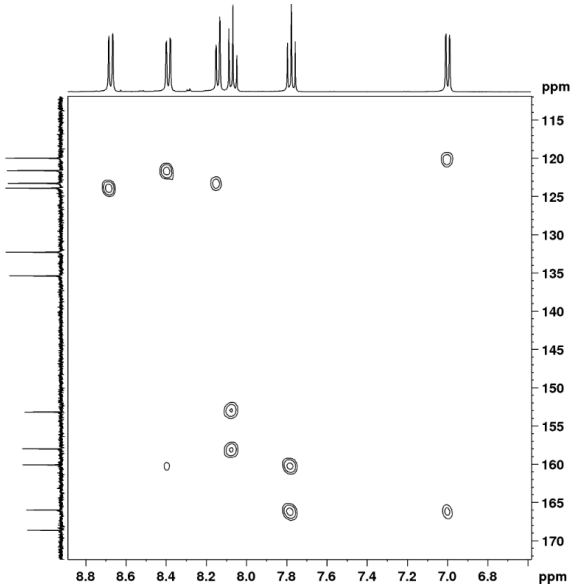

Figure S6. ^{1}H-^{13}C HMBC NMR of **$Na_2[Ru(bda)_2]$** in d_4-Methanol with 5 µl Et_3N at T= 298K.

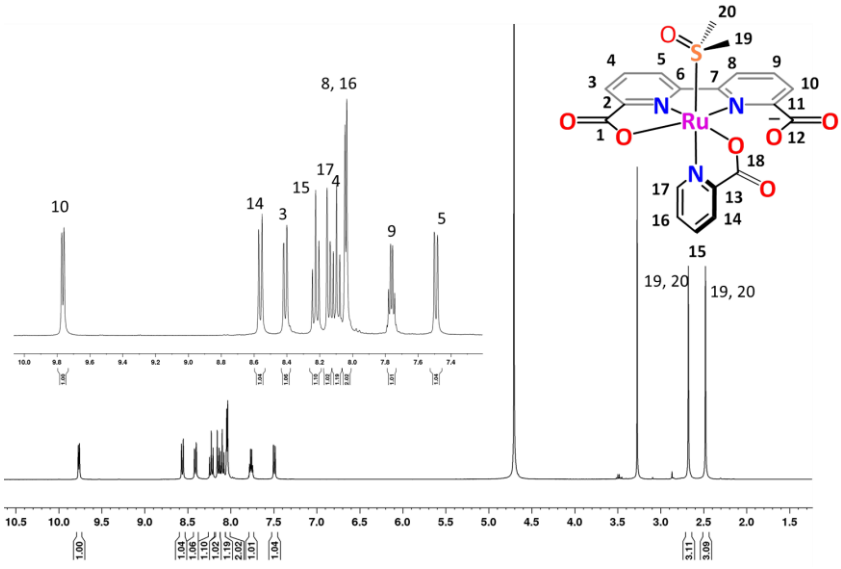

Figure S7. ^{1}H NMR spectrum of **1** in D_2O at T= 298K. Inset: the magnification of the aromatic region.

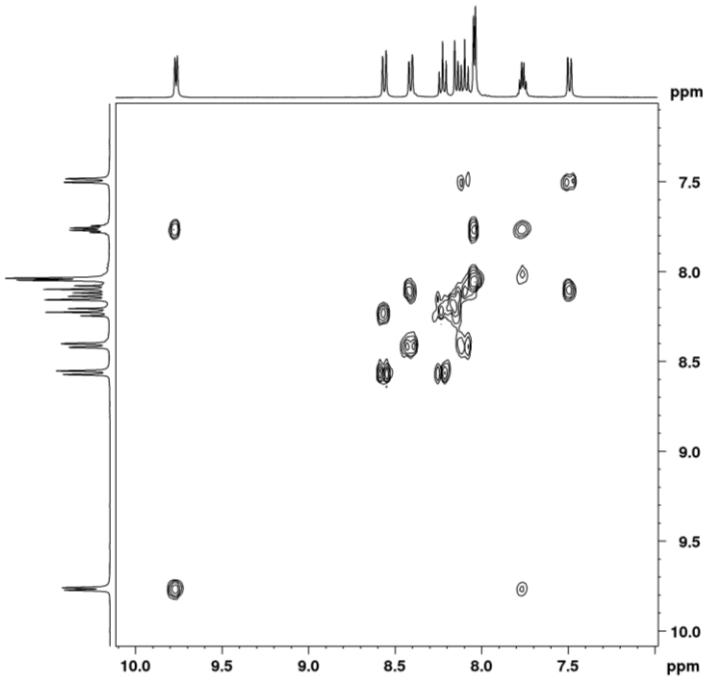

Figure S8. ^{1}H-^{1}H COSY NMR of **1** in D_2O at T= 298K.

V

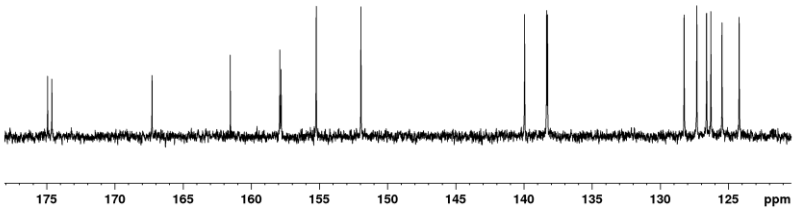

Figure S9. ^{13}C NMR of **1** in D_2O at T= 298K.

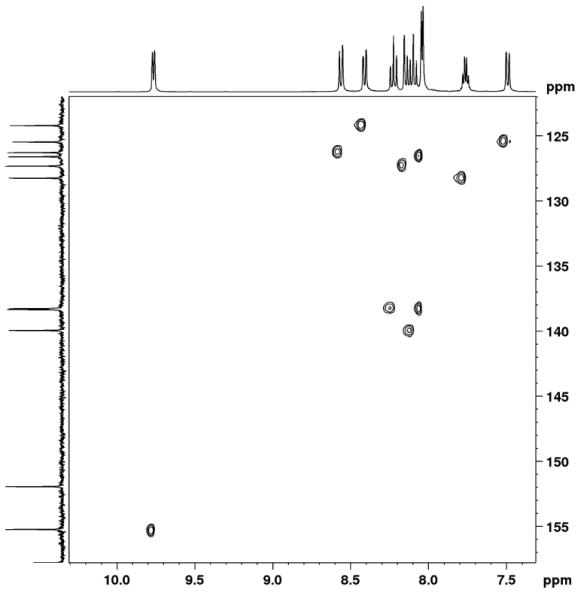

Figure S10. ^{1}H-^{13}C HSQC NMR of **1** in D_2O at T= 298K.

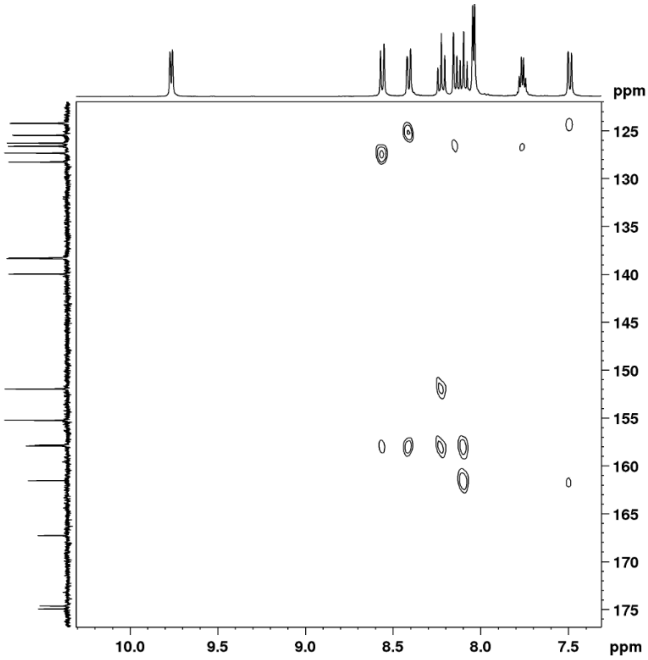

Figure S11. ^{1}H-^{13}C HMBC NMR of **1** in D_2O at T= 298K.

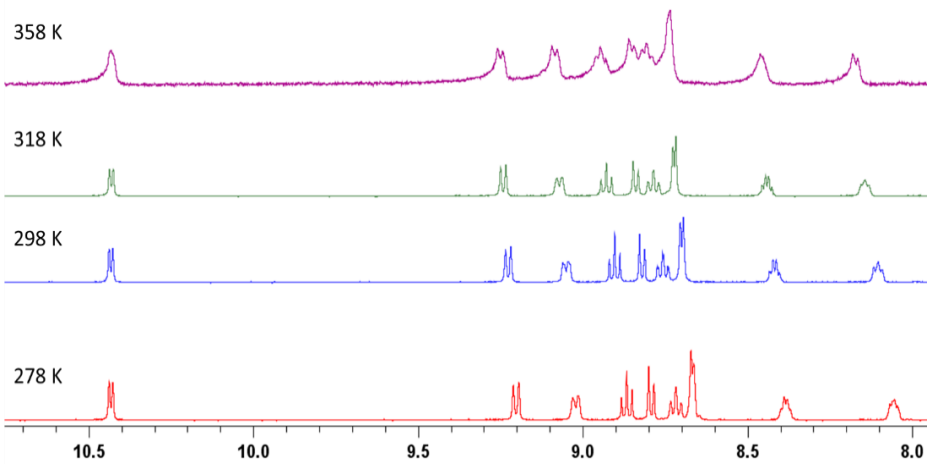

Figure S12. Zoom of the aromatic region of a ^{1}H-NMR of **1** in D_2O at 278 K (Red), 298 K (Blue), 318 K (Green), and 358 K (Purple).

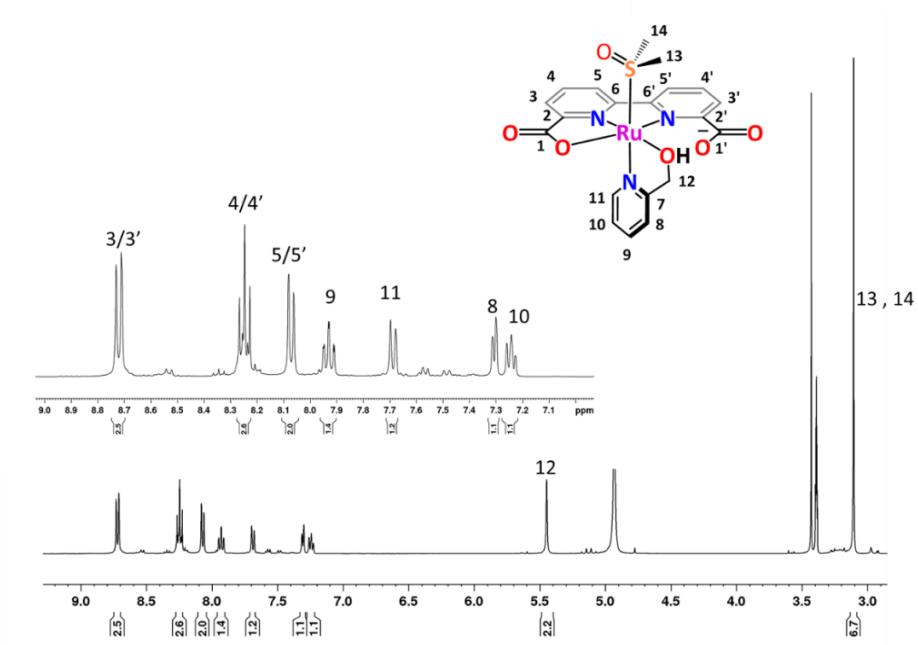

Figure S13. ^{1}H NMR spectrum of **2** in d_4-Methanol at T= 298K. Inset: the magnification of the aromatic region.

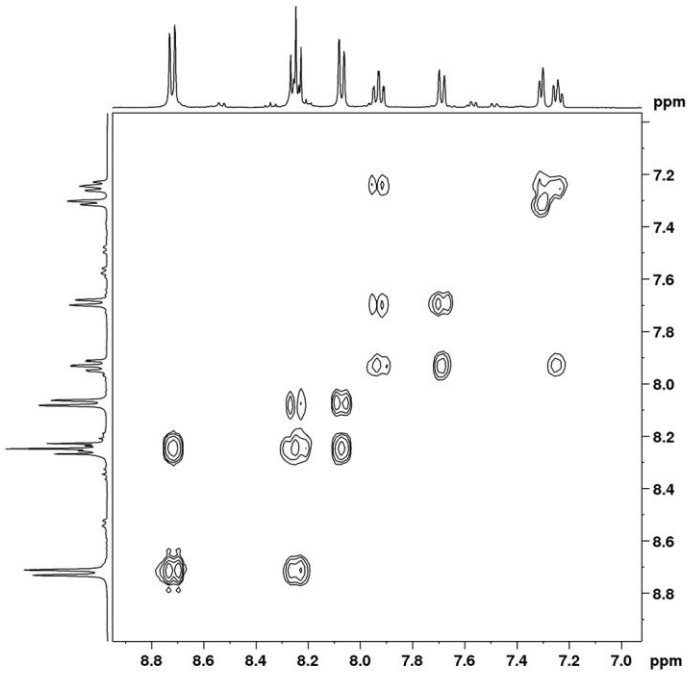

Figure S14. ^{1}H-^{1}H COSY of **2** in d_4-Methanol at T= 298K.

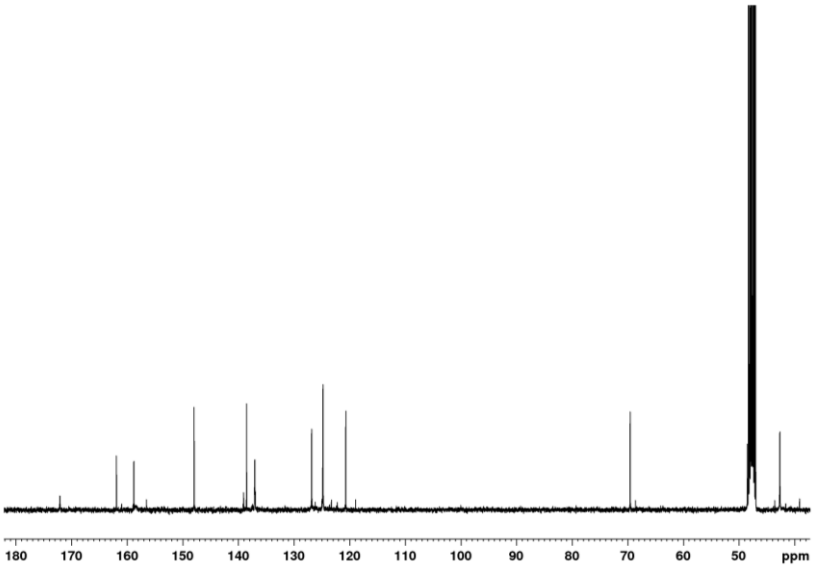

Figure S15. $^{13}C\{H\}$ NMR of **2** in d_4-Methanol at T= 298K.

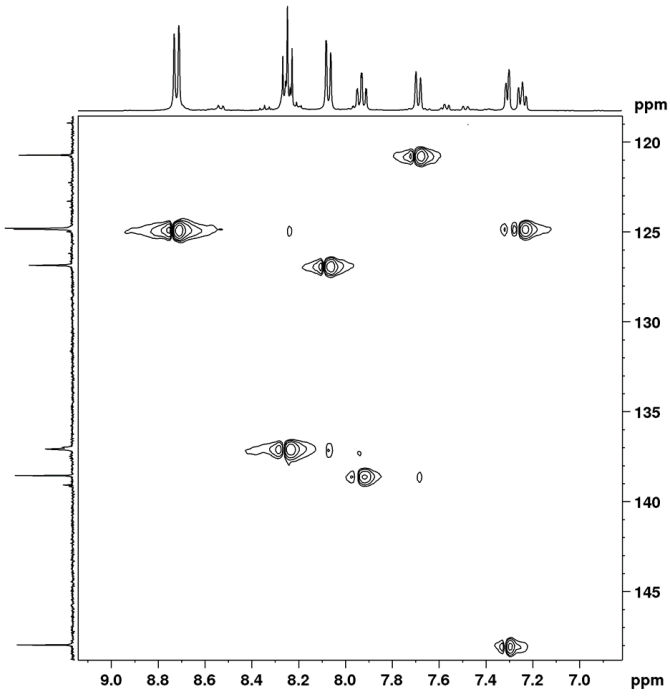

Figure S16. ^{1}H-^{13}C HSQC NMR of **2** in d_4-Methanol at T= 298K.

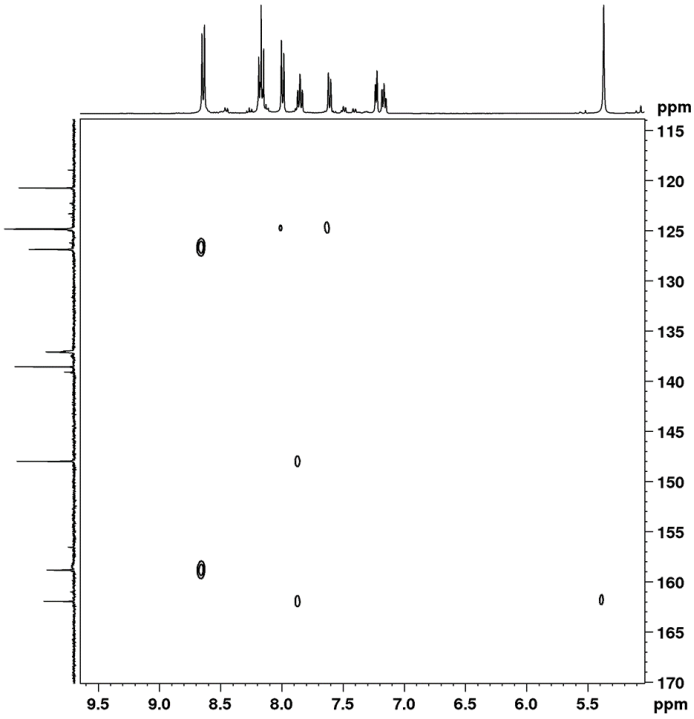

Figure S17. ^{1}H-^{13}C HMBC NMR of **2** in d_4-Methanol at T= 298K.

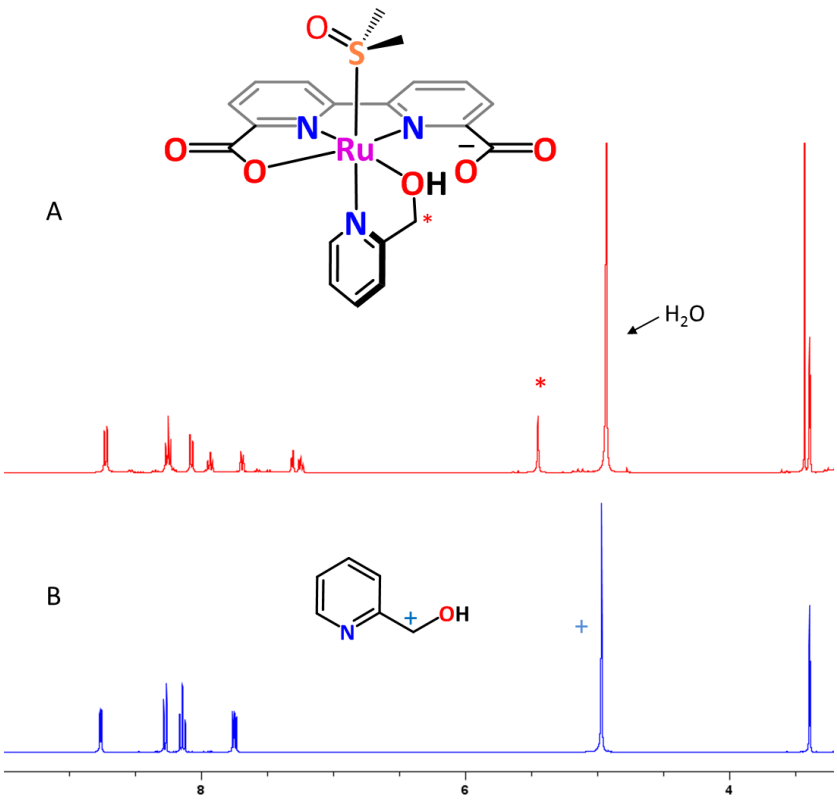

Figure S18. ^{1}H NMR spectrum of **2** in d_4-Methanol (A) and free 2-pyridinemethanol ligand (B) to emphasize the shift of the methylene group resonance indicated by an asterisk (*) and plus (+).

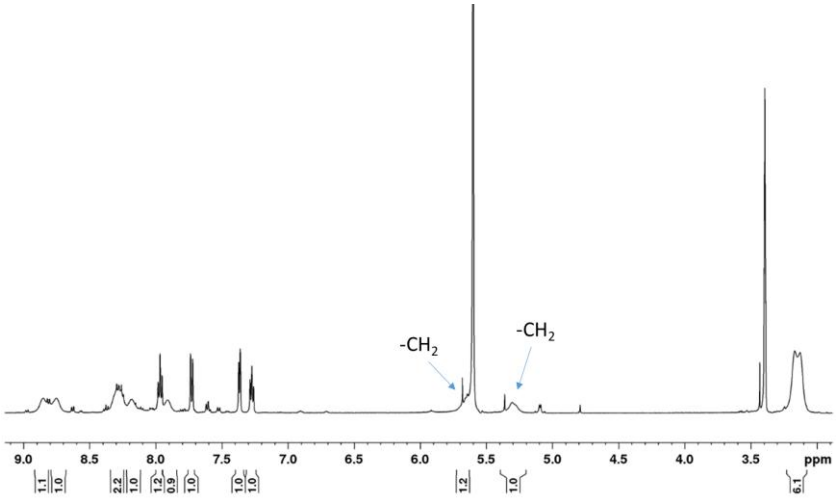

Figure S19. ^{1}H-NMR of **2** in d_4-Methanol at T= 223K.

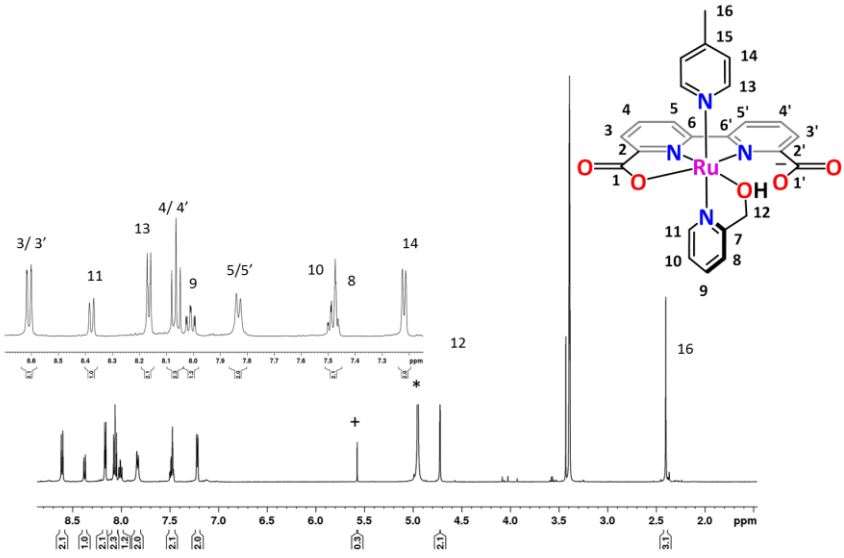

Figure S20. ^{1}H NMR spectrum of **4** in d_4-Methanol at T= 298K. Asterisk (*) and plus (+) signs indicate solvent peaks and an impurity in solvent. Inset: the magnification of the aromatic region.

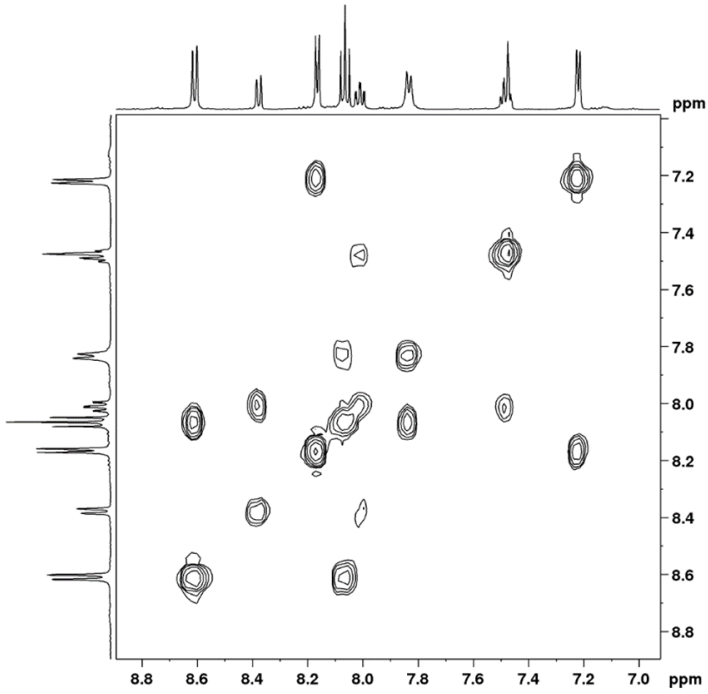

Figure S21. ^{1}H-^{1}H COSY of **4** in d_4-Methanol at T= 298K.

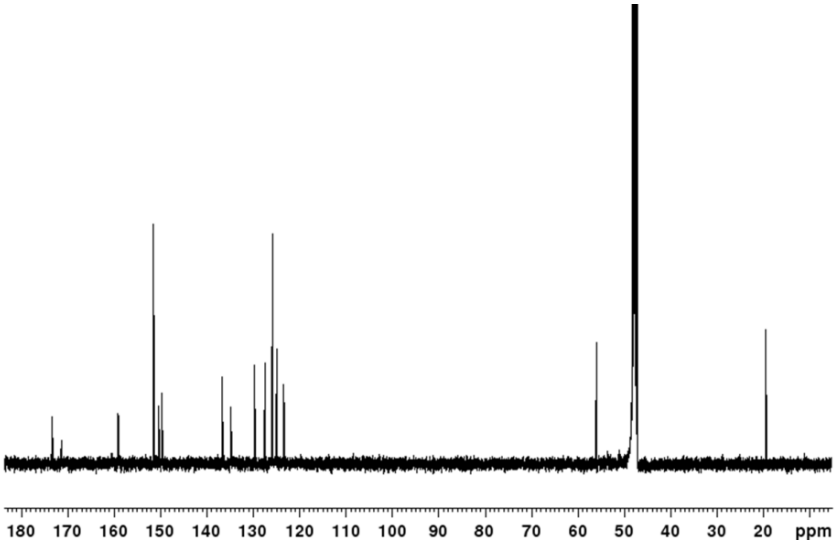

Figure S22. $^{13}C\{H\}$ NMR of **4** in d_4-Methanol at T= 298K.

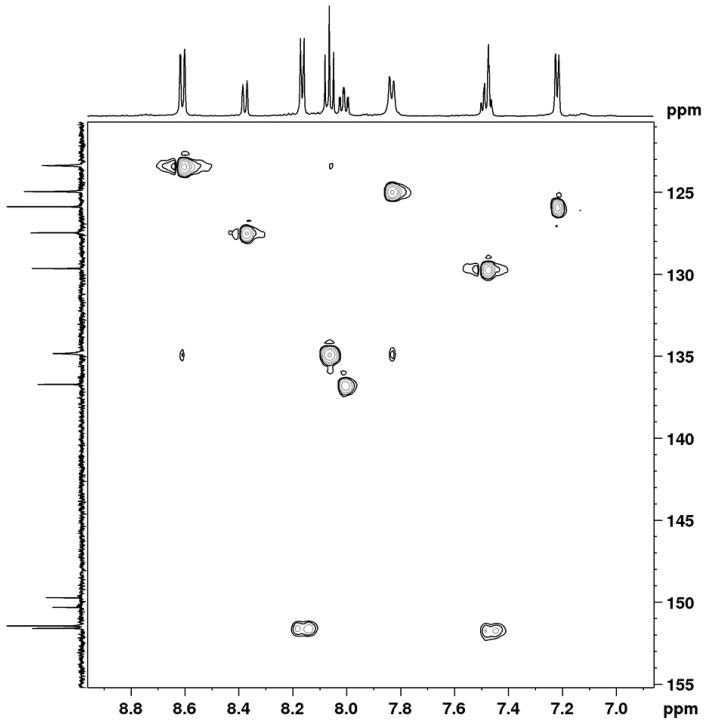

Figure S23. ^{1}H-^{13}C HSQC NMR of **4** in d_4-Methanol at T= 298K.

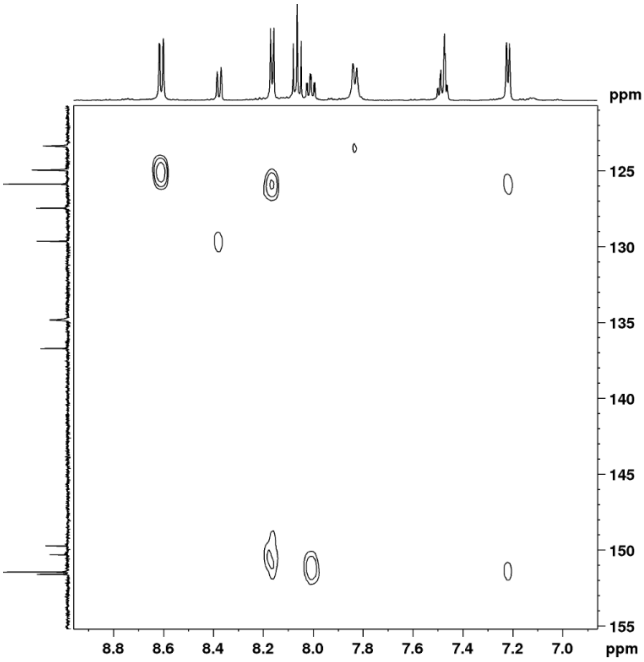

Figure S24. ^{1}H-^{13}C HMBC NMR of **4** in d_4-Methanol at T= 298K.

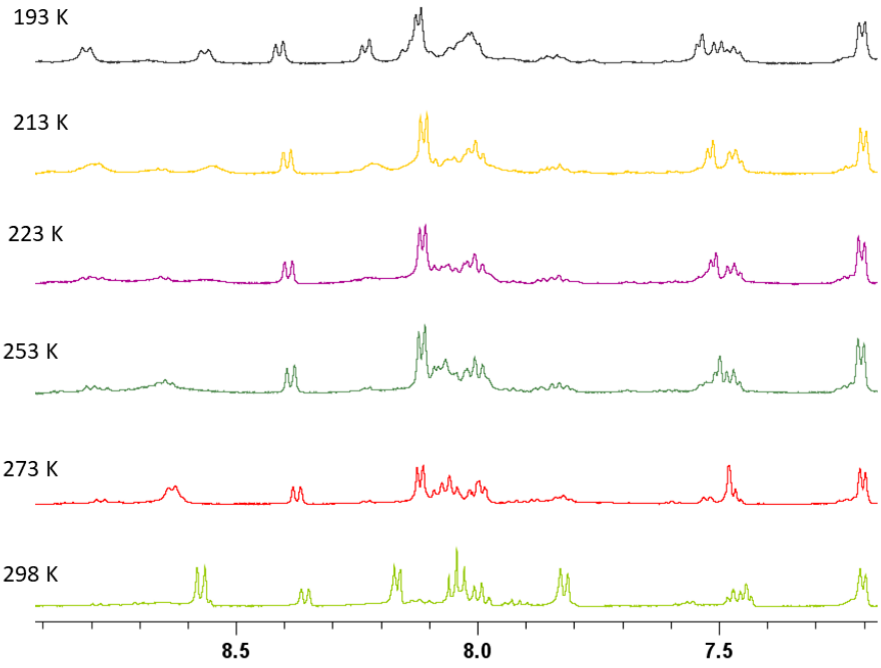

Figure S25. Zoom of the aromatic region of a ^{1}H-NMR of **4** in d_4-Methanol at different temperature from 298 K to 193 K.

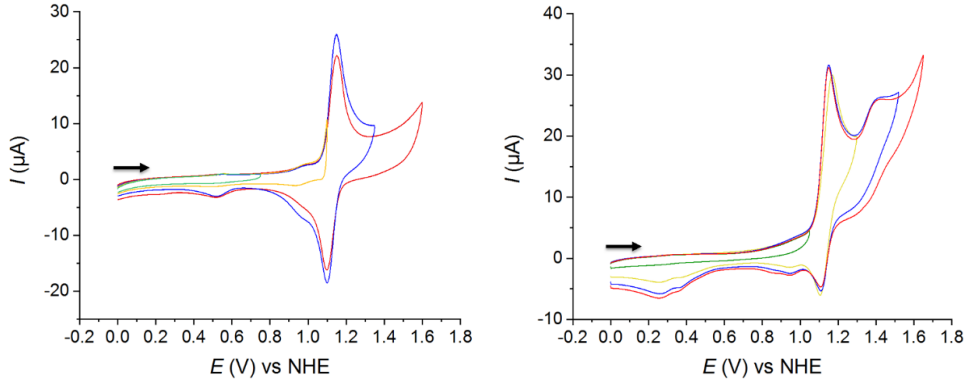

Figure S26. CV experiments of **1** in different potential windows at pH 1 (left) and pH 7 (right). Conditions: v= 100 mV/s, [Ru]: 1mM, WE: glassy carbon electrode; CE: platinum electrode; RE: Hg/Hg_2SO_4.

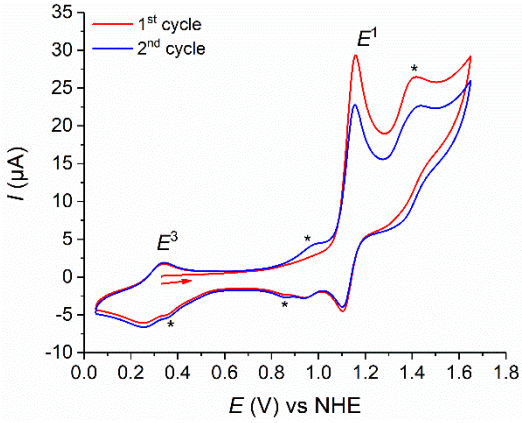

Figure S27. Two consecutive CV cycles of **1** at pH 7 (phosphate buffer solution), v = 100 mV/s. [Ru]: 1mM, WE: glassy carbon electrode; CE: platinum electrode; RE: Hg/Hg_2SO_4. Asterisks (*) show unidentified redox waves.

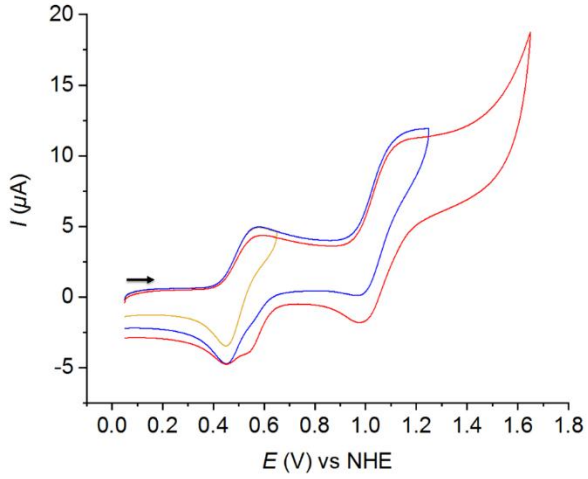

Figure S28. CV experiment of **2** in different potential windows at pH 7. Conditions: v= 100 mV/s, [Ru]: 1mM, WE: glassy carbon electrode; CE: platinum electrode; RE: Hg/Hg_2SO_4. Arrow shows the scan direction.

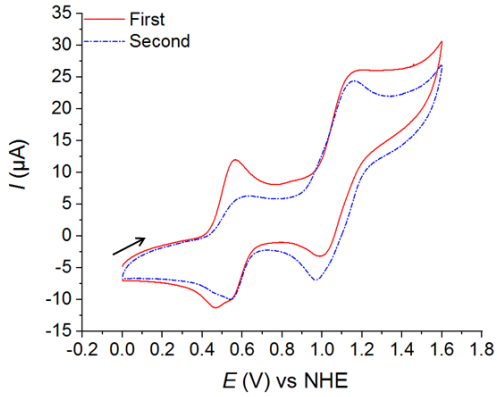

Figure S29. Two consecutive CV scans of **2** at pH 7. Conditions: v= 100 mV/s, [Ru]: 1mM, WE: glassy carbon electrode; CE: platinum electrode; RE: Hg/Hg_2SO_4. Arrow shows the scan direction.

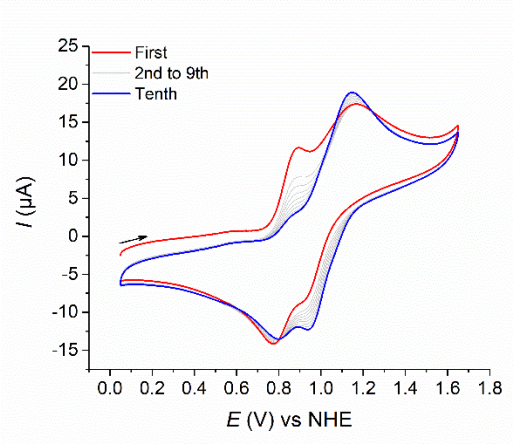

Figure S30. Ten consecutive CV scans of **2** at pH 1 (0.1 M TA). Conditions: v= 100 mV/s, [Ru]: 1mM, WE: glassy carbon electrode; CE: platinum electrode; RE: Hg/Hg_2SO_4. Arrow shows the scan direction.

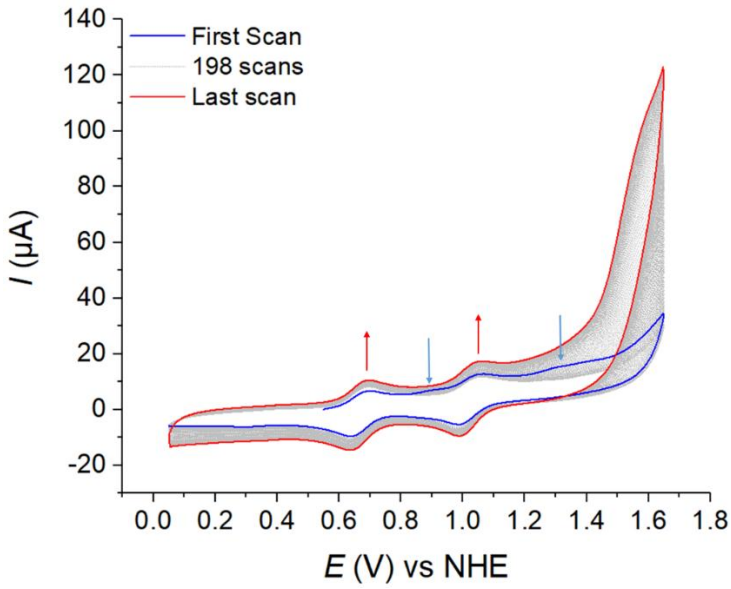

Figure S31. Converting **4** (blue) into **3** (red) by 199 consecutive cycles. Conditions: v= 100 mV/s, [Ru]: 1mM, WE: glassy carbon electrode; CE: platinum electrode; RE: Hg/Hg_2SO_4.

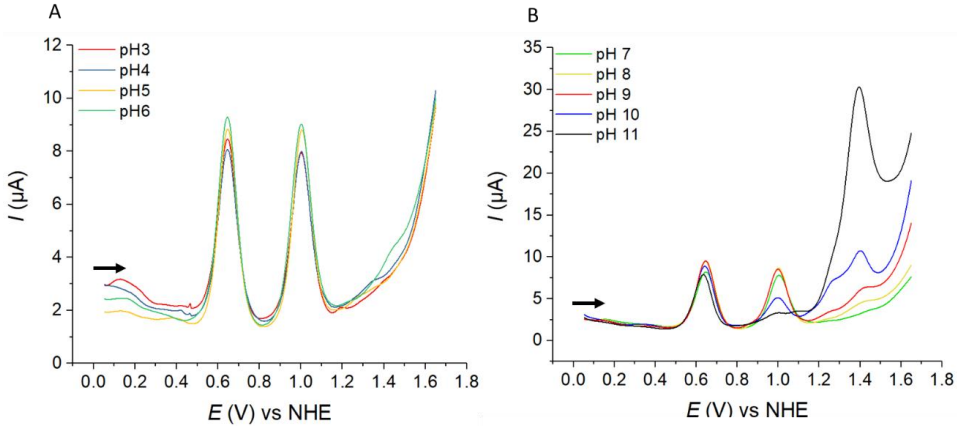

Figure S32. DPVs of **3** (generated *in situ* from **4**) at different pHs A) pH 3 to pH 6, B) pH 7 to pH 11. Conditions: v= 100 mV/s, [Ru]: 1mM, WE: glassy carbon electrode; CE: platinum electrode; RE: Hg/Hg_2SO_4.

Calculation of maximum turnover frequency from cyclic voltammetry (TOF_{max}) and turnover number (TON) from bulk electrolysis experiments.

Equations S1 and S2 were used to calculate TOF_{max} (s^{-1}) and TON, respectively.[3]

$$\frac{i}{i_p} = \frac{4 * 2.24 * \sqrt{\frac{RTk_{obs}}{Fv}}}{1 + \exp(\frac{F(E° - E)}{RT})} \quad \text{(S1)} \qquad \text{TON} = \frac{tk_{obs}}{1 + \exp(\frac{F(E° - E_{app})}{RT})} \quad \text{(S2)}$$

Where R ($J \cdot K^{-1} \cdot mol^{-1}$) is the gas constant, T (K) is the temperature, F ($s.A.mol^{-1}$) is the Faraday constant, E (V) stands for the operating potential in CV and E°(V) stands for the formal potential of the catalyst in the absence of the substrate of catalysis and was extracted from DPV in Figure S35, v is scan rate ($V.s^{-1}$). The intensity of the anodic wave of the Ru^{III}/Ru^{II} was used as i_p (A) as an approximation and i (A) is the current intensity resulted from applying potential during CV.

The k_{obs} is a pseudo-first order constant (s^{-1}), which can be extracted from the slope of the plot of i/i_p vs $1/(1 + \exp[(F/RT)(E^{\circ} - E)])$ by applying Eq. S1 on CV of **3** (Figure S33). The value of k_{obs} in Eq. S1 is equivalent to TOF_{max} (s^{-1}) for a water nucleophilic attack mechanism.[4] A value of TOF_{max} = 3.1 s^{-1} was obtained. A bimolecular mechanism based on I2M pathway (see Equations in Ref. 4) was also considered and gave a value of TOF_{max} = 19.9 s^{-1} (at [Ru] = 1mM), however we believe that this pathway is less likely due to the ortho-carboxylate group in the axial pyridine, which can hamper the approaching of the two Ru=O molecules.

On the other hand, TON was calculated from a bulk electrolysis experiment, when the conversion of **4** to the active catalyst was completed (Figure S34). We estimate that this conversion is finished after 3600 s, at which time 2.8 equivalents of electrons has passed through the system. By using the k_{obs} value calculated as described above, TON was calculated from Eq. S2 from 3600 s to 4553 s (t = 953 s), where E_{app} stands for the operating potential in bulk electrolysis (1.5V) and E°stands

for the formal potential of the catalyst in the absence of the substrate of catalysis and was extracted from DPV in Figure S35. A value of TON = 2990 was obtained from the calculation.

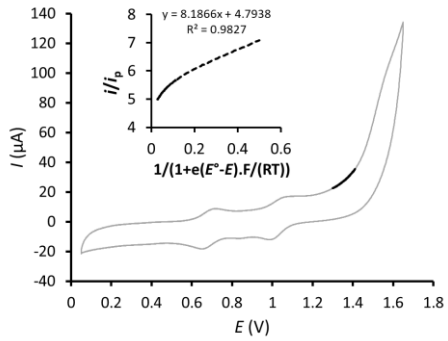

Figure S33. CV of **3** (generated *in situ* from **4** after 200 CV cycles) at pH 7. Inset: FOWA plot of the catalytic current. The black dash line represents the experimental data used for the FOWA analysis, and the black solid line shows the experimental data used for the extraction of TOF_{max} for a water nucleophilic attack mechanism (WNA) (3.1 s^{-1}).[4] Conditions: v= 100 mV/s, [Ru]: 1mM, WE: glassy carbon electrode; CE: platinum electrode; RE: Hg/Hg_2SO_4.

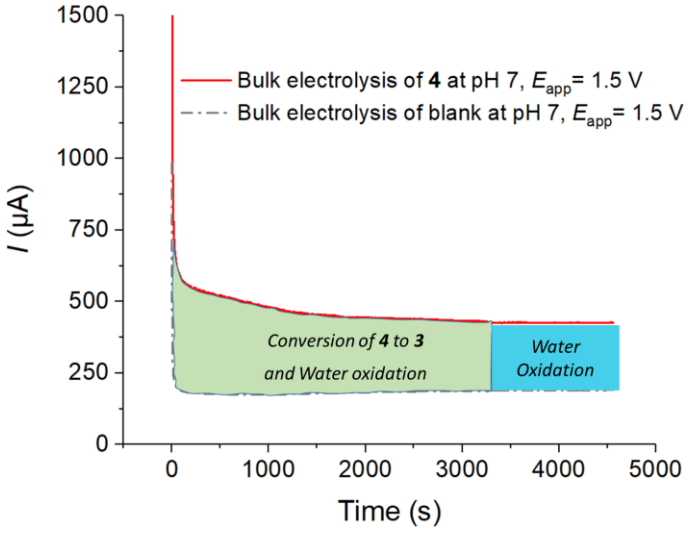

Figure S34. Bulk electrolysis of **4** in a phosphate buffer solution at pH 7 solution at E_{app}= 1.5 V. During the first ca. 60 minutes, complex **4** converts to an active species (green area). From this time, the current passed is attributed only to the water oxidation catalysis process, giving a TON = 2990, based on the active catalyst on the surface, see last two pages.[3b] Conditions: [Ru] = 1 mM, E_{app}= 1.5 V, WE: glassy carbon rod, CE: Pt mesh electrode (simple square mesh net 20*20 mm), RE: Hg/Hg_2SO_4.

V

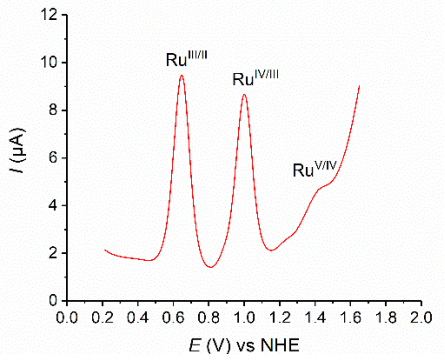

Figure S35. DPV of **3** at pH 7 (generated *in situ* from **4** after bulk electrolysis at E_{app}= 1.5 V). [Ru]: 1mM, WE: glassy carbon electrode; CE: platinum electrode; RE: Hg/Hg_2SO_4.

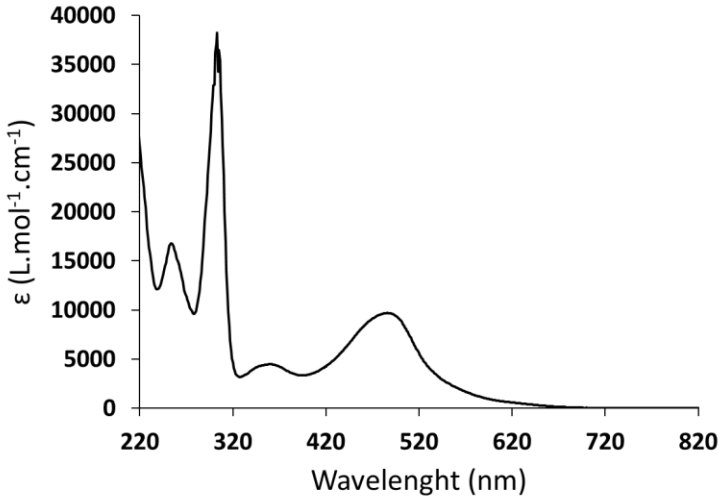

Figure S36. Electronic absorption spectrum of $Na_2[Ru(bda)_2]$ in a phosphate buffer aqueous solution at pH 7.

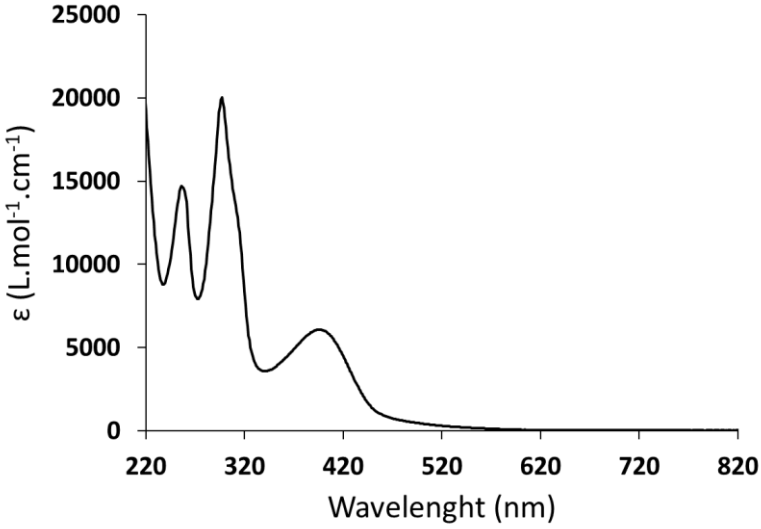

Figure S37. Electronic absorption spectrum of **1** in a phosphate buffer aqueous solution at pH 7.

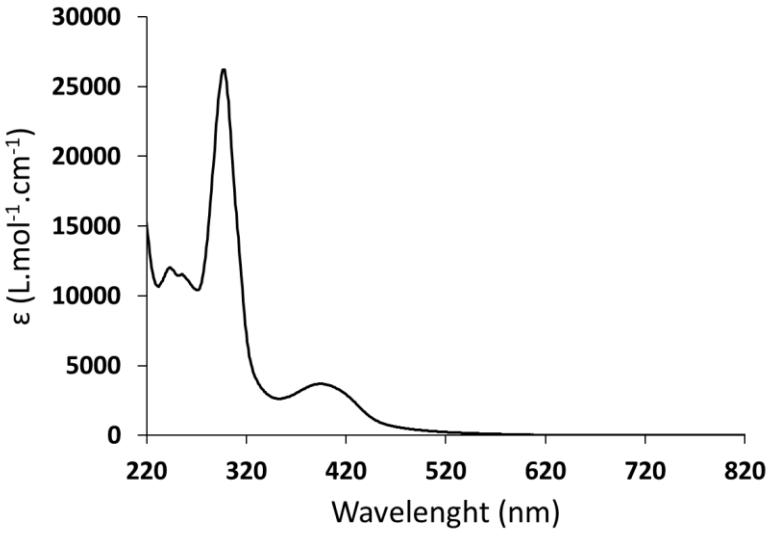

Figure S38. Electronic absorption spectrum of **2** in a phosphate buffer aqueous solution at pH 7.

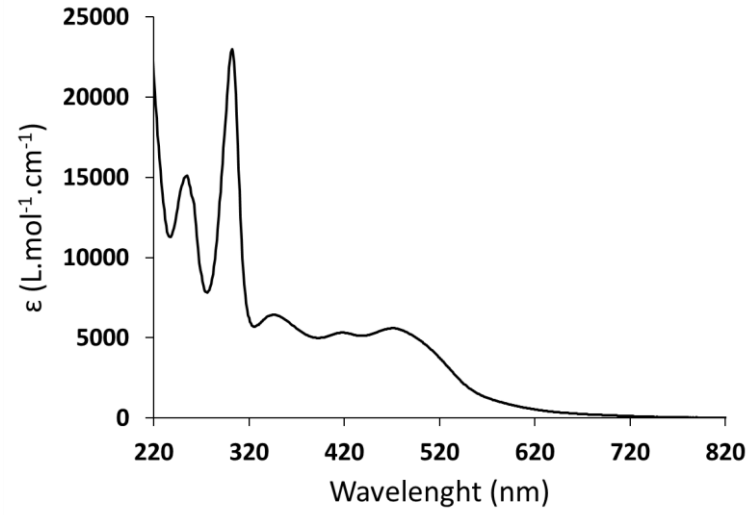

Figure S39. Electronic absorption spectrum of **4** in a phosphate buffer aqueous solution at pH 7.

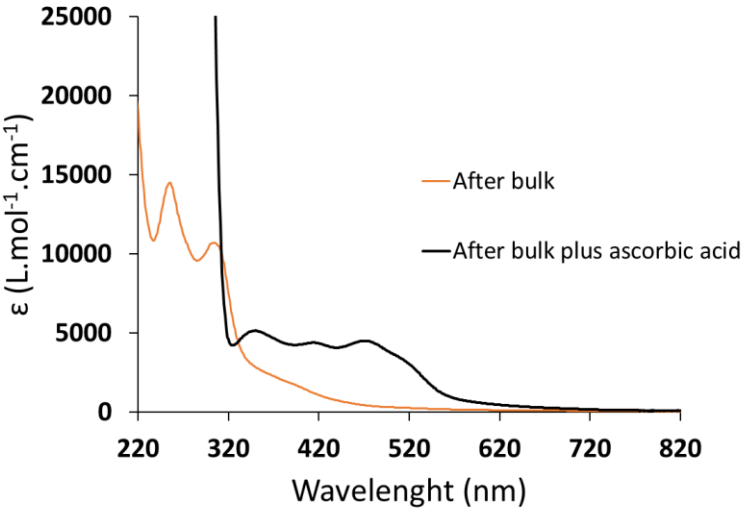

Figure S40. Electronic absorption spectra of **3**, generated *in situ* from **4** by bulk electrolysis at E_{app} = 1.5 V in a phosphate buffer aqueous solution at pH 7 just after the electrolysis (brown) and after adding ascorbic acid (black).

References

1. Wang, L.; Mirmohades, M.; Brown, A.; Duan, L.; Li, F.; Daniel, Q.; Lomoth, R.; Sun, L.; Hammarström, L., Sensitizer-Catalyst Assemblies for Water Oxidation. *Inorganic chemistry* **2015**, *54* (6), 2742-2751.
2. Data collection and reduction with CrysAlisPro 1.171.39.12b (Rigaku OD, **2015**).
3. (a) Matheu, R.; Ertem, M. Z.; Benet-Buchholz, J.; Coronado, E.; Batista, V. S.; Sala, X.; Llobet, A., Intramolecular proton transfer boosts water oxidation catalyzed by a Ru complex. *J. Am. Chem. Soc.* **2015**, *137* (33), 10786-10795; (b) Zhang, T.; Wang, C.; Liu, S.; Wang, J.-L.; Lin, W., A Biomimetic Copper Water Oxidation Catalyst with Low Overpotential. *Journal of the American Chemical Society* **2014**, *136* (1), 273-281.
4. Matheu, R.; Neudeck, S.; Meyer, F.; Sala, X.; Llobet, A., Foot of the Wave Analysis for Mechanistic Elucidation and Benchmarking Applications in Molecular Water Oxidation Catalysis. *ChemSusChem* **2016**, *9* (23), 3361-3369.

v

Chapter 6

A broad view at the complexity involved in water oxidation catalysis based on Ru-bpn complexes

Abstract

A new Ru complex with the formula $[Ru(bpn)(pic)_2]Cl_2$ (where bpn is 2,2'-bi(1,10-phenanthroline) and pic stands for picoline) (**1**Cl_2) is introduced to investigate the true active species involved in water oxidation mechanism electrochemically and chemically. A comprehensive electrochemical (cyclic voltammetry, differential pulse voltammetry, and coulometry), structural (X-ray diffraction analysis), and spectroscopic (UV–vis, NMR, resonance Raman,) characterization are performed together with kinetic studies. Electrochemical oxidation of $\mathbf{1}^{2+}$ triggers a reaction sequence including a picoline ligand de-coordination and a hydroxido ligand coordination to produce $[Ru(bpn)(pic)(OH)]^{2+}$($\mathbf{2}^{2+}$). The former complex is in an equilibrium with an oxo-bridge species with formula $[(Ru(bpn)(pic))_2(\mu\text{-}O)]^{4+}$ ($\mathbf{3}^{4+}$). At neutral media, $\mathbf{3}^{4+}$ is the major compound showing diamagnetic behaviour because of anti ferromagnetism. Hence, the species generated *in situ* have been thoroughly characterized by NMR, mass spectroscopy and UV-Vis. In addition, reduction of $\mathbf{3}^{4+}$ to $\mathbf{2}^{+}$ has been characterized electrochemically, structurally, and spectroscopically. Similarly, chemical oxidation of **1**Cl_2 by $NaIO_4$ results in the conversion of $\mathbf{2}^{2+}$ to $\mathbf{3}^{4+}$ at pH 7 being the rate determining step (k_{dimer}= 1.35 $M^{-1}s^{-1}$) which is in line with electrochemical data at the same pH (k_{dimer}= 1.4 $M^{-1}s^{-1}$). In sharp contrast, electrochemical oxidation of $\mathbf{1}^{2+}$ at pH 1 generates a mixture of products including $\mathbf{2}^{2+}$, which has been characterized in the solid state by monocrystal X-ray diffraction analysis and in solution by UV–vis. Chemical oxidation of $\mathbf{1}^{2+}$ by $(NH_4)_2Ce(NO_3)_6$ shows catalytic water oxidation.

1- Introduction

Coordination and organometallic complexes based on Ru metal are one of most diverse and rich families of compounds.[1] This variety is due to the capacity of the Ru metal center to exist in 11 different oxidation states -2 to +8, and to display a range of geometries within each oxidation state.[2] Further there are nearly an endless number of ligands that can be potentially bonded to the metal center including mono and polydentate ligands that can act as terminal or as bridging ligands. The latter have the capacity to generate polynuclear complexes whose properties are highly dependent on the electronic coupling among metal centers through these bridging ligands.[3] These extreme diversity of Ru complexes is reflected in a myriad of applications that range from photochemical and photophysical applications,[4] magnetochemistry,[5] bioinorganic and medicinal chemistry[6] and catalysis[7] to cite a few of them.

In the catalysis field Ru complexes have been used for many reactions including olefin metathesis,[8] racemization of alcohols,[9] nitrile hydrolysis,[10] and redox catalysis.[11] The latter is especially relevant given the easy access to different metal oxidation states and include hydrogenation reactions and hydrogen transfer,[12] CO_2 reduction,[13] alcohol oxidation,[14] epoxidation,[15] and water oxidation catalysis.[16] The latter is particularly important because of its relevance for the design of new energy conversion schemes based on artificial photosynthesis.[17]

In the context of molecular water oxidation catalysis, Ru complexes have been leading the field among several transition metals[18] and today we have very rugged and efficient catalysts. [16, 19] This has been possible thanks to the spectroscopic characterization of the reaction intermediates as well as due to the kinetic characterization of the different steps involved and complemented with a thorough computational analysis.[20] Further, an additional parameter that helps on the understanding of the catalyst performance is the fine tuning of the redox properties

based on small ligand variation.[21] However, the complete characterization of the reaction intermediates involved in the catalytic cycle is difficult because of the different oxidation states involved that can have different chemical behavior influencing substitution kinetics, isomerization processes and even changes in the first coordination number. For this reason, it is of paramount importance to properly understand and characterize the different parameters that lead to the generation of active species. Equally important is to uncover the reaction pathways that either block catalysis or lead to decomposition process.[22]

Recently a family of Ru complexes containing tetradentate equatorial N_4 ligands (see Chart I for a drawing) and picoline as axial ligands of general formula, $[Ru^{II}(N_4)(pic)_2)]^{2+}$, has been described for N_4 = 2,2'-(1,10-phenanthroline-2,9-diyl)bis(pyridine) dipyridylpheanthroline (pbp)[23] and for N_4 = 2,2':6',2'':6'',2'''-quaterpyridine (qpy).[24] These $[Ru^{II}(N_4)(pic)_2)]^{2+}$ complexes in the presence of an oxidant, undergo ligand oxidation at the two external pyridyl groups forming the corresponding N_4-O_2 di-N-oxide ligands, 2,2'-(1,10-phenanthroline-2,9-diyl)bis(pyridine 1-oxide) (pbp-O_2) and [2,2':6',2'':6'',2'''-quaterpyridine] 1,1'''-dioxide (qpy-O_2). The new $[Ru(N_4\text{-}O_2)(pic)_2]^{2+}$ complexes generated in this manner are powerful water oxidation catalysts and thus it is of interest to understand both the mechanism of the N-oxide formation as well as the active species responsible for catalysis.

Within this context we report here the synthesis of a new $[Ru^{II}(N_4)(pic)_2]^{2+}$ complex containing the equatorial tetradentate N_4 ligand 2,2'-bi(1,10-phenanthroline) abbreviated as bpn shown in Chart I, $[Ru^{II}(bpn)(pic)_2]^{2+}$, $\mathbf{1}^{2+}$, and the related family of complexes obtained under oxidative conditions. We disclose the complex chemistry derived from $\mathbf{1}^{2+}$, based on a thorough kinetic, redox and spectroscopic analysis.

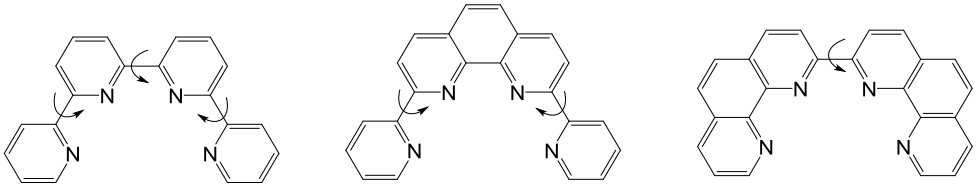

qpy pbp bpn

Chart I. N_4 tetradentate equatorial ligands discussed in this work. The arrows show C-C bond rotational axis.

2-Experimental Section

Materials. The 2-cyano-1,10-phenanthroline[25], 8-amino-7-quinolinecarbaldehyde[26] and 2,2'-bi[1,10] phenanthroline (bpn)[27] were prepared according to the literature. Ruthenium precursor $RuCl_3 \cdot 3H_2O$ and other reagents including 1,10-phenanthroline, 8-nitro-7-quinolinecarbaldehyde, 4-methylpyridine (pic), anhydrous $MgSO_4$, $NaHCO_3$ and 30% H_2O_2, were obtained from Sigma-Aldrich and used as received. When required, solvents were dried by following the standard procedures, distilled under nitrogen and used immediately. High purity de-ionized water used for the electrochemistry experiments was obtained by passing distilled water through a nanopure Milli-Q water purification system. For other spectroscopic and electrochemical studies, HPLC-grade solvents were used.

Instrumentation and methods. The microwave synthesis was performed in a Biotage® Initiator. A 500 MHz Bruker Avance II spectrometer was used to carry out NMR spectroscopy. MALDI-TOF-MS experiment was performed on a Bruker Daltonics Autoflex equipped with a nitrogen laser (337 nm) and Mass accuracy in Reflectron mode: 10-50 ppm. ESI-Mass experiment was performed by using micromass Q-TOF mass spectrometer. The IR measurements were performed on FT-ATR TR0 spectrophotometer. UV/Vis spectroscopy was performed on a Cary 50 (Varian) UV/Vis spectrophotometer in 0.1 cm quartz cuvettes. Elemental analyses were carried out on Perkin-Elmer 240C elemental analyzer. All electrochemical experiments were performed with an IJ-Cambria CHI-660 potentiostat using a three-

electrode cell for cyclic voltammetry (CV) and differential pulse voltammetry (DPV) or two compartment cell for bulk electrolysis. $E_{1/2}$ values reported in this work were estimated from CV experiments as the average of the oxidative and reductive peak potentials ($E_{p,a}$ + $E_{p,c}$)/2 or from DPV. The Reference Electrode (RE) was Hg/Hg_2SO_4 (K_2SO_4 saturated) unless indicated and potentials were converted to NHE by adding 0.65 V. All potentials reported in this work are vs NHE. The pH of the solutions was determined by a pH meter (CRISON, Basic 20+) calibrated before measurements through standard solutions at pH= 4.01, 7.00 and 9.21.

The kinetics experiments of the oxidation of $\mathbf{1}^{2+}$ by $NaIO_4$ were performed in buffered solution (phosphate buffer, from now on phbf, pH 7.2) at 5 or 25 °C with the use of a biologic cryo SFM-4000 four syringe stopped-flow equipped with a 150 W xenon lamp and combined with a J&M TIDAS diode array detector (200−724 nm, integration time 0.5 ms). Complete spectra were recorded between 200 and 724 nm with the integrated J&M software BioKine V4.66. A Huber C-905 cryostat filled with silicon oil was used to maintain constant temperature (± 0.01 °C). The buffered solutions of $\mathbf{1}^{2+}$ and oxidant were mixed in a 1:1 volume ratio (113 μL complex : 113 μL oxidant) with a total flow rate of 5.5 mL/s under pseudo-first order conditions, i.e. at least 7-fold excess of $NaIO_4$ over Ru complex. The spectral changes accompanying the formation and decay of the reaction intermediates as well as kinetic traces at a fixed wavelength were analyzed with the use of the SPECFIT/32 global analysis program (Version 2.10, 1993–1996, Spectrum Software Associates, P.O. Box 4494, Chapel Hill, NC 27515-4494, U.S.A.). The reported k_{obs} values were obtained from the fits of experimental data to two-exponential function using kinetic model A→B→C and they are the average of at least five measurements. Manometric measurements were performed on a Testo 521 differential pressure manometer with an operating range of 0.1-10 kPa and accuracy within 0.5% of the measurements. The manometer was coupled to thermostatic reaction vessels for dynamic monitoring of the headspace pressure above each reaction solution. The

manometer's secondary ports were connected to thermostatic reaction vessels containing the same solvents and headspace volumes as the sample vials. Each measurement for a reaction solution (2.0 mL) was performed at 298 K. The resonance Raman (rR) spectrum was acquired using a Renishaw inVia Reflex RAMAN confocal microscope (Gloucestershire, U.K.) that was equipped with a Laser Nd:YAG (DPSS) 532 nm. Spectra integration time was 10 seconds and spectra shown correspond to ten accumulations on the solid sample. Laser power used was 100 % of the nominal power (50 mW).

Synthesis of [Ru(bpn)Cl_2]Cl. To a 20 mL degassed microwave flask containing $RuCl_3 \cdot 3H_2O$ (16 mg, 0.0613 mmol) and bpn (20 mg, 0.05 mmol), 12 mL of ethanol were added and the solution was heated in a microwave oven for 2 h at 150 °C with a power of 150 W. The resulting reaction mixture was centrifuged and the black solid was collected by decanting the red solution. The black solid was dispersed in ethanol, filtered and washed with ethanol (28 mg, 0.0398 mmol, yield 65%). IR (ATR, cm^{-1}) 723, 860, 1458, 1526, 1598, 3062, 3451 (Figure S1). Anal. Calcd. for $C_{24}H_{14}Cl_3N_4Ru$ {[Ru(bpn)Cl_2]Cl}: C, 50.9; H, 2.5; N, 9.9. Found: C, 51.0; H, 2.4; N, 9.7.

Synthesis of [Ru(bpn)(pic)$_2$]Cl_2, **1**Cl_2. To a 20 mL degassed microwave flask containing 12 mg of [Ru(bpn)Cl_2]Cl (0.021 mM) were added 2 mL of water, 8 mL of ethanol and 2 mL of 4-picoline (20 mmol). Then it was placed in a microwave oven for 2 h at 150 °C with a power of 150 W. The resulting mixture was filtered and the solution concentrated by rotary evaporator. Then diethyl ether was added at which point a solid precipitated that was filtered and re-dissolved in MeOH and precipitated again with diethyl ether. Finally, this solid can be recrystallized from a solution with a mixture of MeOH/DCM (0.1/0.2 mL) and using Et_2O (3 mL) to slowly diffuse. A red crystalline solid was formed, which was filtered (13 mg, 0.0181 mmol, yield 85%). ^{1}H NMR (500 MHz, D_2O): δ= 1.89 (s, 6 H), 6.63 (d, *J*= 6.25Hz, 4 H), 7.74 (d, *J*= 6.40 Hz, 4 H), 7.99 (dd, *J*= 11.66 Hz, 4 H), 8.07ppm (dd, *J*= 4.43 Hz, 2 H), 8.51

(m, 4 H), 8.85ppm (d, *J*= 8.75, 2H), 10.01 ppm (d, *J*= 4.90, 2H). ^{13}C NMR (126 MHz, MeOD): δ= 159.18, 155.30, 150.72, 150.24, 149.82, 137.97, 133.36, 130.74, 129.98, 129.55, 128.10, 126.74, 125.97, 123.12, 19.56 (Figures S2-S6). UV/Vis [λ_{max}, nm (ε, M^{-1} cm^{-1})]: 576.97 (22636), 473.02 (4992.44), 370.01 (27952.88), 354 (20200), 311.00 (22674). Anal. Calcd. (Found) for $C_{37}H_{34}Cl_4N_6O_2Ru$ ($[Ru(bpn)(pic)_2]Cl_2 \cdot CH_2Cl_2 \cdot 2H_2O$: C, 53.1; H, 4.1; N, 10.0. Found: C, 52.7; H, 3.5; N, 9.9. MS (ESI^+ positive mode, methanol) calculated for $[M+Cl]^+$ *m/z* = 681.11, found: 681.1.

Electrochemical synthesis of $\{[Ru(bpn)(pic)]_2(\mu\text{-}O)\}^{4+}$, $\mathbf{3}^{4+}$. A two-compartment electrochemical cell was used for this experiment. The reference electrode and working electrode were placed in one compartment containing 1.39 mM solution of $\mathbf{1}^{2+}$ (4.5 ml) in 0.1 M phbf solution at pH 7 and the counter electrode was placed in the second compartment in pure 0.1 M phbf solution at pH 7. A bulk electrolysis experiment was performed at E_{app}= 1.45 V for 1 h. For NMR characterization of product $\mathbf{3}^{4+}$, the same procedure was repeated using a deutero aqueous solution at pD 7. ^{1}H NMR (500 MHz, D_2O): δ= 1.72 (s, 3 H), 6.43 (d, *J*= 6.20Hz, 2 H), 6.59 (t, *J*= 4.37Hz, 2 H), 7.34 (d, *J*= 5.15Hz, 2 H), 7.43 (d, *J*= 6.50Hz, 2 H), 7.98 ppm (dd, *J*= 6.95 Hz, 4 H), 8.35 (d, *J*= 8.65Hz, 2 H), 9.40 ppm (d, *J*= 8.35, 2H), 9.60 ppm (d, *J*= 8.30, 2H) (Figures S7-S11). UV/Vis [λ_{max}, nm (ε, M^{-1} cm^{-1})]: 367.99 (17371.51), 575.92 (3837.30), 784.98 (2632.77) and $MALDI^+$ (positive mode, methanol): calculated for $[M+3Cl]^+$ m/z^+ = 1227.07, found: 1227.4.

Electrochemical synthesis of $[Ru(bpn)(pic)(OH)]^+$, $\mathbf{2}^+$. A two-compartment electrochemical cell was used for this experiment. The reference electrode and working electrode were placed in one compartment containing a solution of complex $\mathbf{3}^{4+}$ (prepared *in situ* as described above) in 0.1 M phbf at pH 7 and the counter electrode was placed in the second compartment in pure 0.1 M phbf solution at pH 7. A bulk electrolysis experiment was performed at E_{app}= 0.35 V for 2

h. The presence of complex $\mathbf{2}^{+}$ can be confirmed by CV and/or NMR spectroscopy (in the latter case the experiment was carried out in a D_2O phbf at pD 7). ^{1}HNMR (500 MHz, D_2O): δ= 1.8 (s, 3 H), 6.55 (d, *J*= 5.95 Hz, 2 H), 7.65 (d, *J*= 6.20 Hz, 2 H), 8.06 (m, 6 H), 8.42 (d, *J*= 8.65 Hz, 2 H), 8.59 ppm (d, *J*= 8.057, 6 H), 8.69 (d, *J*= 8.65 Hz, 2 H), 9.96 ppm (d, *J*= 4.70, 2H) (Figures S12-S16). UV/Vis [λ_{max}, nm (ε, M^{-1} cm^{-1})]: 584 (448.85), 474 (874), 4069 (369), 3119.11 (355) and MALDI^{+} (positive mode, methanol) calculated for $[M]^{+}$ m/z^{+} = 570.09, found: 570.01.

Single Crystal X-Ray Diffraction.

Data collection. Crystal structure determination for samples $\mathbf{1}Cl_2$ and $[Ru^{II}(bpn)(pic)(H_2O)](CF_3SO_3)_2$ were carried out using a Apex DUO Kappa 4-axis goniometer equipped with an APPEX 2 4K CCD area detector, a Microfocus Source E025 IuS using MoK_α radiation, Quazar MX multilayer Optics as monochromator and an Oxford Cryosystems low temperature device Cryostream 700 plus (T = -173 ^{o}C). Crystal structure determination for samples Full-sphere data collection was used with ω and φ scans. *Programs used:* Data collection APEX-2[28], data reduction Bruker Saint[29] V/.60A and absorption correction SADABS.[30]

Crystal preparation. Crystals of $\mathbf{1}Cl_2$ were grown by slow diffusion of diethyl ether in a solution of $\mathbf{1}Cl_2$ dissolved in a mixture of MeOH/DCM under air. Dark red crystals of $[Ru^{II}(bpn)(pic)(H_2O)](CF_3SO_3)_2$ were grown by slow diffusion of diethyl ether in a mixture of 0.1 M triflic acid (TA) and acetone of $\mathbf{2}^{+}$. The crystals used for structure determination were selected using a Zeiss stereomicroscope using polarized light and prepared under inert conditions immersed in perfluoropolyether as protecting oil for manipulation.

Structure Solution and Refinement. Crystal structure solution was achieved using the computer program SHELXT.[31] Visualization was performed with the program SHELXle.[32] Missing atoms were subsequently located from difference Fourier synthesis and added to the atom list. Least-squares refinement on F^2 using all

measured intensities was carried out using the program SHELXL 2015.[33] All non-hydrogen atoms were refined including anisotropic displacement parameters. The asymmetric unit of structure of **1**Cl_2 contains one molecule of the cationic metal complex, two chlorine anions and two dichloromethane molecules. For $[Ru^{II}(bpn)(pic)(H_2O)](CF_3SO_3)_2$ the crystals obtained were of low quality and after several attempts only a suitable dataset could be collected for structure determination. The asymmetric unit contains one molecule of the metal complex, two triflate anions, 0.4 diethylether molecules and 0.40 water molecules. The metal complex molecule is disordered partially in two orientations (ratio 65:35). The triflate anions are disordered in two orientations (ratio 66:34 and 82:18 respectively). The 0.4 diethylether molecules are disordered in two positions around an inversion center (ratio 20:20). The 0.4 water molecules are disordered in three positions with a ratio of (15:15:10). The Ruthenium atom is attached to an Oxygen atom. It was refined as a $–OH_2$ based on two electron densities detected close to the Oxygen atom.

VI

3-Results and Discussion

3.1- Synthesis, structure and spectroscopy of Ru-bpn complexes

The synthetic strategy followed for the preparation of complexes **1-3** is outlined in Scheme 1. A sample of $RuCl_3{\cdot}3H_2O$ and bpn were dissolved in EtOH and heated in a microwave (μW) apparatus to generate the complex $[Ru^{III}(bpn)Cl_2]Cl$ in good yield. The latter is then treated with excess 4-picoline (pic) and heated again in a μW in EtOH to generate $[Ru^{II}(bpn)(pic)_2]Cl_2$, **1**$Cl_2$, where the axial chlorido ligands are substituted by monodentate pic ligands while the metal center is reduced to oxidation state II.

Applying a potential of 1.45 V to **1**Cl_2 dissolved in an aqueous pH 7 phbf solution, quantitatively generates the oxo-bridged dinuclear Ru complex, $\{[Ru^{III}(bpn)(pic)]_2(\mu\text{-}O)\}^{4+}$, $\mathbf{3}^{4+}$, with concomitant loss of a picoline ligand per each Ru center via the

formation of a mononuclear Ru(III) intermediate species $[Ru^{III}(OH)(bpn)(pic)]^{2+}$, $\mathbf{2}^{2+}$.The degree of protonation of the oxygen atom is based on the Pourbaix diagram shown in Figure S37 for this complex that agrees well with other complexes with similar type of ligands.[34]

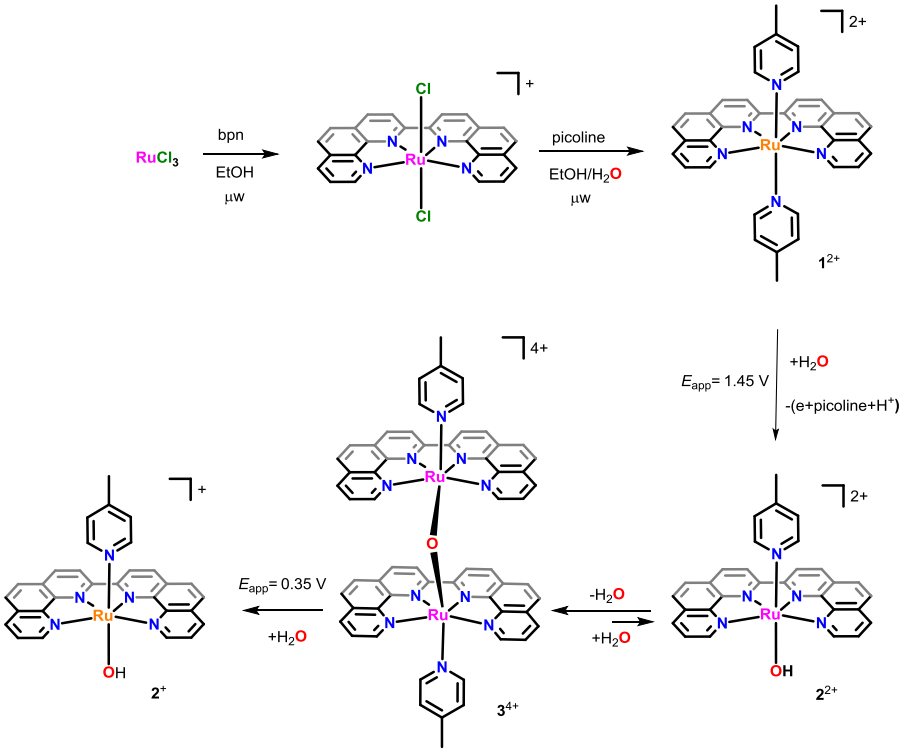

Scheme 1. Reaction sequence used for the synthesis of complexes **1**-**3** and labeling. Orange and fuchsia colors indicate oxidation states II and III for Ru respectively.

This reaction sequence was monitored via ^{1}H-NMR spectroscopy (Figure S10). Adding 4.5 equivalents of $NaIO_4$ as the oxidizing agent to a pH 7 solution of $\mathbf{1}Cl_2$, gives the same result (Figure S11C). Finally, exposure to E_{app} = 0.35 V of a pH 7 phbf of $\mathbf{3}^{4+}$ for 2 h generates quantitatively the Ru(II)-OH mononuclear complex $[Ru^{II}(OH)(bpn)(pic)]^{+}$, $\mathbf{2}^{+}$. This complex can also be obtained chemically by adding excess amount of ascorbic acid as the reducing agent to the electrochemically generated $\mathbf{3}^{4+}$ (Figure S15B).

Sufficiently good crystals for x-ray diffraction were obtained for **1**Cl_2 and for [Ru^{II}(bpn)(pic)(H_2O)](CF_3SO_3)$_2$ and the cationic part of their ORTEP plots are displayed in Figure 1. In both cases the Ru center adopts a slightly distorted octahedral geometry with the bpn ligand occupying the equatorial positions and the pic and aqua occupying the axial ones. Bonding distances and angles are unremarkable for Ru(II) polypyridyl type of complexes[23b, 24, 35] except perhaps for the NRuN angles of the outer pyridyl groups of phenanthroline moieties that turn out to be 122.5^o and 125.3^o for **1**Cl_2 and [Ru^{II}(bpn)(pic)(H_2O)](CF_3SO_3)$_2$ respectively and that reflect the geometrical distortion imposed by the bpn ligand.

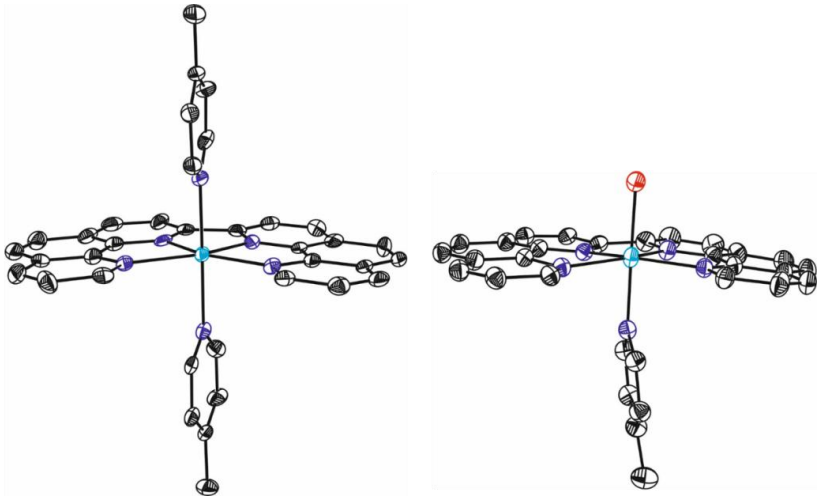

Figure 1. ORTEP plots (ellipsoid drawn at 50% probability) of the X-ray structures of the cationic part of **1Cl**$_2$ (right) and [Ru^{II}(bpn)(pic)(H_2O)](CF_3SO_3)$_2$ (left). Color code: cyan, Ru; red, O; purple, N; and black, C. Hydrogen atoms are omitted for clarity purposes.

Complexes **1**$^{2+}$, **2**$^{+}$ and **3**$^{4+}$ show diamagnetic behavior, thus they were further characterized in solution by 1D and 2D NMR spectroscopy and the spectra are presented in Figure 2A and in the SI (Figures S2-S16). Complexes **1**$^{2+}$ and **2**$^{+}$ are Ru(II) complexes with a high field low spin d^6 electronic configuration whereas in **3**$^{4+}$ the electronic coupling between two d^5 Ru(III) through the oxo bridge generates a

dinuclear complex with all paired electrons at room temperature and thus with a diamagnetic behavior.[36]

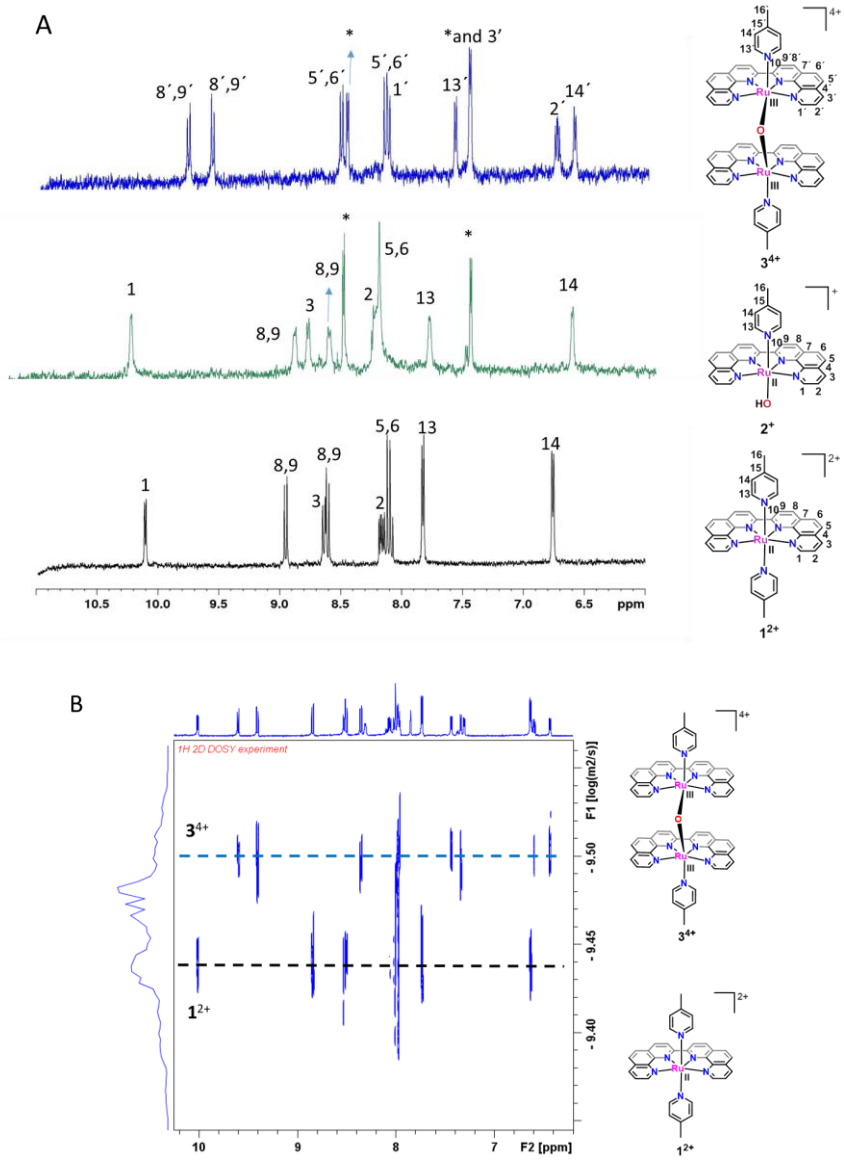

Figure 2. A) Aromatic region for ^{1}H-NMR of $\mathbf{1}^{2+}$, $\mathbf{2}^{+}$ and $\mathbf{3}^{4+}$ at pD 7 phbf solution. * indicates the presence of free pyridine ligand. B) DOSY for $\mathbf{1}^{2+}$ and $\mathbf{3}^{4+}$ at pD 7 phbf solution.

All the resonances in the ^{1}H-NMR spectra for $\mathbf{1}^{2+}$, $\mathbf{2}^{+}$ and $\mathbf{3}^{4+}$ could be unambiguously assigned based on the symmetry of the complexes, the relative integration of the resonances and the COSY spectra and are displayed in Figure 2A. Especially informative are the DOSY spectra recorded for $\mathbf{1}^{2+}$ and $\mathbf{3}^{4+}$ that are shown in Figure 2B where a hydrodynamic radius of 9.44 nm^2/s and 9.50 nm^2/s are obtained for $\mathbf{1}^{2+}$ and $\mathbf{3}^{4+}$ respectively in agreement with the dimeric nature of the latter (9.50 nm^2/s is reported for related dinuclear Ru complexes).[36]

Complexes **1-3** were also characterized by UV-vis spectroscopy that is exhibited in Figure 3. The mononuclear complexes show the typical MLCT at 450-600 nm region together with pi-pi* ligand based transitions at the UV zone. In addition, complex $\mathbf{3}^{4+}$ show a band at 790 nm typical of Ru(III)-oxo bridged complexes. [37]

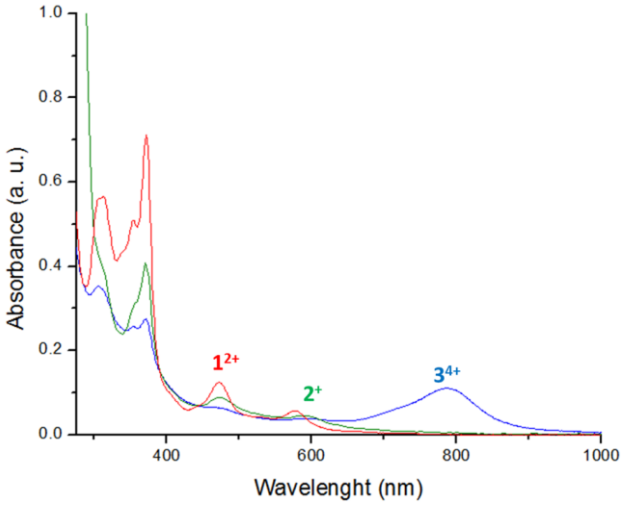

Figure 3. UV-vis spectra of $\mathbf{1}^{2+}$, $\mathbf{2}^{+}$ and $\mathbf{3}^{4+}$ (50 µM) in aqueous solution at pH 7 phbf solution.

3.2-Kinetic analysis of the substitution and dimerization process at pH 7

In order to gain further insights into the sequence of reactions that occur after the oxidation of $\mathbf{1}^{2+}$, a thorough kinetic analysis was carried out using $\mathbf{1}^{2+}$ and a commonly used oxidant such as $NaIO_4$. The kinetic study of the oxidation process was explored under pseudo-first order conditions, i.e., at 7–20 equivalent excesses

of $NaIO_4$ over the concentration of $\mathbf{1}^{2+}$ (0.125×10^{-4} M). The rapid-scan stopped-flow mixing of the solutions of $\mathbf{1}^{2+}$ and the oxidant resulted in spectral changes which indicate the occurrence of three consecutive reactions (Figure 4). The first two reactions are described by the decrease of the absorbance ascribed to the Ru^{II} species with concomitant formation of a new intermediate exhibiting a broad and low-intensity band at 680 nm (Figure 4A). The latter is characteristic for the formation of hydroxido substituted Ru^{III} species, i.e. Ru^{III}-OH intermediate $[Ru^{III}(bpn)(pic)(OH)]^{2+}$, $\mathbf{2}^{2+}$, as indicated in Scheme 1 and 2. The fast reactions are followed by the third, significantly slower reaction which is accompanied by the spectral changes pointing to the formation of Ru^{III} dimer species $\mathbf{3}^{4+}$, as a final product (characteristic bands at 700-800 nm, Figure 4B).

The kinetic traces (at λ = 370 nm) recorded at various concentrations of the oxidant for the first fast step clearly display biphasic behavior and were well fitted to two-exponential function resulting in the pseudo-first order constants, k_{obs1} and k_{obs2}, for the first (oxidation) and second reaction (substitution), respectively.

As shown in Figure 4C, the fast step of the oxidation reaction was significantly accelerated by the higher concentrations of $NaIO_4$. The values of k_{obs1} increase with increasing concentrations of oxidant and the plot of k_{obs1} values vs $[NaIO_4]$ results in the straight line with no meaningful intercept, meaning the rate of the reverse reaction is close to zero (Figure 4C, Figure S19 and Figure S20). The latter indicates that the studied kinetics exhibits no contribution from the reverse reaction under the selected experimental conditions. Therefore, the pseudo-first order constant, k_{obs1}, can be expressed as follows:

$$k_{obs1} = k_1[NaIO_4] \qquad \text{(Eq. 1)}$$

where k_1 represents the second order constant for the forward reaction of $[Ru^{III}(bpn)(pic)_2]^{3+}$, $\mathbf{1}^{3+}$, formation (Scheme 2).

The second-order constant, k_1, obtained from the slope of the linear fit is equal to (2.95 ± 0.1) x 10^2 $M^{-1}s^{-1}$ at 25 °C and pH 7.2. The values of k_{obs2} obtained for the second reaction at various [$NaIO_4$] do not show oxidant concentration dependence. It means that k_{obs2} value remains constant under various [$NaIO_4$] and it is equal to (4.98 ± 0.22) x 10^{-3} s^{-1} at pH 7.2 and 25 °C. This result is in line with the expectation that the second reaction must involve the substitution of picoline ligand in $\mathbf{1}^{3+}$ by the hydroxido ligand to form the intermediate $\mathbf{2}^{2+}$, also labeled as Ru^{III}-OH^{2+}, (Scheme 2).

Finally, the kinetics of the last, slowest reaction involving dimerization of two molecules of $\mathbf{2}^{2+}$ to form the final product $\mathbf{3}^{4+}$, also labeled as Ru^{III}-O-$^{III}Ru^{4+}$, (Eq. 2) was explored by the use of the initial velocities, v_{init}, at low temperature (5 °C) to slow down the formation of the dimer and allow the generation of a significant concentration of $\mathbf{2}^{2+}$.

$$2\ Ru^{III}\text{-}OH^{2+} \underset{k_b}{\overset{k_{dimer}}{\rightleftharpoons}} Ru^{III}\text{-O-}^{III}Ru^{4+} + H_2O \quad \text{(Eq. 2)}$$

$\mathbf{2}^{2+}$ $\mathbf{3}^{4+}$

VI

The rate constant labeled as k_{dimer} represents the second order rate constant for the dimerization reaction (Eq. 2). The value of v_{init} was determined from the initial part of dimerization reaction where the absorbance changes ascribed to the formation of $\mathbf{3}^{4+}$, display linear dependence vs time (Figure S21). It results that v_{init} is equal to 4.69 x 10^{-9} M s^{-1} at 5 °C and pH 7.2. In order to calculate the value of k_{dimer} the initial concentration of $\mathbf{2}^{2+}$ in the solution, $[\mathbf{2}^{2+}]_{init}$, was determined from the spectral changes accompanying the formation of $\mathbf{2}^{2+}$ and the known molecular extinction coefficient for the starting Ru^{II} complex $\mathbf{1}^{2+}$ (Figure S20, Figure S21, Table S1 and Table S2). It follows that the second order rate constant for the dimerization reaction is equal to 1.35 ± 0.02 $M^{-1}s^{-1}$ at pH 7.2 at 5 °C. The value of k_{dimer} was also calculated in a similar way but with the use of spectroelectrochemical experiments

in which the intermediate $\mathbf{2}^{2+}$ was generated by the applied potential of 1.4 V at 5 °C.

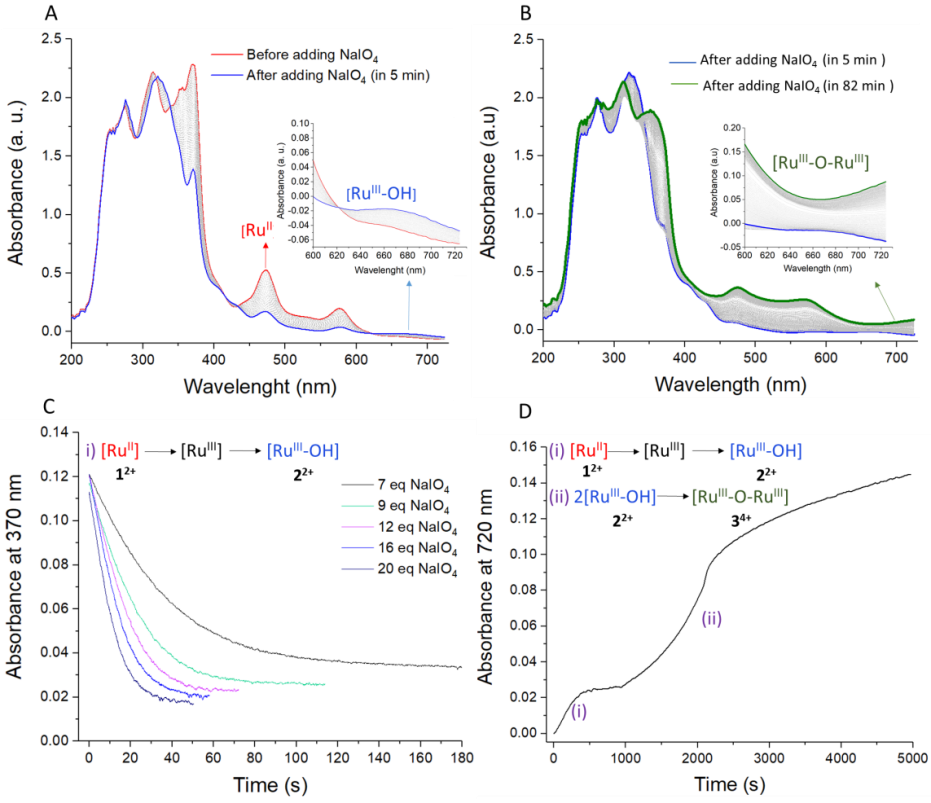

Figure 4. A) Spectral changes of a solution of $\mathbf{1}^{2+}$ before (red) and 5 minutes after (blue) adding 2 eq $NaIO_4$ at 25 °C. B) Spectral changes of a solution of $\mathbf{1}^{2+}$ in 5 minutes (blue) and 82 minutes (green) after adding 2 eq $NaIO_4$ at 5 °C. The gray spectra in A and B show the spectral changes every 26 seconds. C) Kinetic traces recorded at 370 nm at various concentrations of oxidant (($NaIO_4$:7-20 eq), ([$NaIO_4$] = (8.75 – 25) x 10^{-5} M)) and a constant concentration of $\mathbf{1}^{2+}$ (0.125 x 10^{-4} M) at pH 7.2 phbf solution and 25 °C. The experimental data were fitted to 2-exponential function. D) Kinetic traces recorded at 729 nm during 82 min after adding 2 eq $NaIO_4$ at pH 7.2 phbf solution and 5 °C.

The obtained values of k_{dimer} using the spectroelectrochemical experiment equal to 1.40 and 1.54 $M^{-1}s^{-1}$ at pH 7.2 and 9.0, respectively at 5 °C, and are in line with the value found in the chemical oxidation experiments (Figure S22, S23). Scheme 2

summarizes the rate constants obtained for all the processes involved in the chemical oxidation of $\mathbf{1}^{2+}$ at pH 7.

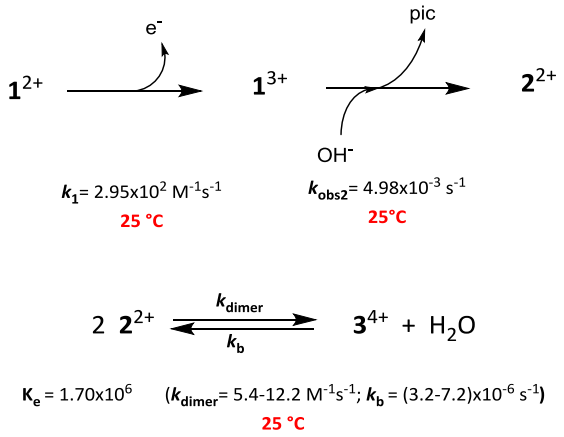

Scheme 2. Summary of the kinetics and thermodynamics involved in the sequence of reactions that occur after the oxidation of $\mathbf{1}^{2+}$.

In order to calculate the equilibrium constant for the dimerization reaction (K_e, Eq. 3) and the second-order rate constant for the reverse reaction (k_b) (Eq. 2), the equilibrium concentrations of Ru^{III}-OH^{2+}, $[Ru^{III}\text{-}OH^{2+}]_e$, and of Ru^{III}-O-$^{III}Ru^{4+}$, $[Ru^{III}\text{-}O\text{-}^{III}Ru^{4+}]_e$, were calculated from the spectral changes after adding various concentrations of oxidant ($NaIO_4$) at 25 °C (see SI for the applied calculation approach).

$$K_e = [Ru^{III}\text{-}O\text{-}^{III}Ru^{4+}]_e \times [H_2O] / [Ru^{III}\text{-}OH^{2+}]_e^2 \quad \text{(Eq. 3)}$$

A plot of $[Ru^{III}\text{-}O\text{-}^{III}Ru^{4+}]_e$ vs $[Ru^{III}\text{-}OH^{2+}]_e^2$ gives a linear dependence (Figure S24). The slope of this plot multiplied by the $[H_2O]$ results in $K_e = (1.7 \pm 0.1) \times 10^6$ at pH 7.2 and 25 °C. The value of k_b for the dimerization reaction can be calculated from the relationship $k_b = k_{dimer}/K_e$. Since the value of $k_{dimer} = 1.35\ M^{-1}s^{-1}$ was measured at 5 °C it was first extrapolated to 25 °C by applying Q_{10} temperature coefficient of 2 – 3. Assuming that $k_{dimer} \sim 5.4 – 12.2\ M^{-1}s^{-1}$ at 25 °C, the second-order rate constant for the reverse reaction of Ru^{III}-OH^{2+} dimerization, k_b, can be estimated to be between

3.2 x 10^{-6} and 7.2 x 10^{-6} $M^{-1}s^{-1}$ at this temperature. Finally, the pseudo-first order rate constant, k_{obs}, for the reverse reaction will be in the range 2 - 4 x 10^{-4} s^{-1} at 25 °C under selected reaction conditions.

3·3-Redox properties of 1-3 and water oxidation catalysis

The redox properties of the complexes described in this work were investigated in organic solvents and in aqueous solutions by means of electrochemical techniques such as cyclic voltammetry (CV), differential pulse voltammetry (DPV) and bulk electrolysis experiments. All potentials in this work were measured vs mercury sulfate electrode (MSE) and reported vs the normal hydrogen electrode (NHE).

The CV of $\mathbf{1}^{2+}$ (1 mM) recorded in TFE is presented in Figure S25 and shows a chemically reversible and electrochemically quasi-reversible wave at 1.44 V ($E_{p,a}$ = 1.48 V, $E_{p,c}$ = 1.40 V) associated with the $Ru^{III/II}$ couple.[38] In sharp contrast, the CV of $\mathbf{1}^{2+}$ (1 mM) in aqueous solution at pH 7 shown in Figure 5 (top, red trace), displays a chemically irreversible process with $E_{p,a}$ = 1.22 V, $E_{p,c}$ = 1.15 V, that clearly indicates the presence of chemical reactions coupled to the first electron transfer. Indeed, a bulk electrolysis of $\mathbf{1}^{2+}$ at 1.45 V for 2 h generates the dimer $\mathbf{3}^{4+}$ quantitatively as indicated in the previous section. A CV of $\mathbf{3}^{4+}$ is also shown in Figure 5 (bottom, blue trace), and shows the presence of several redox processes that can be rationalized based on the presence of a square mechanism where the dimer $\mathbf{3}^{4+}$, and monomer $\mathbf{2}^{+}$ interconvert very fast during the CV time scale upon reduction and oxidation respectively as shown in Scheme 3.

The CV in the bottom of Figure 5, shows that the formation of the monomer $\mathbf{2}^{+}$ occurs upon scanning reductively where two waves appear that can be tentatively assigned to the $Ru^{III,III/III,II}$ and $Ru^{III,II/II,II}$ processes and whose cathodic peaks appear at 0.40 and 0.21 V respectively. The reduction processes are associated with the formation of $\mathbf{2}^{+}$ in agreement with the bulk electrolysis experiment carried out at

0.35 V indicated in the synthesis section. The one electron oxidation of $\mathbf{2}^{+}$ wave to generate $\mathbf{2}^{2+}$, appears at $E_{p,a}$ = 0.92 V and triggers the formation of the dimer $\mathbf{3}^{4+}$.

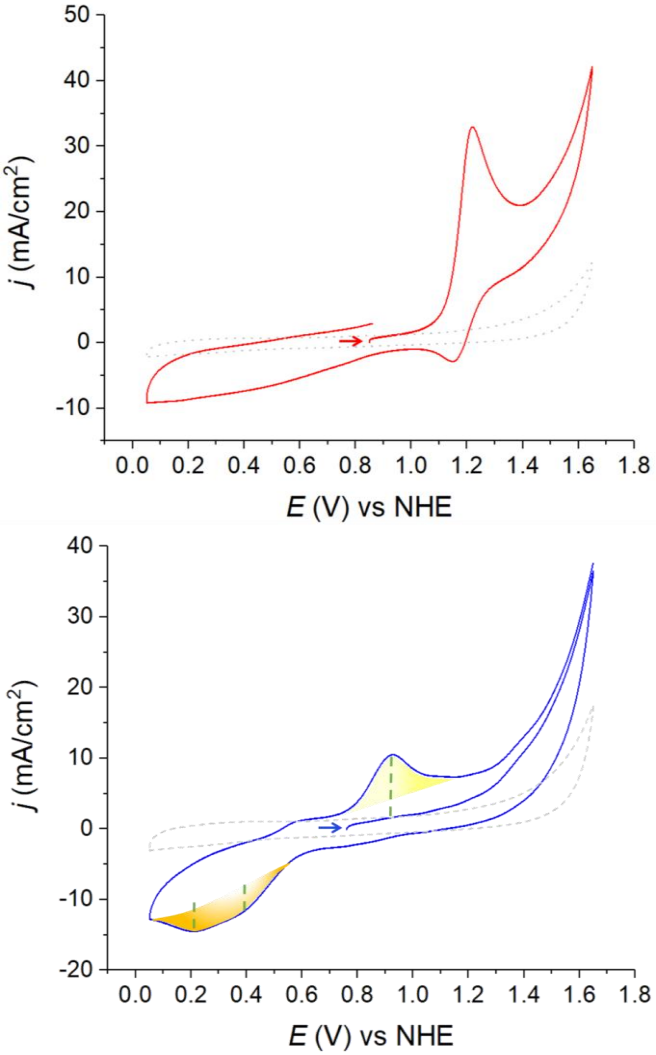

Figure 5. CV of complex $\mathbf{1}^{2+}$ (1.34 mM, red trace) and $\mathbf{3}^{4+}$ (0.67 mM, blue trace) in an aqueous pH 7 phbf solution. The yellow highlight indicates the zone of transformation to the dimer $\mathbf{3}^{4+}$ whereas the orange one that to the monomer $\mathbf{2}^{+}$. Conditions: v = 100 mV/s, WE: glassy carbon electrode; CE: platinum electrode; RE: Hg/Hg_2SO_4. Horizontal arrows show the starting point of the scan.

Thus, the monomer, $\mathbf{2}^{+}$, vastly predominates at low potentials and the dimer, $\mathbf{3}^{4+}$, at high potentials. The yellow highlight indicates the zone where the monomer is

transformed into the dimer and the orange highlight indicates just the opposite. With the equilibrium constant obtained for the dimerization process, K^{III} = (1.7 ± 0.1) x 10^6, and the thermodynamic values for the monomer and dimer redox couples, the equilibrium constant for the transformation of the dimer into the monomer can be calculated giving a value of K^{II} = 1.05.

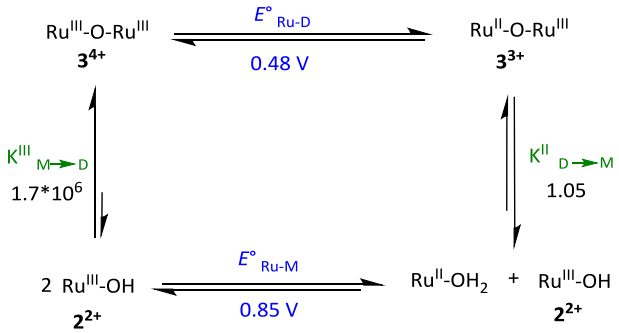

Scheme 3. Square mechanism related to the Monomer – Dimer interconversion.

The dimerization process at oxidation state III for $\mathbf{2}^{2+}$, prevents significant access to higher oxidation states such as $[Ru^{V}(O)(bpn)(pic)]^{3+}$, needed for the water oxidation catalysis using this type of complexes.[20] However, it is interesting to realize that at higher potentials in the range of 1.4-1.6 V, the current density is significantly higher than that of the blank (gray trace in Figure 5, bottom) and thus indicates the potential oxidation of water to dioxygen. This suggests that even if the dimerization process at high potential precludes the formation of $[Ru^{V}(O)(bpn)(pic)]^{3+}$, as the dominant species, a small fraction in equilibrium with the dimer is still present and thus can be responsible for the electrocatalytic current observed. Indeed, in the electrochemical synthesis of the dimer carried out at 1.45 V a total of 5 equivalents were passed which indicates that the extra equivalents were used potentially for catalytic water oxidation (Figures S29 and S30).

Further evidence for the access to high oxidation states by the monomer, even if in very low concentrations, come from a combined bulk electrolysis and rR experiment

using isotopically labeled H_2O. We carried out a bulk electrolysis of $\mathbf{1}^{2+}$ at 1.45 V that generates mainly the dimer, in both H_2O^{16} and H_2O^{18} (98%). Figure 6 shows the two rR spectra where a vibration at 844 cm^{-1} with H_2O^{16} shifts to 801 cm^{-1} in H_2O^{18}. Both, the energy of the vibration and the 43 cm^{-1} isotopic shift are consistent with the vibration of the Ru=O group in $[Ru^{IV}(O)(bpn)(pic)]^{2+}$ that can be considered as the resting species during the electrocatalytic water oxidation cycle.[23c, 36, 39] And additional vibration that presents an isotopic shift of 28 cm^{-1} (790 cm^{-1} in H_2O^{16}; 762 cm^{-1} in H_2O^{18}) appears in the spectra but its assignment has not been elucidated yet.

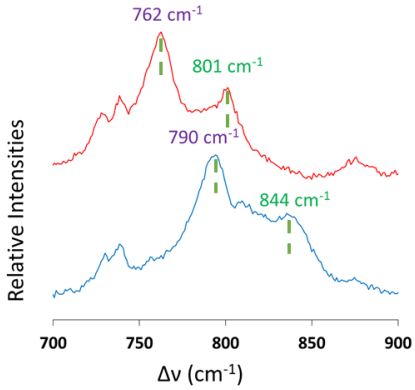

Figure 6. rRaman spectra of an aqueous solution of $\mathbf{3}^{4+}$ prepared *in situ* from $\mathbf{1}^{2+}$ after a bulk electrolysis at E_{app} = 1.45 V at pH 7 phbf solution in H_2O^{16} (blue) and H_2O^{18} (red). Inset shows enlargement of the 700-900 cm^{-1} region.

The redox properties of $\mathbf{1}^{2+}$ in an aqueous pH 1 (0.1 M TA:TFE (2:1)) solution are presented in Figure 7 (left). A nearly reversible wave associated with the III/II couple appears at 1.35 V. However, on the returning scan a new cathodic wave emerges at $E_{p,c}$= 0.78 V that manifests the presence of a new species associated with a chemical reaction following the generation of the Ru(III) complex. CPE of $\mathbf{1}^{2+}$ at 1.65 V under these conditions shows the presence of complex mixtures of species. Among them is the formation of $[Ru^{II}(bpn)(pic)(H_2O)](CF_3SO_3)_2$ that comes out of the solution as dark red crystals (See Figure 1 for the X-ray plot). In addition, a UV-vis of the solution after the bulk electrolysis (Figure S39) shows a band at 810 nm that is

typical of oxo-bridge dimers and thus suggests that at this pH the dimer and monomer coexist in equilibria. Finally, a manometric analysis using 2 mL of a 100 mM CAN (0.2 mmols) solution at pH 1 TA over a 2 mL of 1 mM of $\mathbf{1}^{2+}$ (2 μmols) aqueous pH 1 0.1 M TA:TFE (2:1) solution, generates 20 TONs of O_2 assuming all the pressure is due entirely to the formation of dioxygen. It is important to realize here the presence of about 150 s induction period that suggest the initial transformation of $\mathbf{1}^{2+}$ into the corresponding catalytically active species. Attempts to identify the nature of the active species have not been conclusive.

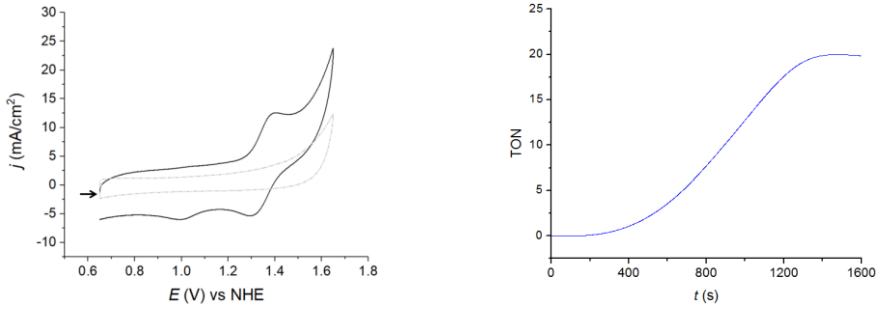

Figure 7. Left, black trace, CV of $\mathbf{1}^{2+}$ dissolved in aqueous pH 1 0.1 M TA:TFE (2:1). Gray trace, CV of the bare glassy carbon electrode under the same conditions. Conditions: v = 100 mV/s, WE: glassy carbon electrode; CE: platinum electrode; RE: Hg/Hg_2SO_4. Right, manometric profile over time observed upon the addition of 2 mL of a 100 mM CAN (0.2 mmols) solution at pH 1 0.1 M TA over a 2 mL of 1 mM of $\mathbf{1}^{2+}$ (2 μmols) aqueous pH 1 0.1 M TA:TFE (2:1) solution.

VI

3-Summary and Conclusions

The synthesis of mononuclear complex with a new N_4 tetradenate equatorial ligand $[Ru^{II}(bpn)(pic)_2]^{2+}$, $\mathbf{1}^{2+}$, is reported. One electron oxidation of $\mathbf{1}^{2+}$ at pH 7 triggers a set of reactions that yield the quantitative formation of the oxo-bridge complex $\{[Ru^{III}(bpn)(pic)]_2(\mu\text{-}O)\}^{4+}$, $\mathbf{3}^{4+}$. Further, reduction of this dimer quantitively yields the formation of the mononuclear Ru-hydroxido complex $[Ru^{II}(bpn)(pic)(OH)]^{+}$, $\mathbf{2}^{+}$. All these complexes have been thoroughly characterized by means of spectroscopic and electrochemical techniques and an X-ray structure have been solved for $\mathbf{1}^{2+}$ and the protonated $\mathbf{2}^{+}$ complex, $[Ru^{II}(bpn)(pic)(H_2O)]^{2+}$. The sequence of reactions that

occur after one electron oxidation of $\mathbf{1}^{2+}$, has been kinetically characterized and is summarized in Scheme 2. Surprisingly it involves the substitution of one of the axial picoline ligands and the formation of the oxo-bridge dimer, in sharp contrast to their $[Ru^{II}(N_4)(pic)_2)]^{2+}$ analogues with the pbp and qpy ligands. In the latter case, the main reaction occurring involves ligand oxidation to form the corresponding N-oxides which is not observed with $\mathbf{1}^{2+}$ at pH 7.

Generally Ru(III)N_6 polypyridyl complexes such as $[Ru(bpy)_3]^{3+}$,[40] are stable at least within the CV timescale showing chemically reversible and electrochemically reversible or quasireversible behavior of their III/II couples. However, the redox potentials of the III/II couples[41] are very high within the range of 1.1-1.3 V. For this reason the Ru(III) oxidation state for this complexes is a highly oxidizing species that has been used in many instances as a sacrificial agent in combination with water oxidation catalysts for the generation of dioxygen.[42] In the absence of a catalyst or substrate, the highly oxidizing Ru(III) species are not stable under long periods of time reacting with the solvent via one electron process and returning to its initial Ru(II) oxidation state. This is the main pathway observed for $[Ru(bpy)_3]^{2+}$ in aqueous solutions where at pH > 5 generates HO· radicals that can attack the coordinated bpy ligands.[43] Other pathways can involve Ru-N O-atom insertion and formation of N-oxide ligands as recently proposed.[44]

In addition, when the transformation involves the formation of a Ru-OH_2 or Ru-OH species it can lead to other ligand based transformation such as C-H O-atom insertion in a bimolecular or unimolecular manner.[45]

For the case of $[Ru^{II}(N_4)(pic)_2)]^{2+}$ complexes with N_4 = pbp, qpy and bpn there are two main pathways that take place depending on the ligands that are depicted in Scheme 4 and that involve Ru-N O-atom insertion for pbp and qpy, and axial ligand substitution for bpn. This radically different reactivity can be mainly associated with the low energy barrier for the C-C bond rotation of the external pyridyl groups of

tetradentate ligand pbp and qpy (see arrows in Chart I). This low C-C energy rotation barrier is indispensable for the formation of the N-oxide bond as represented in Scheme 4.

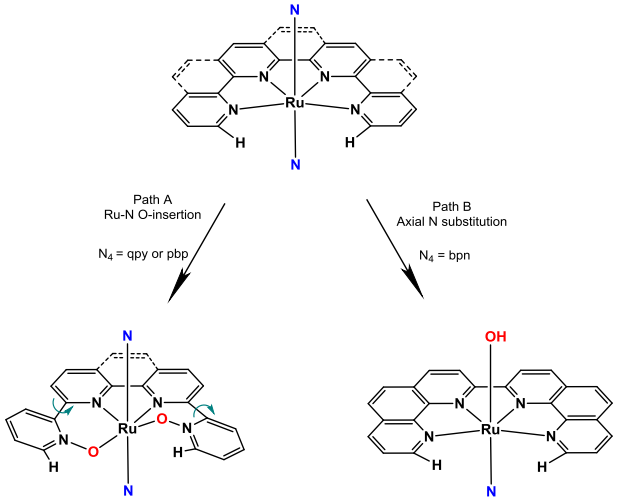

Scheme 4. Competing pathways for Ru(III)N_6 complexes with N_4 equatorial ligands. Blue N represent axial picoline ligands. The green arrows show low energy C-C rotation axis.

Further, the corresponding N-oxide $[Ru(N_4\text{-}O_2)(pic)_2)]^{2+}$ complexes present a highly distorted octahedral geometry, due to the formation of nearly flat 6-member rings (Ru-N-C-C-N-O) containing 4 atoms with sp^2 hybridization, that would be highly unfavorable for the bpn analogue. For the bpn complex $\mathbf{1}^{2+}$, the restricted rotation imposed by the bpn ligand also prevents the interaction of a potential aquo/hydroxido ligand with the Ru metal center at the equatorial zone, due to the steric constrains associated with the presence of the N-alpha C-H bonds schematically shown in Scheme 4. This steric obstruction would also be unfavorable for a potential CN7 coordination at higher oxidation states such Ru(IV) and Ru(V). These steric impediments are avoided in the case of qpy and pbp via the easy rotation of the external pyridyl rings.

Another interesting yet a bit deceiving property from a catalytic perspective, is the square mechanism that operates between the Ru(II) monomer $\mathbf{2}^{2+}$ and the Ru(III) dimer $\mathbf{3}^{4+}$. As represented in Scheme 2, once the monomer is oxidized by one electron to Ru(III) it immediately dimerizes via oxo-bridge formation. In turn when the dimer is reduced to Ru(II) it returns back to the initial monomer. This is an interesting property of this complex, however the fact that the monomer dimerizes at high oxidation states precludes the significant formation of the monomer at high oxidation states such as Ru(IV) and Ru(V) because it is in competition with the dimerization reaction. Since the high oxidation states are responsible for the O-O bond formation, the square mechanism acts as a gate that significantly blocks the access to the catalytic cycle for water oxidation. Nevertheless, even if the concentration of active species is low it is sufficient to observe the Ru(IV)=O active species by rR spectroscopy and hence to display electrocatalytic activity as evidenced in the CV and CPE experiments.

The redox properties of $\mathbf{1}^{2+}$ were also investigated in acidic pH using similar strategies. At low pH the complete monomer-dimer interconversion as a function of oxidation state described at pH 7, is not occurring and comparable amounts monomer and dimer seem to coexist. In addition, NMR monitoring of this reaction shows a very complex spectra, suggesting that besides axial ligand substitution and Ru-OH_2 formation, other reactions might also be operative here.

References

1. (a) Cotton, F. A.; Wilkinson, G., *Advanced Inorganic Chemistry*. Wiley eastern: 1962; (b) Greenwood, N.; Hughes, A.; Fox, M.; Dillon, K.; Wade, K., *Chemistry of the Elements*. Elsevier Science: **2020**.
2. Pagliaro, M.; Campestrini, S.; Ciriminna, R., Ru-based oxidation catalysis. *Chemical Society Reviews* **2005,** *34* (10), 837-845.
3. Ward, M. D.; McCleverty, J. A., Non-innocent behaviour in mononuclear and polynuclear complexes: consequences for redox and electronic spectroscopic properties. *Journal of the Chemical Society, Dalton Transactions* **2002,** (3), 275-288.
4. (a) Yersin, H.; Vogler, A., *Photochemistry and Photophysics of Coordination Compounds*. Springer Berlin Heidelberg: 2012; (b) Juris, A.; Balzani, V.; Barigelletti, F.; Campagna, S.; Belser, P.; von

Zelewsky, A., Ru(II) polypyridine complexes: photophysics, photochemistry, eletrochemistry, and chemiluminescence. *Coordination chemistry reviews* **1988,** *84*, 85-277.

5. (a) Carlin, R. L., *Magnetochemistry*. Springer Berlin Heidelberg: 2012; (b) Nakamura, T.; Asada, M.; Yoshida, M.; Kondo, M.; Masaoka, S., Possibility of Dielectric Material: Magnetic Resonance Study of Oxo-Bridged Dinuclear Ruthenium Mixed-Valence Complex. *ChemistrySelect* **2018,** *3* (37), 10526-10531.

6. (a) Abid, M.; Shamsi, F.; Azam, A., Ruthenium complexes: an emerging ground to the development of metallopharmaceuticals for cancer therapy. *Mini reviews in medicinal chemistry* **2016,** *16* (10), 772-786; (b) van Rijt, S. H.; Sadler, P. J., Current applications and future potential for bioinorganic chemistry in the development of anticancer drugs. *Drug discovery today* **2009,** *14* (23-24), 1089-1097.

7. Dixneuf, P. H.; Bruneau, C., *Ruthenium in Catalysis*. Springer International Publishing: **2014**.

8. Hoveyda, A. H.; Gillingham, D. G.; Van Veldhuizen, J. J.; Kataoka, O.; Garber, S. B.; Kingsbury, J. S.; Harrity, J. P., Ru complexes bearing bidentate carbenes: from innocent curiosity to uniquely effective catalysts for olefin metathesis. *Organic & biomolecular chemistry* **2004,** *2* (1), 8-23.

9. (a) Bosson, J.; Poater, A.; Cavallo, L.; Nolan, S. P., Mechanism of racemization of chiral alcohols mediated by 16-electron ruthenium complexes. *Journal of the American Chemical Society* **2010,** *132* (38), 13146-13149; (b) Markó, I. E.; Gautier, A.; Tsukazaki, M.; Llobet, A.; Plantalech-Mir, E.; Urch, C. J.; Brown, S. M., Novel and efficient isomerization of allylic alcohols promoted by a tetrapropylammonium perruthenate catalyst. *Angewandte Chemie International Edition* **1999,** *38* (13-14), 1960-1962.

10. Mola, J.; Pujol, D.; Rodríguez, M.; Romero, I.; Sala, X.; Katz, N.; Parella, T.; Benet-Buchholz, J.; Fontrodona, X.; Llobet, A., Synthesis and Structure of Novel RuII–N≡C–Me Complexes and their Activity Towards Nitrile Hydrolysis: An Examination of Ligand Effects. *Australian journal of chemistry* **2010,** *62* (12), 1675-1683.

11. Gersten, S. W.; Samuels, G. J.; Meyer, T. J., Catalytic oxidation of water by an oxo-bridged ruthenium dimer. *Journal of the American Chemical Society* **1982,** *104* (14), 4029-4030.

12. Baratta, W.; Da Ros, P.; Del Zotto, A.; Sechi, A.; Zangrando, E.; Rigo, P., Cyclometalated Ruthenium(II) Complexes as Highly Active Transfer Hydrogenation Catalysts. *Angewandte Chemie International Edition* **2004,** *43* (27), 3584-3588.

13. Ono, T.; Planas, N.; Miró, P.; Ertem, M. Z.; Escudero-Adán, E. C.; Benet-Buchholz, J.; Gagliardi, L.; Cramer, C. J.; Llobet, A., Carbon dioxide reduction catalyzed by dinuclear ruthenium polypyridyl complexes. *ChemCatChem* **2013,** *5* (12), 3897-3903.

14. Watson, A. J.; Maxwell, A. C.; Williams, J. M., Ruthenium-catalyzed oxidation of alcohols into amides. *Organic letters* **2009,** *11* (12), 2667-2670.

15. (a) Groves, J. T.; Quinn, R., Aerobic epoxidation of olefins with ruthenium porphyrin catalysts. *Journal of the American Chemical Society* **1985,** *107* (20), 5790-5792; (b) Di Giovanni, C.; Poater, A.; Benet-Buchholz, J.; Cavallo, L.; Solà, M.; Llobet, A., Dinuclear Ru–Aqua complexes for selective epoxidation catalysis based on supramolecular substrate orientation effects. *Chemistry–A European Journal* **2014,** *20* (14), 3898-3902.

16. Matheu, R.; Ertem, M. Z.; Benet-Buchholz, J.; Coronado, E.; Batista, V. S.; Sala, X.; Llobet, A., Intramolecular proton transfer boosts water oxidation catalyzed by a Ru complex. *Journal of the American Chemical Society* **2015,** *137* (33), 10786-10795.

17. Llobet, A., *Molecular water oxidation catalysis: a key topic for new sustainable energy conversion schemes*. John Wiley & Sons: **2014**.

18. Savini, A.; Bucci, A.; Bellachioma, G.; Rocchigiani, L.; Zuccaccia, C.; Llobet, A.; Macchioni, A., Mechanistic aspects of water oxidation catalyzed by organometallic iridium complexes. *European Journal of Inorganic Chemistry* **2014,** *2014* (4), 690-697.

19. (a) Duan, L.; Bozoglian, F.; Mandal, S.; Stewart, B.; Privalov, T.; Llobet, A.; Sun, L., A molecular ruthenium catalyst with water-oxidation activity comparable to that of photosystem II. *Nature chemistry* **2012,** *4* (5), 418-423; (b) Sander, A. C.; Maji, S.; Francàs, L.; Böhnisch, T.; Dechert, S.; Llobet,

A.; Meyer, F., Highly Efficient Binuclear Ruthenium Catalyst for Water Oxidation. *ChemSusChem* **2015,** *8* (10), 1697-1702; (c) Garrido-Barros, P.; Gimbert-Suriñach, C.; Matheu, R.; Sala, X.; Llobet, A., How to make an efficient and robust molecular catalyst for water oxidation. *Chemical Society Reviews* **2017,** *46* (20), 6088-6098.

20. Matheu, R.; Garrido-Barros, P.; Gil-Sepulcre, M.; Ertem, M. Z.; Sala, X.; Gimbert-Suriñach, C.; Llobet, A., The development of molecular water oxidation catalysts. *Nature Reviews Chemistry* **2019,** *3* (5), 331-341.

21. (a) Maji, S.; López, I.; Bozoglian, F.; Benet-Buchholz, J.; Llobet, A., Mononuclear ruthenium–water oxidation catalysts: discerning between electronic and hydrogen-bonding effects. *Inorganic chemistry* **2013,** *52* (7), 3591-3593; (b) Llobet, A., Synthesis, spectral and redox properties of a new series of aqua complexes of ruthenium(II). *Inorganica Chimica Acta* **1994,** *221* (1), 125-131.

22. López, I.; Ertem, M. Z.; Maji, S.; Benet-Buchholz, J.; Keidel, A.; Kuhlmann, U.; Hildebrandt, P.; Cramer, C. J.; Batista, V. S.; Llobet, A., A Self-Improved Water-Oxidation Catalyst: Is One Site Really Enough? *Angewandte Chemie International Edition* **2014,** *53* (1), 205-209.

23. (a) Pineda-Galvan, Y.; Ravari, A. K.; Shmakov, S.; Lifshits, L.; Kaveevivitchai, N.; Thummel, R.; Pushkar, Y., Detection of the site protected 7-coordinate Ru^{V}= O species and its chemical reactivity to enable catalytic water oxidation. *Journal of Catalysis* **2019,** *375*, 1-7; (b) Zong, R.; Thummel, R. P., 2,9-Di-(2'-pyridyl)-1,10-phenanthroline: A Tetradentate Ligand for Ru(II). *Journal of the American Chemical Society* **2004,** *126* (35), 10800-10801; (c) Moonshiram, D.; Pineda-Galvan, Y.; Erdman, D.; Palenik, M.; Zong, R.; Thummel, R.; Pushkar, Y., Uncovering the role of oxygen atom transfer in Ru-based catalytic water oxidation. *Journal of the American Chemical Society* **2016,** *138* (48), 15605-15616.

24. Liu, Y.; Ng, S.-M.; Yiu, S.-M.; Lam, W. W. Y.; Wei, X.-G.; Lau, K.-C.; Lau, T.-C., Catalytic Water Oxidation by Ruthenium(II) Quaterpyridine (qpy) Complexes: Evidence for Ruthenium(III) qpy-N,N'''-dioxide as the Real Catalysts. *Angewandte Chemie* **2014,** *126* (52), 14696-14699.

25. Corey, E.; Borror, A.; Foglia, T., Transformations in the 1, 10-phenanthroline series. *The Journal of Organic Chemistry* **1965,** *30* (1), 288-290.

26. Riesgo, E. C.; Jin, X.; Thummel, R. P., Introduction of benzo[*h*]quinoline and 1, 10-phenanthroline subunits by friedländer methodology. *The Journal of Organic Chemistry* **1996,** *61* (9), 3017-3022.

27. Zong, R.; Thummel, R. P., 2, 2 '; 9 ', 2 ''-Ter [1, 10] phenanthroline. *Inorganic chemistry* **2005,** *44* (17), 5984-5986.

28. Data collection with APEX II version v2013.4-1. Bruker (**2007**). Bruker AXS Inc., Madison, Wisconsin, USA.

29. Data reduction with Bruker SAINT version V8.30c. Bruker (**2007**). Bruker AXS Inc., Madison, Wisconsin, USA.

30. SADABS: V2012/1 Bruker (**2001**). Bruker AXS Inc., Madison, Wisconsin, USA. Blessing,. *Acta Crystallographica* **1995,** *A51*, 33-38.

31. SHELXT; V2014/4 (Sheldrick **2014**). Sheldrick, G. M., *Acta Crystallographica* **2015,** *A71*, 3-8.

32. SHELXle; C.B. Huebschle, G. M. S., B. Dittrich, SHELXle;. *Journal of Applied Crystallography* **2011,** *44*, 1281-1284.

33. SHELXL; SHELXL-2014/7 (Sheldrick **2014**). Sheldrick, G. M., *Acta Crystallographica* **2015,** *C71*, 3-8.

34. (a) Yagi, M.; Tajima, S.; Komi, M.; Yamazaki, H., Highly active and tunable catalysts for O_2 evolution from water based on mononuclear ruthenium(ii) monoaquo complexes. *Dalton Transactions* **2011,** *40* (15), 3802-3804; (b) Concepcion, J. J.; Jurss, J. W.; Templeton, J. L.; Meyer, T. J., One site is enough. Catalytic water oxidation by $[Ru(tpy)(bpm)(OH_2)]^{2+}$ and $[Ru(tpy)(bpz)(OH_2)]^{2+}$. *Journal of the American Chemical Society* **2008,** *130* (49), 16462-16463.

35. (a) Zhang, G.; Zong, R.; Tseng, H.-W.; Thummel, R. P., Ru (II) Complexes of Tetradentate Ligands Related to 2, 9-Di (pyrid-2 '-yl)-1, 10-phenanthroline. *Inorganic chemistry* **2008,** *47* (3), 990-998; (b) Zong, R.; Wang, B.; Thummel, R. P., *trans*-$[Ru^{II}(dpp)Cl_2]$: A Convenient Reagent for the Preparation of Heteroleptic Ru (dpp) Complexes, Where dpp Is 2,9-Di(pyrid-2'-yl)-1,10-phenanthroline.

Inorganic chemistry **2012,** *51* (5), 3179-3185; (c) Llobet, A.; Hodgson, D. J.; Meyer, T. J., Synthesis, structure, and redox properties of the triaqua(tris(1-pyrazolyl)methane)ruthenium(II) cation. *Inorganic chemistry* **1990,** *29* (19), 3760-3766.

36. López, I.; Ertem, M. Z.; Maji, S.; Benet-Buchholz, J.; Keidel, A.; Kuhlmann, U.; Hildebrandt, P.; Cramer, C. J.; Batista, V. S.; Llobet, A., A Self-Improved Water-Oxidation Catalyst: Is One Site Really Enough? *Angewandte Chemie International Edition* **2014,** *53* (1), 205-209.

37. (a) Yoshida, M.; Kondo, M.; Nakamura, T.; Sakai, K.; Masaoka, S., Three Distinct Redox States of an Oxo-Bridged Dinuclear Ruthenium Complex. *Angewandte Chemie International Edition* **2014,** *53* (43), 11519-11523; (b) Rotzinger, F. P.; Munavalli, S.; Comte, P.; Hurst, J. K.; Graetzel, M.; Pern, F. J.; Frank, A. J., A molecular water-oxidation catalyst derived from ruthenium diaqua bis (2, 2'-bipyridyl-5, 5'-dicarboxylic acid). *Journal of the American Chemical Society* **1987,** *109* (22), 6619-6626.

38. Tong, L.; Zong, R.; Zhou, R.; Kaveevivitchai, N.; Zhang, G.; Thummel, R. P., Ruthenium catalysts for water oxidation involving tetradentate polypyridine-type ligands. *Faraday discussions* **2015,** *185*, 87-104.

39. (a) Yamada, H.; Koike, T.; Hurst, J. K., Water Exchange Rates in the Diruthenium μ-Oxo Ion cis, cis-$[(bpy)_2Ru(OH_2)]_2O^{4+}$. *Journal of the American Chemical Society* **2001,** *123* (51), 12775-12780; (b) Wada, T.; Ohtsu, H.; Tanaka, K., Catalytic Four-Electron Oxidation of Water by Intramolecular Coupling of the Oxo Ligands of a Bis (ruthenium–bipyridine) Complex. *Chemistry–A European Journal* **2012,** *18* (8), 2374-2381.

40. Charboneau, D. J.; Piro, N. A.; Kassel, W. S.; Dudley, T. J.; Paul, J. J., Reprint of: Structural, electronic and acid/base properties of $[Ru(bpy)(bpy(OH)_2)_2]^{2+}$ (bpy= 2, 2′-bipyridine, $bpy(OH)_2$= 4, 4′-dihydroxy-2, 2′-bipyridine). *Polyhedron* **2016,** *114*, 472-481.

41. Lever, A., Electrochemical parametrization of metal complex redox potentials, using the ruthenium (III)/ruthenium (II) couple to generate a ligand electrochemical series. *Inorganic chemistry* **1990,** *29* (6), 1271-1285.

42. (a) Francàs, L.; Matheu, R.; Pastor, E.; Reynal, A.; Berardi, S.; Sala, X.; Llobet, A.; Durrant, J. R., Kinetic Analysis of an Efficient Molecular Light-Driven Water Oxidation System. *ACS Catalysis* **2017,** *7* (8), 5142-5150; (b) Grau, S.; Berardi, S.; Moya, A.; Matheu, R.; Cristino, V.; Vilatela, J. J.; Bignozzi, C. A.; Caramori, S.; Gimbert-Suriñach, C.; Llobet, A., A hybrid molecular photoanode for efficient light-induced water oxidation. *Sustainable Energy & Fuels* **2018,** *2* (9), 1979-1985.

43. Akhtar, U. S.; Tae, E. L.; Chun, Y. S.; Hwang, I. C.; Yoon, K. B., Insights into Decomposition Pathways and Fate of $Ru(bpy)_3^{2+}$ during Photocatalytic Water Oxidation with $S_2O_8^{2-}$ as Sacrificial Electron Acceptor. *ACS Catalysis* **2016,** *6* (12), 8361-8369.

44. (a) Ravari, A. K.; Zhu, G.; Ezhov, R.; Pineda-Galvan, Y.; Page, A.; Weinschenk, W.; Yan, L.; Pushkar, Y., Unraveling the Mechanism of Catalytic Water Oxidation via de Novo Synthesis of Reactive Intermediate. *Journal of the American Chemical Society* **2019**; (b) Liu, Y.; Ng, S. M.; Yiu, S. M.; Lam, W. W.; Wei, X. G.; Lau, K. C.; Lau, T. C., Catalytic Water Oxidation by Ruthenium (II) Quaterpyridine (qpy) Complexes: Evidence for Ruthenium (III) qpy-N, N'''-dioxide as the Real Catalysts. *Angewandte Chemie International Edition* **2014,** *53* (52), 14468-14471.

45. Garrido-Barros, P. F., I.; Farràs, P.; Gimbert-Suriñach, C.; Maseras, F.; Llobet, A, Water as an oxygen source for oxidation reactions from "Catalytic oxidation in organic synthesis". *Edited by Muñiz, K. Thieme Chemistry - Stuttgart* **2017**, 63-77.

Supporting information

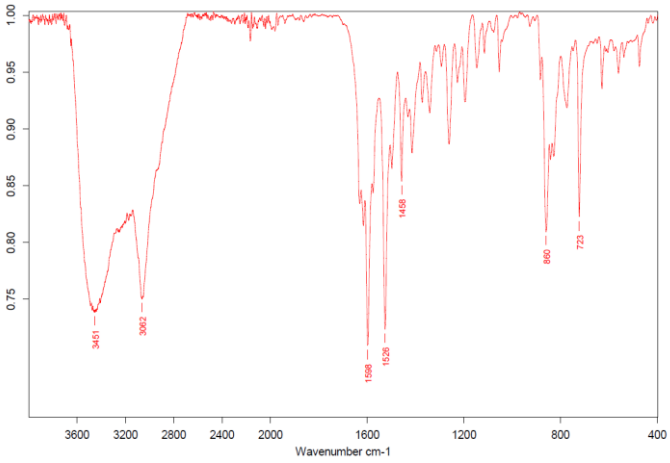

Figure S1. IR spectrum of $[Ru(bpn)Cl_2]Cl$.

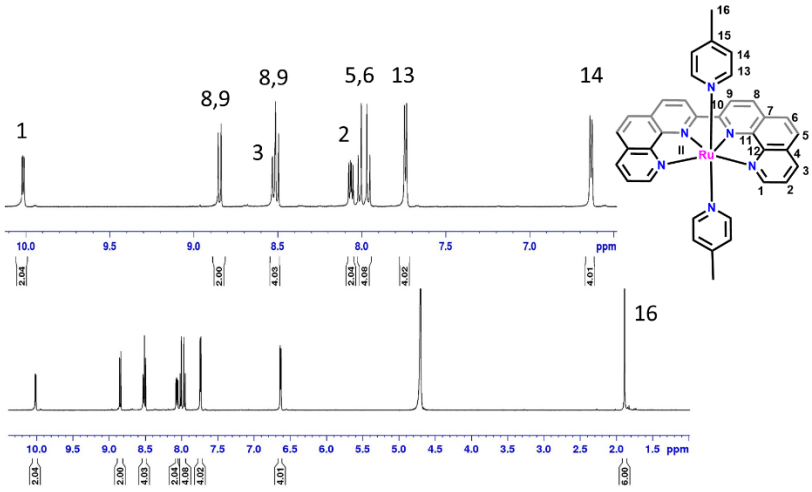

Figure S2. ^1H NMR spectrum of $\mathbf{1}^{2+}$ in D_2O at T= 298K. Inset, enlargement of aromatic region.

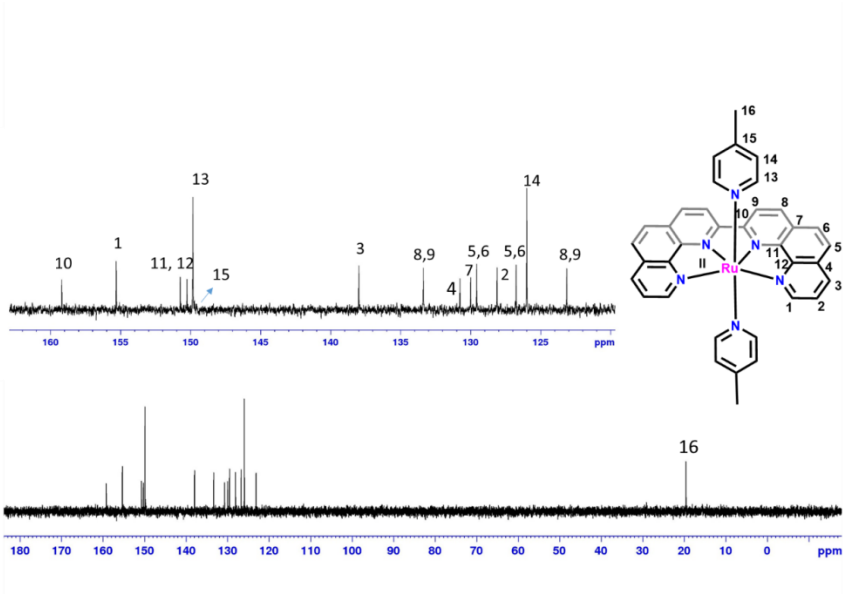

Figure S3. $^{13}C\{H\}$ NMR of $\mathbf{1}^{2+}$ in D_2O at T= 298K. Inset, enlargement of aromatic region.

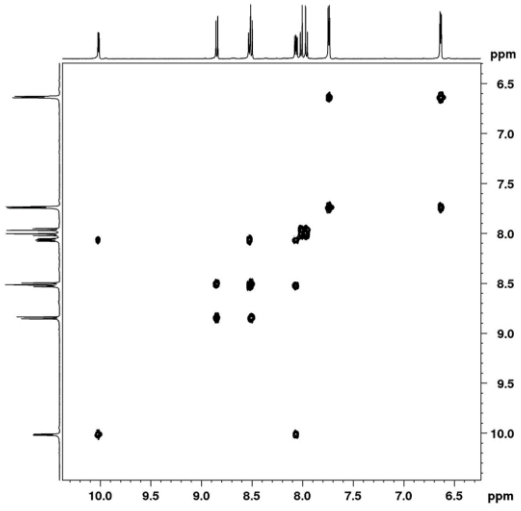

Figure S4. ^{1}H-^{1}H COSY of $\mathbf{1}^{2+}$ in D_2O at T = 298K.

VI

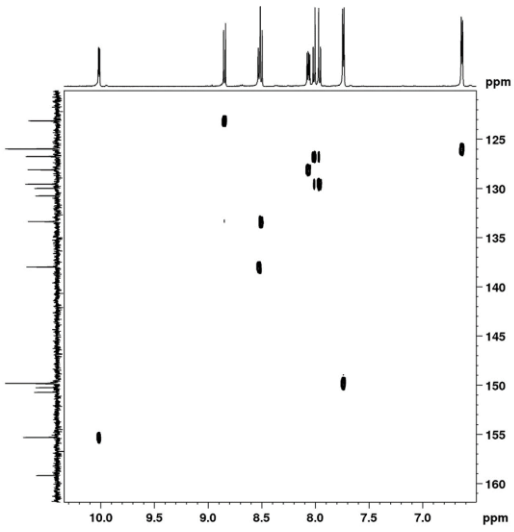

Figure S5. ^{1}H-^{13}C HSQC NMR of $\mathbf{1}^{2+}$ in D_2O at T= 298K.

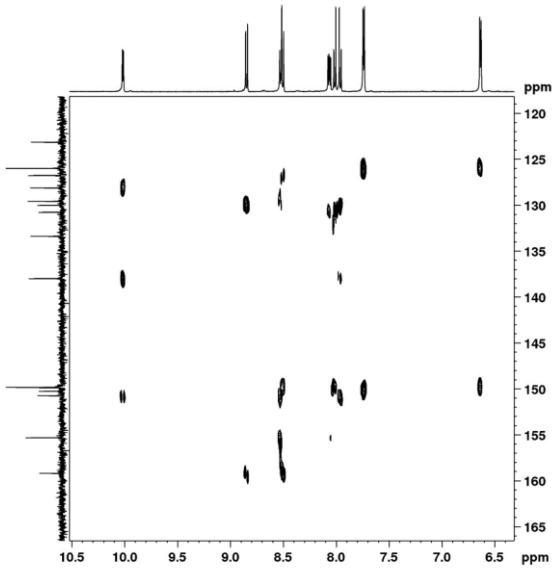

Figure S6. ^{1}H-^{13}C HMBC NMR of $\mathbf{1}^{2+}$ in D_2O at T= 298K.

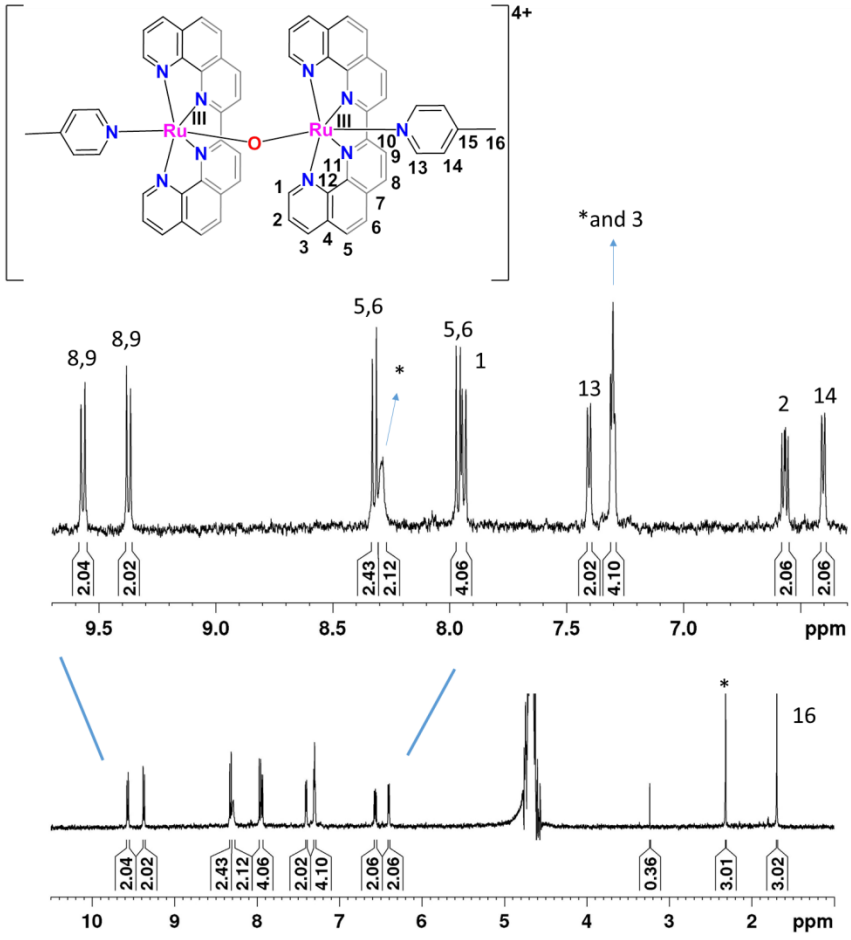

Figure S7. ^{1}H NMR spectrum of electrochemically generated $\mathbf{3}^{4+}$ from $\mathbf{1}^{2+}$ in a phosphate buffer (phbf) aqueous solution at pD 7 see (Figure S31 for CPE details). Asterisks indicate resonances of free picoline. Inset, enlargement of the aromatic region.

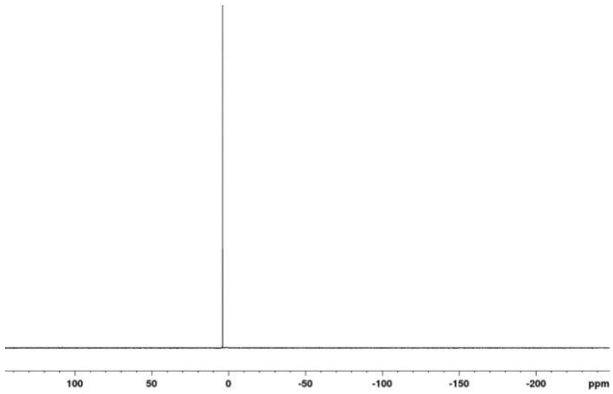

Figure S8. ^{31}P-NMR of **3**$^{4+}$ in a phbf aqueous solution at pD 7.

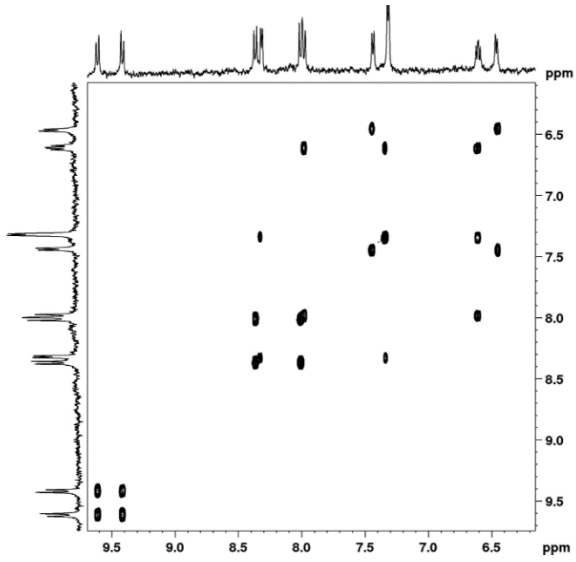

Figure S9. ^{1}H-^{1}H COSY of **3**$^{4+}$ in a phbf aqueous solution at pD 7.

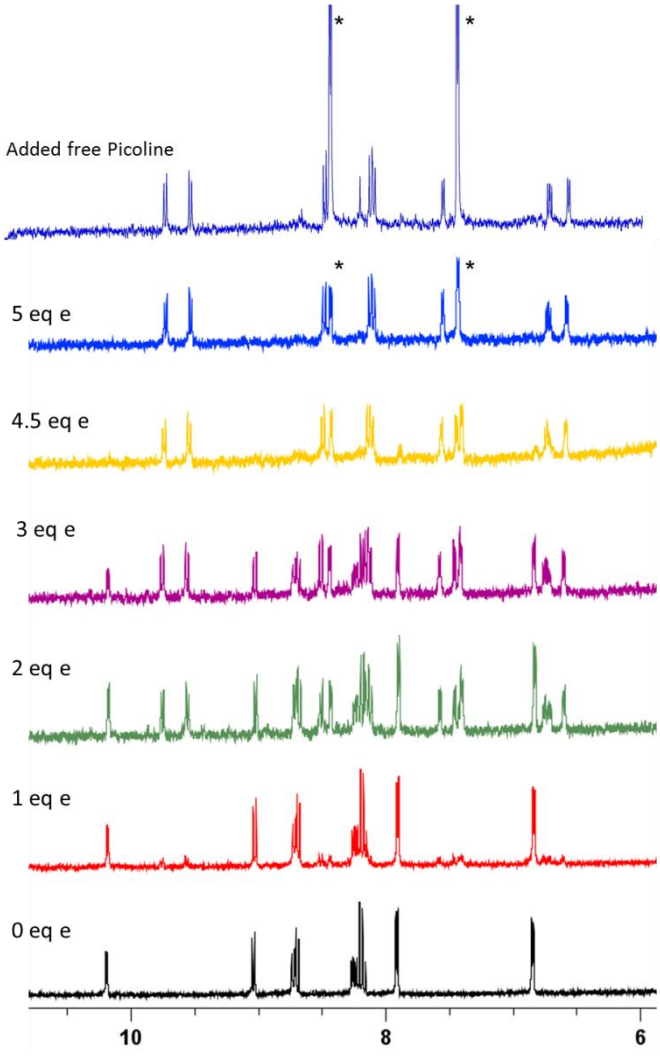

Figure S10. ^{1}H NMR monitoring of the electrochemical conversion of **1**$^{2+}$ into **3**$^{4+}$ in a phbf solution at pD 7 (see Figure S32 for CPE details). Asterisks indicate resonances of free picoline.

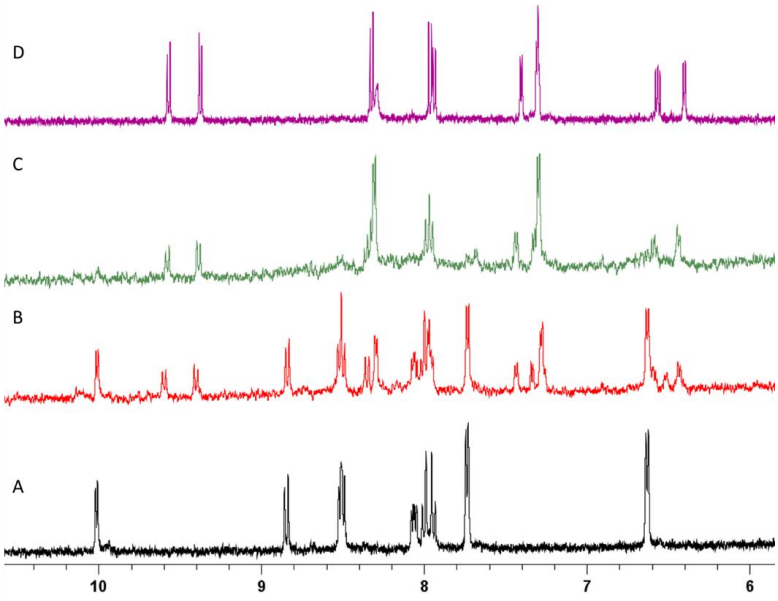

Figure S11. ^{1}HNMR spectra in a phbf aqueous solution at pD 7 of: A) $\mathbf{1}^{2+}$, B) $\mathbf{1}^{2+}$ + 2 eq $NaIO_4$, C) $\mathbf{1}^{2+}$ + 4.5 eq $NaIO_4$ and D) $\mathbf{3}^{4+}$ after bulk at E_{app}=1.45 V vs NHE.

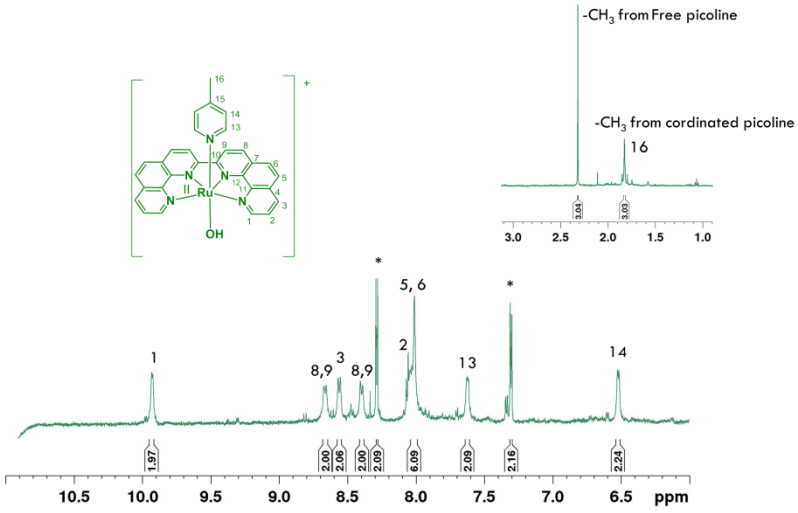

Figure S12. ^{1}H NMR spectrum of electrochemically generated $\mathbf{2}^{+}$ from $\mathbf{3}^{4+}$ in a phbf aqueous solution at pD 7 (see Figure S33 for CPE details). Asterisks indicate resonances of free picoline. Inset, enlargement of the aliphatic region.

VI

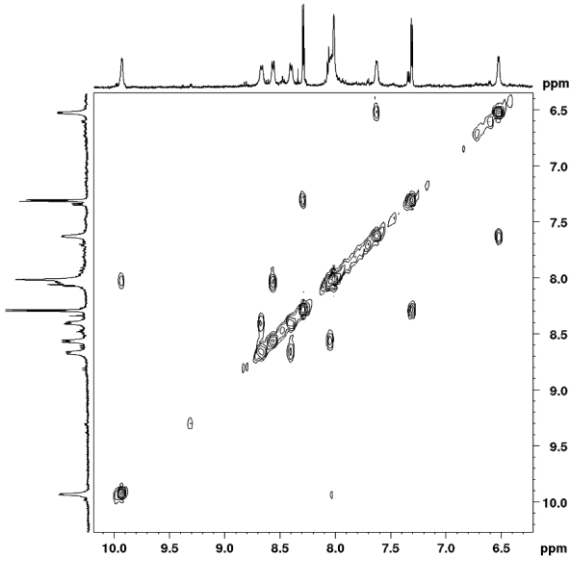

Figure S13. ^{1}H-^{1}H COSY of **2**$^{+}$ at pD 7 at T= 298K.

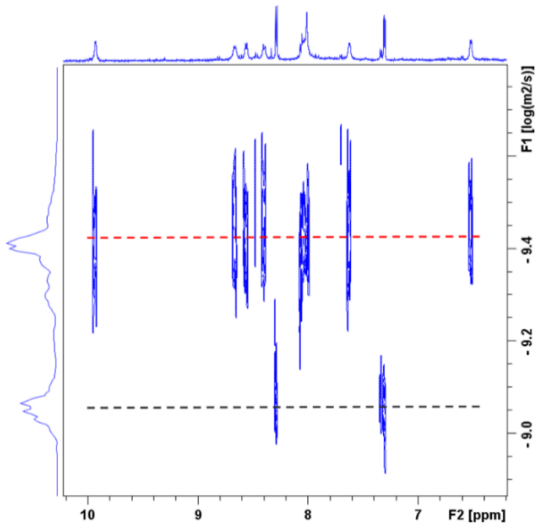

Figure S14. DOSY of **2**$^{+}$ at pD 7. Free picoline appears at *log D* = -9.05.

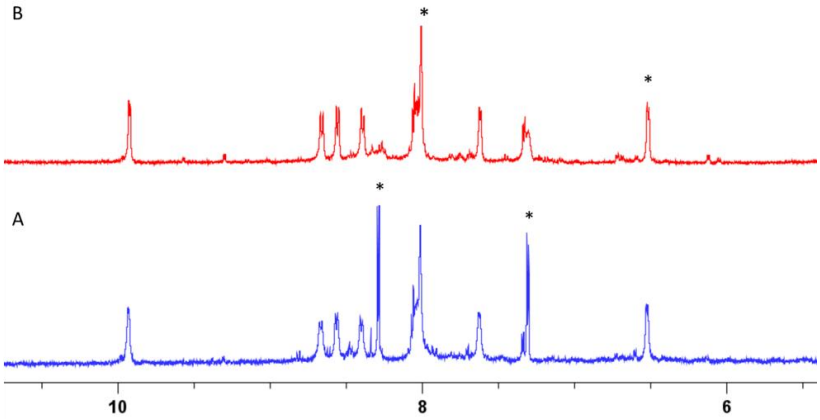

Figure S15. ^{1}HNMR spectra of electrochemically (bulk at E_{app}= 0.35 in a solution of $\mathbf{3}^{4+}$) A) and chemically (addition of L-ascorbic acid) B), generated $\mathbf{2}^{+}$ at pD 7. Asterisk indicate resonances of free picoline.

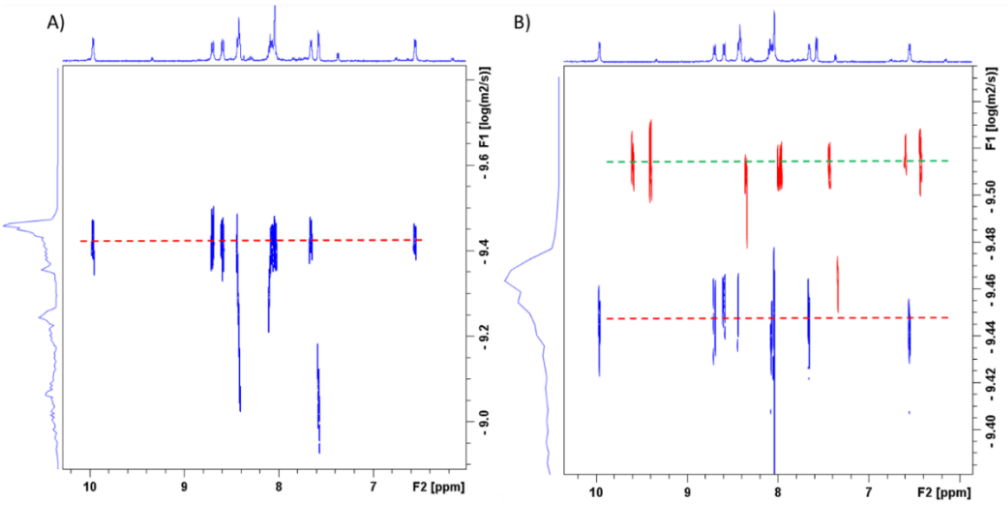

Figure S16. DOSY at pD 7 of: A) $\mathbf{2}^{+}$ and B) $\mathbf{2}^{+}$ (blue trace) + $\mathbf{3}^{4+}$ (red trace).

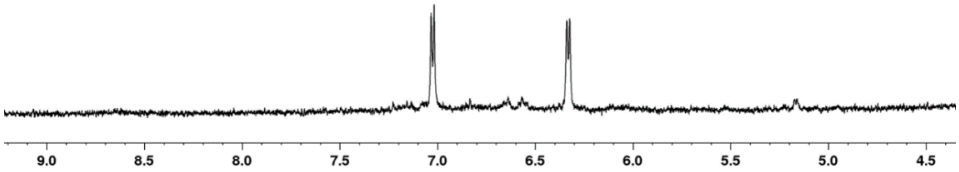

Figure S17. ^{1}HNMR of $\mathbf{1}^{2+}$ after bulk electrolysis at pD 1. (Figure S30 for CPE details).

Kinetic and Thermodynamic data

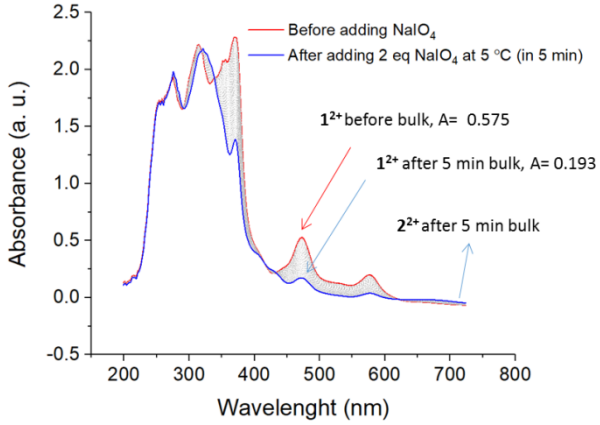

Figure S18. Spectral changes after adding 2 eq $NaIO_4$ ($8x10^{-4}$ mM) in a solution of $\mathbf{1}^{2+}$ ($4x10^{-4}$ mM) at pH 7.2, 0 min (Red color ($\mathbf{1}^{2+}$)) and 5 min (blue color ($\mathbf{2}^{2+}$)). The gray traces show the spectral changes every 10 seconds.

VI

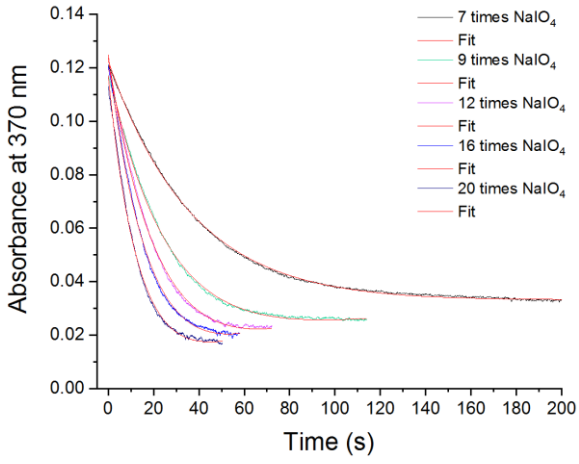

Figure S19. Kinetic traces recorded at 370 nm at various concentrations of oxidant (($NaIO_4$:7-20 eq), and a constant concentration of $\mathbf{1}^{2+}$ (0.125×10^{-4} M) at pH 7.2 phbf solution and 25 °C. The values of k_{obs1}, the pseudo-first order constants, were extracted by fitting this data to a 2-exponential function for each experiment.

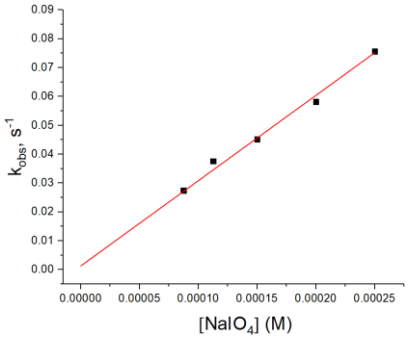

Figure S20. Linear plot of k_{obs1} (s^{-1}) values vs [$NaIO_4$]. 7–20 equivalent excesses of $NaIO_4$ ([$NaIO_4$] = (0.875 – 2.5) x 10^{-4} M) used over the concentration of $\mathbf{1}^{2+}$ (0.125×10^{-4} M) at pH 7.2 phbf solution and 25 °C. The values of k_{obs1} (s^{-1}) were obtained from the experimental data shown in Figure S19. The regression parameters to linear function y = ax + b, a = 295.44 ± 10.31, b = 0.0013 ± 0.0016, R^2 = 0.9952.

Table S1. Spectroscopic data for the calculation of [$\mathbf{2}^{2+}$] is taken from Figure S18.

ΔA [$\mathbf{1}^{2+}$]	Ɛ ($\mathbf{1}^{2+}$)	L	[$\mathbf{2}^{2+}$] = ΔA/ƐL
0.382	6472.52 $M^{-1}\cdot cm^{-1}$	1 cm^{-1}	5.9*10^$^{-5}$ M

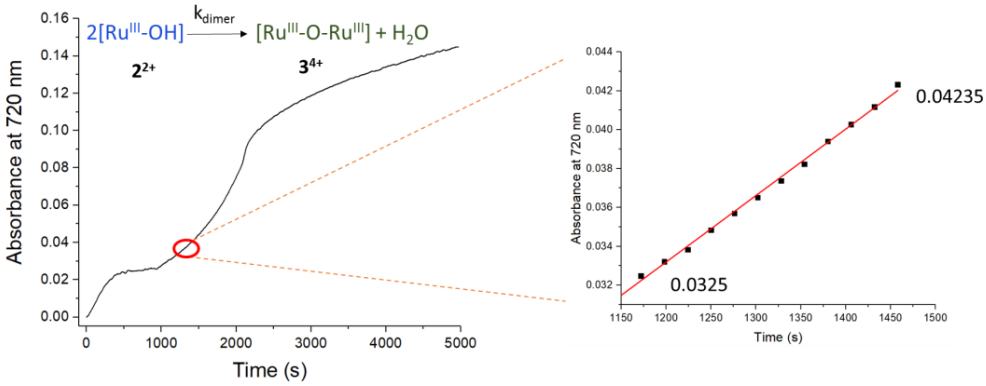

Figure S21. Left, Kinetic traces recorded at 720 nm during 82 min after adding 2 eq $NaIO_4$ at pH 7.2 phbf solution and 5 °C. Right, enlargement of the 1170-1460 s zone used for the calculation of [$\mathbf{3}^{4+}$].

VI

Table S2. Spectroscopic data for the calculation of $k_{initial}$ for the dimerization reaction (optical path length used, L = 1 mm). The data is taken from Figure S21.

Ɛ($\mathbf{3}^{4+}$)	Slope = ΔC/Δt	$v_{initial}$ = slope/ ε_{dim}.L	[$\mathbf{2}^{2+}$]	$k_{initial}$= $v_{initial}$ /[$\mathbf{2}^{2+}$]^2
7281.6 $M^{-1}\cdot cm^{-1}$	(3.42 ± 0.05) x 10^{-5} s^{-1}	(4,696 ± 0.069) x 10^{-9} M s^{-1}	5.9*10^{-5} M	1.349 ± 0.020 M^{-1} s^{-1}

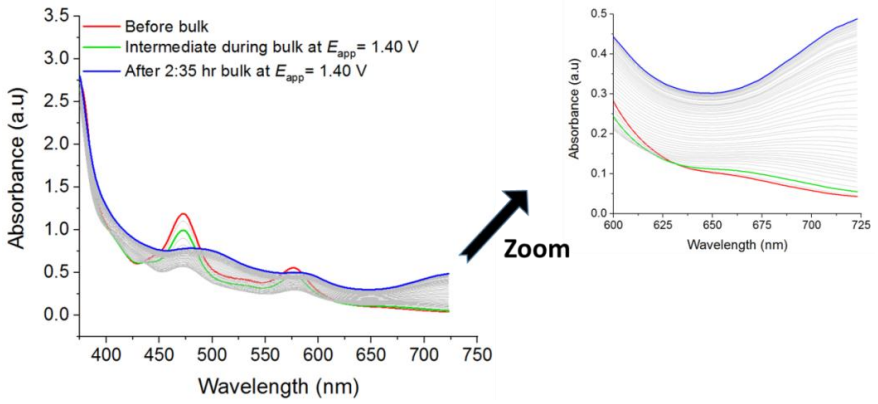

Figure S22. Spectral changes during a bulk electrolysis at E_{app}= 1.45 V in a phosphate buffer solution at pH 7, Red ($\mathbf{1}^{2+}$), Green ($\mathbf{2}^{2+}$), Blue ($\mathbf{3}^{4+}$). Conditions: [$\mathbf{1}^{2+}$] 0.2 mM, 50 mL phosphate buffer aqueous solution at pH 7, WE: Pt net electrode (simple cylindrical Pt wire electrode, diameter: 35 mm and cylinder height: 50 mm); CE: Pt wire; RE: silver wire, the potential reported vs NHE.

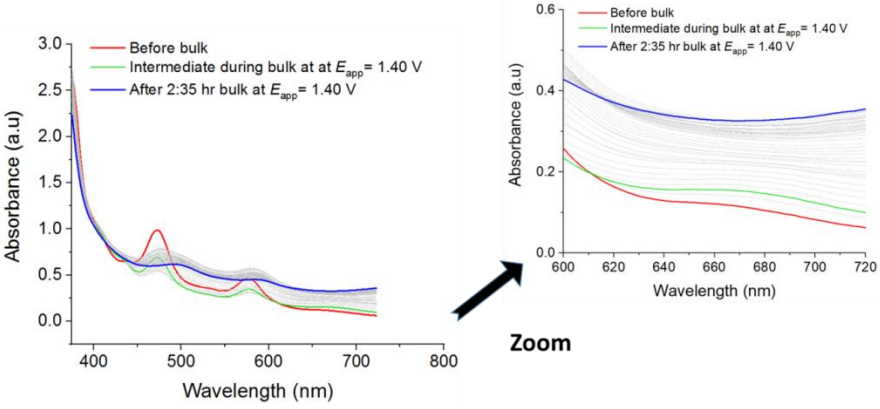

Figure S23. Following spectral changes before (red) and after (blue) a bulk electrolysis at E_{app}= 1.45 V in a phosphate buffer solution at pH 9. Conditions: [$\mathbf{1}^{2+}$] = 0.2 mM, 50 ml Sodium Borate aqueous solution at pH 9, WE: Pt net electrode (simple cylindrical Pt wire electrode, diameter: 35 mm and cylinder height: 50 mm); CE: Pt wire; RE: silver wire, the potential reported vs NHE.

The equilibrium concentrations of Ru^{III}-O-$^{III}Ru^{4+}$, $[Ru^{III}$-O-$^{III}Ru^{4+}]_e$, were calculated from the spectral changes after adding various concentrations of oxidant ($NaIO_4$) and the known dimer extinction coefficient at λ = 791 nm (7281.6 $M^{-1}\cdot mm^{-1}$). In order to calculate $[Ru^{III}$-$OH^{2+}]_e$, first the starting concentration of Ru^{III}-OH^{2+}, $[Ru^{III}$-$OH^{2+}]_0$, was calculated from spectral changes of $[\mathbf{1}^{2+}]$ after adding various amounts of oxidant and the known extinction coefficient of $\mathbf{1}^{2+}$ at λ = 472 nm (ε = 6472.52 $M^{-1}\cdot mm^{-1}$). Then, $[Ru^{III}$-$OH^{2+}]_e$ was calculated from Eq S1 (Table S3).

$$[Ru^{III}\text{-}OH^{2+}]_e = [Ru^{III}\text{-}OH^{2+}]_o - 2\,[Ru^{III}\text{-O-}{}^{III}Ru^{4+}]_e \qquad \text{(Eq. S1)}$$

Table S3. Absorbance changes for after addition of various concentrations of oxidant $NaIO_4$ to $\mathbf{1}^{2+}$.

$\mathbf{1}^{2+}$:$NaIO_4$	A (471 nm) ($\mathbf{1}^{2+}$)	ΔA (at 471 nm) ($\mathbf{2}^{2+}$)	ΔA (at 791 nm) ($\mathbf{3}^{4+}$)
1-0.5	0.616	0.570	0.02032
1-1	0.621	0.4883	0.0405
1-2	0.605	0.3081	0.12150
1-3	0.564	0.1852	0.12239

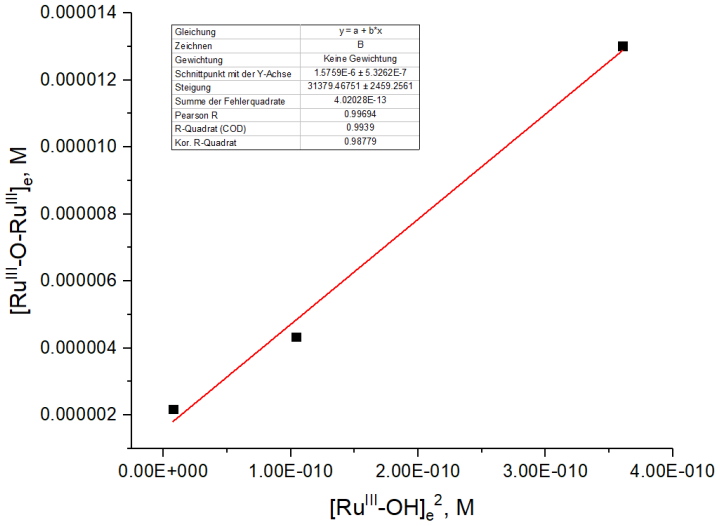

Figure S24. Linear plot of $[Ru^{III}\text{-}O\text{-}^{III}Ru^{4+}]_e$ ($[\mathbf{3}^{4+}]_e$) *vs* $[Ru^{III}\text{-}OH^{2+}]_e^2$, ($[\mathbf{2}^{2+}]_e^2$). to estimate the value of equilibrium constant K_e for the dimerization reaction.

Electrochemical activity in organic and aqueous solution

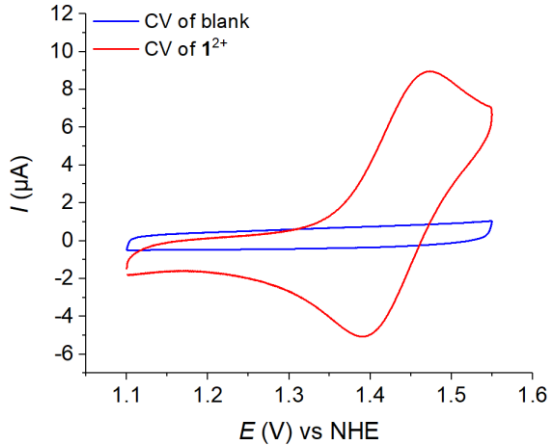

Figure S25. CV of $\mathbf{1}^{2+}$ (1 mM) in a solution of TFE and 0.1 M $(Bu_4N)PF_6$. WE: glassy carbon electrode; CE: platinum electrode; RE: Hg/Hg_2SO_4. SR: 100 mV/s.

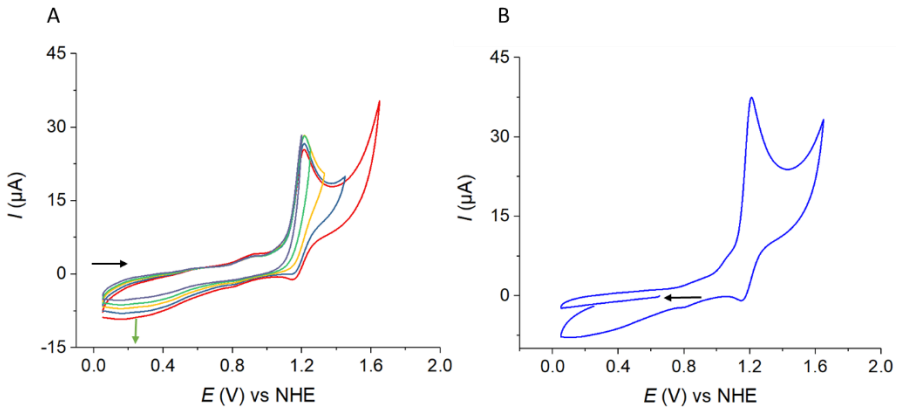

Figure S26. A) CV of $\mathbf{1}^{2+}$ in a phbf aqueous solution at pH 7 in different potential ranges. B) CV of $\mathbf{1}^{2+}$ in cathodic direction. Conditions: [$\mathbf{1}^{2+}$]: 1mM, WE: glassy carbon electrode; CE: platinum electrode; RE: Hg/Hg_2SO_4. Black arrows show the scan direction.

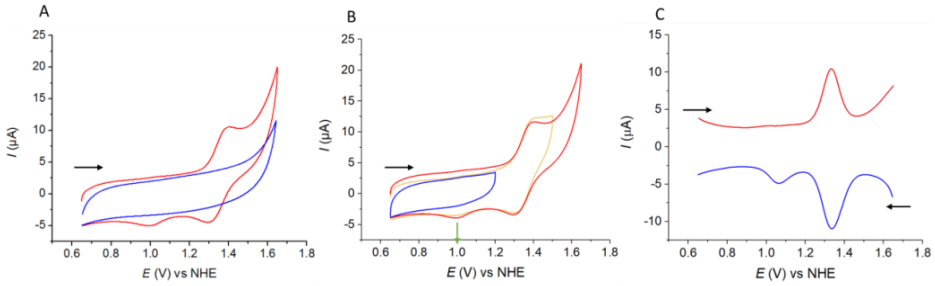

Figure S27. A) CV of $\mathbf{1}^{2+}$ (1mM) in a solution of TA:TFE (2:1) (TA, 0.1 M, pH 1). B) CV of $\mathbf{1}^{2+}$ in different potential ranges. C) DPV (Red line) from cathodic to anodic potential. DPV (blue line) of $\mathbf{1}^{2+}$ from anodic to cathodic potential. WE: glassy carbon electrode; CE: platinum electrode; RE: Hg/Hg_2SO_4. SR: 100 mV/s. Black arrows show the scan direction.

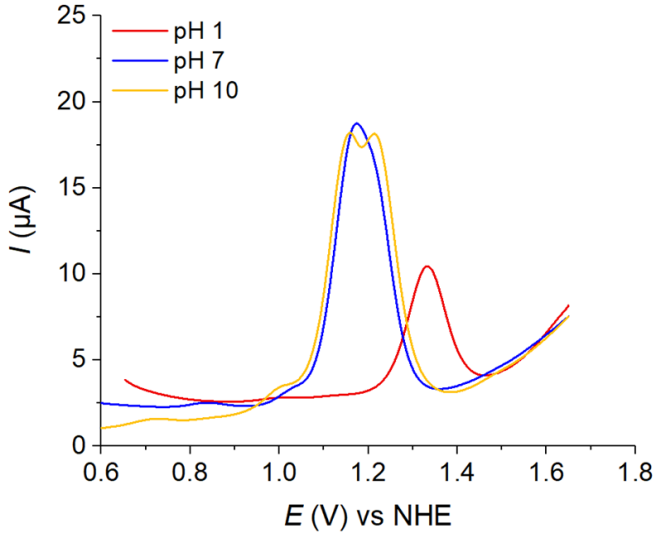

Figure S28. DPVs of $\mathbf{1}^{2+}$ at pH 1, 7, and 10. Conditions: [$\mathbf{1}^{2+}$]: 1 mM, pHs: pH 1 (TA:TFE / 2:1), pH 7 and 10 in a phbf aqueous solution. WE: glassy carbon electrode; CE: platinum electrode; RE: Hg/Hg_2SO_4, SR: 100 mV/s. Arrows show the scan direction.

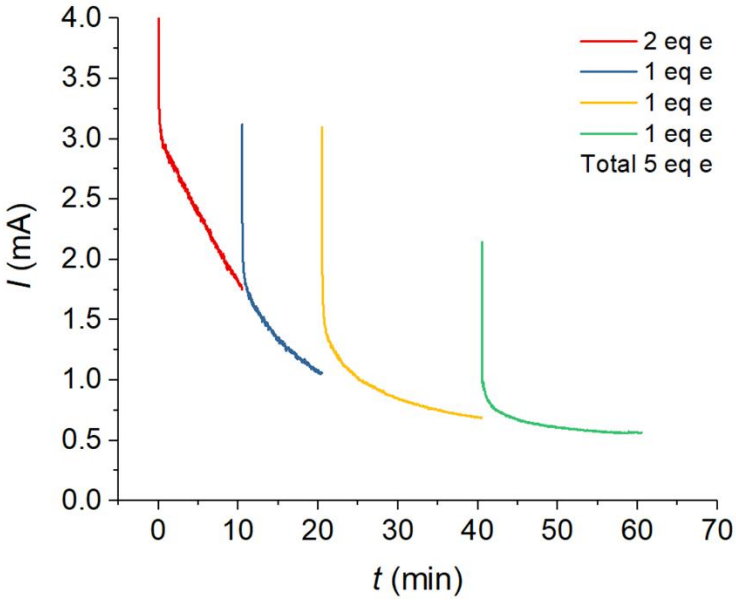

Figure S29. CPE at E_{app} = 1.45 V vs NHE of a solution of $\mathbf{1}^{2+}$ (1.34 mM, 6.4 mL, pH 7 phbf; 8.57 µmols) using a Pt net electrode (cylindrical net; 10 mm diameter, 30 mm height) as a working electrode, Hg/Hg_2SO_4 as reference electrode and a Pt mesh as auxiliary electrode (20*20 mm mesh). The charge passed was integrated to be 4.145 C, giving 5 equivalents of electrons.

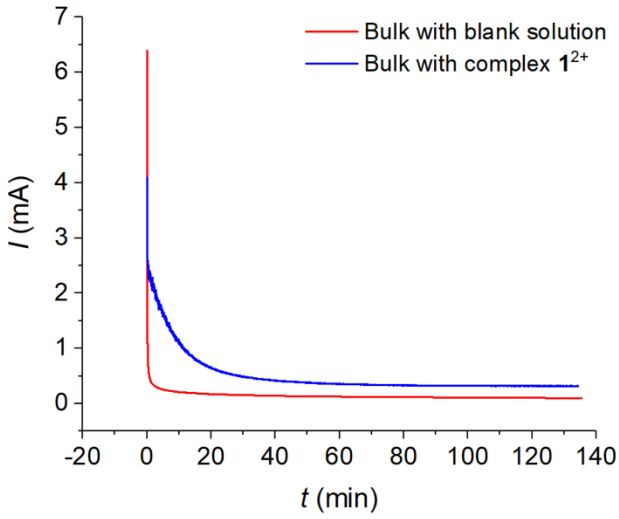

Figure S30. Comparison of bulk electrolysis of $\mathbf{1}^{2+}$ (blue) and blank (Red). The blue current shows that for full conversion of $\mathbf{1}^{2+}$ to $\mathbf{3}^{4+}$, after subtraction from blank current, 4 eq electrons are needed. CPE at E_{app}= 1.45 V vs NHE of a solution of $\mathbf{1}^{2+}$ (1.34 mM, 5 mL, pH 7 phbf; 6.7 µmols) using a Pt net electrode (simple cylindrical Pt net electrode, diameter: 10 mm and cylinder height: 30 mm) as a working electrode, Hg/Hg_2SO_4 as reference electrode and a Pt mesh as auxiliary electrode (simple square mesh net 20*20 mm).

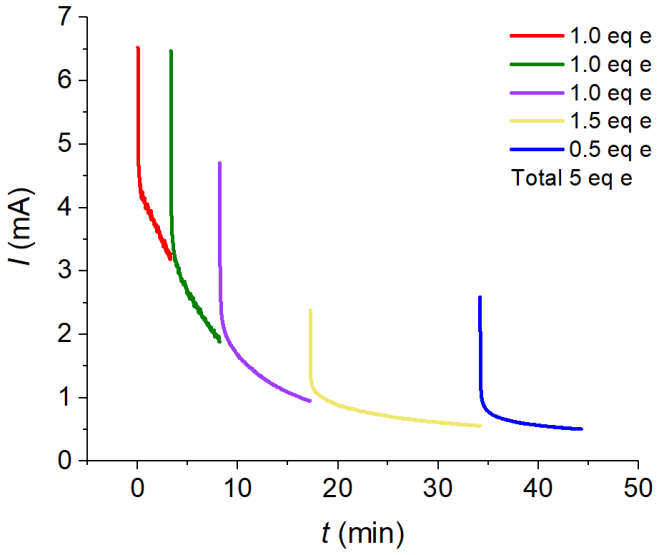

Figure S31. CPE at E_{app} = 1.45 V vs NHE of a solution of $\mathbf{1}^{2+}$ (1.34 mM, 5 mL, pD 7 phbf; 6.7 μmols) using a Pt net electrode (simple cylindrical Pt net electrode, diameter: 10 mm and cylinder height: 30 mm) as a working electrode, Hg/Hg_2SO_4 as reference electrode and a Pt mesh as auxiliary electrode (simple square mesh net 20*20 mm. The charge passed was integrated to be 3.37 C, giving 5 equivalents of electrons.

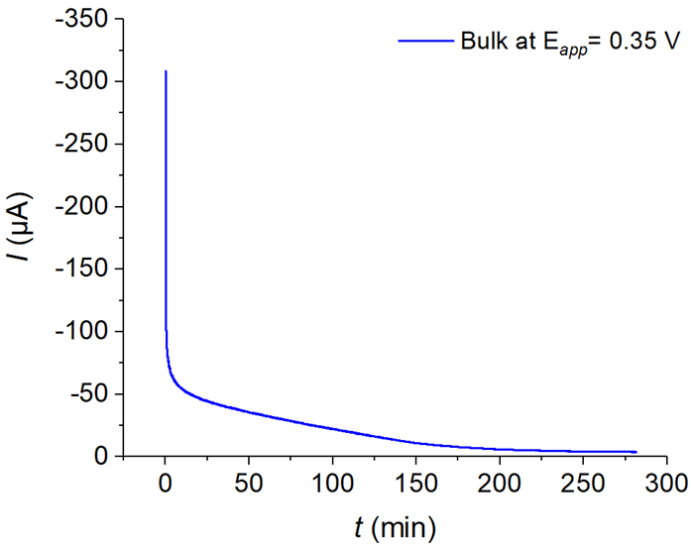

Figure S32. CPE at E_{app} = 0.35 V vs NHE of a solution of $\mathbf{3}^{4+}$ (0.67 mM, 2 mL, pD 7 phbf; 1.34 µmols) using a Pt net electrode (simple cylindrical Pt net electrode, diameter: 10 mm and cylinder height: 30 mm) as a working electrode, Hg/Hg_2SO_4 as reference electrode and a Pt mesh as auxiliary electrode (simple square mesh net 20*20 mm. The charge passed was integrated to be 0.32 C, giving 2.5 equivalents of electrons.

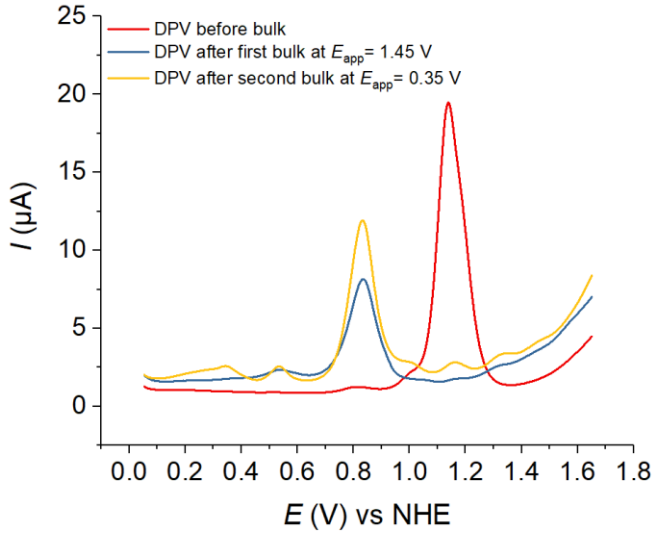

Figure S33. DPVs, before bulk (Red line) in a phbf aqueous solution of $\mathbf{1}^{2+}$ at pD 7**,** after first bulk at E_{app}= 1.45 V (blue line) (Figure S31), and second bulk at E_{app}= 0.35 V (yellow line) in a solution of $\mathbf{3}^{4+}$ (Figure S32), Conditions: WE: glassy carbon electrode; CE: platinum electrode; RE: Hg/Hg_2SO_4.

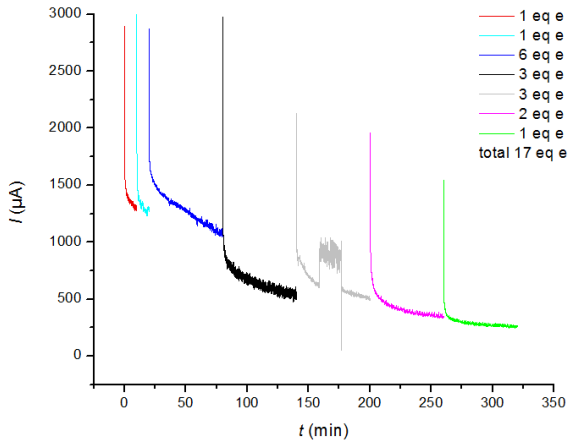

Figure S34. CPE at E_{app}= 1.65 V vs NHE of a solution of $\mathbf{1}^{2+}$ (1 mM, 6 mL, pH 1 (TA:TFE/2:1); 8.04 μmols) using a Pt net electrode (simple cylindrical Pt net electrode, diameter: 10 mm and cylinder height: 30 mm) as a working electrode, Hg/Hg_2SO_4 as reference electrode and a Pt mesh as auxiliary electrode (simple square mesh net 20*20 mm). The charge passed was integrated to be 13.52 C, giving 16.8 equivalents of electrons.

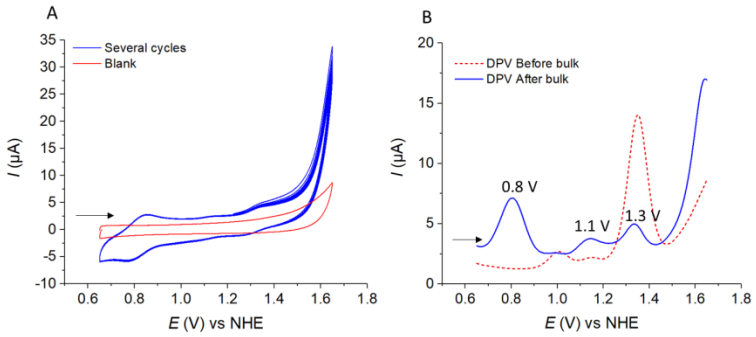

Figure S35. A) 25 Consecutive CVs after bulk at E_{app}= 1.65 V in a solution of $\mathbf{1}^{2+}$ at pH 1 (TA:TFE (2:1), [TA]= 0.1 M). B) DPV of $\mathbf{1}^{2+}$ (1 mM) before and **2** and after bulk electrolysis. WE: glassy carbon electrode; CE: platinum electrode; RE: Hg/Hg_2SO_4. SR: 100 mV/s. Red arrows show the evolving of new species while $\mathbf{1}^{2+}$ is consuming. Black arrows show the scan direction.

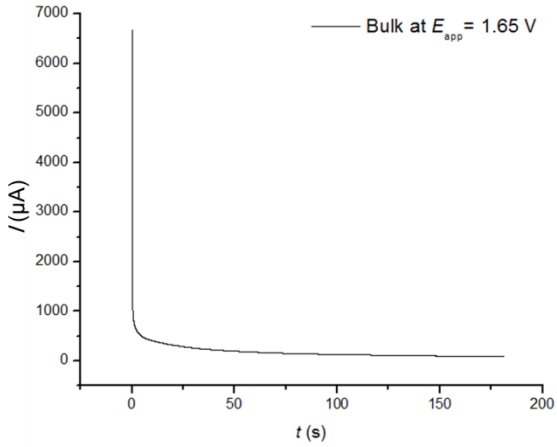

Figure S36. CPE at E_{app} = 1.65 V vs NHE of a solution of $\mathbf{1}^{2+}$ (1 mM, 1.2 mL, pD 1 (CF_3COOD: CF_3CD_2OD, 2:1); 1.2 μmols) using a Pt net electrode (simple square mesh net 20*20 mm) as a working electrode, Hg/Hg_2SO_4 as reference electrode and a Pt mesh as auxiliary electrode (simple square mesh net 20*20 mm). The charge passed was integrated to be 2 C, giving 17 equivalents of electrons.

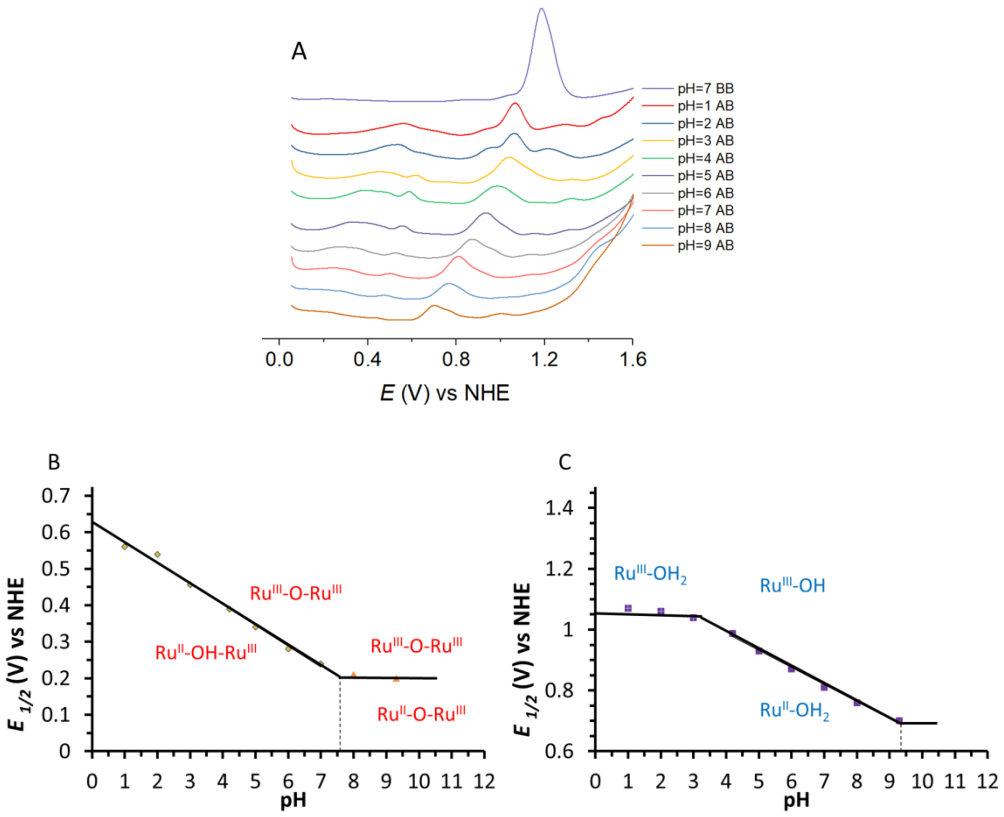

VI

Figure S37. A) DPVs after bulk at E_{app}= 1.45 V at different pHs, the pH of bulk solution was changed from 7 to 1 and from 7 to 12 gradually by adding phosphoric acid and concentrated NaOH respectively. DPV was measured in every different pHs and the redox waves were taken from DPVs. BB before bulk, AB, After bulk B) Pourbaix diagram for $\mathbf{3}^{4+}$ after bulk at E_{app}= 1.45 V in a phbf aqueous solution at pH 7, C) Pourbaix diagram for $\mathbf{2}^{2+}$ after bulk at E_{app}= 1.45 V in a phosphate buffer solution at pH 7.

UV-vis data

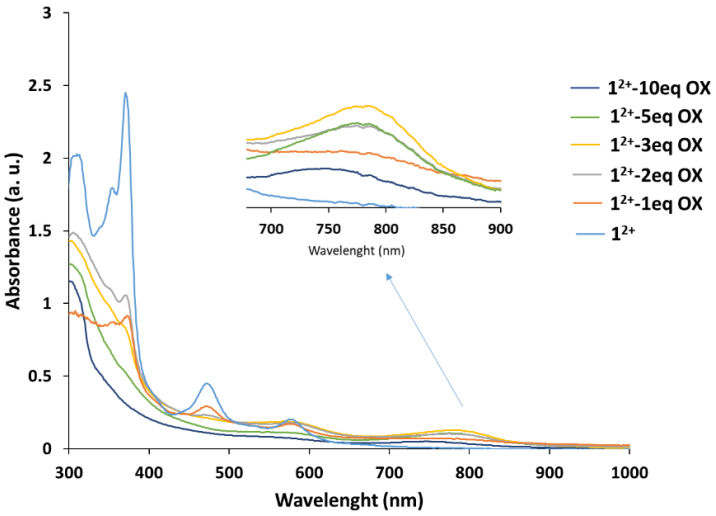

Figure S38. Recorded UV-vis spectra in a solution of $\mathbf{1}^{2+}$ (1mM) after addition of 1 to 10 eq of $NaIO_4$ in a phbf aqueous solution at pH 7. Inset enlargement of the 700-900 nm region.

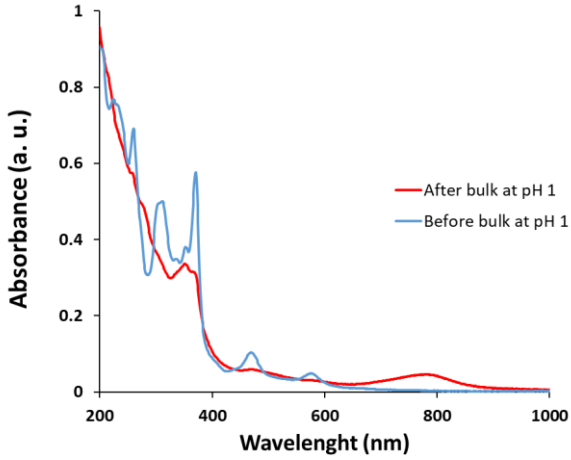

Figure S39. Electronic absorption spectra of $\mathbf{1}^{2+}$ (blue color) and new compound (red color) after bulk at E_{app}= 1.65 V in a 1mM solution of $\mathbf{1}^{2+}$ at pH 1 (TA-TFE (2:1) ([TA]= 0.1 M).

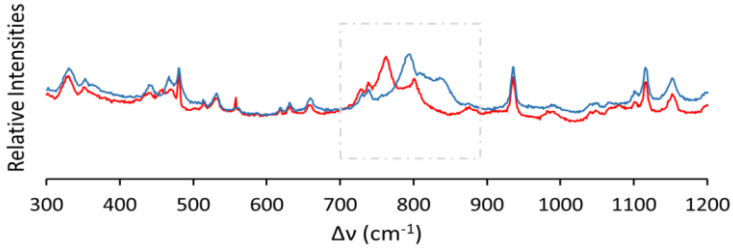

Figure 40. rRaman spectra of an aqueous solution of $\mathbf{3}^{4+}$ prepared *in situ* from $\mathbf{1}^{2+}$ after a bulk electrolysis at E_{app} = 1.45 V at pH 7 phbf solution in H_2O^{16} (blue) and H_2O^{18} (red).

Reference

Tong, L.; Zong, R.; Zhou, R.; Kaveevivitchai, N.; Zhang, G.; Thummel, R. P., Ruthenium catalysts for water oxidation involving tetradentate polypyridine-type ligands. *Faraday discussions* **2015,** *185*, 87-104.

Chapter 7

Conclusions

This thesis is a reflection of the complexity and richness of ruthenium chemistry in the context of water oxidation catalysis. In the next bullet points, the most important conclusions derived from this work are highlighted.

Chapter 3:

- A thorough study of the coordination of a water molecule to Ru-bda type of complexes at low oxidation states has shown the fundamental need for a flexible and adaptable ligand, as is the case for the bda, both from an electronic and geometrical perspective, to comply with the demands of the Ru metal center at the different oxidation states required for the water oxidation catalysis.
- The presence of isomers in Ru-bda complexes where the equatorial bda ligand acts in a κ-NO^2 fashion instead of the typical κ-N^2O^2 or κ-N^2O modes has been described for the first time.

Chapter 4:

- An electrochemical study of two ruthenium complexes of the Ru-bda family with isoquinoline axial ligands containing carboxylic acid (-CO_2H) or methyl ester (-CO_2Me) groups close to the metal center suggests that a strong hydrogen bonding network around the ruthenium is formed in aqueous solution and that it has a significant influence on their catalytic behavior at pH 1.
- While the ester derivative follows the typical bimolecular I2M mechanism for the water oxidation catalysis at pH 7, the acid derivative shows a behavior that differs from the typical unimolecular or bimolecular mechanisms described to date. This unique catalytic nature of the acid derivative is associated with a stronger hydrogen bonding network at this pH, at which the carboxylic acid groups are deprotonated.

Chapter 5:

- A ruthenium complex of the Ru-bda family with a dangling carboxylate group in the ortho position of an axial pyridine has been prepared electrochemically *in situ* through intramolecular oxidation of the corresponding benzylic alcohol derivative, highlighting the reactivity of high valent Ru=O group in the oxidation of aliphatic groups.
- Crystal structures of this family of compounds have shown that the coordination sphere around the ruthenium is close to a perfect octahedral geometry with angles around 90°. This result is in sharp contrast to the geometry of the equatorial ligand in the popular catalyst $[Ru(bda)(pic)_2]$, forcing a distorted octahedral geometry with O-Ru-O angle of 124° at oxidation state Ru^{II}.
- The new ruthenium complex has shown catalytic activity for water oxidation catalysis with TOF_{max} = 3.1 s^{-1} at an onset potential of 1.3 V which is amongst the best reported to date. However, it doesn't overcome the results obtained for $[Ru(bda)(pic)_2]$ under the same experimental conditions (TOF_{max} = 11 s^{-1} at 1.1 V s^{-1}). The lower performance of the new catalyst has been attributed to the different geometrical requirements of the equatorial and axial ligands.

Chapter 6:

- Exhaustive electrochemical, structural, kinetics and spectroscopic studies of a Ru-bpn complex provided a detailed description of the nature of the reactions and produced species involved in water oxidation catalysis.
- The results show that there are three consecutive reactions after the electrochemical oxidation of Ru-bpn including i) the oxidation of Ru^{II} to Ru^{III}, ii) the replacement of an axial picoline ligand with OH^-, and finally iii) the dimerization of two Ru^{III}-OH complexes.
- Chemical water oxidation catalysis using $(NH_4)_2Ce(NO_3)_6$ showed catalytic activity after a short induction time in agreement with the transformation reactions preceding the catalytic behavior.

Annex

Glossary of terms and abbreviations

8-isoq-CO_2H	8-isoquinolinecarboxilic acid
8-isoq-CO_2Me	methyl 8-isoquinolinecarboxilate
ALD	Atomic layer deposition
APT	Atom proton transfer
ATP	Adenosine triphosphate
bda	2,2´-bipyridine-6,6´-dicarboxylate
bpn	2,2'-bi(1,10-phenanthroline)
bpy	bipyridine
CAN	Ceric Ammonium Nitrate
CV	Cyclic Voltammetry
DCM	Dichloromethane
DFT	Density Functional Theory
DPV	Differential Pulse Voltammetry
E	Potential
E°	Standard potential
$E_{½}$	Half wave potential
EDG	Electron Donating Group

ESI-MS	Electrospray Ionization Mass Spectrometry
EWG	Electron Withdrawing Group
FOWA	Foot of the Wave Analysis
HOMO	Highest Occupied Molecular Orbital
i	Current
I2M	Interaction between two M-O entities
i_p	Current intensity
Isoq	Isoquinoline
j	Current density
LUMO	Lowest Unoccupied Molecular Orbital
m/z	Mass-to-Charge ratio
NHE	Normal Hydrogen Electrode
NMR	Nuclear Magnetic Resonance
N-NH_2	4-(pyridin-4-yl)aniline
OEC	Oxygen Evolving Center
P	Photosensitizer
PCET	Proton Coupled Electron Transfer
phbf	Phosphate buffer
Pic	Picoline
PSI	Photosystem I
PSII	Photosystem II

py	pyridine
PyA	pyridine-2-ylmethanol
PyC	2-pyridinecarboxylate
pyE	methyl 2-pyridine carboxylate
r.d.s	Rate limiting step
rR	Resonance Raman
SEA	Sacrificial Electron Acceptor
TA	Triflic acid
tda	[2,2′:6′,2″-terpyridine]-6,6″-dicarboxylate
TOF	Turnover Frequency
TON	Turnover Numbers
tpy	2,2′:6′,2″-terpyridine
TS	Transition State
UV-vis	Ultraviolet-visible Spectroscopy
WNA	Water Nucleophilic Attack
XAS	X-ray absorption spectroscopy
XRD	X-ray diffraction
ε	Extinction coefficient

UNIVERSITAT ROVIRA I VIRGILI
RUTHENIUM COMPLEXES AS MOLECULAR WATER OXIDATION CATALYSTS
Abolfazl Ghaderian

UNIVERSITAT
ROVIRA i VIRGILI